The influence of intraglottal vortices upon the dynamics of the vocal folds

by

Brian Quinn Kettlewell

A thesis
presented to the University of Waterloo
in fulfillment of the
thesis requirement for the degree of
Master of Applied Science
in
Mechanical Engineering

Waterloo, Ontario, Canada, 2015

I hereby declare that I am the sole author of this thesis. This is a true copy of the thesis, including any required final revisions, as accepted by my examiners.

I understand that my thesis may be made electronically available to the public.

Abstract

Intelligibility of speech is of critical importance in many respects. Diminished speech intelligibility causes part or all of the intended message to be lost to listeners; the outcome is frustration of speakers and listeners in the least, but impaired communication may be dangerous in some situations. Consequently, improved understanding of the factors which contribute to intelligibility of speech is of great interest in the speech community. For example, the rapid closing of the glottis in the closing phase of the phonatory cycle is generally understood to contribute favourably to the intelligibility of speech by increasing the high frequency content of the resulting speech signal. Recent experimental and numerical studies have suggested that the presence of intraglottal vortices in the closing phase of the phonatory cycle might promote rapid closing of the glottis due to the pressure gradients which arise in the presence of the vortices. To date, computational studies to assess the impact of vortex shedding within the glottis which incorporate a dynamical model of the vocal fold tissues together with a vortex advection scheme are not prevalent. In a recent computational study, an ad hoc pressure condition, of magnitude on the order of the disturbances observed in experimental work, was superimposed upon the medial vocal fold surfaces to simulate the effect of a perturbation of the pressure field. However, this approach, while it is able to quantify the effect of a perturbation of the pressure field, is not wholly satisfactory because the temporal or spatial evolution of the perturbation of the pressure field is not a consequence of a modelled physical effect or mechanism which is fundamentally related to the physics of the fluid or the fluid-structure interaction.

In the present study, a two-dimensional ideal potential flow model is developed and coupled to a low-order lumped-element dynamical model of the vocal folds. Irrotational vortices are superimposed upon the glottal flow and allowed to advect through the glottis from an upstream station at a rate which ensures that they will arrive at the superior portion of the glottis in the closing phase of the phonatory cycle, when the glottis obtains its diverging configuration. This is to emulate the roll-up and shedding of intraglottal vortices occurring in the closing phase of the phonatory cycle. The vortices may be removed to compare the dynamical response of the vocal fold tissue model in the absence or presence of the intraglottal vortices.

The extension of the glottal flow model to two-dimensions is important in general, not merely because it allows for the inclusion of effects which require higher spatial dimension for their description, such as advecting vortices, but the two-dimensional glottal flow model captures the salient physics of glottal flow with improved fidelity over the standard one-dimensional Bernoulli flow models which have typically been employed in studies of phonation. Additionally, the pressure field, which is unsteady in glottal flow, is determined with the unsteady Bernoulli equation; the unsteady term is found to be significant, thus, again, the model improves upon potential flow models employed to date. The surface pressure on the medial surface of the vocal folds exhibits strong deviation near the inferior and superior margins of the medial surfaces, and, because these entail longer moment arms, larger pitching moments are obtained. It is demonstrated that the mucosal wave, in the transverse motion of the vocal folds, as the cover tissues pitch about their respective nodal

points, a greater amplitude of angular displacement is observed with the two-dimensional model. The resulting glottal area waveform obtains a more skewed appearance which causes it to qualitatively appear more closely akin to clinically obtained glottal waveforms despite that the simulation model is uncoupled from the acoustics of the upper vocal tract.

In comparing the simulation results, the effect of the vortices is seen to be ephemeral; the vortices rapidly advect into the supraglottal space whence they impart little upstream influence. The vortex strength determines two competing effects, which entails that the vortices should have little effect upon the dynamics of the vocal folds. In particular, as the strength of the vortices increases, the magnitude of the pressure perturbation becomes more significant, however, for a given vortex spacing, the vortices will advect more rapidly into the supraglottal region thus rapidly reducing their effect; because the perturbation of the pressure field is brief, it does not impart sufficient impulse to overcome the inertia of the vocal fold tissues. Alternatively, as vortex strength decreases, the intraglottal vortices dwell in the glottal space longer, but the magnitude of the pressure perturbation is significantly diminished. Again, the modified pressure field does not impart sufficient impulse to overcome the inertia of the vocal folds, and their behaviour remains relatively unperturbed. That the glottal area waveform in its closing phase is essentially unaffected by the presence of intraglottal vortices is demonstrated within the proposed modelling framework.

Acknowledgements

Firstly, I owe much to my advisor, Dr. Sean D. Peterson. I am grateful for his patience, encouragement, and, above all else, his perspicacity. His ability to keenly identify the essence of an argument has made my work far better than I could have imagined. He has inspired me to think more critically and systematically about physical meaning in mathematical representation.

I would like to thank my committee members, Dr. Steven L. Waslander and Professor Edward R. Vrscay, for kindly taking time from their busy schedules to provide a careful reading of my thesis. They helped clarify my thinking on several difficult points.

Amongst my countless colleagues and friends who have helped me on this journey, I want to mention, in particular, Kevin Chen, Tom Kirk, Cody Prodaniuk, Lawrence Leung, Adrian Wong, Brian Fan, Chris Morton, Manpreet Bansal, Dave Sommer, Jennifer Book, and Chekema Prince, I offer you thanks and gratitude.

For the Schwarz-Christoffel Toolbox for MATLAB, written by Tobin A. Driscoll, I am indebted. Without such a robust and clearly documented toolbox for computing SC transforms, this thesis would have evolved much differently than it has.

I wish to acknowledge the financial support of the University of Waterloo Fluid Mechanics Graduate Scholarship and the Queen Elizabeth II Graduate Scholarship in Science and Technology, without which this project would not have been possible.

Finally, but not in the least, I would like to thank Jee Young Kim for being a constant source of joy and motivation throughout.

Dedication

To my family,

and to everyone who has helped me on this journey.

Table of Contents

List of Figures

List of Tables

Symbols and Abbreviations

∇	gradient operator
∇_X	gradient operator within XYZ coordinate system
∇^2	Laplacian, $\nabla^2 = \nabla \cdot \nabla$
$\|\cdot\|$	Euclidean vector norm
Γ	circulation, $\Gamma = \oint_{\mathcal{C}} \vec{u} \cdot d\vec{r}$
δ	minimal allowable glottal area for non-vanishing glottal flow
$\delta t^{(n)}$	timestep at n^{th} iteration, $\delta t^{(n)} = t_{n+1} - t_n$
ζ	complex variable in auxiliary plane
ζ_0	a determined point in the auxiliary plane, perhaps the location of a source or singularity
ζ_{0k}	the centre of the k^{th} vortex in the auxiliary plane
η	imaginary part of $\zeta = \xi + i\eta \in \mathbb{C}$
θ	angular displacement of cover from equilibrium
θ_{ng}	neutral glottal angular displacement, also called pre-phonatory angle of convergence
κ	torsional stiffness of vocal fold cover
μ	dynamics viscosity of fluid
ν	kinematic viscosity of the fluid, $\nu = \mu/\rho$
ξ	real part of $\zeta = \xi + i\eta \in \mathbb{C}$
ρ	fluid density
Σ	a patch of surface
φ	potential in auxiliary plane
Φ	potential in physical plane
$\widetilde{\Phi}$	potential in physical plane observed relative to a moving frame of reference
Ω	region of space identified to be flow domain
$\partial\Omega$	boundary of flow domain
A_e	geometric parameter for epilaryngeal cross-sectional area
A_{ng}	neutral glottal area

A_s	geometric parameter for subglottal cross-sectional area
b	translational damping of cover
b_d	mechanical damping of diaphragm
b_t	mechanical damping of tissues of thoracic wall
B	translational damping of body mass
B_c	torsional damping of cover
$C(t)$	a curve in the plane at time t
$\mathbb{C}$	the field of complex numbers
f	complex function of a complex variable, often a conformal mapping
f_s	sampling frequency
f_0	fundamental frequency of phonation produced at the vocal folds
F	complex potential in physical plane
$\widetilde{F}$	complex potential in auxiliary plane
F_a	resultant aerodynamic vocal fold loading
h_e	geometric parameter for epilaryngeal channel width, $h_e = A_e/l$
h_{ng}	neutral glottal width, $h_{ng} = A_{ng}/l$
h_s	geometric parameter for subglottal channel width, $h_s = A_s/l$
I_c	moment of inertial of vocal fold cover
k	translational stiffness of vocal fold cover
k_d	mechanical stiffness of diaphragm
k_{lung}	mechanical stiffness of lung
k_t	stiffness of tissues of thoracic wall
K	translational stiffness of vocal fold body
l	geometric parameter for vocal fold length
l_c	characteristic length scale
L	the dimension of length
m	vocal fold cover mass
M	vocal fold body mass
M	the symbol for the dimension of mass
M_d	mass of diaphragm
M_t	mass of thoracic wall
$\mathbb{N}$	the positive integers
P	static pressure
P_{alveolar}	alveolar pressure
P_c	characteristic pressure scale
P_{contact}	vocal fold contact stress
P_d	diaphragmatic pressure
P_e	epilaryngeal pressure
P_L	static pressure within lung
P_{pleural}	pleural pressure
P_s	subglottal pressure
P_t	pressure due to tissues of thoracic wall
P_0	an arbitrary reference pressure, e.g., far field static pressure

Q	glottal volumetric flow rate
$\vec{r}$	moment arm about nodal point, $\vec{r} = \vec{x} - (0, y + y_{ng}, 0)$
$\mathbb{R}$	the field of real numbers
t	temporal independent variable
t_c	characteristic time scale
t^*	dimensionless time
t_k	k$^{\text{th}}$ timestep
t_{VF}	the geometric model parameter for vocal fold thickness
T	the dimension of time
T_a	resultant aerodynamic torque applied to medial vocal fold surface
T_s	sampling period
v_0	an arbitrary reference velocity
$v^{(n)}_{\text{vortex},j}$	velocity magnitude of j^{th} vortex present in the flow domain at the n^{th} iteration
v_Σ	absolute velocity of surface patch Σ
V_c	characteristic velocity scale
V_e	epilaryngeal velocity
V_s	subglottal velocity
x	real part of $z = x + iy \in \mathbb{C}$
y	imaginary part of $z = x + iy \in \mathbb{C}$, displacement of vocal fold cover mass
y^*	dimensionless displacement of vocal fold cover mass
y_b	displacement of vocal fold body mass
y^*_b	dimensionless displacement of vocal fold body mass
y_{ng}	neutral glottal displacement of vocal fold, also called pre-phonatory displacement of vocal fold
z	complex variable in physical plane, corresponding to the geometric image of a position vector relative to the global origin
z_{fulcrum}	the absolute coordinate of the nodal point
$\tilde{z}$	complex variable in the physical plane corresponding to the geometric image of a position relative to a moving frame, in particular, $\tilde{z} = z^*_k - z_{\text{fulcrum}}$
z_0	a determined point in the physical plane, perhaps locating the centre of a source or singularity
z_{0k}	the centre of the k$^{\text{th}}$ vortex in the physical plane
z^*	a control point on the medial VF surface
z^*_k	the k$^{\text{th}}$ control point on the medial VF surface
$\mathbb{Z}$	the integers

1-D	one-dimensional
2-D	two-dimensional
3-D	three-dimensional
BC	boundary condition
CFD	computational fluid dynamics
CQ	closing quotient

DNS	direct numerical simulation
DOF	degree of freedom
FSI	fluid-structure interaction
GF	glottal flow
KH	Kelvin-Helmholtz
ODE(s)	ordinary differential equation(s)
OQ	open quotient
PDE(s)	partial differential equation(s)
PIV	particle image velocimetry
SQ	speed quotient
VF	vocal fold

1 Introduction

Speech is a uniquely human capacity which pervades all of human activity, whether it be social, political, economic, or cultural; to speak is to partake of the human experience. Voice is the foundation of speech and can be impacted by a number of pathological conditions, which either diminish or impair a speakers capacity to produce intelligible voiced speech [88, 98], severely affecting the sufferer's quality of life. These conditions include hoarseness due to aperiodic vocal fold vibration [33], vocal fatigue due to subglottal pressures too high for vocal register [89], breathy voice due to incomplete glottal closure [88], aphonia due to inability to produce vocal fold vibration [61], reduced phonational range due to difficulty in register transition [101], pitch break due to intermittency between vibratory patterns [94], vocal fold nodules due to excessive vocal fold contact stress [45], and paralysis [63]. Phonation is the quasi-periodic oscillatory response of vocal fold tissues to the glottal flow which drives them; the phonatory oscillation of vocal folds is the primary source of sound in voiced speech [92]. An improved understanding of the mechanisms of phonation grounded on insight into the fundamental physical interaction of the visco-elastic vocal fold tissues and the glottal airflow has the potential to improve clinical implementations of approaches to treat, habilitate, or train voice [98]. Such insight may also contribute to the development of speech processing applications such as speech compression, synthesis, detection, and recognition algorithms [17, 78, 83].

Since the pioneering work of van den Berg [104], glottal flow has been modelled as an ideal one-dimensional potential flow with the steady Bernoulli equation employed to compute the pressure field to determine the loading on the vocal fold surfaces, and has been employed as a model deemed to be sufficiently accurate to describe intraglottal flow behaviour [82, 97, 99, 106]. Past studies have described this flow thoroughly, but the consequences of temporally evolving flow structures and viscous effects had been foregone. In fact, de Vries et al. [18] study a computational model in which a Navier-Stokes solver is coupled to a lumped-element vocal fold tissue model and contrast the results with the same tissue model coupled to a traditional Bernoulli solver. They note that the Navier-Stokes solution determines a lower fundamental frequency, larger peak flow attributed to moving points of flow separation throughout the phonatory cycle, and phonation threshold pressure more similar to clinically measured threshold pressures. Symmetric flow separation is assumed; however, more recent investigations have revealed that in the divergent phases of the phonatory cycle, the glottal flow fully separates from one medial vocal fold surface and adheres to the opposite medial vocal fold surface which may be attributed to a coanda effect

[25, 27, 28, 29]. Additionally, other investigations have shown flow patterns and structures of notable complexity such as vortex shedding [53, 58, 70, 71], shear-layer instabilities [108], transition to turbulence [44], and three-dimensional effects [26]. Features of the supraglottal flow have also been revealed to investigators, and studies which incorporate these effects to quantify their influence on the vibratory mechanism of the vocal fold tissues are beginning to appear [65]. The extent to which temporally evolving flow structures in the intraglottal and supraglottal regions affects the vocal fold dynamics has not been conclusively determined. It is for this reason that these effects must be incorporated into models of phonation and evaluated in terms of their contribution to the overall dynamics.

It is desirable to increase our understanding of factors which affect the intelligibility of speech. Fant [36] showed that the magnitude of the derivative of the glottal volumetric flow rate in the closing phase of the phonatory cycle is proportional to the energies of higher formants. Moreover, it has been determined that improved intelligibility of speech is a subjective correlate of increased energy content of speech at higher frequencies [38]. Consequently, it is desirable to elucidate any mechanism which determines the rate of glottal closure or contributes to increasing the rate of glottal closure in the closing phase of the phonatory cycle. Recent experimental and computational studies have suggested that the presence of intraglottal vortices have the potential to contribute to the rapid closing of the glottis in the closing phase of the phonatory cycle [52, 53, 62]. Therefore, the goal of the investigation presented herein is to ascertain the effect of the presence of intraglottal vortices, and, in particular, determine whether they have any meaningful effect upon the dynamics of the vocal folds in the closing phase of the phonatory cycle.

In order to capture higher dimensional effects within the glottal flow, such as advecting vortices and their concomitant pressure and velocity fields, which vary in more than one spatial dimension, the extension of a one-dimensional glottal airflow model to a two-dimensional version is required. To quantify the effect of intraglottal vortices, a two-dimensional ideal potential flow model of the glottal airflow which incorporates advecting vortices has been developed and coupled to a suitable low-order lumped-element dynamical model of the vocal fold tissues.

1.1 Thesis Outline

Chapter 2 begins with a background of structure and function of the vocal organs. This is followed by the mechanical modelling of vocal fold tissues and glottal aerodynamics. Chapter 3 presents the work which was performed in conjunction with this investigation; the 2-D potential flow model of glottal flow and vocal fold aerodynamics is developed together with a parametric characterization of the overall system dynamics via dimensional analysis. Chapter 4 presents validation against an existing model, and simulation results capturing vortical motion are discussed. In terms of the validation, two points are kept in mind; a primary goal is that a physiologically appropriate self-oscillatory behaviour of vocal fold tissues be captured and the two-dimensional glottal flow include advecting vor-

tices. Ultimately, sufficient but simple models elucidate and clarify the nature of physical effects which might be obfuscated by the results of a complicated numerical simulation. There is greater intellectual appeal of semi-analytic models in spite of the often considerable degree of assumption necessary for tractability. Moreover, because semi-analytic approaches provide mathematical analogues of physical systems, this enables one to focus on the discrepancies between modelled outcomes, which bestows these models their explanatory power. It is precisely the assumptions of the model and the real physics which they discard which cause the deviation of the modelled results from those expected physically, and this allows the investigator to focus on these areas in order to draw conclusions about the adequacy of a model or the significance of a modelled effect. The conclusions drawn based upon the results are then discussed in Chapter 5. Finally, recommendations are supplied based on the work performed in this development and investigation. The document concludes with three appendices: the first provides sufficient background in complex analysis, intended to motivate the reader unfamiliar with this body of theory; the second appendix supplies detailed derivations of the results presented in Chapter 3; and the final appendix presents a discussion of the simulation codes, and is intended to be a user's manual of sorts in order that future researchers at this institution may be able to employ or extend the codes developed in conjunction with this research project.

2 Background

This chapter furnishes background which places the work of this thesis in the framework of the existing science of speech communication, of speech modelling, and of the biomechanics of phonation in particular. Anatomy and physiology specific to speech production is presented firstly in order to develop the language appropriate to discuss the structure and function of the vocal organs but ultimately to justify choices made in the development of the simulation model. Subsequent to the structural and functional background, preceding the model development of the following chapter, is a general discussion of vocal fold (VF) modelling, approaches and outcomes. The desire is to place the present work in the context of existing approaches to the modelling of speech phenomena and place this work on a firm physical basis; this thesis extends one-dimensional glottal flow (GF) models to capture fluid structures of higher dimensionality within the framework of a lower order model in a manner compatible with anatomical constraints and emulating physiological mechanisms. Detail of the complexity of speech production and structures and mechanisms relevant to subsequent model development and simulation outcomes is presented. The discussion herein follows similar development presented in the general references of Titze [98] and Stevens [92], which broadly discuss these ideas with the same intent to provide an appropriate physiological and physical basis for model development and simulation of human speech. It must be maintained that of specific interest herein are the structure of vocal fold tissues, the physiological mechanisms responsible for glottal airflow, and the fluid-structure interaction (FSI) in phonation.

2.1 Anatomy and Physiology of the Vocal Organs

This section on the structure and function of the vocal organs summarizes some of the relevant descriptions and findings of the general references for anatomy and physiology pertaining to speech. In addition to Titze and Stevens [92, 98], specific references are, for example, Hixon's treatise of respiratory anatomy and physiology of respiration for speech, [43], and Seikel, King, and Drumright, [84], which is a more recent general treatment of anatomy and physiology for speech. Dickson and Maue-Dickson, [20], furnish a background to anatomy and physiology from histology of epithelial and connective tissue to neuromuscular and musculoskeletal relationships, including structure and function of

myological tissues; subsequently, they extensively treat anatomy and physiology of respiration, phonation, and articulation, of particular interest to the biomechanical investigation of speech. Additionally, each section of [20] includes a discussion of innervation, and the reference concludes with chapters on audition and the nervous system, specifically as it pertains to speech.

The classification of the organs of the respiratory system due to their involvement in the mechanisms of speech production as vocal organs is a functional classification. Speech is a complicated set of events which necessitates and is a consequence of highly integrated neuromotor co-ordination of respiratory, phonatory, and resonatory and articulatory systems. The gross anatomy of the respiratory system is displayed schematically in Figure 2.1 below. The figure displays the relation between the respiratory passages which comprise the upper vocal tract, the larynx, and the lower vocal tract.

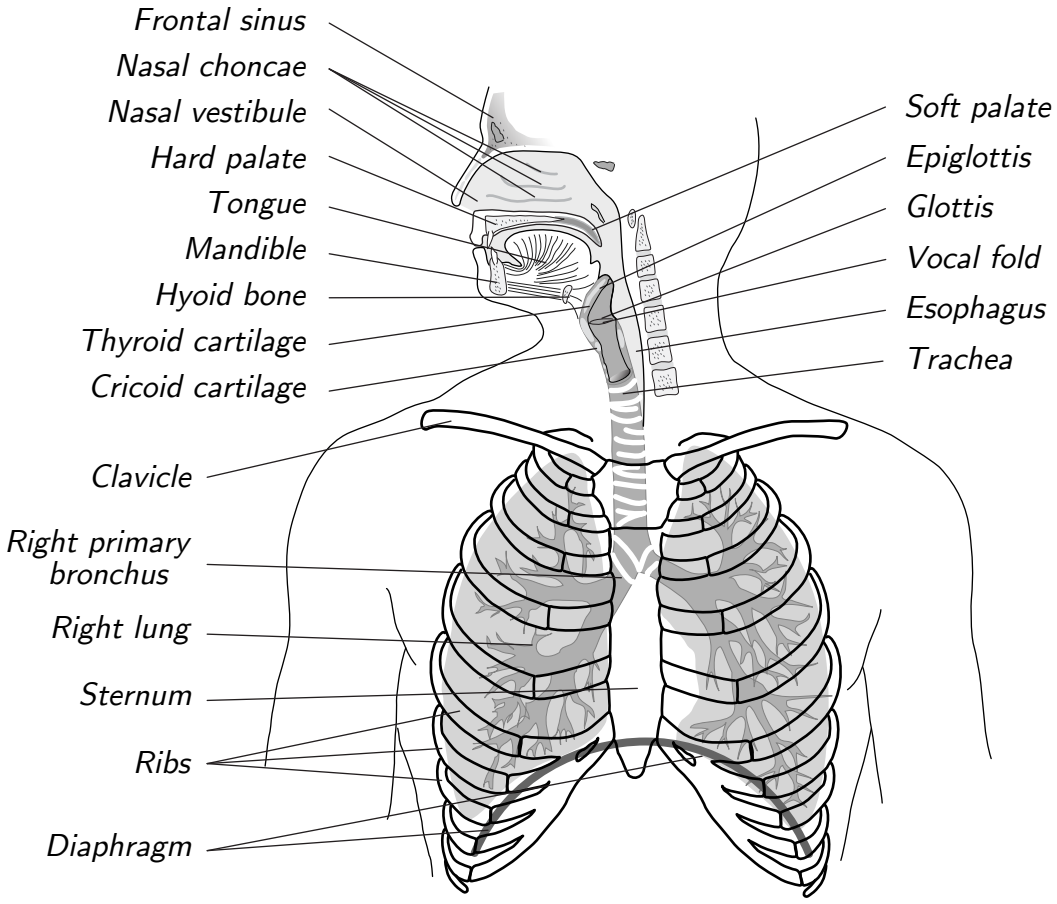

FIGURE 2.1: Gross anatomy of respiratory system, shown schematically from the front with the layers of the thoracic structures transparently and the structures of the skull shown in midsagittal section (adapted from [31]). Many of the important landmarks are shown, placing the lungs, trachea, larynx, and upper vocal tract in the context of local structures of the upper torso, neck, and head.

The upper vocal tract includes the oral and nasal passages and the pharynx. These are the structures of the resonatory and articulatory system. The larynx is located at the juncture of the upper and lower vocal tracts. To provide additional anatomical context, Figure 2.5 provides an anterolateral view of the neck from the front left, it displays the extrinsic musculature and places the trachea and larynx relative to the mandible and to the clavicle and scapula of the shoulder girdle. The larynx supports the vocal folds, and permits their adjustment. The vocal folds are the principal vocal organs involved in the production of voiced speech and will be described in detail in what follows. The lower vocal tract comprises the trachea, which leads to the bifurcating passages of the pulmonary system, the bronchi, bronchioles, and alveolar structures at the finest scale. The primary role of the pulmonary tissues is in the exchange of gases required for cellular respiration, which is of vital importance.

The trachea extends superiorly from the lungs, the larynx sits atop the trachea, and the upper vocal tract is above. That these passages are continuous and form parts of the same continuous airway is acoustically relevant. Egressive airflow from the lungs is influenced by the glottis, the tongue, and cavities of the vocal tract. The sound source for speech may be the quasi-periodic interruption of the pulmonic flow at the vocal folds, an impulsive opening or sudden occlusion of the vocal folds to produce a stoppage of air, or due to turbulence generated at a deliberate narrowing of some part of the tract. In particular, it is phonation, the quasi-periodic opening and occlusion of the glottis, which is the primary source mechanism for voiced speech. The adjustments necessary to place and configure the tongue, palate, teeth, nasal passages, jaw, and lips in order to modify the source to produce intelligible sounds of natural language is referred to as articulation. To reiterate, the vibration of the vocal folds in phonation provides the primary source mechanism for the modal register by periodically modulating the airflow to generate a periodic pressure signal, and this acoustical signal is filtered by the upper vocal tract. This framework for an acoustical model of speech was proposed by Fant in [34]. In what immediately follows, and, because the lungs are the source of the glottal airflow which ultimately provides the energy which drives and sustains the phonatory source mechanism, respiration is discussed.

2.1.1 Respiration

Figure 2.1 presents an anterior view of the torso and neck with head in sagittal section. The trachea and bronchi are shown in the figure. The trachea is a flexible tube of fibrous elastic tissue approximately 11 [cm] long with cross-sectional area approximately 5 [cm^2] in adult humans. it bifurcates into the bronchi, it is punctuated by 16 to 20 discontinuous rings of hyaline cartilage which provide strength and allow the radial expansion and contraction of the trachea. The respiratory passages are lined with a continuous and flexible mucous membrane, beneath which are distributed submucosal glands which facilitate clearing of the trachea. The tracheal rings are actuated by the trachealis muscle, a smooth muscle (involuntary), which is in a state of contraction and relaxes exclusively when the body's oxygen needs increase beyond some threshold. In this case, the trachea expands

diametrically and causes the trachea to be less restrictive until oxygenation of the blood is sufficient. The manifold branching of the passages of the lung ultimately leading to each alveolus have the effect of increasing the surface area required for the exchange of gases; there are approximately 3×10^8 alveoli with diameters of approximately 200-300 [μm], and this yields an overall surface area of approximately 70 [m^2].

The pulmonary tissues are richly vascularized in order to exchange oxygen from the air drawn into the lungs and carbon dioxide dissolved in the blood across the membranes of the alveoli. In inhalation, the thoracic cavity expands, reducing alveolar pressure and causing air to enter the lungs. It is drawn in through the oral and nasal cavities and flows through the larynx and down the trachea into the bronchi which bifurcate. The dendroidal structure of the bronchial passages, which narrow to the bronchioles which have an approximately 1 [mm] diameter and are terminated by the fine structure of the alveoli interconnected via alveolar ducts. Each alveolus is surrounded by a bed of capillaries. It is the membrane of the alveolus which allows the exchange of respiratory gases, oxygen and carbon dioxide via a diffusive process with the surrounding fine structure of blood vessels.

The secondary process of voiced speech is, in some sense, superimposed upon the primary mechanisms of respiration. Phonation, the process of producing voiced speech, entails the aeroelastic interaction of the vocal fold tissues with the glottal airflow ultimately generated by pressures within the lungs. Consequently, the relevant anatomy and physiology of respiration, determines the flows and pressures for phonation. The mechanism which determines the pressures is now discussed. It is seen in Figure 2.1 that the dozen pairs of ribs impart the general volume to the thorax, the cavity of the torso superior to the diaphragm. Anteriorly, the ribs cartilaginously attach to the sternum. Posteriorly, the ribs have arthroidal articulation with the thoracic vertebrae. These connections ensure that the motion of the ribs contributes to the volumetric expansion and contraction of the thoracic cavity. The lungs move with the boundaries of the thoracic cavity due to the pleural interface between the lungs and the deep tissues of the thoracic cavity wall.

The pleural structure of the pulmonary organs located within the thorax is shown in Figure 2.2, and, a schematic of thoracic pressures and their origins is supplied in Figure 2.3. The lungs are not supported with ligament or cartilage, rather, it is the combination of tissues and fluids which allows the shape of the lungs to be determined by the thoracic volume. The deepest layer of the thoracic wall is lined by the parietal pleura. The superficial-most layer of the lungs is lined by the visceral pleura. Regions of the pleural linings and their relations are displayed in Figure 2.2. The visceral and parietal pleurae are continuous with each other and adhere by surface tension due to the fluid between their tightly conforming surfaces. The negative pleural pressure is maintained because the intrapleural space is sealed and separated from atmosphere. At rest, thoracic volume exceeds pulmonary volume. Contraction of the diaphragm, which imparts an upward displacement to it, as shown in Figure 2.4, also enlarges the thoracic cavity in a superior-inferior direction. Elevation of the ribcage enlarges the ribcage in the transverse dimension. The pleural lining transmits these forces from the thoracic wall to the lungs. The regions of the parietal pleura are identified by location in Figure 2.2. The mediastinal pleura covers

the mediastinum, the cavity occupied by the heart. The diaphragmatic pleura covers the diaphragm. The apical pleura covers the superior-most region of the ribcage. Finally, the costal pleura covers the inner lateral surface of the ribcage. In early development, the lungs completely fill the thorax but the ribcage grows more rapidly than the pulmonary tissues, so a negative intrapleural pressure is established.

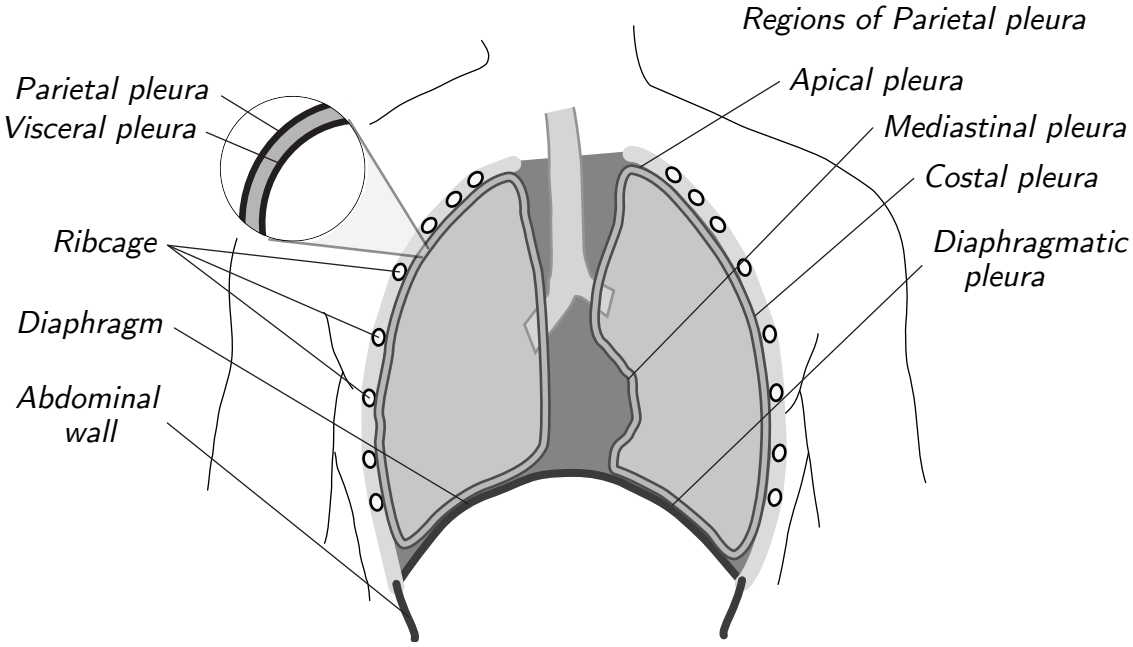

FIGURE 2.2: Thoracic cavity, sagittal section anterior view (adapted from [31, 84, 98]). Regions of parietal pleura are identified by location. These are shown in relation to the ribcage, diaphragm, abdominal wall, and torso.

The bulk movement of air is due to muscular interaction which causes volumetric change in the volume of the thoracic cavity, which, in turn, causes a volumetric change in pulmonary volume. The structure and function of the pleural linings ensure that the lungs conform to the volume of the thoracic cavity and therefore expand and contract in unison with it.

The chondral tissue of the costal cartilage permits significant movement of the ribs, and the joint at the spinal attachment enables the ribs to rock laterally and anteriorly in respiration. The floating ribs, the inferior-most pair, articulate with the eleventh and twelfth thoracic vertebrae, however, are joined to the sternum via connective tissue. The actions of the respiratory muscles displayed in Figure 2.4 serve to reduce thoracic volume upon exhalation and to increase thoracic volume upon inhalation. Elevators of the ribcage cause the ribs to rotate superiorly and therefore increase the sectional area of the thorax in transverse section therefore increasing the thoracic volume. Depressors of the ribcage effect the opposite outcome. During inhalation primary and auxiliary respiratory muscles elevate the ribs and flatten the diaphragm. In exhalation primary and auxiliary respiratory muscles depress the ribs and elevate the diaphragm. When the ribs are elevated or the diaphragm depressed, possibly in concert, thoracic volume increases. Increase of lung volume causes

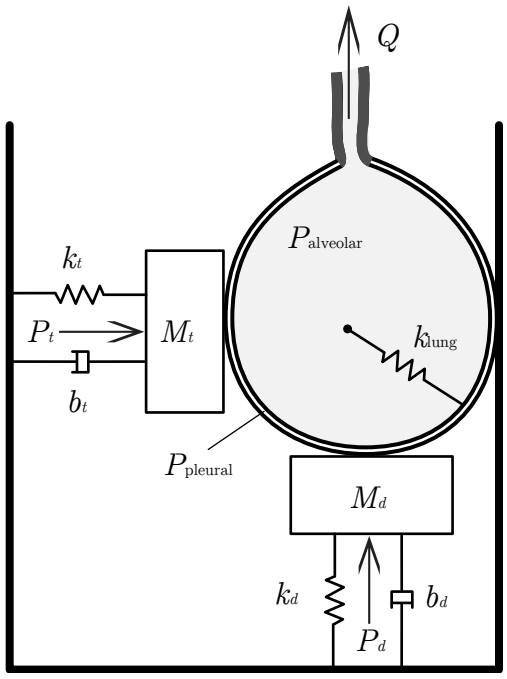

FIGURE 2.3: Schematic of thoracic pressures (adapted from [92, 98]). Q is the volumetric flow rate in the trachea determined by the alveolar pressure P_{alveolar} and the fact that velocity of air within the lung is approximately stationary. P_{pleural} is the pressure which prevails in the intra-pleural space. Subscripts t and d refer to thorax and diaphragm respectively. Labels M, k, b, and P refer to mass, elasticity, damping, and pressure respectively. The dynamics of the thorax and diaphragm are due to the viscoelastic tissues and the masses of the supporting structures and the pressures generated by muscle activation of the muscle tissues of the thorax and abdomen.

atmospheric air to enter the pulmonary organs. The outward and upward motion of the ribs is possible because of the spinal articulation and the general configuration of the protagonistic muscles of the torso which are recruited. The outward movement of the ribs as they are elevated resembles the outward swing of a raised bucket handle. The reverse is true for exhalation.

The number of muscles recruited for inspiration and expiration increase with demand for greater volumetric change of the pulmonary volume. However, the diaphragm alone is able to provide volumetric adjustment which is sufficient for quiet breathing. The diaphragm, a sheetlike structure oriented approximately transversely, is the primary muscle of respiration. It is the inferior separation of the thoracic cavity from the abdominal cavity. It comprises an aponeurosis, a central tendon, which is punctured by three hiatae, which allow communication between abdominal and thoracic cavities. It is surrounded by muscle extending radially and inserting along the lower margin of the ribcage at ribs 7 to 12 along inner borders of to the costal cartilage, and at the sternum at the xiphoid process and dorsally to the lumbar vertebrae 1 to 4. Contraction of the diaphragm displaces the central tendon simultaneously inferiorly and anteriorly. This causes a volumetric increase

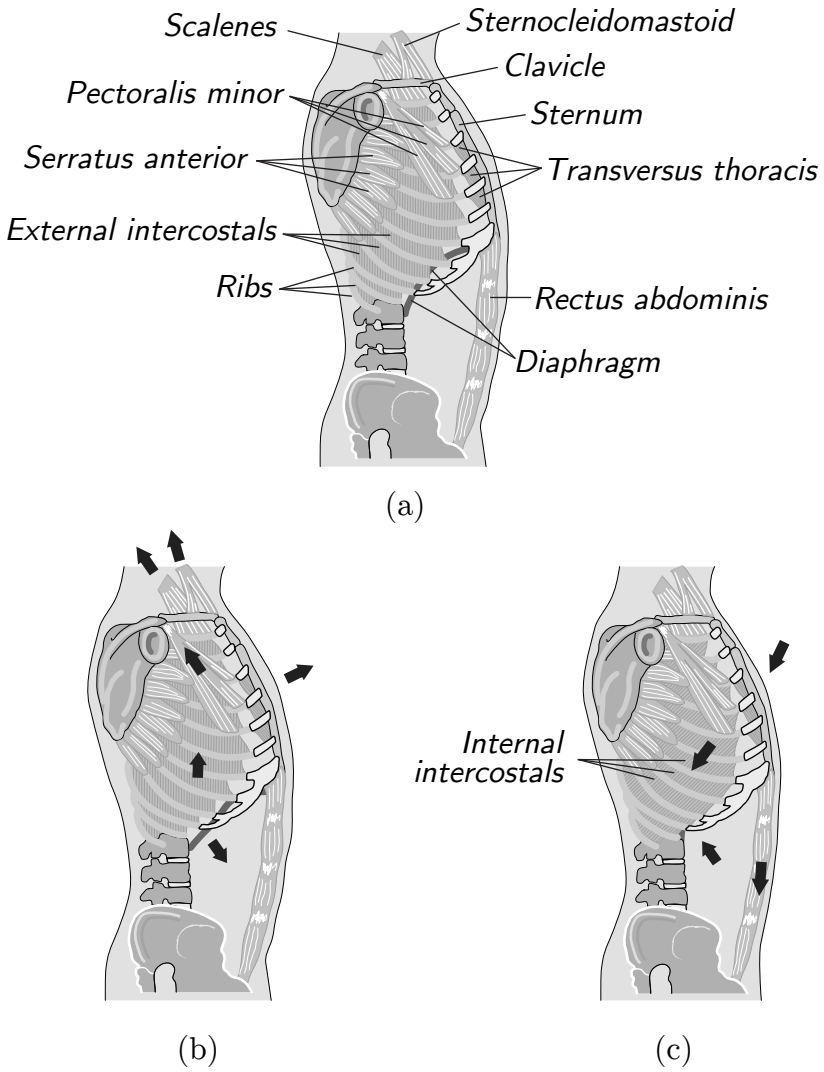

FIGURE 2.4: Action of respiratory muscles (adapted from [31]), (a) at rest, (b) during inhalation, and (c) during exhalation.

of the thoracic cavity by expanding the ribcage superiorly along a superior-inferior axis. Relaxation of the diaphragm reduces the volume of the thoracic cavity along the same axis.

There are some capacities, volumes, and pressures of respiratory system which are worthy of note. Again, with reference to the schematic of Figure 2.3, there is contrast between quiet and forced inspiration as well as passive and active expiration. Forces inherent in tissues due to their elasticity restore the thoracic cavity to some neutral position. Muscular effort is expended to decrease thoracic volume beyond this rest state. Quiet tidal respiration is approximately one half litre per cycle. Tidal volume is the volume of air exchanged per cycle of respiration. Residual volume is quantity of air which may not be

expelled it is the volume remaining in the lungs after a maximum exhalation. Inspiratory reserve volume is volume which may be inhaled after a tidal inspiration. Expiratory reserve volume is resting lung volume, the volume of air which may be expired following a passive tidal expiration. The vital capacity is the volume of air which may be inhaled following a maximal exhalation. The vital capacity is the lung capacity available for speech. Functional residual capacity is the volume of air at the end of passive exhalation. Inspiratory capacity is maximal inspiratory volume possible after tidal expiration. Total lung capacity is the sum of inspiratory reserve volume, tidal volume, and expiratory reserve volume.

Phonation is produced by egressive glottal flow. Consequently, it is the pressures of the thorax which are generated in expiration which are of interest. The pressures which prevail externally are atmospheric. Subglottal pressure exists immediately inferior to the VFs. Alveolar pulmonic pressure $P_{alveolus}$ is lung pressure. Pleaural pressure refers to intraplearal pressure, and it is always negative in adults. The pressures generated by the tissue displayed in 2.3 cause the chest wall to recoil and return to a stasis determined by the muscles of the torso, cartilage, bronchi, bronchioles, blood vessels, and elastic tissue of the lung. Phonation for speech typically entails steady lung pressure and steady volumetric flow rate. The onset of phonation is achieved when the transglottal pressure, the difference between epilaryngeal pressure and subglottal pressure attains some threshold value. The subglottal pressure required to produce speech of a steady intensity is relatively fixed. Subglottal pressure may be adjusted to effect syllabic stress. Utterances are sufficiently short so lung recoil need not be checked but merely supplemented by the contraction of expiratory muscles to force air past a normal breathing level; the thoracic muscles are recruited to ensure that the desired intensity is obtained. The structure of the larynx and vocal folds is now discussed leading up to the detailed discussion of the mechanism of phonation.

2.1.2 The Larynx and the Vocal Folds

The larynx is a musculo-cartilaginous structure; it comprises cartilage, ligament, muscle, and is lined with mucous membrane. The larynx is located within the neck at the superior end of the trachea as shown in Figure 2.1. It is suspended from the hyoid bone. The rigid structure is due to three paired and three unpaired cartilages bound by ligaments. The geometry of the cartilages exhibit reflective symmetry through the midsagittal plane. Three generate the structure of the larynx and articulate only slightly with respect to each other and three exist in pairs and allow greater articulation of tissues. The larynx is supported and positioned by the extrinsic musculature, those muscles which originate externally to the larynx but insert on the larynx. The intrinsic laryngeal muscles, those which originate and insert on the laryngeal cartilages, are responsible for the fine adjustments of the laryngeal cartilages which are essential for speech production.

The vocal folds are bands of mucous membrane, connective tissue, and muscle which are located within the larynx in the path of the pulmonic flow; The vocal folds are attached to the larynx in a manner that they may completely constrict or interrupt the pulmonic flow.

The vocal folds are capable of strong and rapid closure in response to threat of intrusion by foreign objects. Three pairs of muscles are responsible for adducting and one pair of muscles for abducting the vocal folds.

Amongst the non-speech functions are coughing, a reflexive response of respiratory tissues to the presence of foreign material. Coughing is a forceful evacuation of the respiratory passageway; deep inhalation through widely abducted folds, tensing and tight adduction of folds and the elevation of the larynx, and followed by forceful expiration where the high subglottal pressure blows the vocal folds apart under a maximal airflow. Another non-speech function is abdominal fixation, a capturing of air within thorax to provide fixed structure for muscles achieved by a large respiratory charge and tight adduction which follows a deep inspiration. It is, of course, the speech functions which are of interest herein. The remainder of this subsection provides a more detailed discussion of the larynx and the vocal fold morphology and histology.

The Larynx

Figure 2.1 places the larynx in the context of the gross anatomy of the respiratory system. The extrinsic musculature which supports the laryngeal structures is shown in Figure 2.5. Further, the cartilaginous tissues which comprise the larynx are shown in exploded view in Figure 2.7. Figure 2.6 shows the natural configuration of the vocal folds, in which the cartilages are shown with the intrinsic ligaments and connective tissues. Finally, Figure 2.10 exhibits the deep tissues of the larynx in coronal section.

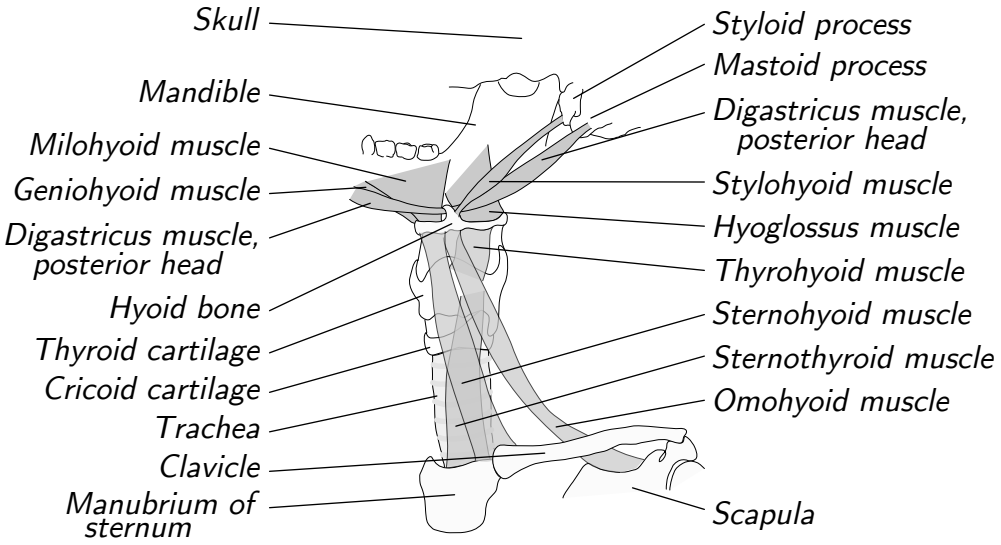

FIGURE 2.5: Anterolateral view of extrinsic muscles of the larynx (adapted from drawings prepared by Harold Lumby in [35]).

The cartilages of the larynx are linked by connective tissues, by median and lateral thyroid ligaments, and by the thyroid membrane. Cartilages are lined with membrane.

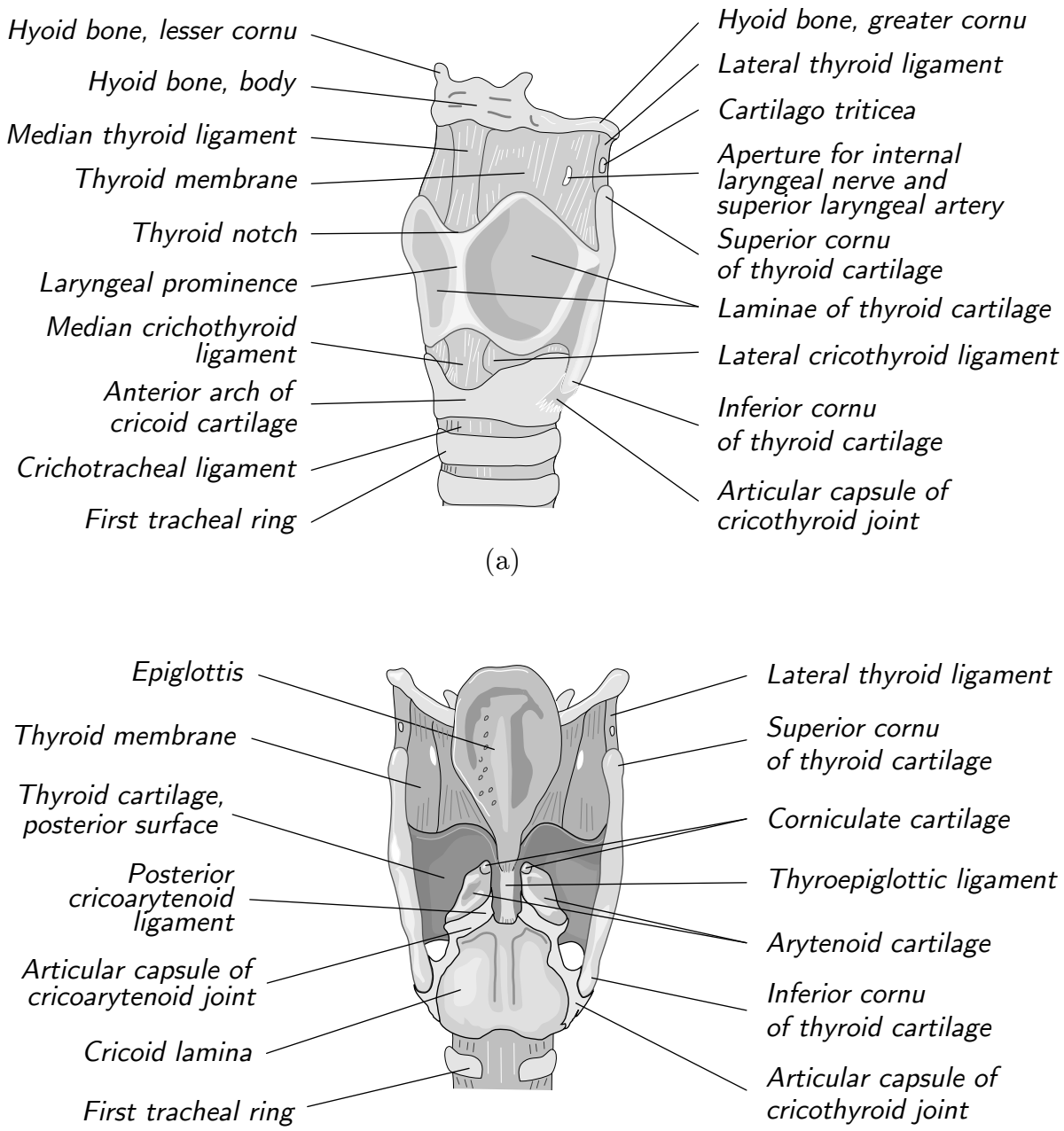

FIGURE 2.6: Laryngeal structure displaying cartilages and ligaments in (a) antero-lateral view and (b) posterior view (adapted from [84, 98]).

The extrinsic ligaments provide attachment between hyoid and trachea and cartilages of the larynx. The thyroid membrane lies between the greater cornu of the hyoid and the lateral thyroid. The lateral thyroid ligament connects superior cornu of thyroid to posterior tip of the greater cornu of the hyoid. Referring to the cartilaginous structure shown in Figure 2.6, the tracheal rings of the trachea are conjoined via firboelastic membrane. The larynx is immediately superior to the most superior tracheal ring. The larynx is parallel to cervical vertebrae 4 to 6 in adults. The average length of the trachea is 36 [cm] in females but 44 [cm] in adult males. Intrinsic ligaments interconnect cartilages of larynx and support laryngeal cavity and vocal folds. The inferior-most cartilages of the larynx is the cricoid, from Greek krikos, ring, meaning ringlike or ringform; it is a full ring with posterior wider than anterior. The thyroid cartilage, the most substantial of the laryngeal cartilages, is located superiorly to the cricoid, it articulates with it at the cricothyroid joints. The paired arytenoid cartilages articulate with the cricoid cartilage on its superior surface. The joint provides a significant range of motion. The arytenoid cartilage is the location for attachment of vocal folds. The corniculate cartilages are located on superior surfaces of arytenoids. Not shown are the cuneiform cartilages which are located within aryepiglottic folds providing some rigidity. The triticeal cartilages might not be present, but when they are, they are located between superior cornu of thyroid and hyoid bones. The epiglottis is an unpaired cartilage of the larynx. It is shaped like a leaf with its stem attached to the anterior part of the thyroid cartilage. The epiglottis drops to cover the opening of the larynx in swallowing, by articulating with the thyroid cartilage at its base. Extrinsic ligaments provide attachment between hyoid trachea and cartilages of larynx, these are the cricotracheal ligament, median thyroid ligament, hyoepiglottic ligament, lateral and medial glossoepiglottic ligaments. The cavities of the larynx are most clearly depicted in Figure 2.10. The aditus laryngis is the entry to larynx from the pharynx above. The anterior boundary of the larynx is the epiglottis. Lateral margins of the aditus are aryepiglottic folds. The first cavity of the larynx is the vestibule, the space between the aditus and the ventricular folds. The vestibule is wide at aditus and narrows to the region between ventricular folds. The lateral walls are the aryepiglottic folds. At the posterior walls, membrane covers the arytenoid. The false folds are made up of mucous membrane and fibrous vestibular ligament. The false folds do not have muscle to adjust their configuration. The laryngeal ventricle, the glottis, is approximately 20 [mm] wide at rest, its posterior is 8 [mm] wide. The glottis is defined as the space between the vocal folds.

The paired arytenoid, meaning pyramidal, contact the superior posterolateral surface of the cricoid cartilage and provide the mechanism for onset and offset of voicing, for adduction and abduction of the vocal folds, i.e., the muscular adjustments necessary to fix the vocal folds in either a closed or open configuration. Their inferior surfaces are concave and they articulate with convex arytenoid facet of the cricoid cartilage. Vocal processes project anteriorly and the posterior portion of vocal folds attach here. The muscular process is the lateral projection and is the point of muscular attachment of abducting and adducting muscles of the vocal folds. Interestingly, the hyoid bone is the only bone of the body not attached to another bone. It forms a union between tongue and laryngeal structure, and it articulates loosely with the superior cornu of thyroid.

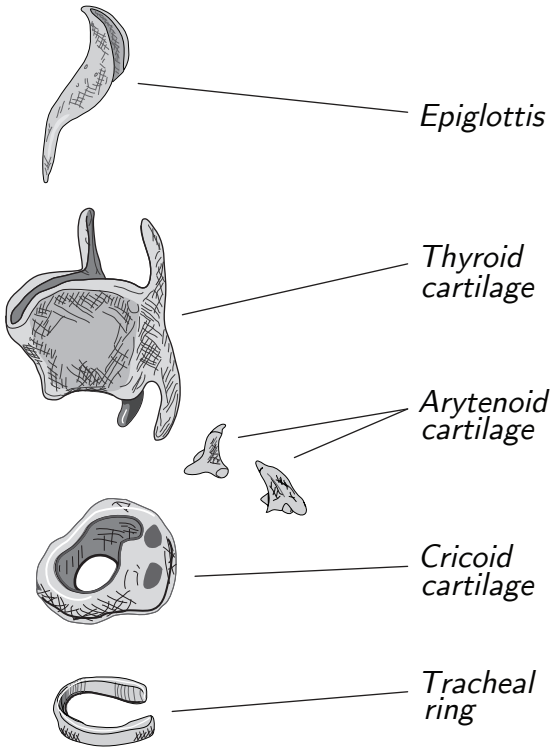

FIGURE 2.7: An exploded anterolateral view of laryngeal cartilages displaying the primary cartilages of the larynx, which impart its structure (sketches of cartilages photographed in [20]).

It is worth repeating that the extrinsic laryngeal muscles originate on structures outside of the larynx and insert on laryngeal cartilages. The intrinsic laryngeal muscles have both origin and insertion on laryngeal cartilages. Whereas the extrinsic laryngeal muscles effect major adjustments to the larynx, elevation and depression motions of tongue, and swallowing, fine adjustments to vocal mechanism are achieved by the intrinsic musculature. Furthermore, because the lateral boundary of the glottis is determined by the vocal fold tissues slung between the thyroid cartilage and the arytenoid cartilage, and the arytenoid cartilages articulate relative to the cricoid cartilage, any adjustment of the arytenoid cartilage must modify the vocal fold configuration and, therefore, the nominal glottal geometry. The intrinsic muscles of the larynx indeed achieve the fine adjustments required for voiced speech and phonation in particular; they effect a continuum of open and closed glottal configurations and some affect the mechanical properties of the vocal folds by tensing and relaxing along the axis of the medial fold boundary. The structure and function of the intrinsic laryngeal muscles responsible for vocal fold configuration will be discussed here, but the function of the muscles responsible for the modification of the mechanical properties will be discussed in the immediately following subsection of fine vocal fold morphology.

The intrinsic muscles of the larynx which are relevant for speech are adductors and abductors of the vocal folds as well as the muscles which contribute to the mass and modify the stiffness of the vocal folds. These muscles and their actions are shown in Figures

2.8 and 2.9. There are three adductors, the paired lateral cricoarytenoid, the transverse arytenoid, which is unpaired, and the oblique arytenoid. There is a lone abductor, and it is a paired muscle, the posterior cricoarytenoid. The cricothyroids are subdivided into the pars recta and the pars oblique, their action is to lengthen or tension the vocal folds. The cricoarytenoid muscles originate on the cricoid cartilage and insert on the arytenoid cartilages. The action of the cricoarytenoid muscles affects pitch by either modifying the length or the tension of the vocal folds. The transverse and oblique are interarytenoid muscles in that they both insert and originate on the medial surfaces of the arytenoid cartilages, and thereby serve to adduct the vocal folds. The intrinsic muscles which form the mass of the vocal folds are the thyroarytenoid muscles, and are displayed in Figure 2.8 and in coronal section in Figure 2.11. The thyroarytenoid muscles originate on the thyroid cartilage and insert on the arytenoid cartilages. Each muscles has two heads, the thyrovocalis is the medial head and the thyromuscularis is the lateral head. The thyroarytenoid muscles form the bulk of the vocal fold mass and structure and control tension, elasticity, and adduction of the VFs. The thyroarytenoid muscles, the interarytenoid muscles, and the lateral cricoarytenoid muscles are innervated by the recurrent laryngeal nerve. The cricothyroid muscles are innervated by the superior laryngeal nerve. With the musculo-cartilaginous framework of the larynx in place, a more detailed description of the vocal folds is possible.

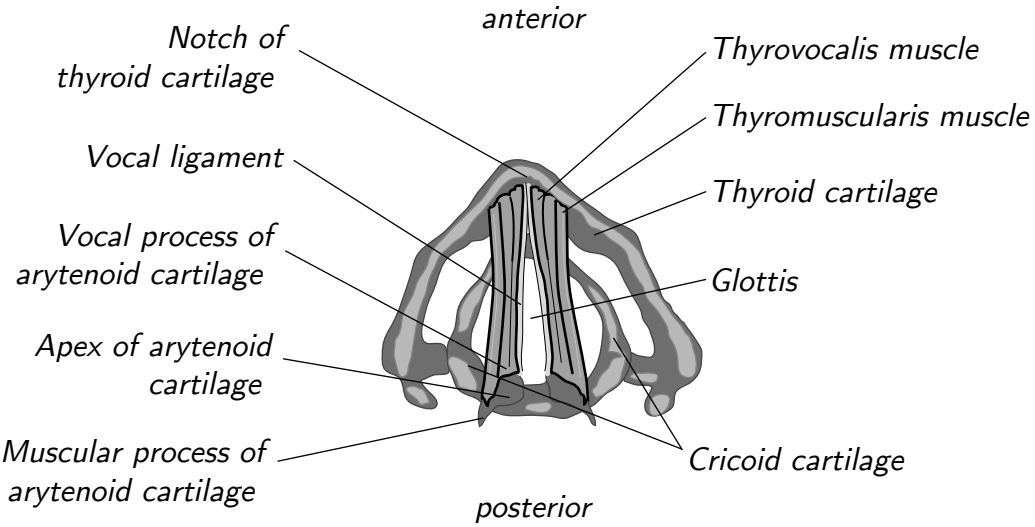

FIGURE 2.8: Superior view of intrinsic muscles of the larynx and their roles in the articulation of the laryngeal cartilages to abduct and adduct the vocal folds. (adapted from [84]).

Morphology and Histology of the Vocal Folds

The immediately preceding section conveyed the overall laryngeal structure. The structure of the vocal folds may be placed in this context. The vocal folds are bands of mucous membrane, connective tissue, and muscle, specifically the thyrovocalis muscle, slung between

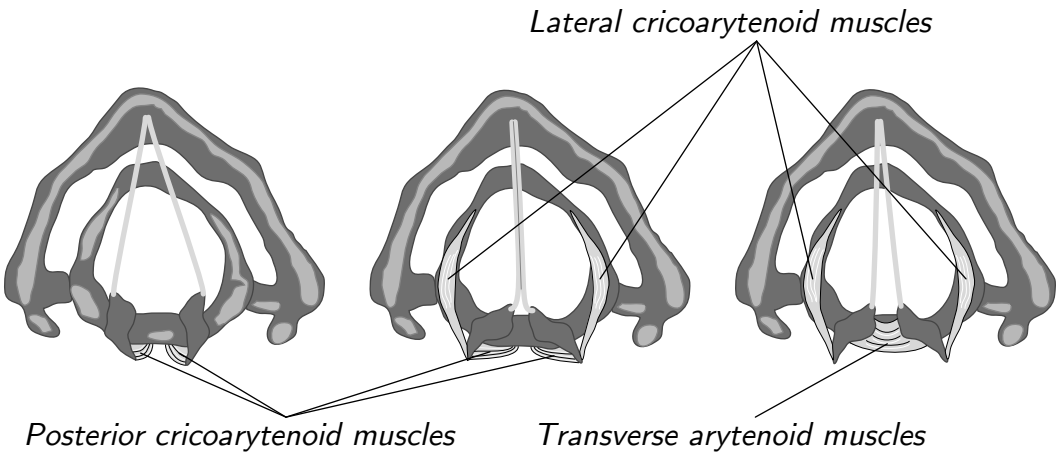

FIGURE 2.9: Superior view of glottis including glottal configurations due to activation of various intrinsic muscles of the larynx to articulate the laryngeal cartilages to abduct and adduct the vocal folds. (adapted from [84]). The posterior cricoarytenoids abduct the arytnoid cartilages, causing the vocal folds to open. The Lateral cricoarytenoid muscles adduct and rotate the arytenoid cartilages, bringing the VFs together. The transverse arytenoid attaches on each side to the whole length of the dorsolateral ridge and the dorsomedial surface of the arytenoid. It approximates the arytenoids and thus adducts the vocal folds.

arytenoid and thyroid cartilages. Figure 2.10 displays a coronal section of the larynx in posterior aspect. The figure shows the relation of the tissues of the larynx, including the gross anatomy of the laryngeal tissues, and places the vocal fold tissues in the context of the overall laryngeal anatomy, together with the spaces and cavities they define.

The vocal folds comprise a layered structure of five histologically distinct layers of tissue. Figure 2.11 exhibits the tissue structure of the vocal folds schematically. The superficial layer is a squamous epithelium, meaning that it comprises flattened and scale like epithelial cells oriented approximately parallel to the surface (in contrast to columnar which are oriented approximately perpendicular to the surface or cuboidal which are symmetrical). The tissue is bound to the layer below via basement tissues. The epithelium protects the vocal fold tissues beneath it and retains moisture to keep the vocal fold tissues moist and compliant. The deeper layers comprise connective tissues and muscle tissues. The next deeper layer of tissue is the superficial lamina propria. The superficial lamina propria is a layer approximately 1-2 [mm] thick of unoriented elastin fibres which are able to store elastic potential energy. Throughout each phonatory cycle, the vocal folds significantly impact each other, and it is hypothesized that the superficial lamina propria and its elastin fibres are able to cushion the vocal folds from impact. Deeper to the superficial lamina is the intermediate lamina propria, which is a layer likewise of 1-2 [mm] thickness of elastin fibres which obtain an anterior-posterior orientation. The isotropy entailed by the orientation entails that these tissues will elastically deform in one axis but not transversely to the fibre orientation. The deepest layer of the lamina propria is, aptly identified as, the deep

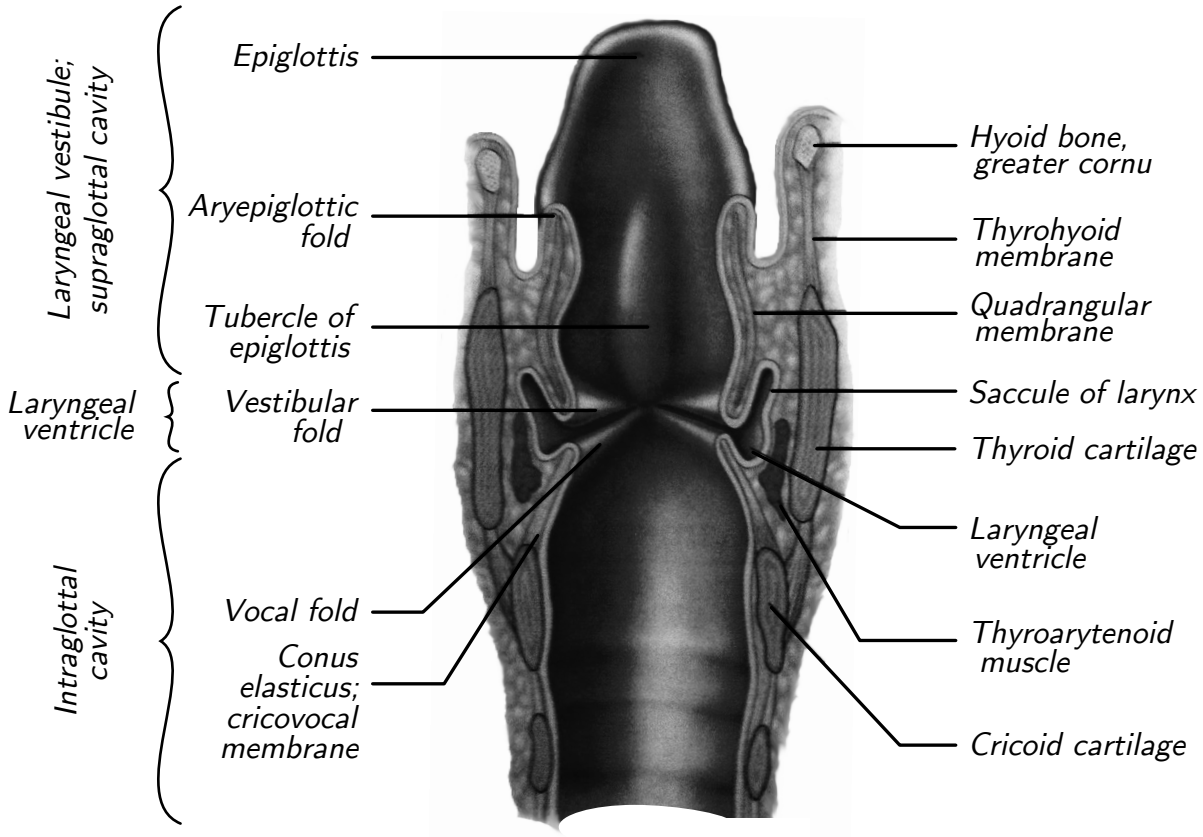

FIGURE 2.10: Posterior aspect of coronal section of larynx (adapted from [32]). This schematic displays the structure and relation of the cartilages and soft tissues of the larynx. The vocal folds are shown in an abducted configuration, open glottis.

lamina propria. It is a layer of collagen fibres approximately 1-2 [mm] thick. Collagen is comparably stiff and resists extension, consequently, this layer stiffens the vocal folds and provides some structural support for the vocal folds. The intermediate and deep laminæform the vocal ligament. Deeper to these are the tissues of the thyrovocalis and thyromuscularis muscles, which form the preponderance of the vocal folds. [41, 42, 98]

The paired vocal folds are symmetric about a midsagittal plane. The VFs comprise multiple and varied layers of tissue. The deepest tissue layers are the muscles of the vocal folds. Superficial to these are the ligaments of the vocal folds, and the superficial-most layers are the mucosa. The mucosa comprises a layer of epithelial tissue with the superficial lamina propria deeper to it. The ligament comprises the intermediate lamina propria superficially and the deep lamina propria deeper to it. The muscle tissue is the tissue of the thyroarytenoid muscle, the thyrovocalis medially and the thyromuscularis laterally, and hence deeper relative to the vocal fold structure. Table 2.1 suggests, in light of the morphology and histology of the vocal folds discussed in [41, 42] that several decompositions into functional groups are useful for understanding and practical from the standpoint of modelling. In table 2.1, amongst the different approaches to classifying these

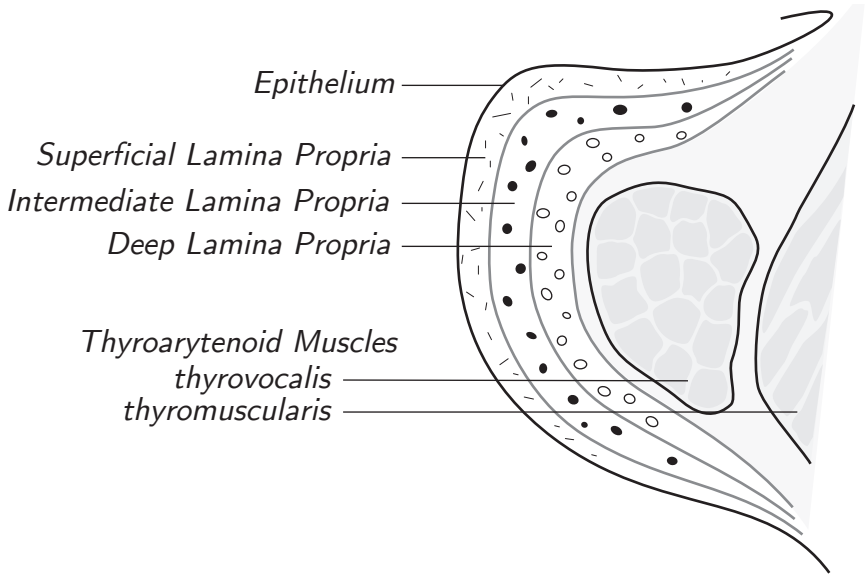

FIGURE 2.11: Schematic of the histological structure of the vocal folds (adapted from [84, 98]).

tissues, in the three layer scheme, the epithelium and superficial lamina propria comprise the mucosal lining of the vocal fold which protects and cushions the fold. The vocal ligament is then formed from the deeper connective tissues which give form and structure to the folds, the elastin of the intermediate lamina propria and the collagen of the deep lamina propria. In the two layer scheme, the cover comprises the epithelium, superficial and intermediate lamina propria. The deep lamina propria and thyroarytenoid muscle, which impart significant mass and potential stiffness to the structure is the body.

The lamina propria is subdivided into deep, intermediate, and superficial based upon histological properties, in particular, density and compliance due to the collagenous fibres. A classification of VF tissues into *body*, comprising thyroarytenoid muscle and deep lamina propria, and *cover*, comprising the tissues superficial to those, i.e., grouping the tissues as shown in Table 2.1, yields a division more suitable for generating tractable models as shall be shown in section 2.2 to follow. The body and cover layers of the VF tissues are grouped in terms of parts with mechanical properties which may be determined by muscle activation and obtain specific mass, in contrast to the cover, which is viscoelastic, compliant, and affixed, but loosely to the base body tissue and is capable of motion relative to the body [12].

The vocal folds are oriented in an anterior-posterior direction. Vocal folds lengths are typically 15 [mm] in adult males and 13 [mm] in adult females. The muscles of the vocal folds are varied in length, thickness, and configuration. The paired arytenoid cartilages rock and slide to adduct and abduct the vocal folds. In normal breathing, the vocal folds are fully abducted. The glottis is a variable opening which lies between the vocal folds. It is approximately 8 [mm] wide at rest. In the myoelastic-aerodynamic theory of vocal fold motion, the oscillatory behaviour is not due to a muscular action. In fact, it is due

TABLE 2.1: Vocal fold tissue layer schemes. [98]

3-layer scheme	5-layer scheme	2-layer scheme
mucosa	epithelium	cover
	superficial lamina propria	
ligament	intermediate lamina propria	body
	deep lamina propria	
muscle	thyroarytenoid muscles	

to a flow induced vibration. Subglottal pressures range from 5 to 15 [cm H_2O] with peak glottal volumetric flow rates of Q_{peak} between 250 and 750 [cm^3/s]. [90]

The motion of the mucosal wave is the primary mechanism of phonation, the source mechanism by which the vocal folds of the larynx convert egressive pulmonic flow within the glottis to sound [12]. The mucosal wave travels along the medial surfaces of the vocal folds. It is shown schematically in Figure 2.12. The physics of the propagation of waves in a visco-elastic medium must be examined in the context of tissue biomechanics and what may be inferred from the histological structure of the vocal folds. For detailed treatment of tissue modelling, consult Fung's monumental treatise of the biomechanics of tissues [39]. The vocal folds comprise a layered tissue structure, described in detail by Hirano in [41, 42] relayed by Titze in [98].

Indeed, after an inhalation to charge the lungs preceding the phonatory process, the vocal folds adduct and completely occlude the trachea. The inspiratory muscles relax and the tissues of the thorax relax to reduce thoracic volume and increase lung pressure. This, in turn, increases the subglottal pressure. When the subglottal pressure has increased sufficiently that the transglottal pressure is above some threshold, the vocal folds are forced open by the wall-normal tractions due to pressure at the fluid-tissue interface. When a self-sustaining oscillation is established in the VF tissues, throughout each period of the phonatory cycle, the propagation of the mucosal wave causes the glottis to evolve in time and therefore modify the GF at relatively fixed frequency. This is the essence of the phonatory process which is now discussed.

2.1.3 Phonation and Vocal Fold Dynamics

Speech communication is made possible by pulmonic airflow, either ingressive or egressive, modified by the constrictions of the glottis and of the vocal tract. The pulmonic airflow is determined by the respiratory muscles and the mechanical properties of the thoracic tissues supported by the thoracic structure. These establish the airflow in the trachea as it enters the larynx. Speech production generates an audible pressure wave by the speaker which is intelligible to the listener. The pressure wave is generated by a source mechanism

within the larynx which modifies the tracheal flow either due to turbulence at a narrowing of a passage or due to the impulsive or quasi-periodic motion of the VF tissues. The acoustical wave generated at the glottis is modified by the resonators and articulators of the vocal tract superior to the glottis. In voiced speech, it is the quasi-periodic oscillation of the VF tissues which produces a glottal waveform of particular frequency. This is phonation. Phonation occurs in the larynx when an egressive pulmonic flow generated at relatively constant pressure by the lungs is interrupted by the quasi-periodic self-sustaining oscillation of the vocal folds. The action of the vocal folds is an aeroelastic response to the flow. The vocal fold tissues merely oscillate due to their inherent elasticity and excitation by the glottal flow, which originates in the lungs entering the larynx via the trachea and supplies the energy for the oscillation. Phonation refers specifically to the quasi-periodic opening and full occlusion of the vocal folds which modulates the tracheal flow to produce an acoustical source of quasi-steady frequency f_0. This is the fundamental frequency of phonation and it correlates to what listeners perceive as pitch.

Figure 2.12 schematically shows the temporal evolution of the VF tissues in one complete phonatory cycle. The figure displays a mid-membranous coronal section of the vocal folds together with corresponding supraglottal view at successive instants of time as the tissues evolve throughout one phonatory cycle. The onset of voiced sound occurs after inhalation when the thoracic cavity is in an expanded state. The vocal folds adduct, occluding the glottis, and maintain a fixed position. Apart from the muscle activation required to hold the muscles in an effectively steady configuration, the subsequent motion of the vocal folds is merely a response of the viscoelastic vocal fold tissues to the prevailing fluidic loading. The thoracic elevators relax and the thorax recoils due to the elastic potential energy of the thoracic tissues. The pressure generated by the contracted lungs elevates the pressure on the inferior surfaces of the vocal folds and pushes them open. Once the vocal folds are initially separated due to the pressure loadings, the tracheal flow produced enters the larynx and loads the vocal folds causing them to separate further. The aerodynamic loading causes an evolving pressure distributions which results in the observed motions. The vocal folds eventually occlude in response to a suction due to the Bernoulli effect at the narrowing passage, and the cycle repeats. Utterances of longer duration are possible not merely due to recoil of thoracic tissue, but are aided by the expiratory muscles which cause the lungs to be contracted beyond their resting position. The wavelike response of the medial surfaces of the VF tissues is known as the vertical medial mucosal wave, or, simply, the mucosal wave, because the most significant tissue displacements occur in the mucosa of the fold. It is worth noting that the mucosa obtain a convergent configuration throughout the opening phase and a divergent configuration throughout the closing phase.

An early description of phonation was presented in 1848 by Johannes Müller, who was a medical doctor and professor of anatomy and physiology at the University of Berlin who proposed, in [66], that the vocal folds vibrate the way a membrane flutters in a musical instrument when it is excited by an airflow. His physiological characterization is compatible with the phonatory cycle described above, entirely accurate, but qualitative. A quantitative theory of phonation was first proposed by van den Berg in *Myoelastic-Aerodynamic Theory of Voice Production* [102]. The theory suggests that the self-oscillatory response of the vocal

fold tissues is a consequence of the interaction of the VF tissues and the glottal flow. The quantitative investigation of phonation was begun in earnest by van den Berg in the mid-20^{th} century in [102, 103, 104]. The mechanism of the mucosal wave has been an object of investigation for quite some time. For example, in [95], Timcke, Von Leden, and Moore investigate the asymmetry of the mucosal wave in various vocal registers. They determined that the opening phase is shorter than the closing phase and discuss the asymmetry in terms of open quotient and speed quotient in relation to variation in pitch and in intensity. The open quotient, OQ, is defined as a duty cycle which identifies the fraction of one period of a phonatory cycle throughout which the glottal area is non-zero. The speed quotient, SQ, is defined, for one phonatory cycle, to be the ratio of time to maximal glottal area from closure and time to close from maximal opening.

More recently, for example in [12], the mucosal wave is described in greater detail and more quantitatively. It has become clear that phonatory output is a consequence of VF tension and elasticity, determined by the intrinsic muscles of the larynx in a coordinated and controlled manner. It must be emphasized that the oscillatory behaviour of vocal folds in phonation is a passive interaction of glottal flow and vocal fold tissues and is not a consequence of periodic activation of laryngeal muscles. The intrinsic muscles of the larynx are held relatively fixed throughout many periods of the oscillatory cycle.

Titze, in [97], relates the mucosal wave to the body cover model of the vocal folds; he also identifies conditions necessary for the condition of propagation of a mucosal wave. He suggests that to sustain self-oscillatory behaviour, the GF must impart more energy to the VFs in the opening phase of the phonatory cycle than they dissipate viscoelastically throughout the cycle. Nominal values for flow rates, lung pressures, and other flow parameters were discussed by Ishizaka and Flanagan [48].

In light of the description of VF morphology in the previous section and the description of phonation and the mucosal wave herein, it is clear that phonatory outputs are regulated by the coordination of the musculature of the thorax and larynx subject to the various mechanical properties of the tissues of the vocal organs. For a comprehensive discussion, see for example [43]. In particular, the motion of the vocal folds is determined specifically by the tissue density, stiffness, and viscosity. The capacity for the body to adjust these parameters allows for variability in the fundamental frequency and loudness of the acoustical signal produced at the larynx. The vibrating mass of the vocal fold tissues may be modified through the various adjustments of the intrinsic muscles of the larynx. Specifically, VF tension may be varied by extension of the vocal folds in contraction of the cricothyroid or by recruitment of the thyroarytenoid muscle. Additionally, flexion of the thyroarytenoid muscles permits alteration of the stiffness of the vocal fold tissues without causing the length of the vocal fold to change [41]. The cover stiffness, while not determined explicitly, is influenced by longitudinal strains imparted by adjacent structures. The tissue viscosity itself damps the oscillatory behaviour, and must be overcome by the energy imparted to the VFs by the GF.

In modal phonation, at conversational intensities, the glottal waveform exhibits a duty cycle of approximately 50% opening, 30% closing, and 13% completely closed [6]. When

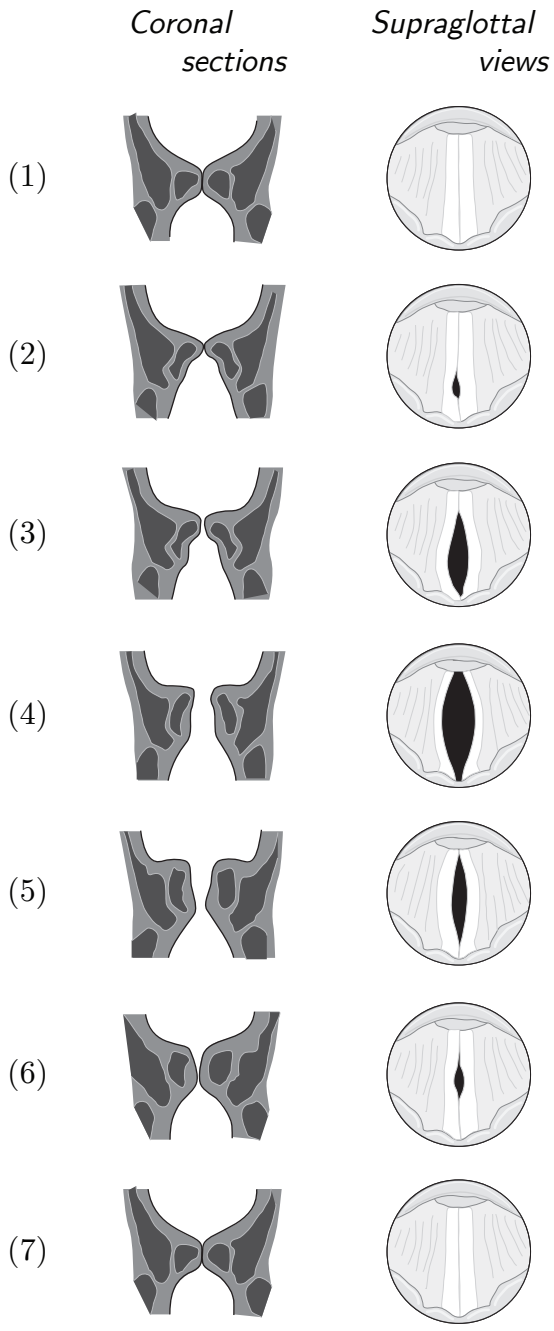

FIGURE 2.12: Schematic of vibratory cycle of vocal folds (adapted from [84]). The schematic displays corresponding pairs of coronal sections and supraglottal views at different instants throughout a vibratory cycle. The sequence of configurations of the mucosa shown in coronal section is the mucosal wave. The numbering corresponds to the sequence in which the sections evolve in time throughout one cycle. Configurations (1) and (7) are closed, configurations (3) shows the opening phase; (5) and (6) are the intermediate phase; and (6) is in the closing phase of the vibratory cycle.

the vocal folds are tightly adducted, the return to closure is rapid and the glottis remains occluded for longer period. In additional to the modal register, registers which have been identified are glottal fry, falsetto and whistle, pressed and breathy phonation, and whisper. Postures of the intrinsic muscles of the larynx determine the configurations necessary to produce these registers. Pitch is the psychological correlate of frequency, and it is determined by the tension, length, and mass of the VF tissues. These parameters are in voluntary control of the speaker. The mass distribution is a function of elongation of the vocal fold [98]. Contraction of the cricothyroid, which effects a tilting of the thyroid cartilage relative to the cricoid cartilage, causes a shortening of the VFs, and this, in turn, causes f_0 to increase. The thyrovocalis is also a VF tenser, it approximates the cricoid and thyroid. Flexion of this muscle causes the VF tension to increase, but also reduces the distribution of mass per unit length of the vocal folds. These competing contributors to f_0 nevertheless allow adjustment. There is also a relation between subglottal pressure, P_s, and fundamental frequency of phonation, f_0. Increasing f_0 increases glottal resistance and, therefore, increases P_s. Loudness is the psychological correlate of sound intensity (measured as a sound pressure level), and is increased as P_s increases. A doubling of P_s typically causes a measurable 8-12 dB increase in vocal intensity [91].

In all investigations of phonation and the mucosal wave, there is an interplay between the clinical measurements and the computational models. However, there are tremendous obstacles to relating experimental results obtained in vitro to the tissue biomechanics of tissues in vivo. Muscle activation is difficult to simulate, and the tissues in vitro are not kept moist and lubricated. These and other difficulties are outlined by, for example, Titze [98]. Determining the mechanisms of self-sustained oscillation of the vocal folds requires characterization of intraglottal aerodynamics. Exactly because the aerodynamics are difficult to determine in vivo, and many in vitro studies exhibit the drawbacks mentioned, much of the current understanding of vocal fold vibration mechanism is a consequence of mechanical, analytical, and computational models. Section 2.2 is entirely devoted to the modelling background necessary to undertake computational model development.

2.1.4 Articulatory and Resonatory Organs

The acoustical signal produced in the larynx is modified by articulatory and resonatory system. Articulation is the process of approximating two or more structures to affect or shape the glottal sound source to produce the intelligible sounds of natural language. The articulatory system comprises mobile and immobile articulators. The tongue is largest and most important mobile articulator. It is capable of adjustments of tip elevation and depression, as well as lateral deviation. The tongue may narrow, a groove may be formed along its centre, the tongue may protrude and retract. The posterior of the tongue may elevate or the body may depress. The three immobile articulators are the alveolar ridge of maxillae, hard palate, and teeth. The cavities of the vocal tract, the oral, buccal, nasal, and pharyngeal cavities, shape acoustic output. The oral cavity is the most significant for speech, capable of undergoing the greatest volumetric and geometric alteration at the

region modified by motions of tongue and mandible. The mouth is the source of orally emitted phonemes. The lips of the mouth are important for articulation of consonants and vowels. The velum, attached anteriorly to the palatine extension of the hard palate, separates oral and nasal cavities. The mandible supports lips tongue and teeth, carries them to maxillary targets, the lips teeth alveolar ridge, and hard palate.

Figure 2.13 shows a close up of the region of the vocal tract superior to the larynx shown in Figure 2.1. The articulatory and resonatory organs comprise the structures and cavities of the upper vocal tract, the region superior to the larynx. This anatomical placement downstream (in exhalation) of the laryngeal structures enables the modulation of the laryngeal sound sources. Oropharyngeal, nasopharyngeal, oral, and nasal cavities are resonating cavities and their geometry is altered by articulation, i.e., the adjustments of the resonatory cavities and spaces which ultimately filter the sound produced by vocal folds in phonation. Figure 2.13 also shows the eight places of articulation, these are specific spaces which may be expanded or contracted in order to produce the consonantal sounds of natural languages. In natural language, vowels are those sounds produced with a relatively open vocal tract, the phonatory source is due to the vocal fold vibration, and it is modified little in the upper vocal tract. Consonantal sounds of natural language are produced from partial or complete closure when articulators are approximated to articulating surfaces within the vocal tract. Consonants may include harmonic components of the fundamental frequency, but they always contain turbulent noise generated as the airflow is modified by sudden stoppage, release, or restricted flow within the upper vocal tract. The anatomy is described in detail by Dickson and Maue-Dickson [20] and also by Stevens [92], who additionally describes the physiological mechanism specifically as it pertains to speech modelling.

Ultimately, the acoustical signal produced in phonation, with fundamental, f_0, has many overtones with intensity inversely proportional to frequency [20]. The fundamental frequency is the physical aspect of the speech signal which is perceived as pitch. The spectrum of voiced speech contains f_0 and higher harmonics. The vocal tract continuously varies its geometry, so speech spectra of voiced speech are not discrete, they are quasi-periodic over tens of milliseconds for one particular sound. The transition between sounds is gradual; the acoustical signal changes from characteristics of one sound to the next on the order of 40 milliseconds [91].

Nothing more shall be said about articulation in this manuscript. This brief discussion has been included merely to round out the picture of speech production. In the framework of the linear source-filter theory of voice production, the volumetric flow rate of the glottal flow is held to be the primary source mechanism which excites the resonators and articulators of the upper vocal tract. This theory, initially proposed by Fant in [34] and discussed thoroughly in Stevens [92], requires that the source mechanism, e.g. vocal folds in phonation, and the vocal tract acoustical filter are independent of each other, in particular, that the acoustics of the upper vocal tract do not influence the volumetric flow rate of the glottal flow. Despite that this assumption may be called into question [70], that coupled acoustics must surely modify the dynamical VF behaviour, it shall be assumed

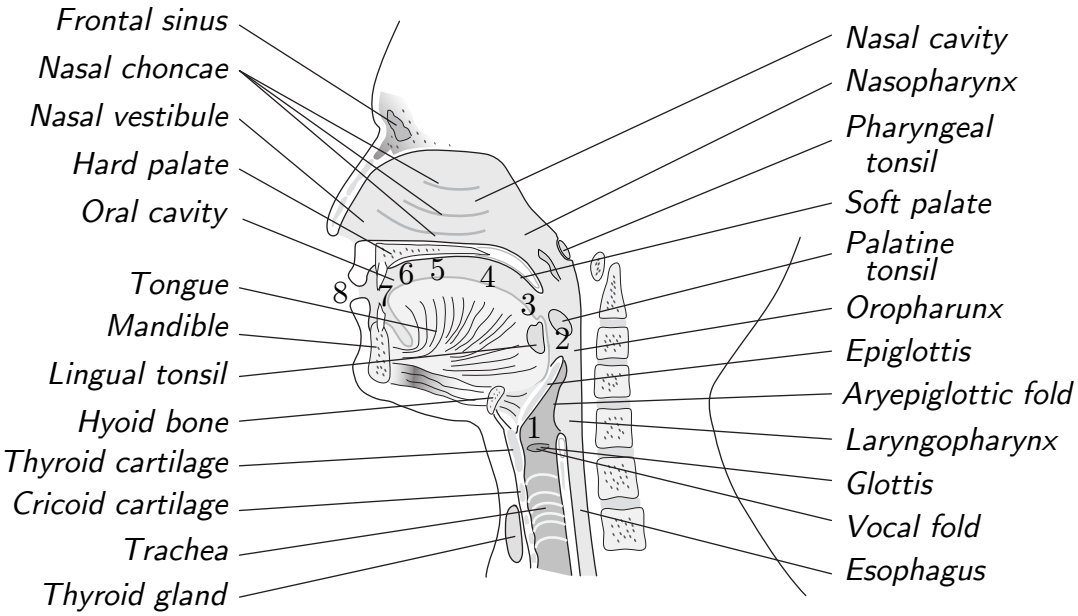

FIGURE 2.13: Schematic of articulators and resonators together with places of articulation: (1) glottal, (2) pharyngeal, (3) uvular, (4) velar, (5) palatal, (6) alveolar, (7) dental, and (8) labial (adapted from [74, 84]).

throughout the remainder of this development that the mechanism of phonation may be investigated independently of the acoustical field.

Before proceeding, as an aside, it should also be mentioned that articulatory phonetics, the subject of Stevens's monograph [92], furnishes a general framework to study the intelligible phonetic sounds of natural language and their production. Ladefoged, in [55], supplies a detailed account of the mapping between the physiological configurations and the phonatory structures of natural languages. Additional context in terms of natural language, speech synthesis, and communication theory is furnished in [74]. Again, the discussion in the remainder of this thesis focuses on the models of phonation in the absence of the acoustical field.

2.2 Approaches to the Modelling of Phonation

The first section, Section 2.1, of this chapter introduced the anatomy and physiology of the vocal organs of the body and the physiological mechanisms involved in the production of voiced speech. The respiratory organs of the chest together with the structure and musculature of the larynx are capable to furnish the flow conditions necessary to incite self-sustaining oscillations of the vocal fold tissues in phonation. It was briefly mentioned that the resonators and articulators modify the acoustical waveform generated at the glottis to produce the sounds of spoken natural languages. It is the mechanism of phonation

which is of particular interest herein because the question which this thesis attempts to address pertains to whether the intraglottal vortices, whose presence has been observed in simulation and experimentally to form in the closing phase of the phonatory cycle when the glottis obtains a divergent configuration, contribute significantly to the observed dynamical response of the VF tissues. It has been hypothesized that intraglottal vortices determine negative (gauge) pressures in the intraglottal spaces in the closing phase of the phonatory cycle near the superior edge of the vocal folds, and that these vortices possess sufficient strength to incite significant accelerations of the vocal fold tissues due to fluidic loading. This section attempts to furnish a treatment of glottal modelling and glottal aerodynamics sufficient to comprehend and appreciate these hypotheses and to place the work of this thesis within the modelling framework of the existing body of literature of the speech science community.

Recall Figure 2.12, which displays a simplified schematic of the mucosal wave produced in one phonatory cycle, the mucosal wave is a consequence of the fluid-structure interaction of the glottal flow and the vocal fold tissues. The determiners of f_0, the fundamental frequency of VF vibration, are the tension of activated vocalis and cricothyroid muscles and the compliance of the VF epithelial tissues which cover them, as well as the other connective tissue of the vocal fold body. Consequently, the tissues may be modelled as a continuum and characterized by a distribution of density, compliance, and visco-elastic damping. The GF imparts energy to the tissues, which respond dynamically. The mere fact that the tissues may be quantified in terms of their geometry and mechanical properties suggests the desirability of modelling the dynamics of phonation, with the idea that greater quantifiable and therefore predictive insight and understanding of voiced speech may be gained. Ultimately, a practical dynamical model of phonation will capture this behaviour, and will, moreover, model appropriate physical effects and therefore suggest relevant physical causes for the simulated dynamics. It is the goal of this section to describe how such simulation models may be constructed, especially how they are constructed subject to the physiological phenomena which determine the actual dynamics of vocal folds in phonation. The overall interaction of glottal flow and vocal fold tissues is one of fluid-structure interaction.

2.2.1 Computational Fluid-Structure Interaction

FSI is a burgeoning field in engineering [11, 22], with applications, for example, in aeroelasticity [21], design of turbine blades [9, 10], flapping and bending bodies [85], the inflation of parachutes [76], and energy harvesting with immersed flexible bodies [4, 77]. Generally, in problems of engineering, FSI leads to improved design decisions because it sheds light on processes which lead to fatigue failure of critical components, as well as an improved understanding of processes which involve the interaction of solids and fluids. More relevant to and aligned with this thesis are the biomechanical applications of FSI techniques; biological fluid mechanics interact with flexible tissue structures. For example, pulsatile flow of viscous fluid through compliant tubes, i.e., cardiovascular hemodynamics, see for

example [47]. Again, in the context of this thesis, it should be apparent from the development of Section 2.1, that the GF-VF interaction is an example of FSI and is amenable to the methods of computational fluid-structure interaction. The glottal flow imparts a fluidic loading to the vocal folds which respond by deforming and thereby alter the flow and consequently modify the loading. This process of continuous coupled interaction between the glottal flow and the vocal fold dynamics is the focus of this thesis.

Due to the shortcomings of experimental studies, a program of computational studies in parallel to experimental work and clinical investigation with actual subjects enriches the collective understanding of the phenomena of interest. In the case of glottal airflow and of vocal fold dynamics, real VF tissues have infinitely many degrees of freedom as tissue properties are distributed, additionally, real GF is constant viscous Newtonian with uniform density (phonation is isothermal; the vibration of vocal cords does not cause significant heating and therefore does not modulate the viscosity of the fluid which, in general, is a strong function of temperature) but with some compressibility (the acoustical field, which is due to the transmission of compression waves in a fluid medium, in general, requires the compressibility of the medium). Computational studies may be performed in a way in which they neglect some effects. If the simulation outcomes exhibit no physiological basis or differ from experimentally observed behaviours, a measure of confidence is obtained that the ignored effect is important and may not be discarded. Alternatively, if the discarding of an effect does not seem to impact simulation outcomes, the effect may be deemed to be minor, and subsequent computational or experimental studies may neglect these effects. This is perilous, however, because coupled GF and VF dynamics are highly non-linear, an effect considered to be minor in one context might be significant in another. Nevertheless, the computational complexity of the overall fluid-structure interaction problem for the GF-VF interaction requires that simplifying assumptions be made in order that the problem remain tractable. These assumptions will be carefully stated in model development in Chapter 3; this is to ensure that the outcomes of the computational study undertaken herein may be directly related to the assumptions of the model so that the simulated behaviour may be explained in light of the assumptions to which it is subject.

The vibration of the vocal folds is a consequence of the coupling of visco-elastic tissue excited by the air expelled from the lungs. It is a problem of FSI in which the airflow supplies the energy and the tissue provides a varying boundary determined by elastic potential energy and viscous damping due to the tissue structure. The problem is difficult to solve in a general or complete sense because neither the tissue structure, the geometry of the glottis, nor the coupled acoustical pressure fields which modify the flow are known or have been characterized completely. Solutions to the problem are subject to computational limitations due to the approach of the FSI problem, strong dependence on tissue properties for the visco-elastic tissue deformation problem and boundary conditions for the fluid flow problem.

Whereas, full-blown monolithic solvers must recast the FSI problem to a purely numerical basis, the partitioned approach to FSI allows analytical or semi-analytical solution of part of the problem. In the case of the fluid loading due to the glottal flow in the

vocal fold dynamics problem, the flow field, subject to appropriate constraints, may be written analytically and obtained via a direct numerical computation of various analytical expressions.

The monolithic approach to FSI problems simultaneously solves a system of equations derived from the discretization of the governing equations which govern the multiple phenomena and solves them simultaneously. In a partitioned approach, the solver is decomposed to treat distinct physical effects separately. For example, the physics of the deforming and displacing vocal fold tissues is treated separately from the loading due to the aerodynamics of air driven through a deforming channel by an upstream source of constant pressure and velocity conditions.

The monolithic approach to the problem of glottal flow and vocal fold dynamics, because solutions are strongly influenced by material properties and boundary conditions of the flow, in addition to being computationally expensive, is inherently complex, and the uncertainties of the boundary conditions and tissue properties yield simulations with difficult to justify outcomes. This approach has not been pursued aggressively in the literature, whereas the partitioned approached with lumped-element models of the vocal fold tissues coupled to simple aerodynamics models to determine the fluidic loading on the medial surfaces of the vocal folds due to glottal flow have been carefully studied and well established [30, 65].

A significant advantage of the partitioned approach in vocal fold modelling is that it has fostered the development of increasingly complicated models of the vocal fold dynamics with increasing explanatory power. The flexibility of allowing simple one-dimensional Bernoulli solvers, two-dimensional flow solutions employing ideal fluid, or CFD solutions of two- or three-dimensional Navier-Stokes equations coupled to tissue models of varying complexity, has permitted investigators to focus on various phenomena of interest while providing a basis of comparison with existing models.

2.2.2 Vocal Fold Tissue Models

The structure of vocal fold tissues has been described in Subsection 2.1.2 to be rather complex. To restate this more precisely, the tissues of the vocal folds are nonlinear, viscoelastic, inhomogeneous, and nonisotropic. Furthermore, significant uncertainty in measured properties of excised tissue persist because moisture content and muscular activation levels obtained in-vitro are unlike the actual tissues in-vivo [15, 98]. Additionally, mechanical properties of the vocal fold tissues are spatially distributed; VF tissue models have infinitely many degrees-of-freedom in general, but may be reduced to lumped-element models of significantly fewer degrees of freedom. Lumped-element models combine a small finite number of lumped masses linked by springs and dampers, and they attempt to capture the distributed VF tissue structure and appropriate physiological behaviour. The validity of this approach hinges on the serendipitous fact that the most significant modes of vibration also account for nearly all of the energy exchange between the glottal flow and vibrational response of the vocal folds; therefore, the response which is rendered with a small finite

number of degrees of freedom is sufficient to emulate the mucosal wave in computational models with some measure of accuracy.

Amongst the prevailing approaches to the modelling of vocal fold tissues, sophisticated continuum models. These possess the advantages that they represent relevant physiological structures via detailed constitutive models with greater fidelity than do lower order lumped-element models. Lamentably, this quality is also to their detriment; whereas, in principle, their accuracy enables them to be more directly mapped to experimentally measured tissue properties and to physiological structures, the good measures of tissue properties that this would require have not been devised. Consequently, many higher order models are dependent upon parameter tuning, e.g. [81, 100, 105]. This is in contrast to lower order lumped-element models which merely seek to phenomenologically reproduce the temporal evolution of glottal waveforms either of minimal projected cross-sectional transverse area of the glottis or of the mean glottal volumetric flow rate, the signals of greatest significance in driving the acoustics of the upper vocal tract. Mapping of parameter values from clinically observed tissue behaviour to lower-order vocal fold tissue models requires that values be assigned in a meaningful way to the finite number of spring rates, damping coefficients, and masses which comprise the model. Typically, the biomechanical tissue properties have been assigned by fitting the behaviour of the model to dynamical response of VF tissues in clinically obtained visualization of the phonatoy cycle [19]. In investigations which employ reduced-order VF tissue models, there is an attempt to continually improve the extent to which the models emulate, in a manner representative of the physiological vocal sound source, the dynamical behaviour of the vocal fold tissues. The development of lumped-element models is described at length in the review [13], and, more generally, within the overall context of speech modelling, in [30]. Consequently, the particular bar-plate model which is employed in the model developed in this thesis is briefly described. The mathematical details of the chosen model are subsequently stated in Section 3.1.1 in the following chapter.

A lower order lumped-element model of the VF tissues has been selected for the present study because it has been deemed sufficient to capture the salient features of vocal fold oscillation in a physiologically representative manner, but, more importantly, because the model is computationally tractable. The model will allow the rapid computation of many phonatory cycles. The model employed herein is the bar-plate body-cover model of Titze, it is displayed schematically in Figure 2.14 below. This has been chosen for its amenability to the glottal flow in contrast to block and spring models, which are aerodynamically unreasonable. The model is a modified version of one initially set forth by Liljencrants, who had proposed a translating and pitching 2 DOF single-mass model in [59]. This single-mass would capture the phase of the mucosal wave in the inferior-superior axis, but would not reveal a transverse phase relationship between body and cover of the vocal fold tissues in the phonatory cycle. Titze coupled this model to a translating body mass to add an additional degree of freedom to account for transverse phase between the body and cover. The lumped-element model which is employed herein is this bar-plate model used to investigate the regulation of glottal airflow in phonation by Titze in [99] and Titze and Story in [100]. This layered body-cover model attempts to capture the layered structure of

body and cover which is evident in the mid-membranous coronal section of the vocal folds. Again, the model does this with a surface which is not stepped as in other multi-mass models, so that it is aerodynamically more reasonable. Three mass models with a single body mass and a pair of cover masses possess three translational degrees of freedom, but the surface, where fluidic loadings would be computed, are stepwise discontinuous, and this introduces unreasonable flow conditions at the transition between masses.

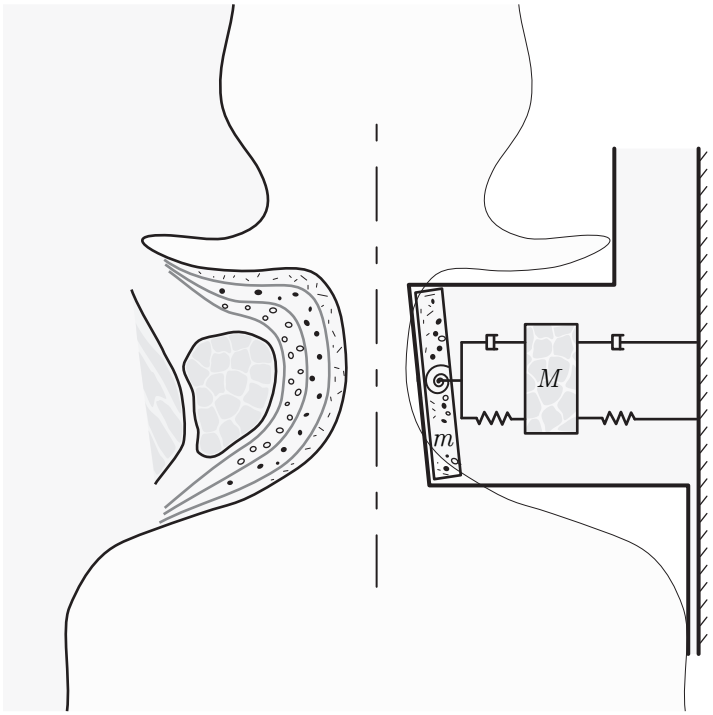

FIGURE 2.14: A schematic showing the layered tissue structure of a vocal fold together with the 3 DOF bar-plate body-cover lumped-element model of the VF tissues which attempts to capture tissue structure in an aerodynamically reasonable fashion. The body mass M models the contribution to the dynamics due to the combination of deep lamina propria and thyroarytenoid muscles and the mass m pitches and translates with respect to m as the mucosa and intermediate lamina propria would move relative to the body. The visco-elastic translational and torsional coupling models the linkages between these layers. The model cannot account for displacement of the VF tissues in the axial direction.

2.2.3 Glottal Aerodynamics

Most reduced-order computational simulations of phonation employ a one-dimensional inviscid irrotational incompressible flow solver and compute the pressure distribution with the steady one-dimensional Bernoulli equation along the glottal centreline and impress this pressure condition upon the medial surfaces of the vocal folds. However, phonation is

the outcome of a fluid-structure interaction of the glottal flow and the vocal fold tissues (possibly coupled to the acoustical effects due to the articulators and resonators of the upper vocal tract), and, due to significant variation of geometry within the larynx, viscous effects, for which ideal potential flow models do not account without ad hoc assumptions about the presence and behaviour of singularities, cause simulated glottal flow fields to differ from the observed flows in the clinic and the laboratory. Consequently, the pressures which arise in the neighborhood of the glottis and, thereby, modify the aerodynamic loading of the vocal fold tissues and the resulting behaviour of the vocal fold tissues, are not adequately captured by these models.

Increasingly realistic flow solvers which determine glottal flow fields coupled to lumped-element VF models in the partitioned FSI architecture are facilitated by increasing computational power. The drawback of ideal potential-flow fluid physics centre on the ad hoc utilization of singularities which are required in the attempt to model viscous effects which are not implicitly captured in an ideal flow model. The trade-off of runtime associated with glottal flow solvers of higher fidelity over potential flow solvers become less significant as computational power increases. Nevertheless, ideal potential flow models together with their accompanying ad hoc assumptions have the capacity to elucidate flow physics which are otherwise obscured by numerical solvers. They allow investigators to rapidly test dynamical response to hypothetical conditions.

In the present computational study, an ideal incompressible unsteady two-dimensional potential flow solver is developed and coupled to the 3 DOF VF tissue model described above in Section 2.2.2. To account for viscous effects in an inviscid model, ad hoc assumptions about the point of flow separation are employed together with ad hoc assumptions about the locations and strengths of advecting irrotational vortices to capture the effects of coherent intra-glottal flow structures. The nature of flow separation and intra-glottal vortical structures is examined in the remaining two sections of this background chapter.

2.2.4 Flow Separation and the Glottal Jet

Flow separation is a viscous effect. Flow separation of a viscous glottal airflow occurs in the presence of an adverse pressure gradient in the closing phase of the phonatory cycle when the glottis has obtained the geometry of a diverging channel. The results of an experimental particle image velocimetry (PIV) study of a driven scaled-up mechanical model of a glottis are shown in Figure 2.15. Flow is from left to right in these images and the grey areas are the vocal folds. The image shows a sequence of four consecutive instants in the closing phase of the phonatory cycle; the glottal jet is seen to issue from the glottis into the quiescent supraglottal region. The jet forms when the glottal airflow separates from the surface of the vocal fold at some point at or upstream of the glottal exit during the closing phase of the phonatory cycle when the glottis has obtained a diverging configuration. The glottal jet is initially symmetrical, but, as the glottis closes, the jet skews and adheres to one of the vocal folds creating a recirculation of fluid between the jet

and the opposite vocal fold. The roll-up of vortices is also apparent in this recirculation region; the vortices shall be discussed in the following subsection.

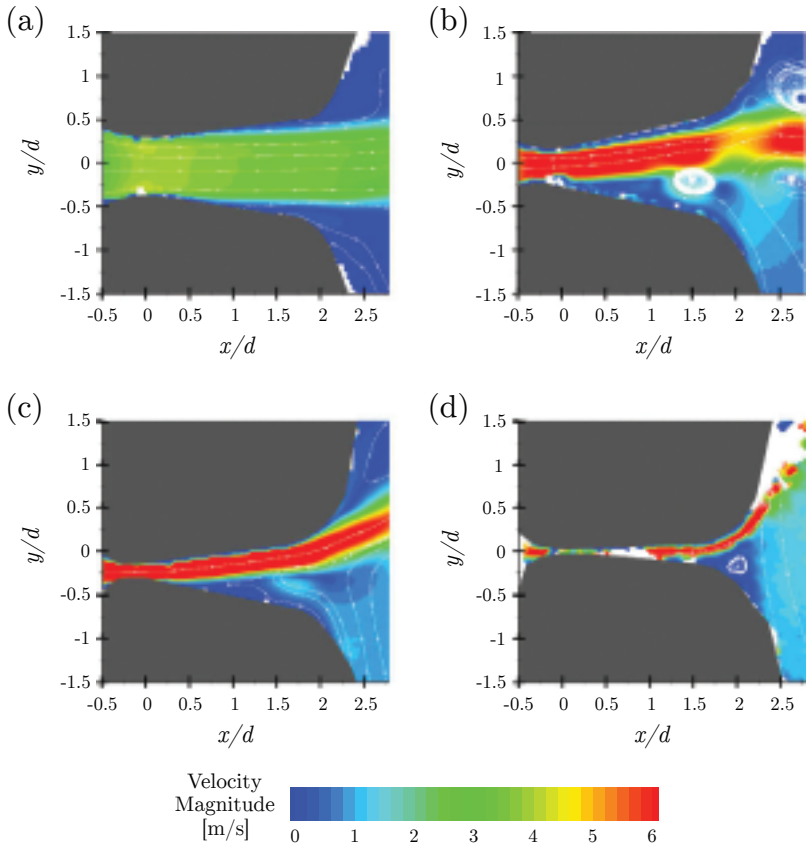

FIGURE 2.15: PIV study of glottal flow in a scaled-up physical model of a driven vocal fold model at four consecutive instants in the phonatory cycle. Instant (a) is at $t = 0.60\,T_{\text{open}}$, (b) $t = 0.70\,T_{\text{open}}$, (c) $t = 0.80\,T_{\text{open}}$, and (d) $t = 0.90\,T_{\text{open}}$, in which T_{open} is the amount of time the glottis is open in a single phonatory cycle. (Reproduced from [28]).

To account for flow separation in an ideal potential flow solver, the point at which flow separates from the medial vocal fold surface must be prescribed in an ad hoc manner. This will be based upon some criterion derived from a physical understanding of flow separation in oscillatory flow, such as that presented in [87]. In early glottal flow models, flow separation was specified to occur at an axial station where the minimal glottal area is achieved; however, if this approach were employed in the bar-plate lumped-element model described in Section 2.2.2, the flow would separate at the inferior medial edge in a diverging glottal configuration but would separate at the superior medial edge otherwise. This would exclude the possibility of pressure recovery in the glottal jet in the diverging configuration of the glottis, it would also constrain the computation of pressure on the medial vocal fold surface; either an ad hoc pressure would be applied in the separation region or pressure would not be defined there. A point of flow separation on the medial

surface which moves along the surface would circumvent this deficiency. Several studies to assess and determine the moving location of the point of flow separation have been undertaken, for example [2, 59, 75]. In [59], Liljencrants proposed another ad hoc correction in which the separation occurs at a point at which the ratio of the cross sectional area the point of flow separation to the minimal glottal area obtains a specific fixed value. In [99], Titze employs a value of 1.2 for this ratio of glottal area at separation to minimal glottal area. This separation model is employed in the validation of the simulation model developed herein against the simulation model of Titze described therein. In the extension of the simulation model which incorporates advecting vortices developed herein, the ad hoc condition that the flow always separates at the trailing edge is employed. This is required to ensure that the pressure perturbation due to the presence of the vortices is communicated to the portion of the vocal folds near the glottal exit and will be discussed below.

2.2.5 Intraglottal and Supraglottal Vortices

The discussion of flow separation in Section 2.2.4 above is critical from the standpoint of determining the pressure distribution impressed upon the medial surfaces of the vocal folds because, in an inviscid flow model, the sole contributor to aerodynamic loading of the vocal fold tissues is pressure, which is significantly diminished in the separation region. Moreover, as seen in Figure 2.15, because intraglottal vortices form downstream of the point of separation of the glottal jet, in order to ascertain the influence of intraglottal vortices, the point on the medial surface of the vocal folds at which flow separates must be determined with relative accuracy. That is, the influence of intraglottal vortices, if at all, is due to the presence of intraglottal vortical structures downstream separation.

The precise mechanism which incites the formation of intraglottal vortices has not been identified [65]. Early studies which suggested the presence of intraglottal vortices were [107, 109]. More recently, shear layer instabilities in the supraglottal free jet leading to supraglottal vortices has been observed in [53, 68, 70]. Vortices have been found in computational studies of the glottal flow. For example, supraglottal vortices have been observed in the computational simulations in the investigation of the asymmetry of the glottal jet in [110]. As well, intraglottal vortices were observed in [107, 108], in which two-dimensional direct numerical simulations (DNS) of the governing equations for a rigid channel with deforming obstruction with prescribed motion were performed. Intraglottal vortices were also observed in unsteady flow but with a static glottal configuration in the computational study [62]. Experimental work has also indicated the presence of coherent vortical structures, for example, in physical models [28, 70], and, in excised canine larynges [1, 52, 53, 54, 68]. As has been mentioned, excised tissue is problematic because tissue moisture does not reflect in vivo moisture and muscular tension does not reflect in vivo tensions, but physical models suffer from the fact that the mechanical properties of the model may or may not reflect in vivo or even in vitro tissue properties or structures. However, physical models and their outcomes do serve to validate simulation codes, especially

when the modelled behaviour corresponds to an analogous physical model in a meaningful way.

Khosla et al. [53] performed PIV measurements in a supraglottal mid-membranous coronal plane of excised canine larynges. They identified starting vortices; Kelvin-Helmholtz (KH) vortices, which are due to shear layer instabilities; and standing and advecting vortices supraglottally with shape and point of origin determined by the instant in the phonatory cycle. More recently, in [72], a PIV study of the intraglottal vortices to determine the parameters which influence the mechanism of intraglottal vortex formation have been performed. Figure 2.16 displays a sequence of consecutive glottal configurations in the closing phase of the phonatory cycle obtained therein. Figure 2.17 displays a simplified

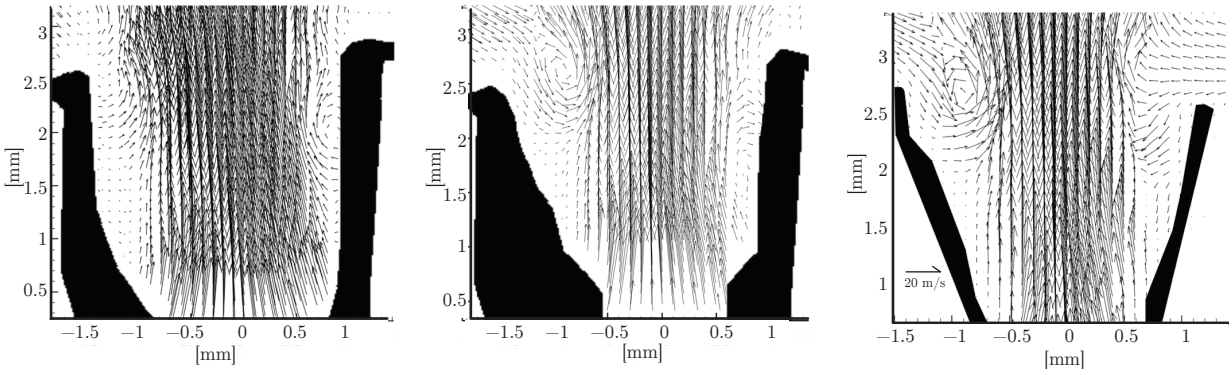

FIGURE 2.16: PIV study of intraglottal vortex formation in excised canine larynges. The PIV data was obtained at a mid-membranous coronal section of the glottis. The images show a sequence three consecutive instants in the closing phase of the phonatory cycle. The velocities suggest the formation of coherent vortical structures in the separations region between the glottal jet and the medial vocal fold surface near the glottal exit. (Reproduced from [72])

schematic of intraglottal flow structures observed in their PIV studies in mid-membranous coronal section of the glottis at some arbitrary instant of the closing phase of the phonatory cycle. The schematic shows a diverging glottal configuration, and vortical structures are observed within the recirculation zones of the separation regions at or near the superior medial edges of the vocal folds.

In terms of the importance of intraglottal vortices in the study of speech, in addition to modification of the pressure field within the glottis, and, therefore, potentially modifying the vocal fold tissue response and thereby the glottal waveform [51, 52, 62], the intraglottal vortices advect into the supraglottal region where they may amplify the effects of shear layer instabilities or otherwise evolve into or interact with the glottal jet to yield vortical structures in the supragralottal region. These supraglottal vortical flow structures are able to influence the trajectory of the glottal jet and are hypothesized to be a potential source of vortex sound as they advect or interact with the tissues and cavities of the vocal tract [65]. In particular, vortices colliding with the walls of the vocal tract may produce a dipole acoustical source [7].

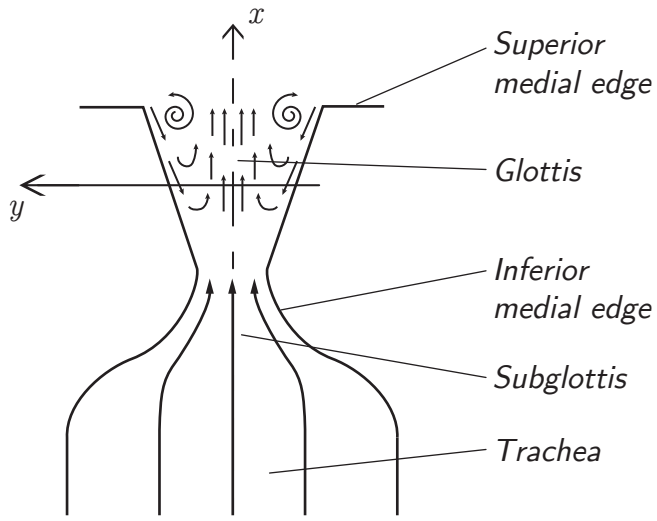

FIGURE 2.17: Schematic which shows intraglottal flow structures observed in PIV studies in a mid-membranous coronal section of the glottis shown for an arbitrary instant in the closing phase of the phonatory cycle (Reproduced from [73]).

Of relevance to this thesis is that Khosla et al. have hypothesized that the presence of vortical structures is of significance in phonation, in particular, that the presence of intraglottal vortices leads to a more rapid closing of the glottis reducing the duration of the closing phase in the phonatory cycle. They have hypothesized that the low pressure vortex core imparts a negative (gauge) pressure upon the medial surfaces of the vocal folds inducing the medial surfaces of the vocal folds to be drawn together more rapidly. To relate the derivative of the glottal waveform in the closing phase, in [36], Fant employs the source filter theory of voiced speech to demonstrate that the magnitude of the derivative of the glottal volumetric flow rate determines the amplitudes of the formants, peaks in the frequency spectrum of the speech signal. The glottal area waveform is a strong correlate of the volumetric flow rate; the volumetric flow rate is determined by glottal area together with transglottal pressures, which may be perturbed by the acoustical field due to the presence of the upper vocal tract coupled to the glottal airflow. In [52], Khosla et al. correlate the presence of intraglottal vortices with increased magnitude of high frequency content of the glottal source. In particular, strong correlation of intraglottal vorticity and high frequency acoustical energy is shown. Formants of higher amplitude enhance the intelligibility of voiced speech [36, 92], consequently, there is interest in determining the factors which may contribute to a more rapid closing phase of the phonatory cycle. If indeed the presence of intraglottal vortices contributes to a more rapid closing of the glottis, then ensuring that subsequent speech models incorporate or capture this effect would be of interest to improve model fidelity.

Most recently, in [37], a computational model is employed to study the hypothesis that suction force due to the presence of the vortex is small compared to tissue recoil forces. therein, a prescribed negative pressure is applied at the medial surface of the vocal fold,

and the results suggest that intraglottal vortices might have merely a small effect on VF tissue vibration. This is, in part, due to the experimental observations [73] that vortices only appear for a small fraction of time and quite near the superior edge of the medial VF surface close to the glottal exit.The results of the simulation suggest that, because exposure of the medial surface of the VF tissues to the intraglottal vortex is fleeting, that it does not impact the VF dynamics significantly.

To test the hypothesis that intraglottal vortices influence the phonatory dynamics of the vocal folds in the present thesis, a more physical approach is taken, rather than imposing an ad hoc pressure correction to the pressure distribution at the medial VF surface. In order to determine the effect of intraglottal vortices upon the dynamics of the vocal fold tissues, a two dimensional fluid structure interaction problem is solved with a pair of counter rotating advecting vortices which begin at an initial upstream station and advect in the axial direction due to prevailing glottal velocity conditions and influenced by their mutual induction. The behaviour of the vocal fold tissues is compared against an identical case but in the absence of the vortices. The influence of the vortices is quantified in terms of pressure fluctuation on the medial vocal fold surfaces. The dynamical response of the vocal folds is determined in simulation. The model is developed in Chapter 3, results of the simulation are presented and discussed in Chapter 4, and recommendations and conclusions in Chapter 5.

3 | Model Development

As shown in the previous chapter, speech may be viewed as a system in which a source of sound is modified by the acoustics of the vocal tract. The act of producing voiced speech is a complex coordination of thoracic musculature to control respiration, laryngeal muscles to establish the configuration and tension of the vocal folds, and the articulators of the upper vocal tract to shape the glottal source to produce intelligible sound. Despite the fact that the source mechanism of voiced speech, the elaborate interaction of glottal flow with the vocal fold tissues, is influenced by the acoustics of the vocal tract, the phonatory mechanism may be viewed as the source of a fundamental frequency somewhat independently. Therefore, the modelling and simulation effort herein focuses on the vocal fold tissues together with a model of glottal airflow subject to steady pressure and flow boundary conditions.

In particular, phonation, the primary mechanism of sound source generation in voiced speech, is due to the modulation of the flow of air from the lungs in the proximity of the glottal constriction. The quasi-periodic modulation of the glottal area is due to the excitation of the VF tissues by the glottal flow. There are additional sound source mechanisms at the glottis such as the generation of turbulence near a partial obstruction or the generation of impulsive modulation of air pressure due to a sudden release of air pressure as in a glottal stop. Nevertheless, it is the quasi-periodic self-sustaining oscillations of the vocal folds and their potentially modified behaviour in the presence of advecting vortices which are the phenomena of principal interest herein. The primary thrust of this work is to determine, in a simple and physiologically justifiable manner, whether intraglottal vortices influence the dynamical behaviour of the vocal folds.

To address this research question, a potential flow model allowing the superposition of vortices is developed. This chapter details the formulation of the model as well as the numerical implementation. In addition, the overall simulation architecture is summarized. To remain consistent with the goal of rapid simulation enabled by a low-order dynamical vocal fold tissue model, the loading of the vocal fold tissues due to the glottal flow is modelled as an incompressible potential flow. The vocal fold tissue model employed is the reduced-order bar-plate described in section 2.2.2 described in great detail in [99]. The 1-D potential flow model proposed by Titze in [99], also described in section 2.2.2, is extended to include advecting vortices. This 2-D model captures the variability of the velocity field due to the presence of vortices, and, together with the unsteady Bernoulli

equation, captures unsteady pressure variation on the medial surfaces of the vocal folds as they pitch and heave and the velocity potential evolves temporally and spatially.

3.1 Problem Formulation

The self-sustaining oscillation of the vocal folds is due to a strongly coupled fluid-structure interaction. Visco-elastic vocal fold tissues deform under loadings either due to their contact at glottal closure or, when open, due to the aerodynamic loadings induced by the glottal flow. In their closed state, the vocal folds are subject to surface tractions of visco-elastic origin due to their mechanical interaction and to wall-normal tractions due to subglottal and epilaryngeal pressures. In their open state, GF induced loadings generate surface tractions on the medial surfaces of the vocal folds due to viscosity and fluid pressure. The vocal fold tissues respond to the surface loadings by deforming. Ultimately, the loadings are determined by the instantaneous vocal fold geometry and local dynamical state, as well as complex tissue structure and mechanical characteristics.

The problem is formulated as a two-dimensional fluid-structure interaction in which an incompressible inviscid glottal flow persists within a confined channel. The walls of the channel are rigid superior to and inferior to the vocal folds, where they are allowed to deform. The GF determines the pressure distribution on the medial surfaces of the vocal folds, which are symmetrically disposed about the axis of the channel and permitted to translate laterally as well as pitch about a fulcrum in order to approximate a mucosal wave.

The present section begins with a presentation of the VF tissue model in order to frame the ensuing discussion of the glottal flow model. The GF model follows from a general perspective narrowing to the specific 2-D incompressible potential flow model which is ultimately solved. The contact model is presented in this section, whereas the presentation of the separation model and vortex advection scheme are delayed until the solution framework employing complex variable techniques is firmly in place. There is a continual effort to justify the assumptions of the framework in light of the anatomy and physiology of the speech organs described in the preceding chapter.

3.1.1 The Vocal Fold Tissue Model

The Titze bar-plate model described in Section 2.1.2 has been selected. It captures the body-cover structure of the vocal folds and the geometry of the glottis suitable to couple to a 2-D fluid flow domain. Figure 3.1 displays the planar dynamical model which is now simply stated. The model captures the trajectories of the VF masses in one particular mid-membranous coronal section. A coordinate system is imposed with the x-axis on the glottal mid-plane and oriented in the inferior-superior direction. The y-axis is oriented in the transverse direction as shown in Figure 3.1. The origin is placed at the axial position to ensure that the nodal point is confined to the y-axis. The distance from the inferior

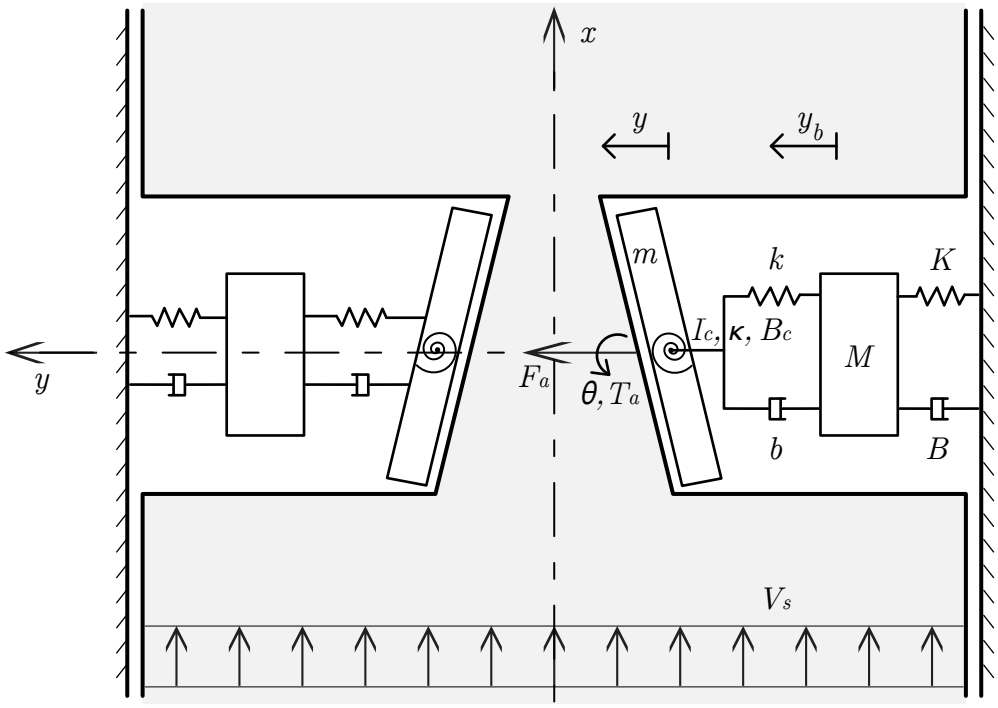

FIGURE 3.1: Schematic of the vocal fold dynamical model. Body mass M displaces y_b from equilibrium, plate m displaces y and pitches through angle θ measured counter-clockwise from equilibrium. V_s is the subglottal velocity.

edge of the vocal fold to the nodal point is denoted by l_{node}, therefore, the axial coordinate of the inferior edge of the vocal fold is $-l_{\text{node}}$. The vocal fold thickness is denoted t_{VF}, and, therefore, the axial coordinate of the superior edge of the vocal fold is $t_{\text{VF}} - l_{\text{node}}$. These geometric relations and parameters are reiterated in Section 3.1.2 subsequently.

The dynamical state of the VF tissues is given by y, the lateral displacement of the node of the right VF from its equilibrium position, y_b, the lateral displacement of the corresponding body mass from its equilibrium position, θ, the angular displacement of the plate from its equilibrium angular position, and their temporal derivatives, denoted using the standard "dot" notation. y and y_b are taken positive towards the glottal midplane, and θ is taken positive counter-clockwise. The plate pitches about a fulcrum which coincides with the nodal point, and the plate possesses a polar moment of inertia. The plate is mechanically coupled to the node via a torsional spring and damper. It is confined to translate transversely along the y-axis and is coupled to the body mass via linear spring and damper. The parameters y_{ng} and θ_{ng} locate the absolute neutral glottal translational and angular positions, and, therefore, the absolute translational position of the nodal point is $y + y_{ng}$ and the angular position of the plate is determined by $\theta + \theta_{ng}$ measured counter-clockwise from the negative x-axis (see Figure 3.5). The mechanical parameters are gathered in Table 3.1 below. Note that the model is defined for the right vocal fold, shown as the system on the right hand side of Figure 3.1, and a condition of symmetry is imposed to determine the motion of the left VF; the behaviour of the left vocal fold is

simply a reflection of the right through the glottal midplane.

TABLE 3.1: Summary of model mechanical parameters.

parameter		dimensions
M	body mass	M
m	cover mass	M
I_c	moment of inertia of cover	ML^2
K	translational stiffness of body	MT^{-2}
k	translational stiffness of cover	MT^{-2}
κ	torsional stiffness of cover	ML^2T^{-2}
B	translational damping of body mass	MT^{-1}
b	translational damping of cover	MT^{-1}
B_c	torsional damping of cover	ML^2T^{-1}
y_{ng}	neutral glottal position of node	L
θ_{ng}	neutral glottal convergence angle	1

For the system which models the behaviour of the right vocal fold tissues, conservation of linear momentum for the plate and mass together with conservation of angular momentum for the plate yield the following equations of motion

$$m\,\ddot{y} + b\,(\dot{y} - \dot{y}_b) + k\,(y - y_b) = F_a, \tag{3.1}$$

$$M\,\ddot{y}_b + B\,\dot{y}_b + b\,(\dot{y}_b - \dot{y}) + k\,(y_b - y) + K\,y_b = 0, \text{ and} \tag{3.2}$$

$$I_c\,\ddot{\theta} + B_c\,\dot{\theta} + \kappa\,\theta = T_a, \tag{3.3}$$

which may be cast in matrix form, as a first-order dynamical system, as

$$\frac{d}{dt}\begin{pmatrix}\theta\\ \dot{\theta}\\ y\\ \dot{y}\\ y_b\\ \dot{y}_b\end{pmatrix} = \begin{pmatrix} 0 & 1 & 0 & 0 & 0 & 0\\ -\frac{K}{I_c} & -\frac{B_c}{I_c} & 0 & 0 & 0 & 0\\ 0 & 0 & 0 & 1 & 0 & 0\\ 0 & 0 & -\frac{k}{m} & -\frac{b}{m} & \frac{k}{m} & \frac{b}{m}\\ 0 & 0 & 0 & 0 & 0 & 1\\ 0 & 0 & \frac{k}{M} & \frac{b}{M} & -\frac{K+k}{M} & -\frac{B+b}{M}\end{pmatrix}\begin{pmatrix}\theta\\ \dot{\theta}\\ y\\ \dot{y}\\ y_b\\ \dot{y}_b\end{pmatrix} + \begin{pmatrix}0\\ \frac{T_a}{I_c}\\ 0\\ \frac{F_a}{m}\\ 0\\ 0\end{pmatrix} \tag{3.4}$$

in which F_a and T_a are aerodynamic loadings which vary temporally and are functions of the geometry and boundary motions determined by the dynamical state of the VF tissues. The forcing terms, F_a and T_a are integrated surface tractions which arise due to the glottal flow. In the absence of viscous forces, given that the plate is confined to translational motion, the resultant force acting on the plate may be determined by

$$F_a = \iint\limits_{\Sigma(t)} P\,(\vec{x},t)\;(-\hat{n})\cdot\hat{\jmath}\,dS \tag{3.5}$$

in which the pressure field at time t, $P(\vec{x}, t)$, is defined for all positions $\vec{x}$ throughout the flow domain, and the integral is taken over the medial VF surface, denoted by $\Sigma(t)$ at instant t, with surface normal $\hat{n}$ taken to be positive when oriented into the flow domain. The dot product with $\hat{j}$ recovers the projection of the resultant force in the transverse direction. In order to obtain the pitching moment about the nodal point, define moment arm $\vec{r} = \vec{x} - (0, y + y_{ng}, 0)$ which gives the position $\vec{x}$ relative to the nodal point. The pitching moment of the right medial vocal fold surface is therefore determined by

$$M_a = \iint\limits_{\Sigma(t)} \vec{r} \times \left(P\left(\vec{x}, t\right)\left(-\hat{n}\right)\right) dS. \tag{3.6}$$

Details of the determination of the glottal flow and, therefore, equations (3.5) and (3.6) follow subsequently.

3.1.2 The Glottal Flow

Broadly speaking, the glottal aerodynamics are determined by the properties of the fluid, the geometry of the flow domain, and the strain rate of the boundary of the flow domain. The properties of the fluid are taken to be those of dry air at standard pressure and temperature. These assumptions are valid insofar as glottal flow is dry, steady, and incompressible. This is not strictly the case, as air coming from the lungs is approximately at 37°C and saturation relative humidity [49]. Nevertheless, the consequences of this assumption are not dire because the forces due to the transglottal pressure gradient determined by the difference of epilaryngeal pressure, P_e, and subglottal pressure, P_s, drive the glottal flow and dominate any body force or buoyancy effect arising from density variation. Body forces due to gravity are discarded and, hence, body forces are not incorporated into the expressions of the governing equations developed below. These parameters of the glottal flow, together with subglottal velocity, V_s, and vortex strength and spacing, Γ and a, of a pair of symmetrically disposed advecting vortices are gathered in Table 3.2. The parameters and their roles in the simplified model of glottal flow shall be discussed in greater detail subsequently.

The boundary $\partial\Omega(t)$ of the flow domain $\Omega(t)$ is collocated with the fluid-solid interface determined by the boundary between the cavities and tubes comprising the respiratory and vocal tracts and the bodily tissues which define them. Boundary conditions will be imposed at $\partial\Omega(t)$ both in the glottal flow model and in the vocal fold tissue model. To reiterate, the GF determines the BCs for the dynamical VF tissue model and the dynamical state of the VF tissue model feeds back to determine the BCs for the GF problem on the boundary determined by the VF state. Finally, if flow velocities are sufficiently small, the flow may be assumed to be incompressible. Maximal glottal flow velocities are approximately an order of magnitude smaller than the speed of sound in air at standard conditions. Furthermore, whereas compressibility effects are necessary for acoustics, the glottal simulation presented herein is uncoupled from the upper acoustical tract. Consequently, the compressibility of

TABLE 3.2: Aerodynamic parameters and their dimensions

parameter		dimension
ρ	fluid density	ML^{-3}
P_s	subglottal pressure	$ML^{-1}T^{-2}$
P_e	epilaryngeal pressure	$ML^{-1}T^{-2}$
Q	volumetric flow rate	M^3T^{-1}
V_s	subglottal velocity	LT^{-1}
Γ	circulation due to a vortex	L^2T^{-1}
a	vortical spacing of symmetric vortex pair	L

the flow shall be neglected in the present model. These assumptions combine to yield a general description of the glottal flow on domain $\Omega(t)$ embedded in $\mathbb{R}^3$ shown in Figure 3.2 subject to appropriate boundary conditions applied at $\partial\Omega(t)$ and governed by the Navier-Stokes equations in the absence of body forces,

$$\frac{D\vec{v}}{Dt} = -\frac{1}{\rho}\nabla P + \nu\nabla^2\vec{v} \quad \text{and} \tag{3.7}$$

$$\nabla \cdot \vec{v} = 0, \tag{3.8}$$

in which ν is kinematic viscosity and ρ is fluid density. Both equations are defined on $\Omega(t)$ at time t and are subject to the boundary condition, in which $\vec{v}_\Sigma$ is the wall velocity,

$$\vec{v} \cdot \hat{n} = \vec{v}_\Sigma \cdot \hat{n} \tag{3.9}$$

which holds on the portions of $\partial\Omega(t)$ corresponding to the wall, and subject to a far field condition on the velocity,

$$\vec{v} = V_s \tag{3.10}$$

which holds at the inlet. The governing equations together with the boundary conditions determine an incompressible velocity field $\vec{v}$ and concomitant pressure field P for a particular configuration and dynamical state of the boundary. Far field conditions on the pressure field, P_s and P_e, to enable its determination will be discussed after the model is sufficiently specialized.

The discussion has thus far framed a 3-D fluid-structure interaction problem in which an appropriate material model is coupled to a fluid model, and the fluid generates tractions which load the structure and cause it to displace with some velocity. The deformed structure, in turn, modifies the configuration of $\Omega(t)$, and, therefore, the flow and subsequent surface tractions which develop at the immersed solid boundary. Hence, the model has significant complexity due to the multi-physical nature of the problem. Additional complexity arises from mismatch of temporal scales; fluid structures may evolve and advect at rates which differ significantly from the natural frequencies corresponding to the dynamical

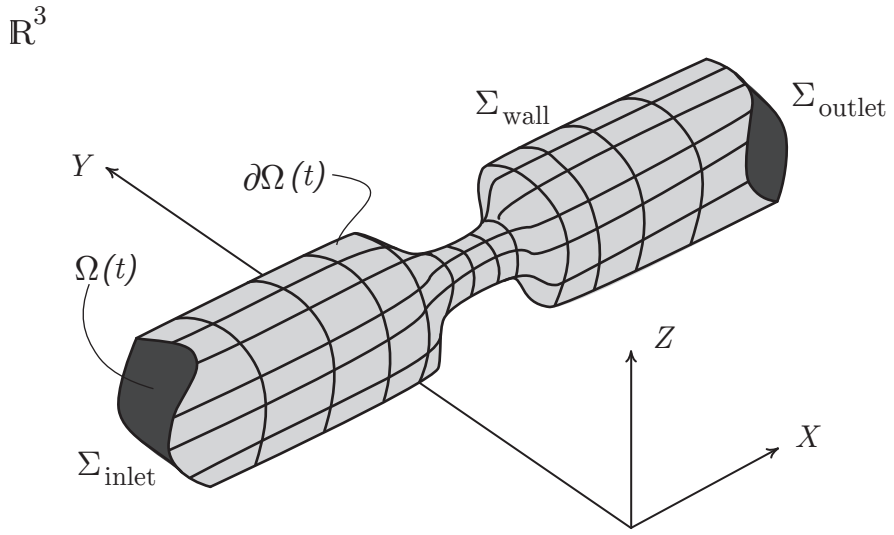

FIGURE 3.2: The general 3-D FSI problem with an internal flow on $\Omega(t)$ and deforming boundary $\partial\Omega(t)$, both allowed to vary temporally. The boundary is decomposed into patches Σ_{inlet}, Σ_{outlet}, and Σ_{wall} which identify parts of the boundary of the flow domain where various conditions are applied.

behaviour of the tissues. The model is now specialized to the one ultimately employed in simulation.

In the absence of viscosity, the tangential components and the viscous normal components of the surface tractions vanish, and the sole loading of the solid surface is due to pressures, which impart a component of the traction acting only in the wall-normal direction. This justifies the determination of VF surface loadings given by equations (3.5) and (3.6). Furthermore, this allows the governing equations of the glottal flow to collapse to Euler's equations (with no body force as before), namely

$$\frac{D\vec{v}}{Dt} = -\frac{1}{\rho}\nabla P \tag{3.11}$$

on flow domain $\Omega(t)$ subject to the same BCs as before.

Towards the goal of reducing the spatial complexity of the model for tractability, a particular representative section in two dimensions of the overall three dimensional geometry is selected. To this end, consider the supraglottal view of the vocal folds in Figure 3.3 below. The glottal geometry is highly complex and three-dimensional. The Reynolds number of the flow is not well defined at the ends of the vocal folds, and, even if it were, it would be highly variable from point to point. Consequently, viscous effects become more significant in determining the flow in these regions. Nevertheless, as was done in Chapter 2, in the development of the tissue model, it may be argued that, because the midsagittal plane is a plane of symmetry, the variation of the flow field at or near a mid-membranous coronal section exhibits sufficient similarity from coronal section to coronal section, insofar as viscous effects at the anterior and posterior ends where the vocal folds meet the car-

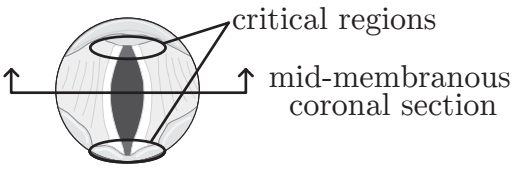

FIGURE 3.3: Vocal folds in open state shown schematically from supraglottal perspective. Critical regions of the flow domain are identified. The glottal flow may be approximated as a 2-D flow in a mid-membranous coronal section. This is due to the large aspect ratio of the vocal fold geometry. However, this approximation bears less validity near the critical regions distal to the mid-membrane due to significant spatial variation of geometry in these regions.

tilages do not account for significant tissue loadings. Taking a mid-membranous coronal section of the region of Figure 3.2 to be representative, the geometry of the flow domain collapses to that displayed schematically in Figure 3.4. The inlet is labelled Σ_1, the outlet Σ_3, and the right and left walls are labelled Σ_2 and Σ_4 respectively. Σ_1 and Σ_3 are open to the flow, and inlet and outlet velocity and pressure conditions apply there. Boundaries Σ_2 and Σ_4 are rigid, except at the glottal constriction where the vocal folds may pitch about some fulcrum and translate to and from the midplane of the glottis. Superior and inferior surfaces of the vocal folds extend and contract transversely to accommodate this motion but are otherwise fixed axially. With this, the simplicity of a 2-D flow domain is achieved, and, together with solution techniques for the computation of 2-D flows governed by equations (3.11) and (3.8), this is a suitable simplification from the physiological standpoint, and, from a mathematical standpoint, highly desirable.

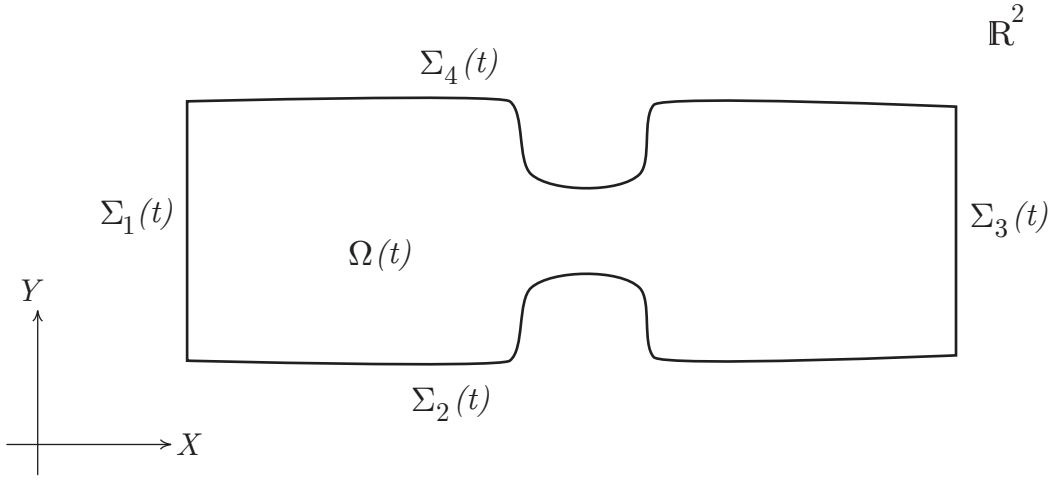

FIGURE 3.4: The specialization of the FSI problem depicted in Figure 3.2 to the 2-D case with an internal flow on domain Ω with deforming boundary $\partial\Omega$ decomposed into patches Σ. Inlet conditions are applied on Σ_1, outlet conditions on Σ_3, and wall-normal relative velocity conditions are applied on Σ_2 and Σ_4.

3.1.3 2-D Glottal Flow Model Geometry

To make the geometry of Figure 3.4 more concrete, Figure 3.5 displays the specific model geometry employed in the simulations. The relevant geometric parameters identified in the figure are also gathered in Table 3.3 below.

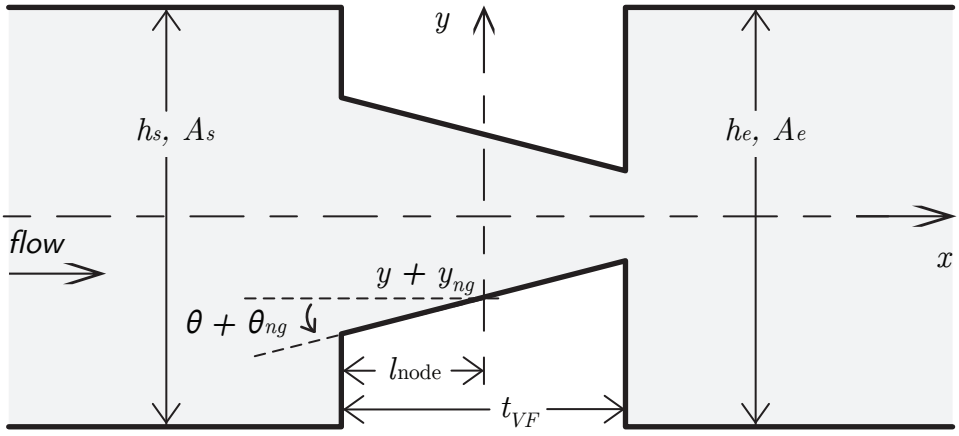

FIGURE 3.5: Schematic identifying geometric parameters which describe glottal configuration.

The flow domain is assumed to be 2-D as discussed, the depth into the page is determined by the vocal fold length l, and is assumed to be constant along the section. Tracheal geometry is assumed to be of constant width and determined by the subglottal channel width h_s. Consequently, the subglottal cross-sectional area is given by $A_s = h_s l$. Similarly, the supraglottal cross-sectional area, also called epilaryngeal area, is determined by the epilaryngeal channel width h_e and depth into the page l as $A_e = h_e\, l$. The axial length of the blockage is assumed to be of fixed length t_{VF}, the vocal fold thickness, and assumed to be arranged so that the nodal point of the mucosal wave, the fulcrum about which the plate pitches, is constrained to the transverse axis of the global frame. The inferior edge of the vocal fold is located at $x = -l_{\text{node}}$ and the superior edge at $x = t_{\text{VF}} - l_{\text{node}}$. Finally, specification of the neutral configuration of the vocal folds allows coupling of the dynamical model to the geometry of the flow domain and therefore to the aerodynamics of the glottal flow. The neutral glottal area, A_{ng}, and neutral glottal angular position, θ_{ng}, couple dynamics and geometry in the following way: the dynamics are defined in terms of displacements from equilibrium, but the equilibrium positions are identifiable geometric parameters, so the actual angular displacement of the medial surface of the right vocal fold, taken positive counter-clockwise and measured from the negative x-axis, is $\theta + \theta_{ng}$, which is the equilibrium angular configuration augmented by the displacement from equilibrium. Similarly, the equilibrium y position of the nodal point of the right vocal fold is $y_{ng} = -h_{ng}/2$ where h_{ng} is the neutral glottal width defined by $h_{ng} = A_{ng}/l$, where A_{ng}. With the displacement from equilibrium, y, determined by the dynamical equations of motion, the absolute position of the nodal point of the right vocal fold is $y + y_{ng} = y - h_{ng}/2 = y - A_{ng}/(2l)$.

TABLE 3.3: Geometric parameters and their dimensions

parameter		dimension
t_{VF}	vocal fold thickness	L
l	vocal fold length (depth into page)	L
A_s	subglottal cross-sectional area	L^2
h_s	subglottal channel width, $h_s = A_s/l$	L
A_e	epilaryngeal cross-sectional area	L^2
h_e	epilaryngeal channel width, $h_e = A_e/l$	L
A_{ng}	neutral glottal area	L^2
h_{ng}	neutral glottal width, $h_{ng} = A_{ng}/l$	L
y_{ng}	neutral glottal position of node, $y_{ng} = -h_{ng}/2$	L
θ_{ng}	neutral glottal angular displacement	1

3.1.4 Boundary Conditions for the 2-D Glottal Flow Model

For the planar flow domain obtained for the glottal flow, the governing equations remain (3.11) and (3.8) but specialized to two dimensions. The boundary conditions must also be specified in particular for this model. The no-slip condition does not hold because the flow is inviscid; the wall-tangent components of velocity are non-vanishing except at stagnation points; in fact, it is the non-zero velocity which contributes to the determination of the local pressure field at the wall. The no wall-normal flow condition expressed in equation 3.9 is a consequence of the impermeability of the tissues. We have

$$(\vec{v} - \vec{v}_\Sigma) \cdot \hat{n} = 0 \quad \text{or} \quad \vec{v} \cdot \hat{n} = \vec{v}_\Sigma \cdot \hat{n} \tag{3.12}$$

which expresses the fact that the velocity of the fluid relative to the possibly moving wall vanishes in the wall-normal direction. For a rigid wall which heaves and pitches, $\vec{v}_\Sigma = \dot{y}\hat{\jmath} + \dot{\theta}\vec{k} \times \vec{r}$ in which, as before, $\dot{y}$ is the velocity of the nodal point, $\dot{\theta}$ is the angular velocity of the plate about its fulcrum, and $\vec{r}$ is simply the position vector relative to the node of some point of interest along the medial VF surface. Consequently, $(\vec{v} - \vec{v}_\Sigma) \cdot \hat{n}$ becomes $\left(\vec{v} - \left(\dot{y}\hat{\jmath} + \dot{\theta}\vec{k} \times \vec{r}\right)\right) \cdot \hat{n}$. This may be written $\vec{v} \cdot \hat{n} = \dot{y}\hat{\jmath} \cdot \hat{n} + \left(\dot{\theta}\vec{k} \times \vec{r}\right) \cdot \hat{n}$, which collapses to $\vec{v} \cdot \hat{n} = \dot{y}\cos\theta + \left(\dot{\theta}\vec{k} \times \vec{r}\right) \cdot \hat{n}$ where θ is the angular displacement of the medial VF surface. θ may be taken to be sufficiently close to zero so that $\cos\theta$ is sufficiently close to unity. Extreme values of angular displacement observed in simulation have an approximate range from $-5°$ to $20°$, so the assumption of small angles is not entirely unreasonable. Furthermore, the component of velocity due to rotation is always oriented in the wall-normal direction, hence, the above condition reduces further to $\vec{v} \cdot \hat{n} \approx \dot{y} + r\dot{\theta}$. Finally, the velocity of the VF tissue is at least two orders of magnitude smaller than $\vec{v}$. Physiologically, glottal flows obtain a maximal velocity of approximately 40 m/s, whereas

vocal folds with peak to peak displacement on the order of 1 mm travel on the order of 2 mm per phonatory cycle, and, at nominally 120 Hz, may have an average velocity of 0.25 m/s. The peak velocity may not be much higher. Consequently, a vanishing wall-normal boundary condition holds approximately. This condition allows complex variable techniques to be employed without much complication which would otherwise be introduced by a non-homogeneous von Neumann condition.

Finally, for the geometry displayed in Figure 3.4, the fully simplified glottal flow problem requires the satisfaction of the governing equations at each instant of time, namely Euler's equation for conservation of linear momentum, equation (3.11), and the incompressible continuity equation, equation (3.8), which is a statement of the conservation of mass appropriate to the assumptions. These equations determine fluid velocity and pressure temporally and in two spatial variables. The boundary conditions on the velocity field are summarized at each instant of time as

$$\vec{v}\,\big|_{\Sigma_1} = V_s\,\hat{\imath} \tag{3.13}$$

$$\vec{v}\,\big|_{\Sigma_3} \cdot \hat{t}_\Sigma = 0, \text{ and} \tag{3.14}$$

$$\vec{v}\cdot\hat{n}\big|_{\Sigma_k} = 0 \text{ on each immersed solid surface } \Sigma_k \tag{3.15}$$

where V_s is the subglottal velocity, that is, the velocity in the upstream far field, and $\hat{t}_\Sigma$ is any unit tangent to surface patch Σ at a point of the boundary. Boundary condition (3.15) is exact on every rigid boundary and approximate on every moving boundary.

It is physiologically possible to start the fluid from rest. Because the fluid is inviscid and there are no non-conservative body forces acting on the fluid, if the fluid is impulsively started from rest, where there is no vorticity, the flow will remain irrotational. For an irrotational flow, a velocity potential exists (and its harmonic conjugate, a stream function, which, in a 2-D flow, has components related to the potential by the Cauchy-Riemann equations), and, additionally, because the flow is incompressible, the divergence of the gradient of the potential vanishes, that is, the continuity equation yields Laplace's equation for the velocity potential. Euler's equation, when integrated, will yield the unsteady Bernoulli equation which may be employed to recover the pressure field once the velocity has been determined from the potential. At each instant, the problem is one which is amenable to solution via complex variable techniques. This fortuitous combination of outcomes suggests a determination of the glottal flow and vocal fold dynamics via temporal marching where, at each instant, the geometry is determined from the dynamical state, the flow is obtained at the given instant via complex variable techniques, the fluidic loadings of the VF surfaces are obtained from this solution and fed into the dynamical model which responds over one timestep. The specifics of this approach are discussed in sections 3.2 and 3.3. Before proceeding, what follows is a brief discussion of pressure BCs and of the VF contact model.

3.1.5 Far-Field Pressure Conditions

For the quasi-steady process of phonation over short durations, lung pressure remains approximately constant. Consequently, the lungs are approximated as a constant source of pressure. The trachea is assumed to be effectively lossless so that the conditions at the glottal inlet are steady. Furthermore, because the flow is inviscid, the upstream velocity field may be assumed to be uniformly distributed and of some fixed magnitude V_s. Physiologically, subglottal pressures are between the minimal pressure required for the onset of VF vibration, 300 Pa, and some maximal subglottal pressure ultimately determined by the maximal alveolar pressure of the lungs, possibly as high as 1.5 kPa. The subglottal velocity, V_s and the subglottal pressure, P_s, furnish inlet boundary conditions for the model presented above. The downstream boundary condition for pressure, i.e., the condition at the glottal exit, is the epilaryngeal pressure P_e, which is taken to be atmospheric and simply set to 0 so that all model pressures are gauge pressures relative to P_e. Downstream velocity conditions would over-determine the velocity field. In particular, equation (3.14) does not stipulate the magnitude of the velocity field at the outlet. Physiologically, the subglottal pressure and subglottal velocity are determined by the alveolar pressure, which may be assumed to be the lung pressure P_L. The lungs are a constant pressure zero velocity source. The trachea, bronchi, and bronchioles are assumed to be somewhat lossless, so

$$P_L = P_s + \frac{1}{2}\rho V_s^2.$$

The outlet condition is set to P_e, but this would over-determine the pressure. P_e is only set because it is employed as the pressure loading in the separation region downstream of the point of separation in the separation model, see Section 3.2.4. It is also the pressure which determines the fluidic force in the closed condition as well as the transglottal pressure and the contact force in the collision model of the vocal folds.

3.1.6 The Contact Model

The vocal fold tissues are considered to be in a state of contact when the minimal glottal area is achieved and remains below some small threshold, $L\delta$ where δ is the minimal inter-glottal distance between medial surfaces and L is the vocal fold length. In this case, the glottal flow is not active and the surface tractions on the VF medial surfaces are determined by subglottal and epilaryngeal (supraglottal) pressures on the exposed portions of the medial surfaces as well as a primitive contact model which simply applies a constant contact force equal to half of the transglottal pressure over the area of contact. The contact model may be summarized in terms of the pressure distribution over the VF surfaces

$$P(z) = \begin{cases} P_s, & z \in \Sigma_{\text{sub-contact}} \\ P_{\text{closure}}, & z \in \Sigma_{\text{contact}} \\ P_e, & z \in \Sigma_{\text{supra-contact}} \end{cases} \tag{3.16}$$

where $P_{\text{closure}} = P_{\text{hydrostatic}} = \frac{P_s+P_e}{2}$ and the surfaces Σ are shown corresponding to one of the three possible configurations in Figure 3.6, complete closure, partial closure in a converging glottis, and partial closure in a diverging glottal configuration.

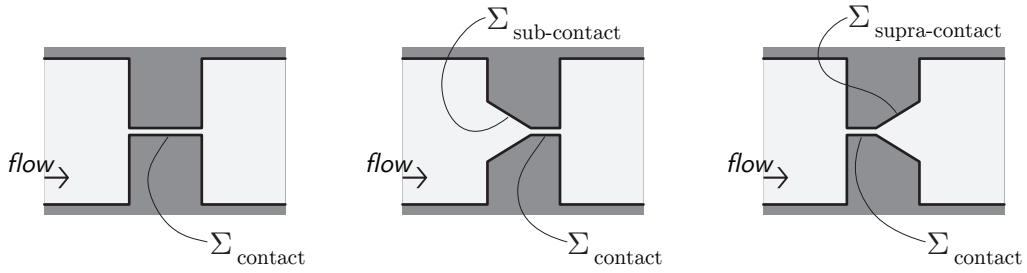

(a) (b) (c)

FIGURE 3.6: Possible configurations of the vocal folds in contact, (a) complete closure, (b) partial closure in converging configuration, and (c) partial closure in diverging configuration. Contact pressure acts on the surface patch Σ_{contact}. Subglottal pressure acts on the part of Σ inferior to contact. Epilaryngeal pressure acts on the part of Σ superior to closure.

3.2 Towards a Solution of the Problem

The simulation employs a temporal marching scheme in which, at each timestep, given the current geometry, the fluidic loading is computed based on the solution of the GF problem together with the current dynamical state, specifically wall velocities. The loading is resolved as a pitching moment and translational force upon the medial VF surface. The dynamical problem is solved for displacements and velocities of the wall to determine the next VF configuration and wall velocity of the confining boundary. The dynamics of the vortices, if they are present, is also computed prior to the next iteration.

3.2.1 Obtaining the Glottal Flow

Due to the structure of the flow problem, complex variable techniques may be employed. These are described in Appendix A.

Given the vocal fold configuration determined by the dynamical model of the VF tissues, together with the velocities of the VF surfaces, tractions due to fluid flow may be determined. As discussed in previous sections, the tractions are due solely to pressure and may be expressed as

$$P\left(z_k^*\right) e^{-i\pi/2} \frac{z_{k+1} - z_k}{|z_{k+1} - z_k|} \tag{3.17}$$

where $P(z_k^*)$ is the pressure at the k^{th} control point along the medial VF surface, i.e., at

$$z_k^* = \frac{z_k + z_{k+1}}{2}$$

where z_k and z_{k+1} are the initial and terminal endpoints of the k^{th} panel; hence $\frac{z_{k+1}-z_k}{|z_{k+1}-z_k|}$ has unit magnitude but real and imaginary parts which correspond to x and y components of a vector parallel to the right medial VF surface and oriented in the downstream direction such that $e^{-i\pi/2}\,\frac{z_{k+1}-z_k}{|z_{k+1}-z_k|}$ is normal and directed outwards from the flow domain. Consequently, positive pressures correspond to a compression of the VF tissue, and negative fluid pressures (gauge) correspond to a suction on the medial VF surfaces.

For a flow field which is irrotational and satisfies (3.8), the velocity field is given by $\vec{v} = \nabla\Phi$ for an appropriate potential Φ. If the flow is two-dimensional, complex variable techniques may be employed to advantage. The rudiments of these techniques are furnished in Appendix A. The main thrust of the argument follows from the fact that irrotational flows yield a velocity potential which allows us to represent the velocity field as the gradient of a scalar field. Upon substitution into the incompressible continuity equation, we obtain Laplace's equation for the potential Φ, namely

$$\nabla^2\Phi = 0.$$

For the boundary conditions given in (3.9), that $\vec{v}\cdot\hat{n} = 0$, we have $\nabla\Phi\cdot\hat{n} = 0$ or simply $\partial\Phi/\partial n = 0$ at solid boundaries. At time t, this condition is instantaneously satisfied on boundaries of $\Omega(t)$ if they are modelled as streamlines of the flow. The inlet conditions, (3.10), are prescribed by a uniform velocity. When these conditions prevail, the mere construction of a real potential is required. The potential has upstream velocity which is uniformly V_s, the subglottal velocity, and has streamlines which adhere to the parts of $\partial\Omega(t)$ corresponding to the immersed solid boundaries of the VF tissues and respiratory tract walls. This is achieved via conformal mapping techniques, in particular, via the Schwarz-Christoffel mapping from a horizontal strip where the potential is easy to obtain to the complicated physical plane.

To elaborate, if $\widetilde{F}(\zeta,t)$ is a complex potential, i.e., its real part, $\mathfrak{Re}\left(\widetilde{F}(\zeta,t)\right) = \varphi(\zeta,t)$, satisfies $\nabla\varphi = 0$ and its imaginary part, $\mathfrak{Im}\left(\widetilde{F}(\zeta,t)\right) = \psi(\zeta,t)$, is the harmonic conjugate of φ, and, if, additionally, f_t is a conformal mapping at time t which maps points ζ in the auxiliary plane to points z in the physical plane according to $z = f(\zeta,t)$, then

$$\widetilde{F}\left(f^{-1}(z,t),t\right) \tag{3.18}$$

is a complex potential on $\Omega(t)$ with the desired properties.

The temporal evolution of the GF and VF models may be summarized more abstractly. Suppose $U, V \subseteq \mathbb{C}$ are open and $X \subseteq U$ is closed. Construct two families of functions both indexed by $t \in [0,\infty)$, namely

$$\mathcal{F} = \{f_t : X \to \Omega_t \subseteq V \mid t \in [0,\infty)\}$$

and

$$\mathcal{G} = \{\varphi_t : U \to \mathbb{R} \mid t \in [0, \infty)\}$$

in which each Ω_t is a closed subset of V, each f_t is holomorphic on U with non-vanishing derivative, each φ_t is the real part of some function which is holomorphic on U, and

$$\bigcap_{t\in[0,\infty)} \Omega_t \neq \emptyset.$$

Finally, define a function

$$\Phi : \left(\bigcap_{t\in[0,\infty)} \Omega_t \right) \times \mathbb{R} \to \mathbb{R}$$

by

$$\Phi(z, t) = \left(\varphi_t \circ f_t^{-1}\right)(z).$$

The problem of obtaining the temporal evolution of the velocity field may be thought of as obtaining the families $\mathcal{F}$ and $\mathcal{G}$ so that Φ may be obtained at each instant of time and its derivative may be computed as necessary.

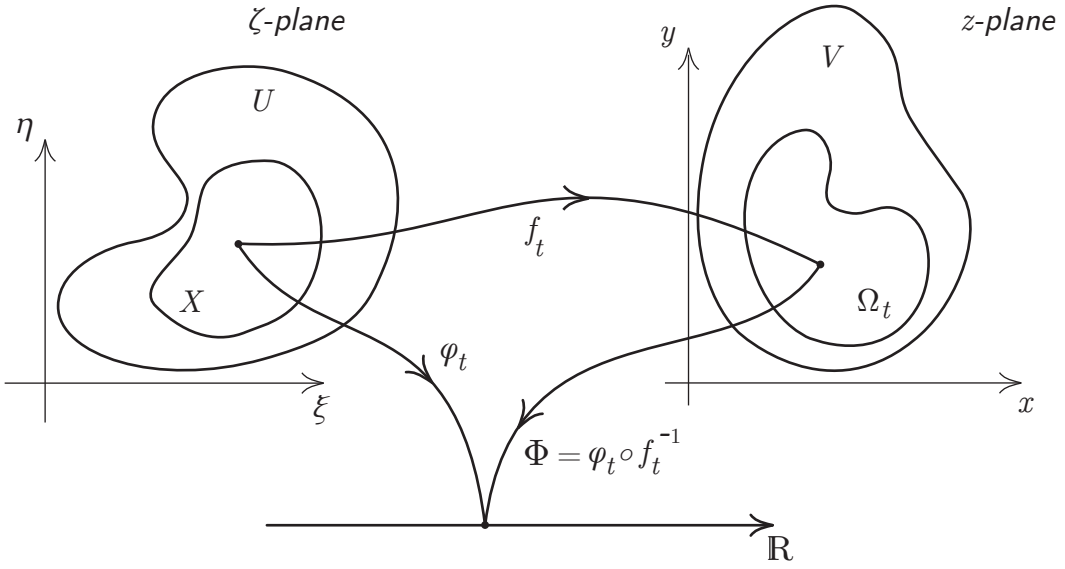

FIGURE 3.7: Arrow diagram showing relations between mappings and regions at instant of time t.

3.2.2 The Pressure Field

In computing the velocity field $\vec{v} = \nabla\Phi$, where $\nabla^2\Phi = 0$ subject to the prescribed boundary conditions, a velocity field which merely conserves mass has been determined. Equation (3.11), conservation of linear momentum for an inviscid incompressible flow in the absence

of body forces, is integrated along a curve in the flow, $C(t)$ at time t to obtain a relation between the prevailing velocity field and concomitant pressure field necessitated by the conservation of linear momentum. It is shown in Appendix B that, once the real velocity potential is known, the pressure field may be obtained as equation (B.24), repeated here, for global absolute position vector $\vec{x}$ and position vector in the moving frame $\vec{\tilde{x}}$

$$P\big(\vec{x},t\big) = P_0 + \frac{1}{2}\,\rho\left(v_0^2 - \|\nabla_x\Phi\|^2\right) - \rho\left(\frac{d}{dt}\widetilde{\Phi}\left(\vec{\tilde{x}},t\right) - \nabla_x\Phi\cdot\left(\vec{v}_A + \vec{\Omega}\times\vec{\tilde{x}}\right)\right)$$

in which $\|\cdot\|$ gives the magnitude of a vector, ∇_x is the gradient in the global frame, $\vec{x}$ is an absolute position in the global frame, $\vec{v}_A$ is the absolute velocity of the origin of a moving frame which is rotating about A with angular velocity $\vec{\Omega}$, v_0 and P_0 are reference velocity and pressure, $\widetilde{\Phi}$ is the velocity potential in the moving frame, and $d\widetilde{\Phi}/dt$ is obtained as in section B.2.4 likewise in Appendix B. The equation above may be re-written in terms of the complex analytic framework in which vectors in the plane are geometric images of corresponding complex numbers. The conjugate of the complex velocity, $\overline{w}$, has real and imaginary parts which correspond to the x and y components of the fluid velocity, the square magnitude of the velocity is therefore $\overline{w}w$, and, finally, the dot product in terms of complex variables which represent vectors, may be determined as[1]

$$z\cdot w = \mathfrak{Re}\left(z\overline{w}\right) \tag{3.19}$$

hence, the pressure equation for the medial VF surfaces becomes

$$P\big(z,t\big) = P_s + \frac{1}{2}\,\rho\left(V_s^2 - \overline{w}w\right) - \rho\left(\frac{d}{dt}\widetilde{\Phi}\left(\tilde{z},t\right) - \mathfrak{Re}\left(\overline{w}v_A\right)\right) \tag{3.20}$$

where v_A is a complex number with real and imaginary parts which correspond to the x and y components of $\vec{v}_A$. Additionally, subglottal pressure, P_s, and subglottal velocity, V_s, have been substituted for P_0 and v_0 respectively. Finally $\tilde{z}$ is simply a point along the medial VF surface relative to a local frame affixed to the nodal point of the medial vocal fold surface, i.e., $\tilde{z} = z^* - z_{\text{fulcrum}}$ for some point z^* on the medial VF surface. An additional simplification is possible because the flow velocity is always tangential to the wall and, therefore, perpendicular to the velocity of the wall due always to rotation, and this is why the cross-product term has vanished. Thus, to obtain the resultants, the pressure determined by equation (3.20) is evaluated control points z_k^* and added (effectively a midpoint rule to approximate the integral) to obtain the resultant force and similarly for the pitching moment to be fed into the dynamical solver as described above.

[1]The dot product of vectors with components $(z_1,z_2,0)$ and $(w_1,w_2,0)$ is $z_1w_1+z_2w_2$, and, for corresponding complex numbers z_1+iz_2 and w_1+iw_2,

$$\mathfrak{Re}\left(z\overline{w}\right) = \mathfrak{Re}\left(\left(z_1-iz_2\right)\left(w_1+iw_2\right)\right) = \mathfrak{Re}\left(z_1w_1+z_2w_2+i\left(z_1w_2-z_2w_1\right)\right) = z_1w_1+z_2w_2$$

as required.

3.2.3 Obtaining the Dynamics of the Vocal Fold Tissues

The system of equations (3.1), (3.2), and (3.3) is solved numerically, given the forcing functions F_a and T_a at time t_k, assumed to be fixed over the short period $\delta t^{(k)}$, with initial conditions determined by the state of the system at time t_k. This is an explicit formulation of the dynamical problem. The MATLAB ODE solver `ode45` was employed; it is based on an explicit and adaptive stepsize Runge-Kutta formulation which employs six function evaluations to obtain 4^{th} order accuracy [60].

To obtain the forcing terms, equations (3.5) and (3.6) are integrated numerically over the medial VF surface. The surface is discretized into a number of panels of length δL and width corresponding to the VF length. Control points are located at midpoints of the panels. Pressure is obtained at the control points via equation (B.18) described in detail in Appendix B. This integration scheme to obtain the resultant force at some instant is

$$F_a = \iint_{\Sigma} P\left(\vec{x}\right)\,\left(-\hat{n}\right)\,dS\cdot\hat{\jmath} = \sum_{k=1}^{N} P\left(z_k^*\right)\,L\,\delta L\,\left(-\hat{n}\cdot\hat{\jmath}\right) \tag{3.21}$$

where N is the total number of panels, z_k^* is the midpoint of the k^{th} panel, i.e., the k^{th} control point, δL is the length of the k^{th} panel, and L is the length of the vocal fold. It is also worth noting that this tacitly assumes that the intraglottal pressure obtained at the mid-membranous coronal plane is representative of the pressure obtained along the entire length of the vocal fold. Recalling Figure 3.3 and corresponding discussion, this is not actually the case, but a model simplification. Now, when the components of the normal vector are evaluated by employing the geometry of the complex plane, equation (3.21) may be written

$$F_a = \mathfrak{Im}\left(\sum_{k=1}^{N} P\left(z_k^*\right)\,L\,\delta L\,e^{-i\pi/2}\,\frac{z_{k+1}-z_k}{\left|z_{k+1}-z_k\right|}\right) \tag{3.22}$$

because the rightmost factor is the negative normal vector, then taking the imaginary part recovers the projection onto the imaginary axis, that is, the y component of the force. It is clear that, because F_a is taken as the projection onto the transverse axis, the translational motion of the VF is one dimensional.

Similarly, for the pitching moment,

$$M_a = \iint_{\Sigma} \vec{r}\times P\left(\vec{x}\right)\,\left(-\hat{n}\right)\,dS = \sum_{k=1}^{N} P\left(z_k^*\right)\,L\,\delta L\,\left(z_k^*-z_{\text{fulcrum}}\right)\times\left(-\hat{n}\right) \tag{3.23}$$

where, z_{fulcrum} is the location of the fulcrum of the plate at some specified location on the medial surface of the vocal fold, and, also, for two complex numbers which correspond to vectors, the out of plane component of their cross-product is determined as[2]

$$z\times w = \mathfrak{Im}\left(\bar{z}w\right) \tag{3.24}$$

[2]For vectors with components $(z_1, z_2, 0)$ and $(w_1, w_2, 0)$, their cross product is $(0, 0, z_1w_2 - z_2w_1)$, and,

From the dynamical response of the vocal folds, it is possible to obtain physiologically relevant metrics such as plots of minimal glottal area, open and closed quotients, etc.. The dynamical system describes transverse displacement of the system from equilibrium and corresponding velocities. The velocities are in phase with the motion and are absolute, but absolute displacements are obtained by superposing the displacements from equilibrium to the neutral glottal transverse position and the neutral glottal angular displacement. Absolute positions obtained in this manner determine the overall glottal geometry and the velocities of points on the boundary of the flow domain.

3.2.4 A Flow Separation Model

The glottal flow model is extended in an ad hoc fashion to capture viscous effects, specifically flow separation and the consequent glottal jet structure, as well as the presence of advecting vortical structures which are discussed in the following subsection.

A flow separation model is introduced as a modified flow domain within the geometric region determined by the tissue model. This is shown in Figure 3.8 as the shaded region. Flow separation occurs on the medial vocal fold surfaces in the divergent configuration due to an adverse pressure gradient in a viscous fluid. The flow model is inviscid, nevertheless, an ad hoc determination of a point of separation may be incorporated so that the model captures some effects due to viscosity which would otherwise not be included [59]. At the point of separation, the structure of the wake is not modelled further, it is merely taken to remain constant cross-section. The pressure applied to the vocal fold surface downstream of separation is P_e. The flow and concomitant pressure field in the attached region is determined in the modified polygonal region as it would be in an attached flow.

3.2.5 A Vortex Advection Scheme

Appendices A and B furnish the details of the development of this section. The discussion corresponds to the geometry displayed in Figure 3.9 of the horizontal strip in the auxiliary plane and the flow domain in the physical plane related by the Schwarz-Christoffel map f. At time t, given strip S in the auxiliary plane and flow domain Ω in the physical plane with vortices located at z_{01} and z_{02} with strengths Γ oriented as shown in Figure 3.9 in order to cause the induced velocity at one vortex due to the other to mutually advect them downstream. Locations of vortices in S are determined as

$$\zeta_{0k} = f^{-1}(z_{0k}). \tag{3.25}$$

---

for corresponding complex numbers $z_1 + iz_2$ and $w_1 + iw_2$,

$$\mathfrak{Im}(\bar{z}w) = \mathfrak{Im}((z_1 - iz_2)(w_1 + iw_2)) = \mathfrak{Im}(z_1w_1 + z_2w_2 + i(z_1w_2 - z_2w_1)) = z_1w_2 - z_2w_1$$

as required.

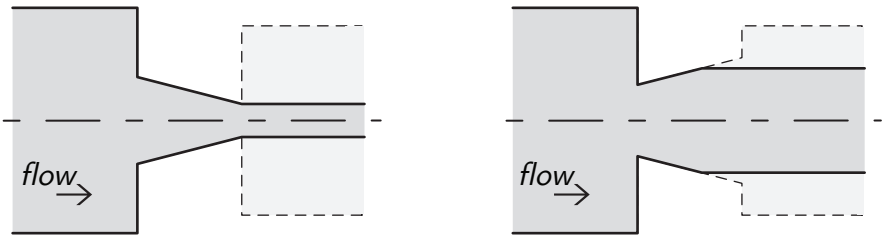

FIGURE 3.8: A schematic of the separation model. The Schwarz-Christoffel map is obtained for the shaded polygonal region which represents the separated flow domain. (a) shows trailing edge separation and a glottal jet extending downstream. (b) shows a point of separation at some point on the medial vocal fold surface; the glottal jet extends similarly downstream.

It can be shown that the complex velocity at $\zeta \in S$ due to vortices symmetrically disposed in the channel at ζ_{01} and ζ_{02} is

$$w(\zeta) = \begin{cases} \frac{\Gamma_1}{4}\cot\left(\pi\ \mathfrak{Im}\left(\zeta_{01}\right)\right) + \frac{\Gamma_2}{4i}\left(\coth\left(\frac{\pi}{2}\left(\zeta_{01}-\zeta_{02}\right)\right) - \coth\left(\frac{\pi}{2}\left(\zeta_{01}-\overline{\zeta}_{02}\right)\right)\right), & \zeta = \zeta_{01} \\ \frac{\Gamma_2}{4}\cot\left(\pi\ \mathfrak{Im}\left(\zeta_{02}\right)\right) + \frac{\Gamma_1}{4i}\left(\coth\left(\frac{\pi}{2}\left(\zeta_{02}-\zeta_{01}\right)\right) - \coth\left(\frac{\pi}{2}\left(\zeta_{02}-\overline{\zeta}_{01}\right)\right)\right), & \zeta = \zeta_{02} \\ \sum_{n=1}^{2}\frac{\Gamma_n}{4i}\left(\coth\left(\frac{\pi}{2}\left(\zeta-\zeta_n\right)\right) - \coth\left(\frac{\pi}{2}\left(\zeta-\overline{\zeta}_n\right)\right)\right), & \text{otherwise} \end{cases}$$

If the complex potential $\widetilde{F}(\zeta)$ is known in the auxiliary plane, the complex velocity in the physical plane may be determined as the z derivative of

$$F(z) = \widetilde{F}\left(f^{-1}(z)\right)$$

that is

$$w(z) = \frac{dF}{dz} = \frac{d\widetilde{F}}{d\zeta}\frac{df^{-1}}{dz} = \frac{d\widetilde{F}}{d\zeta}\frac{1}{f'(\zeta)} = w(\zeta)\frac{1}{f'(\zeta)}$$

where $\zeta = f^{-1}(z)$ so

$$w(z) = \left.\frac{w(\zeta)}{f'(\zeta)}\right|_{\zeta=f^{-1}(z)} \tag{3.26}$$

where w is defined casewise above and f is the Schwarz-Christoffel transform which corresponds to the particular flow domain. Note that the derivative of f is trivial to compute because the Schwarz-Christoffel transform is defined as an integral.

Finally, the quantity of interest may be obtained: the velocity at z in the physical plane due to vortices located at z_{01} and z_{02}. The complex velocity at z in the physical plane due to vortices located at z_{01} and z_{02} is $w(z)$ defined in equation (3.26) where ζ_{01} and ζ_{02} in the casewise definition for w are given by the pre-images of the vortices determined by equation (3.25) above. The real and imaginary parts of the conjugate of the complex velocity yield the x and y components of the velocity vector in the physical plane. Consequently, the

velocities $v_{0k} = \overline{w}(z_{0k})$ of the vortices may be obtained and the next positions determined at time t_{n+1} according to

$$z_{0k}^{(n+1)} = z_{0k}^{(n)} + v_{0k}\,\delta t^{(n)} \tag{3.27}$$

in which $\delta t^{(n)} = t_{n+1} - t_n$.

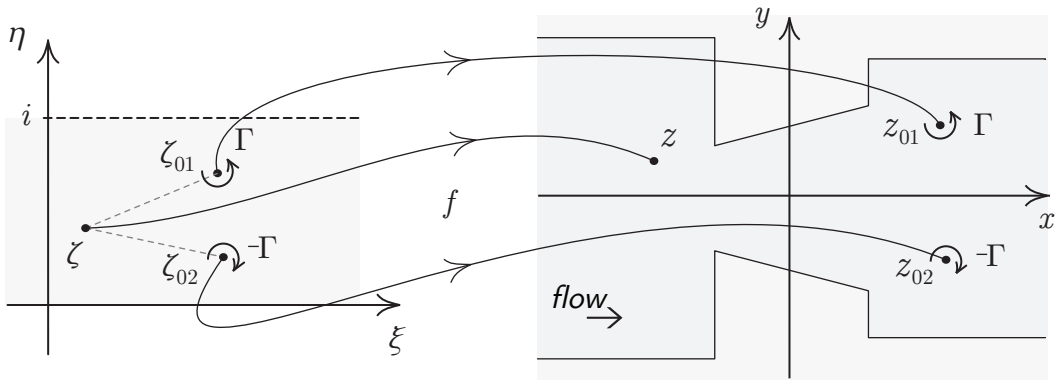

FIGURE 3.9: A schematic of the Schwarz-Christoffel mapping f between the horizontal strip of the auxiliary plane on the left and the flow domain within the physical plane on the right. Points in these regions correspond via f.

3.3 Summary of Overall Simulation Architecture

The overall simulation architecture is shown in the flow chart of Figure 3.10. A temporal marching approach is taken in which geometry is obtained based on the current state of the vocal folds. The geometry determines the glottal flow, hence the flow is determined based upon current geometry, vortex positions, and the freestream. These, in turn, determine the pressure distribution on the medial vocal fold surfaces. In a closed configuration, the contact model determines the pressure distribution on the medial vocal fold surfaces. The pressures are integrated to obtain pitching moment and resultant forces. These are the forcing terms of the dynamical model which are solved over one timestep with initial conditions taken to be the current state. Vortices are advected in parallel. The new vortex positions and the new dynamical state determine the geometry and velocity potential become initial conditions for the next iteration. A check is performed to ensure that the next position of the vortices remain within the next glottal configuration. Specifically, at each iteration, when the vortices are advected, the new positions are either interior to the flow domain or not. In the case the new positions of the vortices are within the flow domain, the simulation proceeds; however, if the vortices would end up outside of the flow domain at the current iteration, the entire iteration is repeated, but with a timestep of half the size. This local iteration at the current instant of time is performed until the new vortex positions lie within the flow domain. At the beginning of each iteration, there is an attempt to increase the timestep but not beyond its maximal value. The overall iteration proceeds until the desired simulation duration has been attained.

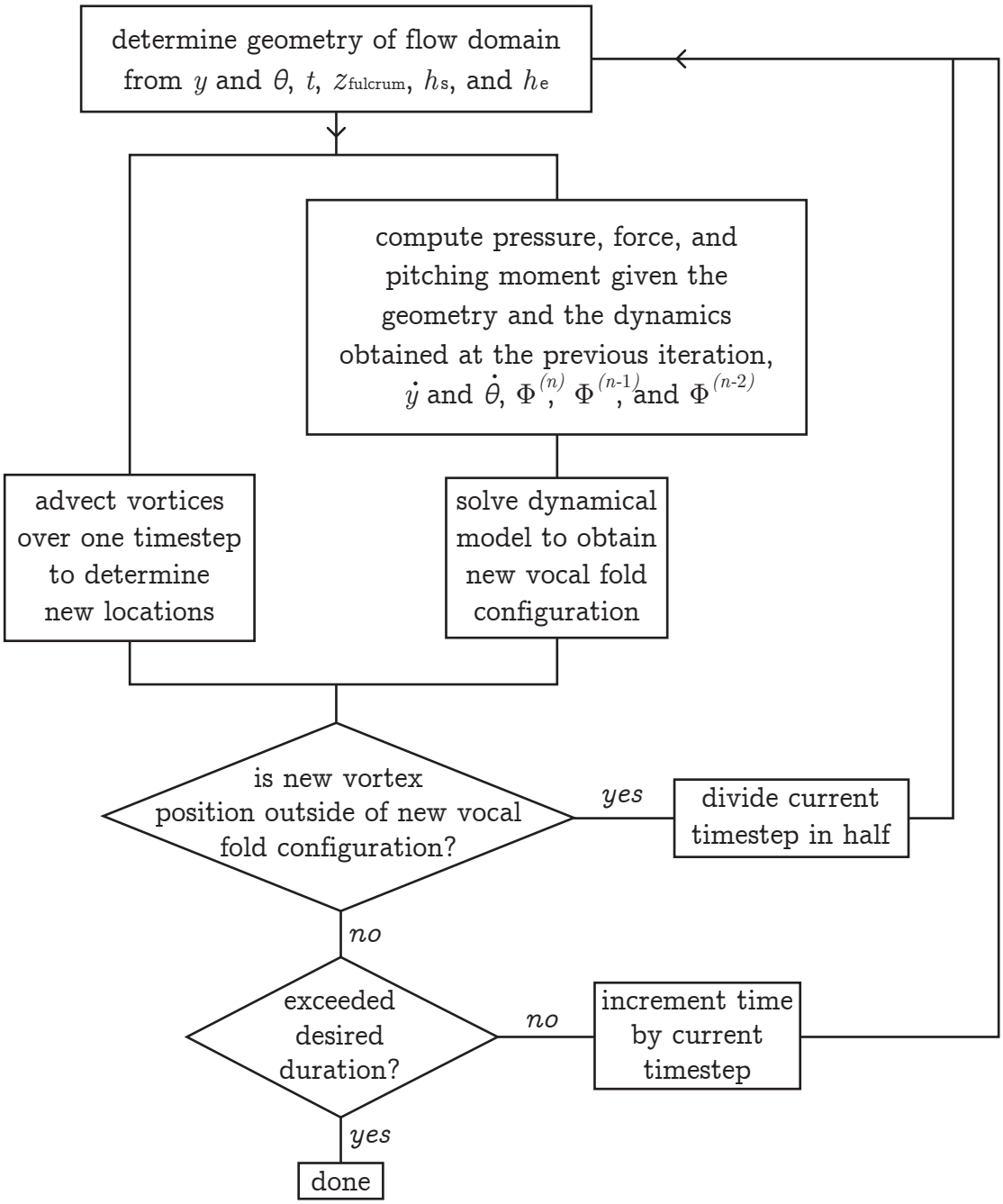

FIGURE 3.10: Flow chart of single iteration of simulation. To begin, flow geometry is determined from initial conditions and subsequently from values determined at the previous time. The pressure, force, and pitching moment are computed and supplied to the dynamical model. Vortex advection is computed in parallel after geometry is determined. The new vortical positions are tested against the predicted new geometry, and they must remain interior to flow domain, otherwise the timestep is cut in half and the problem iterates until this condition is satisfied before ultimately proceeding to the next timestep.

3.3.1 An Adaptive Timestep

The purpose of an adaptive timestep is not merely for computational stability or for improved runtime to the exclusion of other considerations, but, rather, to optimize runtime while capturing relevant physical effects which occur at multiple timescales. In some sense, this is similar to selecting a temporal step to ensure stability because larger timesteps would allow too much motion, and the behaviour of the solution would deviate inaccurately from the true motion of the system. The timestep is selected to be sufficiently small so that small changes in flow geometry do not cause large swings in aerodynamic response. A computation is well conditioned, i.e., computationally stable if and only if small perturbations of inputs do not cause large variability in outputs. The timestep, $\delta t^{(n)} = t_{n+1} - t_n$, employed at iteration n of the temporal marching adapts from one iteration to the next to ensure that the simulation resolves the relevant modelled effects with sufficient accuracy. The timestep is continually determined by mechanical and aerodynamic timescales. In particular, the timestep is scaled for the simulation to capture the dynamics of the motion of the medial surface of the vocal folds, including pitching and heaving, and, also, to capture the trajectories of vortices with sufficient spatial resolution. Because the body mass and damping are large in comparison with the corresponding cover properties, the body mass, in any reasonable physical sense, will respond more slowly than the pitching and heaving of the cover or the displacement of vortices. The larger time constant of the body mass suggests that resolution of its behaviour does not constrain the timestep; i.e., if the motion of the vortices and the cover mass are resolved with sufficient accuracy, the motion of the body mass is surely determined with enough accuracy.

Of concern are the displacements of the vortices and the medial surfaces of the vocal folds over a single timestep δt. The scales of interest are the maximal speed of advection of the vortices and the time constants of pitching and heaving of the cover masses. The maximal vortex advection speed (with units [m/s]) at iteration n may be written as

$$\max_j v^{(n)}_{\text{vortex},j},$$

in which j indexes the set of vortices present in the flow field and $v^{(n)}_{\text{vortex},j}$ is the magnitude of the velocity of the j^{th} vortex at the n^{th} iteration. The desired timestep must be some submultiple of the sampling period which assures that a vortex does not advect more than some fraction of glottal width t_{VF} in a single timestep, and that twice the frequency of the pitch and heave oscillation are captured. The following timestep (measured in seconds) at the n^{th} iteration is proposed

$$\delta t^{(n)} = t_{n+1} - t_n = C \cdot \min\left(\frac{t}{\max\limits_j v^{(n)}_{\text{vortex},j}}, 2\pi\sqrt{\frac{m}{k}}, 2\pi\sqrt{\frac{I_c}{\kappa}} \right) \tag{3.28}$$

in which $C < 0.5$ ensures that the motion of the medial surface is captured without aliasing and that a vortex displaces at most $(1/C)^{\text{th}}$ of the vocal fold thickness from time t_n to

time t_{n+1}. The value $C \cdot \frac{t}{\max\limits_j v^{(n)}_{\text{vortex},j}}$ is the ratio of the allowable vortex advection speed to the actual instantaneous vortex advection speed. Furthermore, by selecting the maximal vortex advection speed for the denominator, the smallest possible value of the timestep is determined to ensure that all vortical motions are captured with adequate resolution. The remaining two arguments in (3.28) are characteristic periods of translational and angular oscillation of the cover mass; hence the need for $C < 0.5$, it ensures that the Nyquist criterion is satisfied. The actual $\delta t^{(n)}$ must be strictly less than half of these values to ensure that the simulation captures their trajectories unaliased. In simulations, a value of $C = 1/50$ was selected. Also note that the value of time at iteration n is easily determined as

$$t_n = t_0 + \sum_{k=1}^{n} \delta t^{(k)}. \tag{3.29}$$

3.4 Non-dimensional Model Parameters

The parameters of the dynamical vocal fold model shown in Figure 3.1 and related by dimensional equations of motion (3.1), (3.2), and (3.3) are gathered in Table 3.1. These are subsequently combined with the geometric parameters and the fluid parameters to obtain dimensionless groups such as mass ratios and frequency ratios which enable an overall characterization and summary of the vocal fold model developed. Model parameters are summarized in Table 3.4 below.

From these dimensional parameters, characteristic scales are selected and gathered in Table 3.5. Neutral glottal width is selected as the characteristic length scale because it ostensibly determines the glottal flow; since V_s is constant and volumetric flow rate is the product of velocity and cross-sectional area, $A_{ng} = h_{ng} l$ determines nominal glottal flow. The velocity scale is the vortex advection speed in absence of a free stream, $V_c = \Gamma/a$. The pressure scale is proportional to a dynamic pressure determined by the characteristic velocity scale. Finally, characteristic time is the ratio of characteristic length and velocity.

TABLE 3.5: Characteristic scales.

dimension	characteristic scale	interpretation
L	$l_c = h_{ng}$	neutral glottal width, characterizes intraglottal flow
LT^{-1}	$V_c = \Gamma/a$	characteristic velocity, due to vortex configuration
$ML^{-1}T^{-2}$	$P_c = \rho\Gamma^2/a^2$	a dynamic pressure
T	$t_c = ah_{ng}/\Gamma$	characteristic time determined by l_c/V_c

The dimensional equations of motion may be transformed via the change of variables that time is replaced with the ratio of dimensional time and characteristic time, $t^* = t/t_c$,

TABLE 3.4: Summary of model parameters.

parameter	description
M	body mass
m	cover mass
I_c	cover moment of inertia
K	body translational stiffness
k	cover translational stiffness
κ	cover torsional stiffness
B	body mass translational damping
b	cover translational damping
B_c	torsional damping of cover
h_s	subglottal width of larynx
A_s	subglottal sectional area
h_e	epilaryngeal width of larynx
A_e	epilaryngeal sectional area
t_{VF}	vocal fold thickness
l	vocal fold length
l_{node}/t_{VF}	nodal position as fraction of vocal fold thickness
A_{ng}	neutral glottal area
h_{ng}	neutral glottal channel width
θ_{ng}	neutral glottal convergence angle
ρ	fluid density
P_L	lung pressure
P_s	subglottal pressure
P_e	epilaryngeal pressure
Q	volumetric flow rate
V_s	subglottal velocity
Γ	circulation due to vortex
a	intra–vortex spacing

and similarly that displacements are scaled with characteristic length as $y^* = y/l_c$, via chain rule for the substitutions, the dimensionless form of (3.1) is then

$$\frac{m\Gamma^2}{a^2 h_{ng}}\frac{d^2\,y^*}{dt^{*2}} + \frac{b\Gamma}{a}\frac{d}{dt^*}\left(y^* - y_b^*\right) + kh_{ng}\left(y^* - y_b^*\right) = P^*\rho\,\frac{\Gamma^2}{a^2} l t_{VF}$$

the right hand side of which follows by observing that the aerodynamic loading term F_a in (3.1) may be written as a mean pressure over the projected area of the medial surface of the vocal fold,

$$F_a = P\,l\,t_{VF} = P^*\rho\,\frac{\Gamma^2}{a^2} l\,t_{VF}\,.$$

So, by dividing through by the coefficient of the dimensionless pressure, $\rho\,\frac{\Gamma^2}{a^2} l t_{VF}$, we obtain the dimensionless form of (3.1) given by

$$\frac{m}{\rho\,l\,t_{VF}\,h_{ng}}\frac{d^2\,y^*}{dt^{*2}} + \frac{b}{\frac{\Gamma}{a}\rho\,l\,t_{VF}}\frac{d}{dt^*}\left(y^* - y_b^*\right) + \frac{kh_{ng}}{\rho\,l\,t_{VF}\frac{\Gamma^2}{a^2}}\left(y^* - y_b^*\right) = P^* \tag{3.30}$$

The coefficients of the terms in (3.30) determine dimensionless groups, a mass ratio, a damping ratio, and a stiffness ratio. To obtain a frequency ratio, if one recalls that the natural frequency of a simple spring-mass system is $\omega_n = \sqrt{k/m}$, and that, after dividing the differential equation through by the coefficient of the second-order term, the coefficient of the zeroth-order term is the square of the natural frequency, one obtains a frequency ratio as follows

$$\frac{\frac{kh_{ng}}{\rho\,l\,t_{VF}\frac{\Gamma^2}{a^2}}}{\frac{m}{\rho\,l\,t_{VF}\,h_{ng}}} = \frac{\frac{k}{m}}{\frac{\Gamma^2}{a^2 h_{ng}^2}} = \frac{\omega_n^2}{\left(\frac{\Gamma}{a\,h_{ng}}\right)^2}$$

So that a characteristic frequency is given by

$$f_c = \frac{\Gamma}{2\pi\,a\,h_{ng}} \tag{3.31}$$

however, notice that this is simply the reciprocal of the characteristic time. This yields an interpretation of the characteristic time that it is a characteristic period.

A similar argument may be applied to (3.3). However, despite that θ is dimensionless, upon dividing through by I_c,

$$\ddot{\theta} + 2\zeta\omega_n\dot{\theta} + \omega_n^2\theta = \frac{T_a}{I_c} \tag{3.32}$$

in which the damping ratio and natural frequency are given by

$$\zeta = \frac{B_c}{2\sqrt{\kappa I_c}} \quad \text{and} \quad \omega_n = \sqrt{\frac{\kappa}{I_c}}\,, \tag{3.33}$$

equation (3.32) remains dimensional. However, as before, with $t^* = t/t_c$, application of chain rule yields

$$\frac{d\theta}{dt} = \frac{1}{t_c}\frac{d\theta}{dt^*} \quad \text{and} \quad \frac{d^2\theta}{dt^2} = \frac{1}{{t_c}^2}\frac{d^2\theta}{dt^{*2}}\,,$$

which, upon substitution into (3.32) yields

$$\frac{\Gamma^2}{a^2 {h_{ng}}^2}\frac{d^2\theta}{dt^{*2}} + \frac{2\zeta\omega_n\Gamma}{ah_n g}\frac{d\theta}{dt^*} + {\omega_n}^2\theta = \frac{T_a}{I_c}$$

These frequency ratios, mass ratios, and various other useful dimensionless groups, are summarized in Table 3.6.

TABLE 3.6: Dimensionless groups

dimensionless group	characterizes
$\frac{m}{\rho l t_{VF} h_{ng}}$	ratio of plate mass to fluid mass
$\frac{b}{\frac{\Gamma}{a}\rho l t_{VF}}$	damping ratio
$\frac{k}{\rho l t_{VF}\frac{\Gamma^2}{a^2 h_{ng}}}$	stiffness ratio
$\frac{\omega_n}{\frac{\Gamma}{a h_{ng}}}$	frequency ratio
a/h_s	geometry of vortex distribution
$\frac{\Gamma/a}{V_s}$	relative strength of vortex

4 Results

The simulation model developed in Chapter 3, with steady and unsteady versions of Bernoulli's equation employed to obtain the pressure field, is validated against the bar-plate body-cover model of Titze [99], which employs a 1-D steady potential flow model of the glottal flow. This validation is discussed in Section 4.1. In order to address the question of this thesis, whether intraglottal vortices influence the rate of closing of the vocal folds, the vortex advection scheme is employed, and advecting vortex pairs are introduced at some upstream position and allowed to advect into the glottis. In Section 4.2, the results of the study of the influence of advecting vortices are discussed. The 2-D glottal flow model employing trailing edge flow separation together with the unsteady Bernoulli equation to determine the pressure field in the presence of the advecting vortices is employed for the simulations. The advecting vortices account for the intraglottal vortices which are shed from the medial surface of the vocal folds downstream of flow separation in actual glottal flow. The simulation was performed with a trailing edge separation to ensure that the pressure variation due to the presence of advecting vortices would be impressed upon the medial surfaces of the vocal folds in a natural way regardless of their axial position. Finally, Section 4.3 presents a discussion of the limitations of the model, whereas mention of possible approaches to overcome the limitations of the model or to extend it shall be postponed until Chapter 5.

4.1 Model Validation

To validate the two-dimensional glottal flow simulation model developed in Chapter 3, simulation results from the model are compared against the Titze bar-plate model proposed and documented in [99]. The results of three simulations are compared herein, (1) Titze bar-plate body-cover model with its 1-D GF model, (2) the same bar-plate VF tissue model but coupled to the 2-D GF model developed herein with the same flow separation criterion and with pressure at the medial VF surface determined via the steady Bernoulli equation, and (3) identical to (2) but, by tracking the temporal evolution of the velocity potential, the pressure field is determined by the unsteady Bernoulli equation. All three models employ Liljencrats's criterion [59] for flow separation, that, in the closing phase of the phonatory cycle when the vocal folds obtain a diverging configuration, flow separation occurs at a point on the medial vocal fold surface at which the cross-sectional area is some

multiple of the minimal glottal area. In these simulations, a value of 1.2 is employed for this ratio. In all three cases, the simulations are performed with the no-tract condition, i.e., the glottal flow is not coupled to the acoustical field determined by a vocal tract model. In this case, therefore, no perturbation of the glottal waveform occurs due to varying boundary pressures because the transglottal pressure is effectively fixed.

For clarity, one example of each of the three cases is computed with the same set of model parameters and from zero-state initial conditions, that is, the displacements and velocities are initialized to zero. The set of simulation parameters employed is provided in Table 4.1 below. These values are identical to the parameters employed by Titze in [99],

TABLE 4.1: Summary of simulation model parameters employed in simulations.

parameter		value	units
M	body mass	1.0×10^{-4}	kg
m	cover mass	1.0×10^{-4}	kg
I_c	cover moment of inertia	1.0×10^{-10}	$\mathrm{kg\,m^2\,rad^{-1}}$
K	body translational stiffness	200	$\mathrm{N\,m^{-1}}$
k	cover translational stiffness	50	$\mathrm{N\,m^{-1}}$
κ	cover torsional stiffness	5.0×10^{-5}	$\mathrm{N\,m\,rad^{-1}}$
B	body mass translational damping	2.83×10^{-2}	$\mathrm{kg\,s^{-1}}$
b	cover translational damping	1.41×10^{-2}	$\mathrm{kg\,s^{-1}}$
B_c	torsional damping of cover	1.414×10^{-8}	$\mathrm{kg\,m^2\,s^{-1}\,rad^{-1}}$
A_s	subglottal sectional area	3.0×10^{-4}	$\mathrm{m^2}$
A_e	epilaryngeal sectional area	2×10^{-5}	$\mathrm{m^2}$
t_{VF}	vocal fold thickness	3.0×10^{-3}	m
l	vocal fold length	1.5×10^{-2}	m
l_{node}/t_{VF}	nodal position	0.51	–
A_{ng}	neutral glottal area	0	$\mathrm{m^2}$
θ_{ng}	neutral glottal convergence angle	3.33×10^{-2}	rad
ρ_f	fluid density	1.14	$\mathrm{kg\,m^{-3}}$
V_s	subglottal velocity for 2-D model	1.05	$\mathrm{m\,s^{-1}}$
P_s	subglottal pressure	625	$\mathrm{kg\,m^{-1}\,s^{-2}}$
P_e	epilaryngeal pressure	0	$\mathrm{kg\,m^{-1}\,s^{-2}}$

and yield physiologically reasonable glottal waveforms. Consequently, this enables a direct comparison between the simulation models developed herein and this well documented Titze model. It is worth noting that the subglottal velocity is a parameter which is neglected in the Titze 1-D potential flow model of GF but is essential in the 2-D GF model. A physiologically reasonable magnitude has been selected for subglottal velocity based upon [99]. All simulations are performed over a period of one second.

One significant determiner of the quality of a VF-GF model is that it achieves a self-

sustaining oscillatory behaviour. This is a necessary condition for the validity of the models because actual vocal folds achieve a relatively steady periodic motion in modal speech. That the models exhibit this desirable behaviour is evident in the phase portraits shown in Figure 4.1 for the three simulations. The phase portraits also exhibit many of the same features and they occur at identical phases of the phonatory cycle. The steadiness of the oscillatory behaviour is less apparent in the third set of plots because the amplitude of oscillation exhibits significantly greater variability than observed for the Titze model. This variability manifests as a much wider annular region containing the phase portraits of the angular position and velocity.

Now, to elucidate the behaviour of the model in the time domain, for comparison, Figure 4.2 shows a single phonatory cycle for all three cases superimposed. To convey the periodic behaviour, four or five consecutive phonatory cycles are displayed in the plots of the temporal evolution of the dynamical system in Figures 4.3, 4.5, and 4.7. In all of these plots, the uppermost series correspond to the glottal area waveform produced by the respective simulation model. The glottal area is the minimal projected cross-sectional area of the glottis in a transverse section at any instant. The glottal area waveform records the temporal evolution of this quantity. The glottal area may at any instant be computed from the dynamical state of the system, knowledge of the neutral glottal configuration, and the purely geometrical parameters such as nodal position and VF length and thickness. Furthermore, in actual patients, glottal area may be clinically determined with photoglottographic techniques, for example, see [6]. Finally, the glottal area waveform is a strong correlate of the glottal sound source. For these reasons, the glottal area waveform is amongst the significant determiners of the physiological quality of a particular VF-GF model, in particular, the wave shape and features may be directly compared to clinically observed waveforms in order to assess the validity of a VF-GF model.

The glottal volumetric flow rate is considered to be the primary source signal in phonation, in fact, the volumetric flow rate is the signal which acoustically excites the upper vocal tract [92]. It is strongly correlated to the glottal area waveform, primarily because the glottal area determines the mean volumetric flow rate. Both of these signals may be related to each other and to the acoustics generated by the glottal sound source. In particular, see [46] for a critical discussion of the way in which the shape and characteristics of these waveforms determine the acoustical features of the sound signals with which these waveforms are correlated. Because the glottal flow rate is not merely a consequence of the glottal area, but also of the prevailing acoustically determined transglottal pressures, and, because the models examined herein are not coupled to the acoustical field determined by the upper vocal tract, solely the area waveform is employed as a basis for comparison of the models and as a basis for assessing the physiological validity of the models.

There are several conventional time domain numerical parameters which summarize the wave shape and, in terms of speech, relevant characteristics of the glottal area waveform: the fundamental frequency f_0 or fundamental phonatory period $T_0 = 1/f_0$, the open quotient (OQ), speed quotient (SQ), and closing quotient (CQ), see, for example [92, 96]. The open quotient is a duty cycle which identifies the fraction of a fundamental period

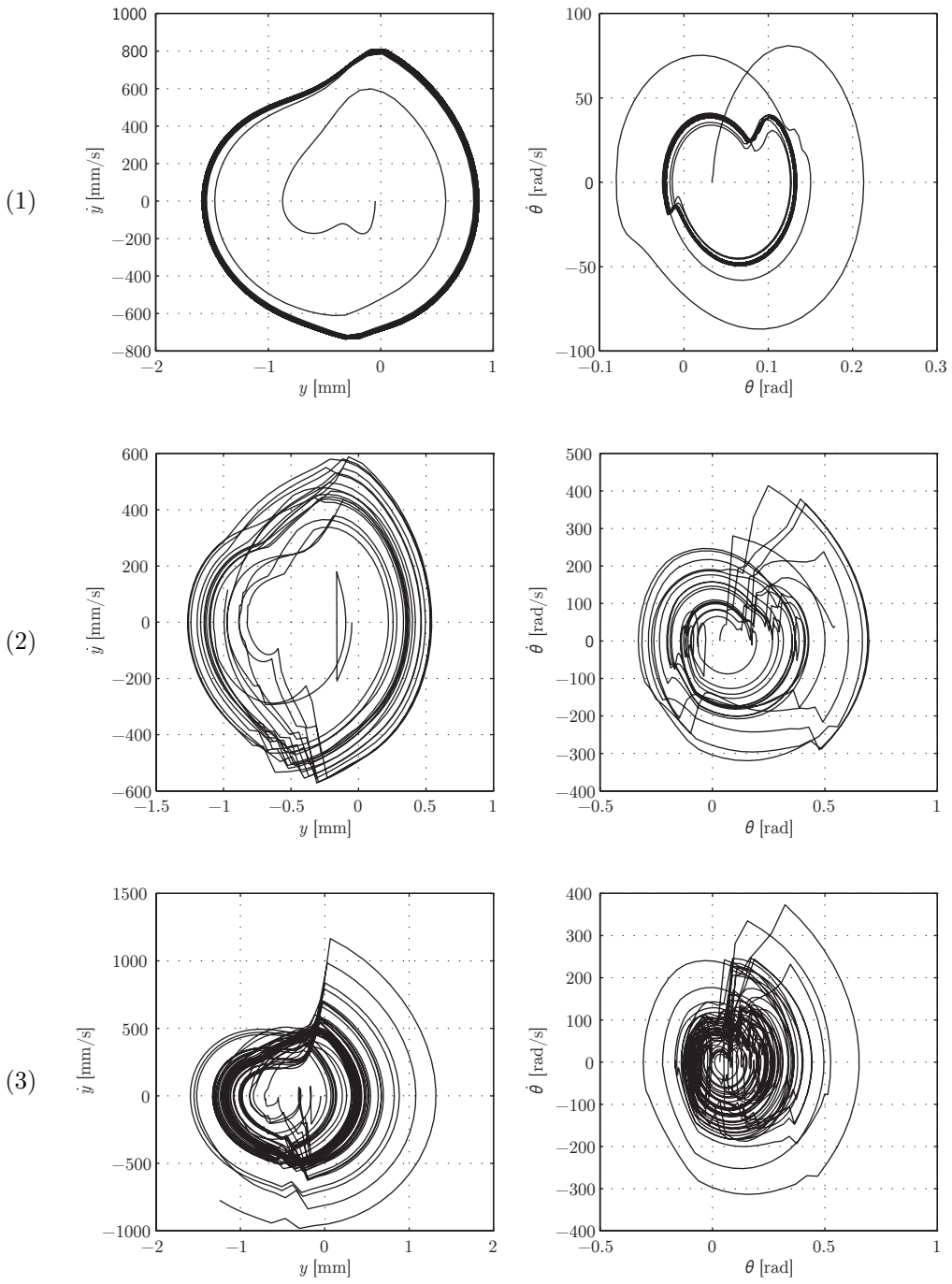

FIGURE 4.1: Representative translational and rotational phase portraits for (1) Titze simulation, (2) 2-D simulation with steady Bernoulli equation to compute pressure distribution, and (3) with unsteady Bernoulli. For each, the first column displays translational velocity vs. absolute position of the cover mass and the second column displays angular velocity vs. absolute angular position. The trajectories exhibited in these plots confirm the self-sustaining oscillatory behaviour of the plate in translation and rotation.

throughout which the glottis is open; in particular, OQ is the ratio of the total time the glottis remains open throughout a phonatory period to the fundamental phonatory period. The speed quotient is the ratio of the time required, beginning from a closed state, for the glottis to achieve its maximal area to the time required for the glottis to return to a closed state where flow is fully impeded. The SQ is close to 1 when the peaks of the glottal waveform exhibit symmetry between the opening and closing phases of a phonatory cycle. Values of SQ are less than unity whenever the peaks are skewed to the right, i.e., when they exhibit slow rates of opening and rapid rates of closing. The closing quotient is a duty cycle which identifies the fraction of a fundamental period throughout which the glottis is closing; in particular, CQ is the ratio of the time required, from the instant of maximal glottal area, for the glottis to close to the fundamental period of phonation. On the basis of these numerical summaries, the simulation results may be validated.

The numerical parameters are provided for the three models together with typical ranges of the values in Table 4.2 below. The physiological range of CQ may be from 0.22 to 0.32 for pressed voice, between 0.26 and 0.36 for normal voice, and between 0.29 and 0.48 in breathy voice [3]. Other physical ranges are obtained from clinical investigations of the glottal waveform presented and discussed in terms of their outcomes for voiced speech in, for example, [6, 46]. These time domain parameters are easily determined from clinically obtained photoglottographic data and, more robustly, via inverse analysis of acoustical signals [3, 36, 78]. Table 4.2, in addition to the frequencies and quotients, also lists maximal glottal width, which provides a measure of the amplitude of the glottal waveform. In the case of the model, notwithstanding the discussion of glottal geometry in Chapter 3 with reference to Figure 3.3, because a constant glottal cross section is assumed, the maximal glottal width is simply the maximal glottal area divided by the fold length parameter l.

TABLE 4.2: Comparison of glottal waveforms based upon physiologically relevant numerical summaries which characterize their shape.

parameter and physiological range		(1) Titze 1D	(2) 2-D no $\partial\Phi/\partial t$	(3) 2-D $\partial\Phi/\partial t$
f_0 [Hz]	80–220	90.8	87.9	87.3
max glottal width [mm]	~ 1	2.9	2.0	1.9
OQ	0.4–1.0	0.63	0.57	0.65
SQ	0.6–1.6	0.95	1.5	1.6
CQ	0.22–0.48	0.32	0.22	0.23

The glottal waveform for case (1), the Titze model, shown in Figure 4.3, together with the waveforms corresponding to the aerodynamic loading, i.e., the resultant force and pitching moment, exhibit strong qualitative agreement to the no-tract three-mass VF model simulations discussed in [93]. Furthermore, based on the fact that the time domain numerical summaries of the glottal area waveform provided in Table 4.2 are physiologically

reasonable, it may be concluded that the waveform of (1) is physiologically representative. Moreover, cases (2) and (3) exhibit glottal waveforms which are qualitatively similar to case (1). Together with the numerical summaries in the table, cases (2) and (3) are also placed within physiologically reasonable bounds. Consequently, it may be concluded that glottal area waveforms in cases (2) and (3) are also physiologically representative. The waveforms do differ, but this is a consequence of model differences.

A direct comparison of the area, force, and pitching moment waveforms over a single period for cases (1), (2), and (3) is provided in Figure 4.2. The area waveform of (1)

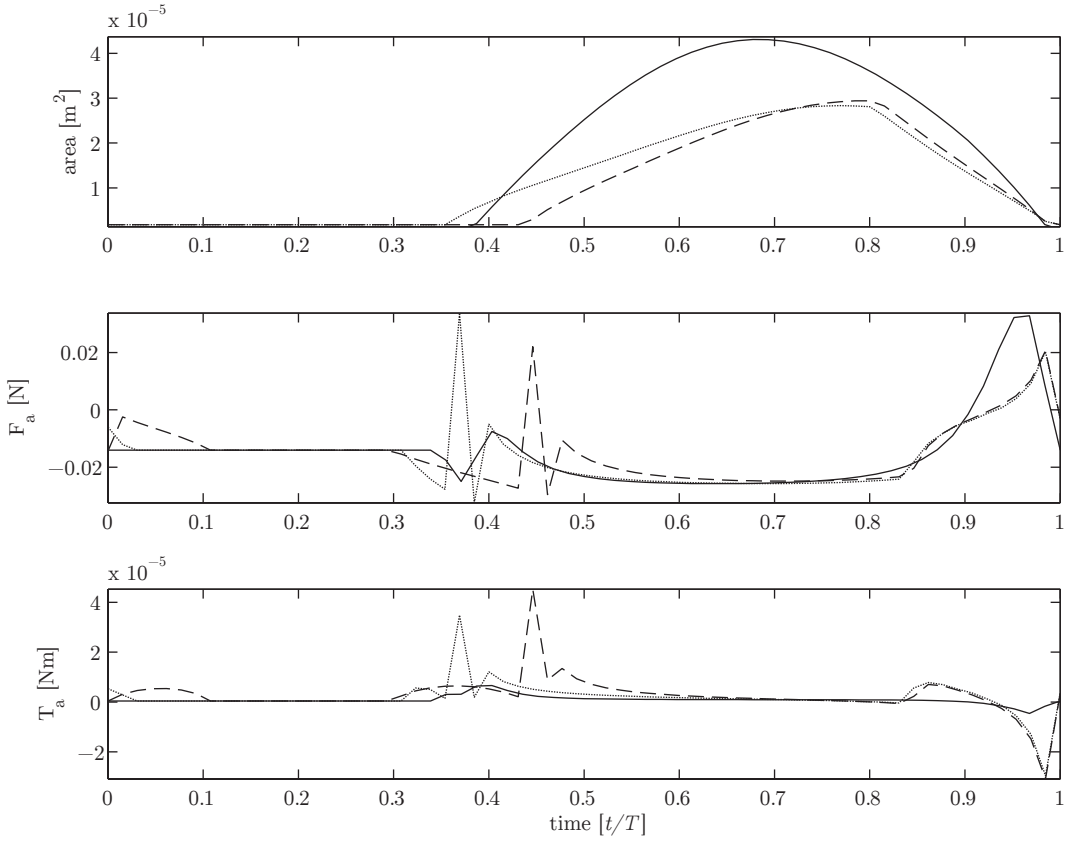

FIGURE 4.2: Comparison of area waveforms and resultant force and pitching moment. Solid trace corresponds to model (1) Titze 1-D GF model, the hatched line corresponds to (2) the 2-D GF model with steady Bernoulli, and the finely dotted trace corresponds to (3) 2-D model with unsteady Bernoulli.

is symmetric throughout the phonatory cycle, while those of (2) and (3) exhibit some skewness. This is characterized by their SQ (Table 4.2) which, for (1), is close to unity but greater than unity in the latter two cases. In cases (2) and (3), the angle of convergence throughout the opening phase is of greater magnitude than the angle of divergence in the closing phase of the phonatory cycle. The asymmetry between these phases is due to the efficacy of the flow separation in models (2) and (3) which causes the magnitude of the pitching moment in the closing phase of (2) and (3) to be much diminished from the

pitching moment in the opening phases of these cases. This is in contrast to case (1), in which the pitching moment is of approximately the same magnitude in the opening and in the closing phases of the phonatory cycle. Because the pitching moment in (1) is never of sufficient magnitude to cause the cover to pitch sufficiently for the point of flow separation to move very far inferiorly along the vocal fold surface, which only occurs briefly at the tail of the closing phase of the phonatory cycle, the effect of separation to induce an asymmetry of the loading between the opening and closing phases of the phonatory cycle is almost entirely absent in (1).

The use of the unsteady Bernoulli equation appears to advance opening and increase the peak magnitude of the resultant force and decrease peak magnitude of pitching moment. However, in the closing phase, force and pitching moment waveforms for (2) and (3) are effectively identical. The change in peak values of resultant force and pitching moment is due to a difference in the pressure distributions which arise during the opening phase of the phonatory cycle in these two models. The tractions due to pressure are momentarily higher in (3) than in (2) shortly after opening and the pressure distribution is more uniform, consequently, the peak pitching moment is reduced in (3) relative to (2) while the overall resultant force increases in (3).

There is notable disagreement between the pressure distributions in (1) and the pressure distributions in the 2-D GF models. One significant reason for this is that, in order to determine the pitching moment in model (1), firstly, two resultant forces are obtained, one by integrating pressure over the portion of the medial VF surface above the nodal point and one by integrating the pressure over the portion of the medial VF surface below the nodal point. These resultant forces are then applied at the midpoints of their respective, either superior or inferior, portions to develop a pitching moment. In model (1), this computation effectively smoothes the pressure distribution and diminish the capacity of any asymmetry of the pressure field to induce a strong pitching moment. In contrast, in the 2-D GF models, significant curvature of the streamlines entails significant pressure gradients developing in the wall-normal direction oriented inwards to the flow domain at the corners of the vocal folds. The pressure fields thus developed have a strong inferior-superior asymmetry because the upstream streamline curvature is a consequence of the flow trying to negotiate the glottal entrance at the interface between the inferior edge of the vocal fold, but at glottal exit, the flow is separated, and no significant curvature manifests. This causes a strong asymmetry in the pressure distributions on the medial vocal fold surfaces, and, therefore, a strong pitching moment develops in models (2) and (3). This is easily seen in the plots of pressure in Figures 4.6 and 4.8 where the pressure variation at the inferior and superior margins is significant. Moreover, models (1) and (2) do not account for variation in pressure due to temporal variation of glottal geometry, although, it is reassuring that models (2) and (3) are quite similar qualitatively. The following paragraphs prior to closing out this section provide more detailed description of Figures 4.4, 4.6, and 4.8 and corresponding pressure distributions, Figures 4.4, 4.6, and 4.8.

The characteristics in time and phase amongst the three models may be reconciled

upon examination of the time series and the glottal configurations at various critical instants and the concomitant medial VF pressure distributions. The transverse and angular displacement of the cover and the forces which produce these responses are displayed in Figures 4.3, 4.5, and 4.7. These plots also show the glottal configurations, streamlines, and representative surface traction distributions (scaled by the traction of largest magnitude at each instant) at critical instants in one particular period of the respective phonatory cycle. The fluid pressures at the medial vocal fold surfaces which produce these surface tractions corresponding to these configurations are provided in Figures 4.4, 4.6, and 4.8 respectively.

The plot in Figure 4.3 corresponds to (1) the Titze bar-plate VF tissue model with 1-D ideal potential GF model. The only streamline determined by this model lies along the centreline of the glottis and is shown in all frames when glottis is not closed. According to equation (B.39), pressure at some locations along the medial VF surface is related to the square of the ratio of the area at the location to the area at flow detachment; this is the reason for the curvature in the pressure profile in configuration (c) of Figure 4.3, for example. Pressures are obtained via the steady Bernoulli equation evaluated along the glottal centreline and modified to account for flow separation and kinetic energy recovery. These centreline pressures are impressed upon the medial surfaces of the vocal folds by the 1-D assumption. The manner in which pressure is obtained is described in Appendix B; pressures are effectively a function of the transglottal pressure, epilaryngeal area, and quadratically with the areas at transverse cross sections at each axial station.

When the glottis is fully closed, a constant uniform contact stress determines a constant resultant force and small but non-zero pitching moment. If the nodal point were located at the midpoint of the plate such that the plate would be symmetrically disposed about the nodal point, the pitching moment would indeed vanish. As it is, because the inferior medial VF area below the nodal point is larger, the resultant moment tends to rotate the plate positively, and, therefore, a small positive pitching moment prevails. The configuration at the first instant of interest, a fully closed glottal configuration prior to opening, is shown in Figure 4.3 configuration (a). The tractions exhibited at this instant are due purely to the contact stress model, which results in uniform applied loads, which tend to cause the glottis to open.

Figure 4.3 configuration (b) corresponds to partial closure in the opening phase of the phonatory cycle, that is, the leading edge of the vocal folds have begun to open, while the superior portion remains in contact. During the opening phase, the glottis obtains a converging configuration. The inferior portion of the vocal fold surfaces are exposed to the subglottal pressure, which applies uniformly, and the contact patch continues to experience the contact force. The surface pressure is consequently discontinuous. Because the subglottal pressure is greater than the contact pressure, the resultant force increases in magnitude. The glottis remains closed at this instant, so the glottal area waveform is zero, but in the following instant, the glottal area waveform begins to increase as the glottis opens. In Figure 4.3 configuration (c), in early stages of the opening phase of the phonatory cycle, glottal flow through the narrow superior margin of the glottis is rapid

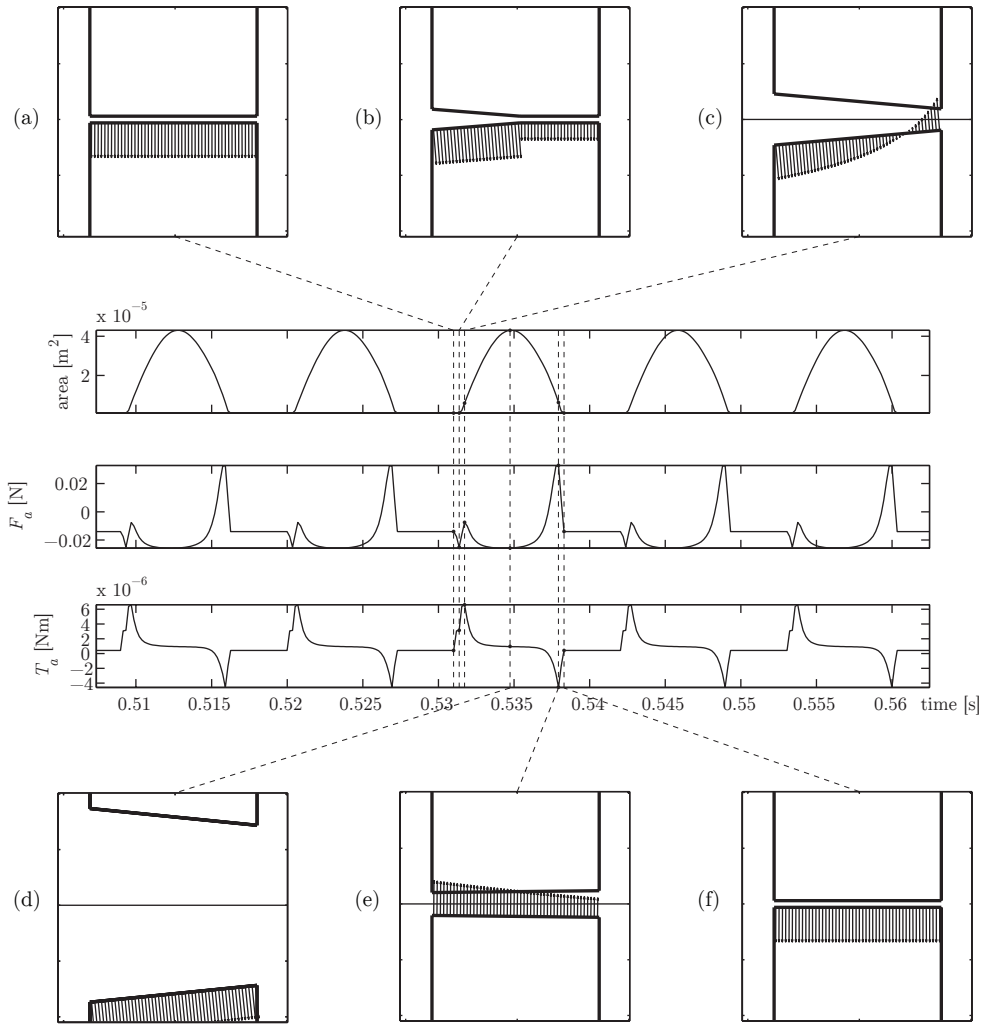

FIGURE 4.3: Time series for Titze bar-plate model together with glottal configurations, streamlines, and scaled surface tractions at various critical instants. The series are, from top to bottom, glottal area waveform, resultant transverse force due to pressure, and resultant pitching moment due to pressure. Figure 4.4 provides medial VF pressures corresponding to configurations (a) – (f).

due to conservation of mass. The large velocity entails that the static gauge pressure is large but negative in this region. This reduces the magnitude of the resultant force but the strong asymmetry in the surface tractions imparts a strong positive resultant pitching moment. This is the instant at which positive pitching moment is maximal and tends to increase the convergence of the opening. Inertia dominates, however the glottis continues to open.

At (d), the glottal area is maximal, the translational displacement of the plate is maximal, and the pressure distribution along the medial surface is nearly uniform. The pitching of the cover is out of phase with the translation of the body. As the body begins to return

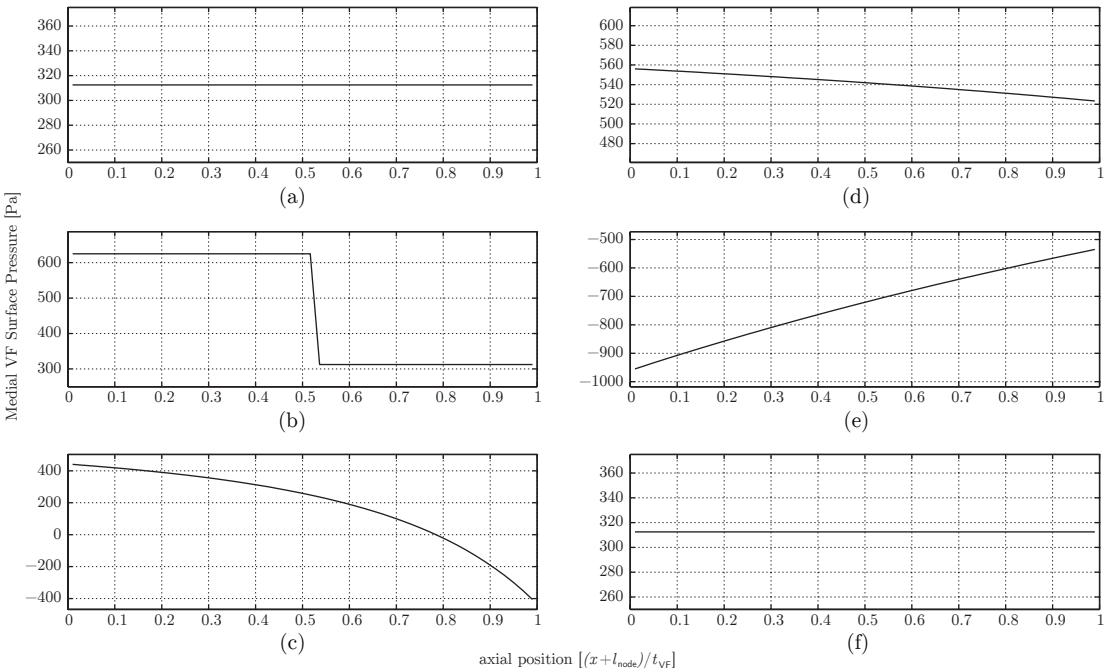

FIGURE 4.4: Pressure distributions for Titze bar-plate model corresponding to configurations (a) – (f).

to its equilibrium position, the glottis will begin to obtain a diverging configuration in which the conditions for separation begin to manifest. The plots transition smoothly from the instant of maximal glottal area to the instant of maximal negative pitching moment and maximal positive resultant force immediately prior to closing. This smoothness is a consequence of the fact that the plate does not pitch sufficiently throughout the closing phase; separation only occurs near the end of the closing phase in model (1) and, then, only briefly.

Immediately prior to closing, the resultant force obtains its maximal positively oriented magnitude. This is due to the tractions tending to draw the glottis closed due to the Bernoulli effect. The pitching moment obtains its maximal magnitude oriented negatively, meaning that it is causing the glottis to obtain a diverging configuration, and this is due to the strong asymmetry of the pressure distribution. Figure 4.3 configuration (e) shows this instant, immediately prior to closure. Configuration (f) displays the instant at which the glottis has fully closed at the termination of the closing phase of the phonatory cycle. The body masses are moving towards each other at this instant and are decelerating due to the contact force.

Figures 4.5 and 4.7 display time series and glottal configurations for (2) the 2-D GF model with steady Bernoulli equation and (3) with unsteady Bernoulli, and Figures 4.6 and 4.8 provide the corresponding pressure distributions.

Because the flow field is determined via a 2-D ideal potential flow model, streamlines may be obtained, and these are also displayed in the open glottis configurations in these plots.

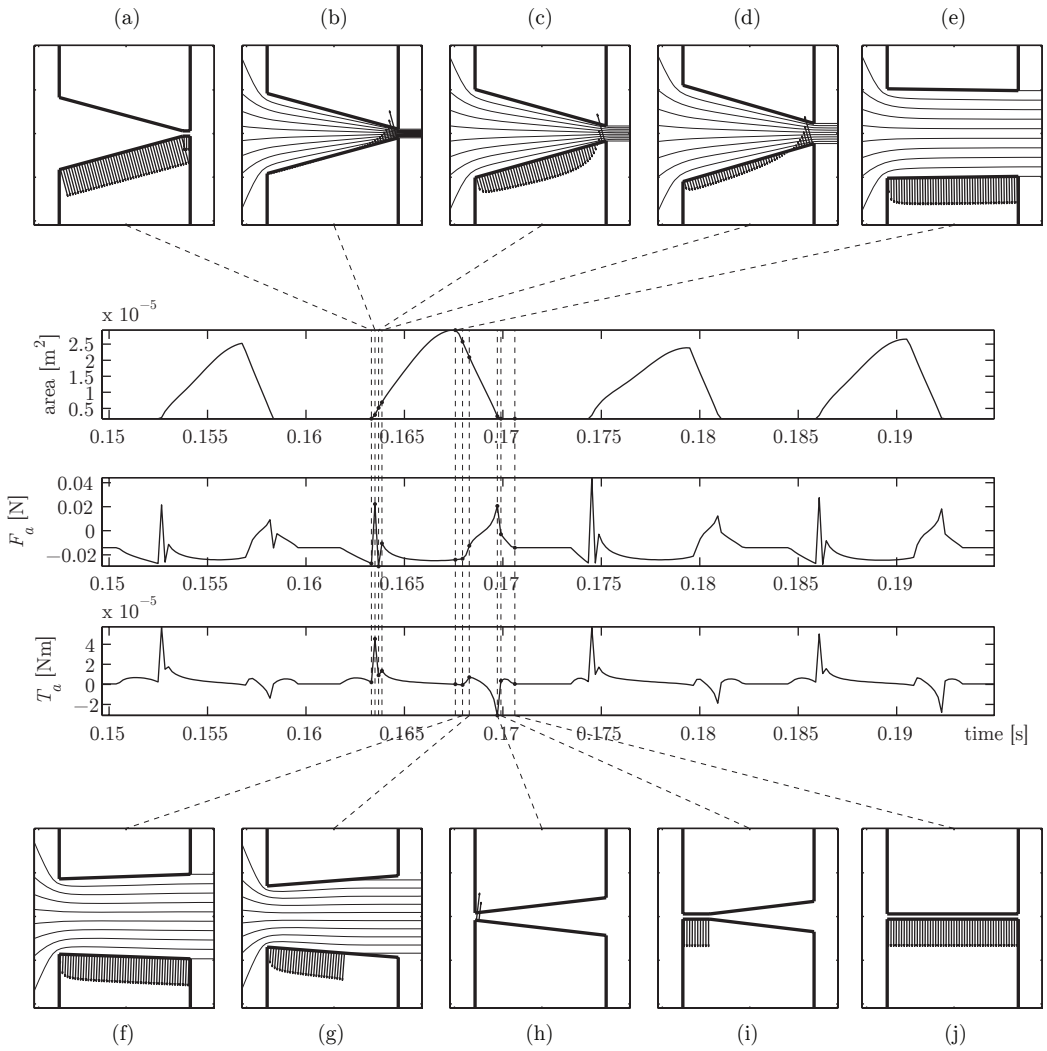

FIGURE 4.5: Time series for 2-D GF model with steady Bernoulli together with glottal configurations, streamlines, and scaled surface tractions at various critical instants. The series are, from top to bottom, glottal area waveform, resultant transverse force, and resultant pitching moment due to pressure. Figure 4.6 provides medial VF pressures corresponding to configurations (a) – (j).

As in the previous simulation, when the glottis is fully closed, a constant uniform contact stress determines a constant resultant force and small but non-zero pitching moment. The nodal point is located in the same position as before, so the surface area over which the contact force is applied is different inferior to the node and superior to it. This asymmetry ensure that the pitching moment in the fully closed state will tend to open the glottis into an initially convergent configuration as before. The configuration at the first instant of time is a partially closed glottal configuration. At the given instant, the inferior margin of the glottis has separated and allowed subglottal pressure to prevail in this region. Because this is greater than the contact pressure, the pitching moment is even greater.

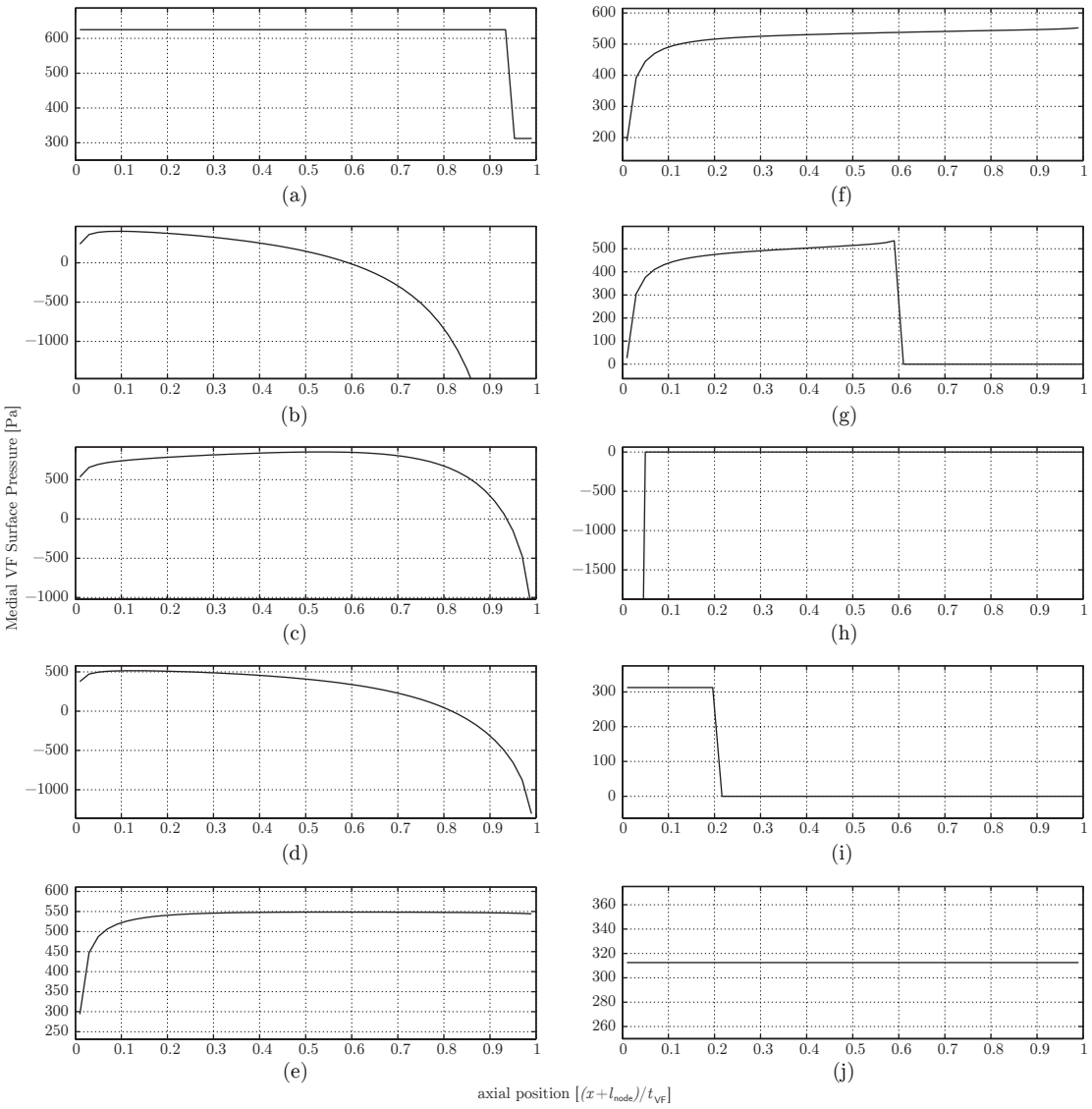

FIGURE 4.6: Pressure distributions for 2-D model with steady Bernoulli for configurations (a) – (j).

Figure 4.5 configuration (b) and 4.7 configuration (c) show the open glottis with flow through the narrow superior margin, which yields large velocities due to conservation of mass. The corresponding pressure distributions are qualitatively similar in this region. The unsteady term has not begun to contribute significantly at this instant. The asymmetry of the loading also causes a pitching moment as before, but the forces are short lived and insufficient to overcome the inertia of the body mass. The moment of inertia is only briefly overcome; the significant pitching moment decelerates the pitching of the plate and a noticeable change in the magnitude of θ is observed. Additionally, this is also one of the points at which the phase portrait 4.1 (b) exhibits a small deviation from a purely circular trajectory. The Titze model does not exhibit this behaviour, consequently the

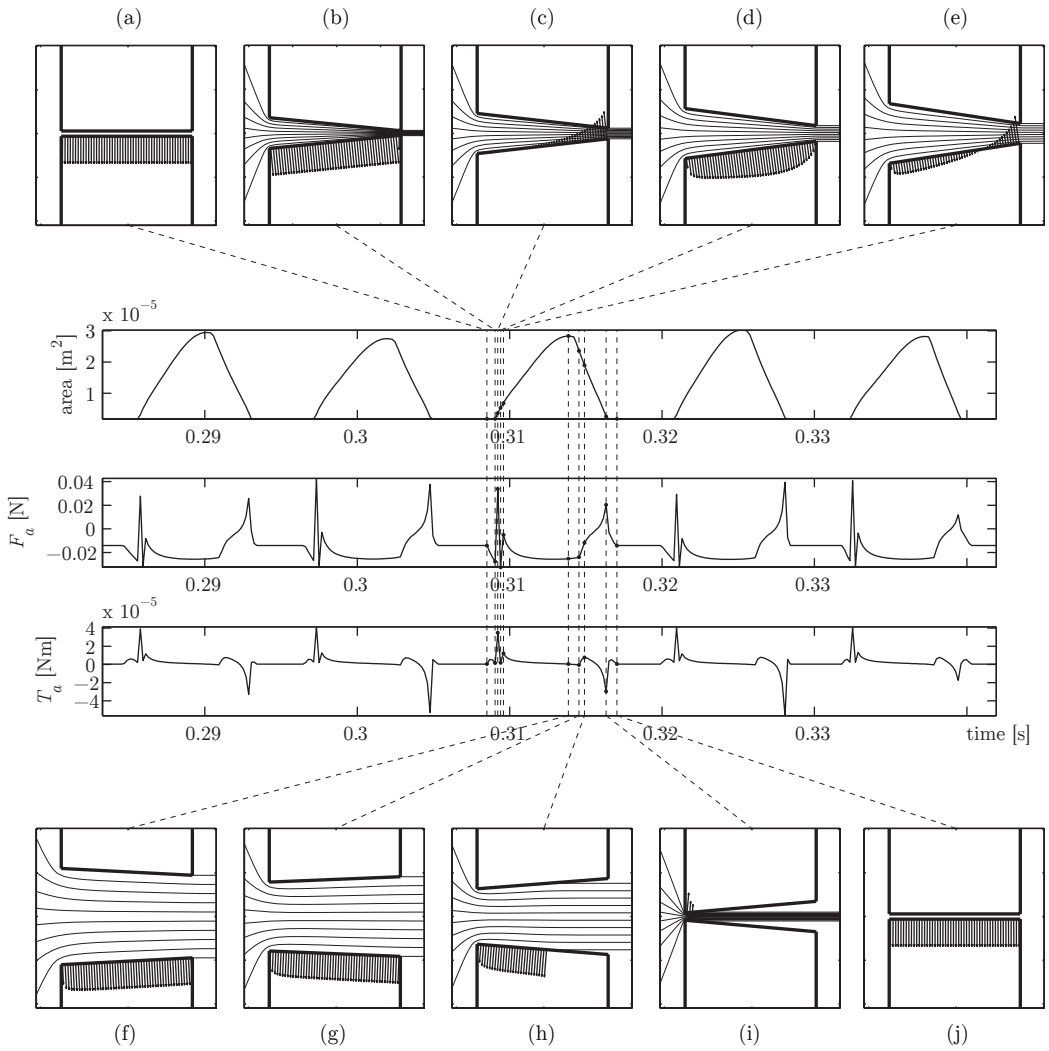

FIGURE 4.7: Time series for 2-D GF model with unsteady Bernoulli together with glottal configurations, streamlines, and scaled surface tractions at various critical instants. The series are, from top to bottom, glottal area waveform, resultant transverse force due to pressure, and resultant pitching moment due to pressure. Figure 4.8 provides medial VF pressures corresponding to configurations (a) – (j).

phase portrait is more circular and the time series for the angular displacement is smoother.

At the next instant, Figure 4.5 configuration (c) and 4.7 configuration (d), the magnitudes of force obtain their negative value of greatest magnitude but pitching moment falls. The vanishing pitching moment is due to the overall symmetry of the pressure distribution which gives rise to the surface tractions. At the same instant, there is a noticeable difference in models (2) and (3) in the pressure distribution and, therefore, the resultant forces in each. Due to the unsteady term, the forces which tend to open the glottis are more significant in (3). The configuration rapidly evolves from one with large prevailing velocities to one with lower velocities, so the temporal derivative of Φ goes negative, this

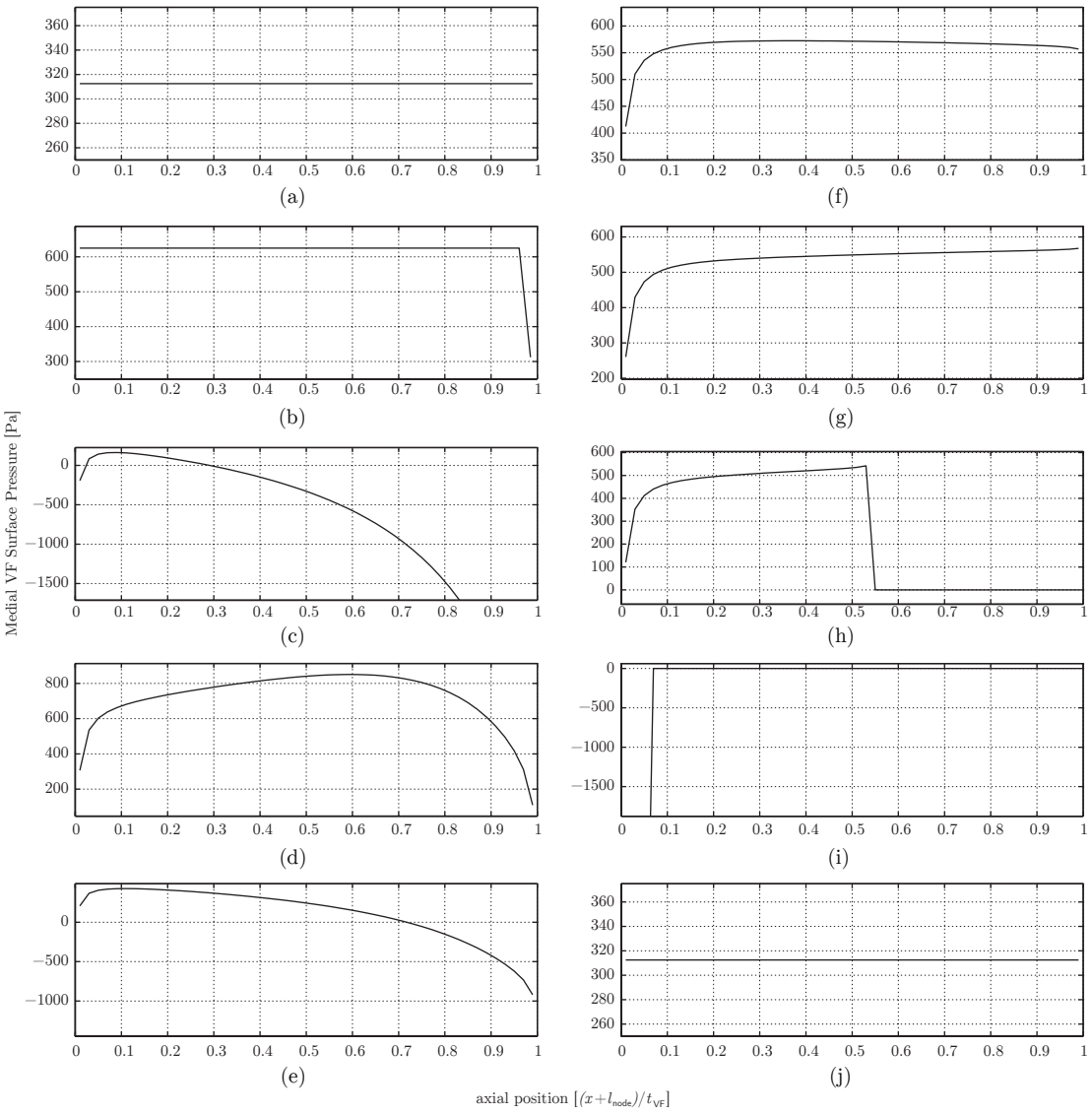

FIGURE 4.8: Pressure distributions for 2-D model with unsteady Bernoulli for configurations (a) – (j).

augments the pressure at the medial VF surface at this instant.

As the cover mass returns from its extreme excursion towards the midplane, the pitch angle is virtually 0, and this maximizes the cross-sectional area. As in the Titze simulation, the pressure distribution is nearly uniform, and, therefore, the pitching moment is vanishing. The pitching of the cover is out of phase with the translation of the body, therefore, as the body begins to return to its equilibrium position, the glottis will begin to obtain a diverging configuration in which the conditions for separation begin to manifest. The force and moment plots do not transition as smoothly as they do in the Titze model. This is again due to the fact that the point of separation does not move far upstream along the medial vocal fold surface in the Titze model, so the discontinuity of the pressure field

which would yield a highly asymmetrical pressure distribution and therefore significantly modify the loadings does not occur in (1) as it does in cases (2) and (3). Flow separation is shown in configurations (g) in Figure 4.5 and configuration (h) in Figure 4.7. In both cases, because epilaryngeal pressure, $P_e = 0$, is applied superior to the point of separation, there is a discontinuity in the pressure distribution which entails a significant asymmetry in the pressure distribution. This asymmetry causes the plate to obtain a greater divergent configuration where the pitching moment is more severe. This process continues and is augmented by the Bernoulli effect causing the glottis to close rapidly in configurations (h) in Figure 4.5 and configuration (i) in Figure 4.7. These are the instants of greatest magnitude of the pitching moment. The glottis eventually returns to its closed state where the contact stresses are uniformly applied over the entire contact patch and the phonatory cycle repeats.

4.2 The Role of Intraglottal Vortices in VF Dynamics

To assess the influence of intraglottal vortices upon the dynamics of the vocal folds, specifically whether the presence of intraglottal vortices affects the rate of closure of the glottis in the closing phase of the phonatory cycle, two sets of simulations are performed: with and without advecting vortices. The case without vortices serves as a baseline, and comparison of these cases shall enable the determination of the effect of the vortices. The simulations are performed with a trailing edge separation model to ensure that, when the vortex advection scheme is employed, the disturbance of the flow field due to the vortices is impressed upon the boundaries of the flow domain along the entire length of the medial surfaces of the vocal folds. A schematic of the vortical positions just prior to exit from the glottis is shown in Figure 4.9. This figure also shows the trailing edge separation schematically.

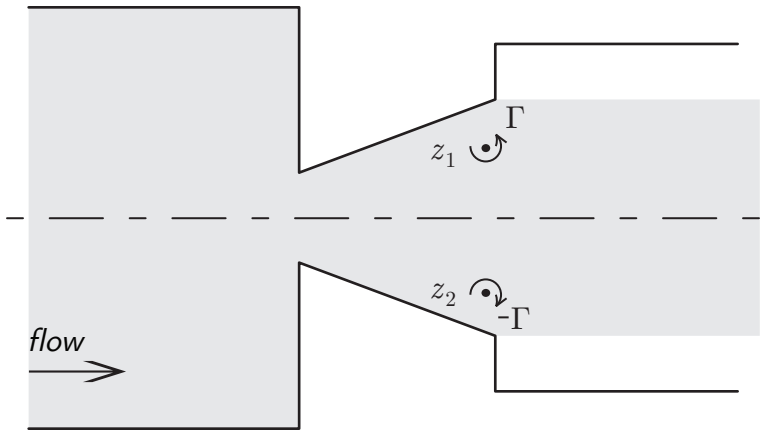

FIGURE 4.9: Schematic of intraglottal vortices by the time they have reached the glottal exit. Trailing edge separation ensures that the presence of the vortices is impressed upon the entire medial vocal fold surface.

The vortex advection scheme is employed in such a way that the vortex pair advects from

its upstream station and arrives at the glottis at a physically reasonable moment of its closing phase in the phonatory cycle. The pair quickly advect downstream, and is replaced at its upstream position ready for the next phonatory cycle. In this manner, the glottal waveform is perturbed in each cycle.

Firstly, the physiological validity of the baseline case with trailing edge separation is discussed prior to proceeding with a presentation of the simulation results in the presence of the advecting vortices. For the baseline study, the simulation parameters are identical to those listed in Table 4.1, except for the differences summarized in Table 4.3 below. In the simulations with trailing edge separation, the nodal point differs from the case with separation at some upstream point on the medial vocal fold surface, in order to compensate for the loss of inferior-superior flow asymmetry due to a separation point which always remains at the glottal exit. The subglottal pressure was reduced slightly and the damping coefficient was increased from 0.1 to 0.11; the new values of damping which correspond to the modified damping coefficient are also listed in the table. The modified set of parameters was selected to ensure that a strong self-sustaining oscillatory behaviour would quickly be established in the dynamical response of the vocal fold model.

TABLE 4.3: Summary of model parameters employed in simulation.

parameter		value	units
B	body mass translational damping	3.11×10^{-2}	$\mathrm{kg\,s^{-1}}$
b	cover translational damping	1.56×10^{-2}	$\mathrm{kg\,s^{-1}}$
B_c	torsional damping of cover	1.556×10^{-8}	$\mathrm{kg\,m^2\,s^{-1}\,rad^{-1}}$
l_{node}/t_{VF}	nodal position	0.52	–
P_s	subglottal pressure	600	$\mathrm{kg\,m^{-1}\,s^{-2}}$

The phase portraits shown in Figure 4.10 correspond to the case with no vortices, and they exhibit remarkably uniform amplitudes and this manifests as narrow annuli occupied by the trajectories of the motions in phase space. Additionally, they exhibit qualitative features which possess strong similarity to the simulations discussed in the previous section.

Time series which correspond to several periods of the phonatory cycle of the baseline (dotted trace) and the case with advecting vortices (solid trace), to be discussed, are shown in Figure 4.12. Again, the waveforms exhibit remarkable similarity to those discussed in the previous section. The numerical parameters which describe the shape of the glottal waveform corresponding to the baseline case are summarized in Table 4.4 below. The table shows that the values computed for the simulation are similar to the previously validated model and are well within physiological range, that is, $80 < f_0 < 220$, the maximal glottal width is on the appropriate order, $0.4 < OQ < 1.0$, $0.6 < SQ < 1.6$, and $0.22 < CQ < 0.48$. It may be concluded that this model generates physiologically reasonable glottal area waveform.

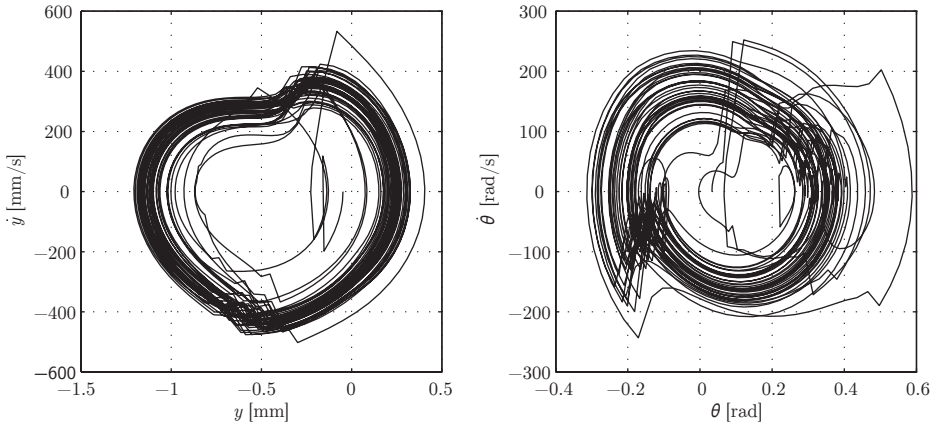

FIGURE 4.10: Representative translational and rotational phase portrait trailing edge separation with unsteady Bernoulli and no vortex advection. Velocity and absolute position plotted against each other, and angular velocity and absolute angular position of the plate are plotted against each other. The trajectories exhibited in these plots confirm the strong self-sustaining oscillatory behaviour of the plate in translation and rotation.

TABLE 4.4: Numerical summary of glottal area waveform for baseline case.

parameter	value
f_0 [Hz]	84.0
max glottal width [mm]	2.1
OQ	0.55
SQ	1.31
CQ	0.24

For the set of simulations with vortex advection, the additional parameters of vortex strength and starting position are required. For a specific case discussed herein, these values are provided in Table 4.5. These values were selected to ensure that the vortices would advect in the manner described. Consequently, consideration of the rate of vortex advection in the presence and absence of the free stream were required. Because the velocity of the glottal flow is an outcome of the model, many simulations were performed to obtain a value of vortex strength, for a given vortex spacing, which would cause the vortices to advect through the glottis at the necessary speed.

Specifically, the strength, Γ of the vortices is determined to be on the order of Γ which satisfies the following relation

$$\left(\frac{\Gamma}{a}\right)\left(2\pi\sqrt{\frac{m}{k}}\right) = t_{\mathrm{VF}} \tag{4.1}$$

TABLE 4.5: Summary of vortex parameters employed in simulation.

parameter		simulation value(s)	units
Γ	vortex strength	$\pm 8.4405 \times 10^{-4}$	$\mathrm{m^2\,s^{-1}}$
z_0	initial vortical positions	$[-9.0 \pm 4.0i] \times 10^{-3}$	m

in which the factors on the left hand side are characteristic velocity of vortex advection, $\frac{\Gamma}{a}$, for vortices with vortex separation a, and period of undamped oscillation of the cover mass in translation, $2\pi\sqrt{\frac{m}{k}}$. These quantities were discussed in Section 3.4. The right hand side, t_{VF}, is vocal fold thickness. The vortex strength which satisfies this relation will yield a rate of vortex advection in the absence of a free stream which ensures that they will advect in the axial direction approximately the length of one vocal fold thickness in the time required for one period of the phonatory cycle to complete. This should give an approximation for the order of magnitude of the vortex strength, but, because the rate of advection of the vortices is also a strong function of the free stream, the intraglottal velocity also determines the rate of advection of the vortices. For initial vortex spacing, the value of vortex strength predicted by this relation is approximately 2.7×10^{-3} [$\mathrm{m^2/s}$], for the vortex spacing when the vortices are within the glottis, their spacing is as little as 7.427×10^{-4} [m], and this predicts a value of Γ of approximately 2.5×10^{-4} [$\mathrm{m^2/s}$]. The actual value employed for the specific simulation discussed, was 8.4405×10^{-4} [$\mathrm{m^2/s}$], a value intermediate between these.

Again, the vortex strength and vortex spacing are determined in order to provide a pair of vortices advecting through the glottis in its divergent configuration during the closing phase of the phonatory cycle to emulate the vortex shedding which occurs in this phase of the phonatory cycle of an actual glottal flow. The perturbation due to the advecting vortex is determined by such a pair of advecting singularities, and for the specific case discussed herein, the perturbation of the pressure distribution on the medial VF surface is shown as it corresponds to the axial position of the advecting vortex pair in Figure 4.11. This figure displays a sequence of consecutive instants of vortex advection and the attendant pressure distribution on the medial vocal fold surfaces which prevails at the given instant. The abscissa of the pressure distribution is the fraction of the vocal fold thickness at which the vortex is located downstream from the glottal entrance. The vortices are initially near the glottal entrance, they perturb the pressure distribution slightly. The vortices have negligible downstream or upstream effect at any instant, they perturb the pressure locally. The medial vocal fold pressure distribution is slightly augmented everywhere, but most significantly near the instantaneous axial position of the vortex. The vortex increases the local pressure in the neighbourhood of its position, and this is because it tends to decrease the wall velocity due to its orientation, and this, in turn, increases the static pressure in the neighbourhood of the vortex.

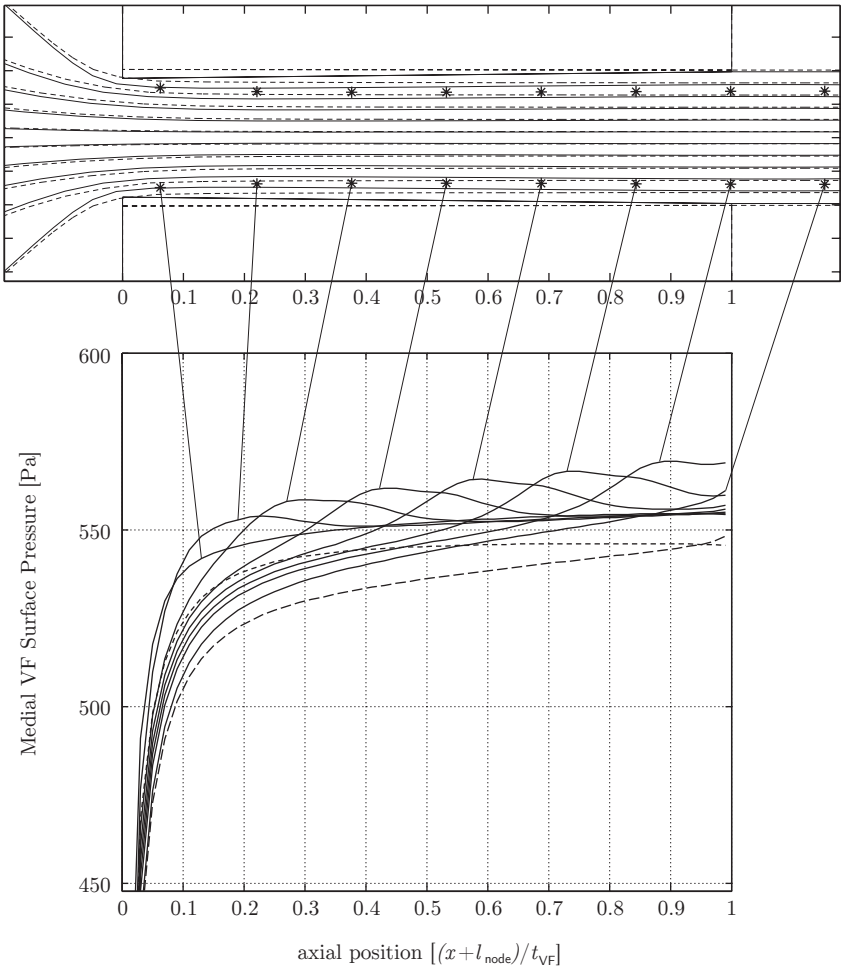

FIGURE 4.11: Configurations and pressure distributions corresponding to different axial positions of the intraglottal vortices. In the upper frame, positions of the advecting vortex pair are shown at various axial stations. Simultaneously, two glottal configurations and corresponding streamlines are displayed. The hatched VF outline and set of streamlines corresponds to the geometry and flow at the instant the vortices enter the glottis. The solid VF configuration and set of streamlines occurs at the instant the vortices exit the glottis. The lower frame exhibits the medial vocal fold surface pressures at the corresponding instants. Two additional pressure curves are superimposed; the finely hatched curve represents the medial VF pressure in the baseline case at the first instant and the large hatched trace corresponds to the medial VF pressure distribution of the baseline case at the final instant.

This situation is repeated in each phonatory cycle in the simulation, the vortices advect through the glottis at a rate determined by the vortex strength and spacing of the vortex pair as well as the free stream velocity within the glottis. Time series presenting outputs for this simulation are shown in Figure 4.12. The five time series are, from top to bottom, glottal area waveform, translational and angular displacements, translational force, and pitching moment. The dotted trace corresponds to the baseline, and the solid trace corre-

sponds to the case with advecting vortices. The plot shows that translational displacement of the cover obtains a more stable amplitude with vortex advection. The pitching moment is destabilized somewhat, and this contributes some variability to the glottal waveform. Remarkably, the glottal waveform in the case of vortex advection is more regular, despite that it is perturbed from the baseline. In fact, the closing phases of both baseline case and case with advecting vortices are remarkably consistent and similar, whereas the opening phases are significantly different in several of the cycles. To quantify this, Figure 4.13 combines the plots of the derivative of the glottal area waveforms of the baseline and the case with vortex advection overlaid with the glottal area waveforms (greyed out) as a point of reference.

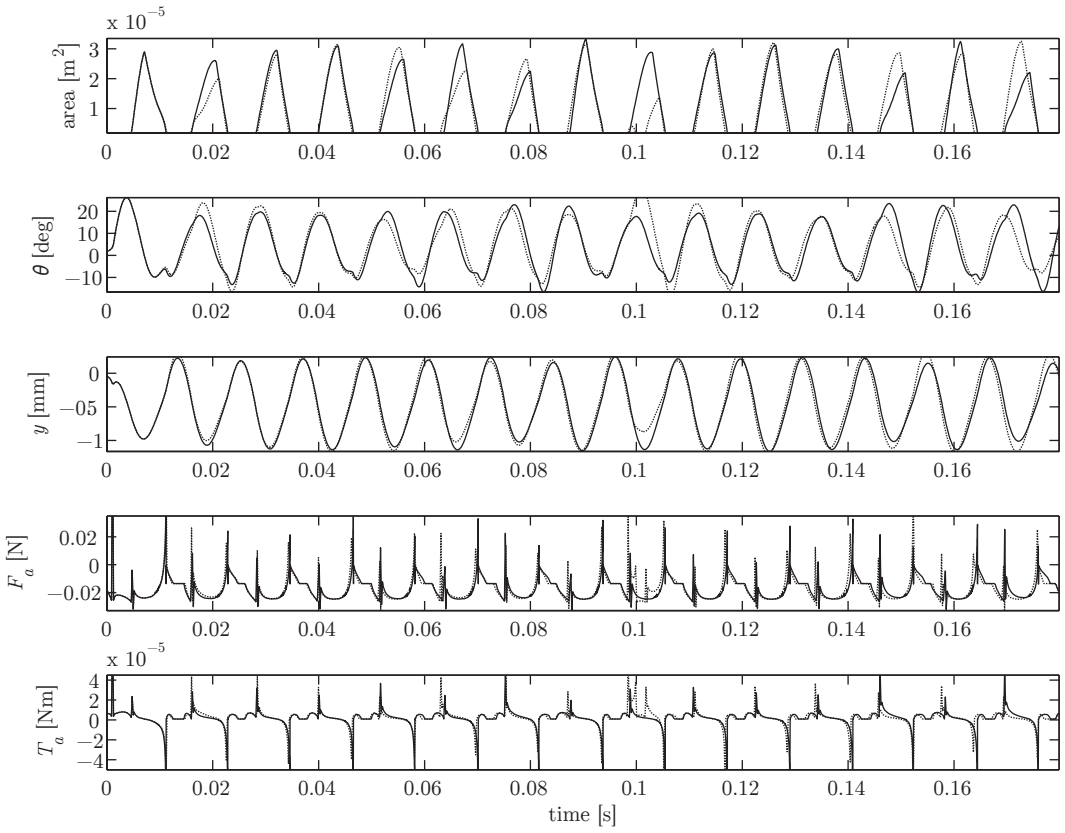

FIGURE 4.12: Time series with and without vortex advection plotted simultaneously. The solid trace corresponds to the case with advecting vortices, and the dotted trace corresponds to the baseline case.

The derivatives shown in Figure 4.13 are negative in the closing phase of the phonatory cycle, they have qualitatively identical structure. Quantitatively, their magnitudes are similar during the closing phase, in many cycles they are nearly identical, but in some cycles they differ by as much as 25% up or down. These plots show that the presence of the intraglottal vortices does not present a mechanism which systematically causes the vocal folds to close more rapidly in the closing phase of the phonatory cycle.

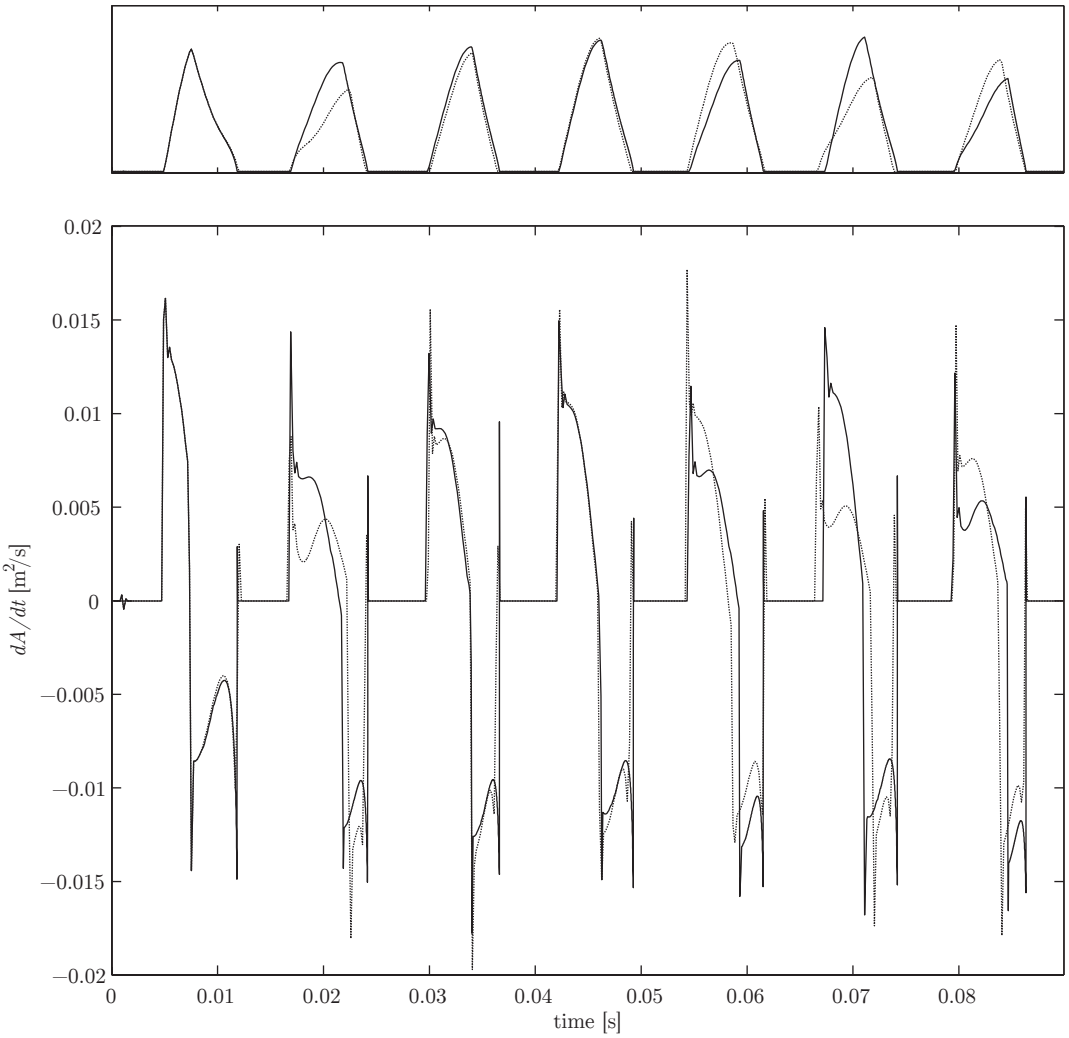

FIGURE 4.13: In the upper frame, the glottal area waveforms are shown to provide a reference for the instants shown in the plot of their derivatives exhibited in the lower plot. In both frames, the solid traces correspond to the 2-D GF model with vortex advection, and the dotted traces correspond to the baseline case, with no vortices.

4.3 Model Limitations

As shown in Section 4.1, the predicted glottal area waveforms generated by the models coincide with glottal waveforms which manifest physiologically. The agreement is strong and suggests that the models emulate the self-oscillatory behaviour of the vocal fold tissues driven by the glottal flow at constant lung pressure, that is, the models are physiologically representative in some meaningful sense. This is essential for the explanatory capacity of any extension of the model which attempts to capture the influence of intraglottal vortices. The purpose of this work is to answer a fundamental question: whether advecting vortices affect the glottal waveform and, thereby, contribute to the character of voiced speech. That there is a link between the features of the glottal waveform and the corresponding features of voiced speech was established by Fant amongst others and has already been discussed. Thus, in particular, this work addresses the specific question of whether the glottal waveform is influenced by intraglottal vortices; specifically, whether the presence of intraglottal vortices increase the speed at which the glottis closes in the closing phase of the phonatory cycle. The simulation results presented in Section 4.2 do not confirm the conclusion that intraglottal vortices consistently increase the speed at which the glottis closes. It may be concluded that the presence of intraglottal vortices do not contribute to this aspect of voiced speech.

The fundamental limitation of the glottal flow model developed in Chapter 3 is the manner in which the pressure forces due to intraglottal vortices are impressed upon the medial surfaces of the vocal folds and the mechanism by which the intraglottal vortices arrive at their positions during the closing phase of the phonatory cycle. In particular, the enforced trailing edge separation condition employed in order to transmit the influence of the vortices to the boundaries of the flow in a meaningful manner within the framework of the model is not entirely satisfactory; it is neither physically nor physiologically representative. In actual glottal flows, the glottal jet forms aftwards of some point of separation which occurs on the medial surface of the vocal folds in their divergent configuration during the closing phase of the phonatory cycle. The vortices are seen to roll up in the separation region between the glottal jet and the medial VF surface within the glottis. The vortices rapidly advect into the supraglottal region downstream of the glottal exit. The region of vortex formation was shown schematically in Figure 2 of Chapter 2.17 and repeated here in Figure 4.14. In contrast, the model developed merely captures the effect of an advecting singularity which perturbs the pressure field, it does so in a conservative manner compatible with the framework developed, but it does so ad hoc rather than in a way which captures the fluid physics with greater fidelity. Specifically, within the model, the intraglottal vortex does not form in a region downstream of a purported separation point as dictated by the flow in this region; rather, the vortex merely advects through the glottis from some initial upstream station. This was shown schematically in Figure 4.14 in contrast to the schematic of Figure 4.14, which is more physically representative. In the model, the vortex strengths and positions are not determined according to the mechanisms of fluid physics which govern the formation of vortices within the separation region, they

are determined in an ad hoc manner to ensure that the rate at which the vortices advect through the glottis is somewhat matched to the rate at which the glottis oscillates and therefore, proportional to the rate at which it closes. This is to ensure that the vortices appear within the glottis in its diverging configuration in the closing phase, and that the influence of the advecting singularities is impressed on the boundaries throughout a physically reasonable period of time in the closing phase of the phonatory cycle in which they enter the glottis.

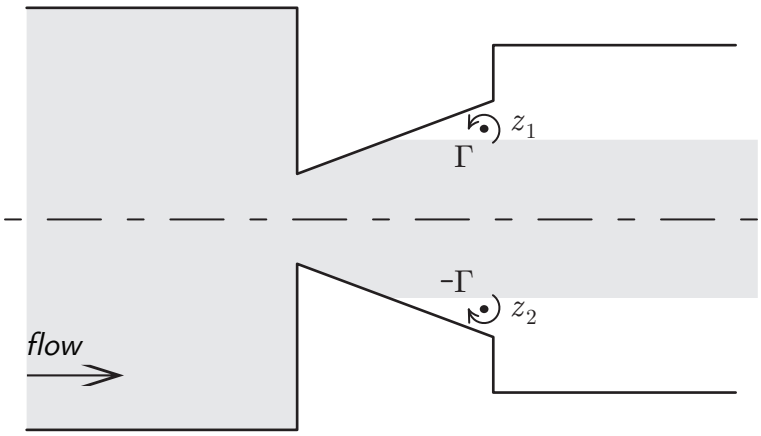

FIGURE 4.14: Schematic of intraglottal vortices near glottal exit in separation region.

Despite the foregoing discussion, it may be argued that the conclusions drawn herein are not invalidated by the shortcomings of the ad hoc representation. If the question is simply framed to ask whether an advecting singularity which perturbs the pressure field at the flow domain boundary in a conservative and, therefore, physically reasonable manner, then the conclusions are certainly not invalidated by the limitations of the model. In fact, the conclusions are compatible with other ad hoc studies, such as [37], mentioned in Section 2.2.4. Whereas it may be more satisfactory to have a model which exhibits the observed flow structure as an outcome of physical mechanisms which cause them rather than an ad hoc imposition of a representative condition, this is difficult within a potential flow framework, which does not account for viscous effects. The singularities are advected within the framework of the model, they perturb the pressure field, the contribution of the perturbation to the integrated pressure perturbs the dynamical vocal fold model, but in some cases, causes it to close more rapidly and in other cases, causes it to close more slowly. This conclusion remains firm within the modelling framework. Possible extension of the current model are discussed in Section 5.3 of the following chapter.

5 Conclusions, Recommendations, and Future Work

In this thesis, a two dimensional model of the glottal airflow is developed and computed as a two-dimensional inviscid incompressible potential flow. This extended glottal flow model has been coupled to an existing low-order bar-plate body-cover model of the vocal fold tissues which is well documented in the literature together with parameters which ensure that the model self-oscillates in a physiologically reasonable manner. Irrotational vortices placed at some upstream station are allowed to advect through the glottis at a rate which ensures that they will arrive near the superior region of the glottis during the closing phase of the phonatory cycle, when the glottis obtains its diverging configuration. This is to emulate the roll-up and shedding of intraglottal vortices which occurs in the closing phase of the phonatory cycle when the glottis has obtained its diverging configuration.

The two dimensional glottal flow model employs a Schwarz-Christoffel mapping technique in which the geometry of the physical plane is mapped to an auxiliary plane in which the pre-image geometry is an infinite horizontal strip. The appropriate Schwarz-Christoffel mapping is computed numerically. The fluid problem, including advecting vortices, is rapidly computed in the auxiliary plane via analytical expressions derived herein which determine the fluid behaviour, and the solution is easily mapped back to the physical plane to yield the velocity field. The pressure field is subsequently computed using the framework of complex analysis including an unsteady pressure term in the Bernoulli equation.

The extension of the glottal flow model to a two-dimensional version is important, not merely because it allows the model to capture the advection of point singularities within the flow domain, but the two-dimensional glottal flow model captures the salient physics of glottal flow with improved fidelity over the standard one-dimensional Bernoulli flow models employed in the past. Additionally, the pressure field, which is unsteady in glottal flow, is determined with the unsteady Bernoulli equation. The unsteady term significantly augments the pressure distribution, leading to greater inferior-superior asymmetry of the glottal pressure distribution than predicted by standard one-dimensional models.

Within the model, once the glottal flow field has been determined, the pressures on the medial surfaces of the vocal folds are integrated to obtain resultant forces which drive the

dynamical vocal fold model. The two-dimensional model captures significant variation of the velocity field near the glottal inlet and outlet, and these cause a significant variation near the inferior and superior margins of the medial vocal fold surfaces. Furthermore, because these entail longer moment arms, larger pitching moments are obtained. It has been shown that the mucosal wave, in the transverse motion of the vocal folds, as the covers pitch about their respective nodal points, a greater amplitude of motion is observed within the two-dimensional model. The resulting glottal area waveform obtains a more skewed appearance, and this causes it qualitatively to appear more like clinically obtained glottal waveforms than the standard one-dimensional models despite that the simulation model is uncoupled from the acoustical field of the upper vocal tract which would modify the wave shape.

5.1 Conclusions

The thrust of the development of the glottal flow model coupled to a low-order vocal fold model has been to address a specific question about the nature of the influence of the intraglottal vortices upon the dynamics of the vocal folds; specifically, whether they would increase the rate at which the vocal folds close in the closing phase of the phonatory cycle. The vortices have been found to rapidly advect into the supraglottal space whence they impart little upstream influence. The vortex strength determines two competing effects. On one hand, as the strength of the vortices increases, the magnitude of the pressure perturbation becomes more significant, however, for a given vortex spacing, the vortices will advect more rapidly into the supraglottal region, where their influence will rapidly diminish. In fact, it may be argued that because the modified pressure exists briefly, it does not impart sufficient impulse to overcome the inertia of the system. On the other hand, a reduction in vortex strength allows the intraglottal vortices to remain within the glottal space throughout a longer period of time. However, reduction of vortex strength reduces the influence of these vortices; consequently, the magnitude of the pressure perturbation is significantly diminished. Again, the modified pressure field does not impart sufficient impulse to overcome the inertia of the dynamical system, and the system is relatively unresponsive to this perturbation.

To recapitulate, in light of the outcome of the simulations presented in the previous chapter, it may be concluded that intraglottal vortices, although they influence the dynamics of the vocal folds, do not influence the dynamics of the vocal folds in a way which ensures that the vortices systematically affect the rate of closing of the vocal folds in the closing phase of the phonatory cycle. Although the pressure distribution on the medial surfaces of the vocal folds is perturbed by the presence of the advecting singularities, the effect is either short lived, weak, or both. Also, depending upon the precise instant at which the perturbation occurs in the phonatory cycle, the glottis may close slightly more rapidly, slightly more slowly, or close at exactly the same rate as it would have in the absence of an advecting vortex pair. Consequently, the shape of the glottal waveform is not significantly altered; specifically, the rate of closure of the glottis is not systematically

affected by this mechanism. Therefore, the intraglottal vortices do not have a significant impact on the intelligibility of voiced speech due to increased high frequency content from a vocal tract excited by a more rapidly closing glottis.

5.2 Recommendations

Low-order speech models, especially those incorporating either potential flow techniques for glottal flow or reduced DOF models for the VF tissue mechanics has significant drawbacks in terms of model fidelity, specifically in terms of the capacity of the model to capture significant effects due to viscosity. Nevertheless, much is gained in terms of the computational tractability of these models. The model and model framework developed herein are powerful and sufficiently flexible to incorporate various other extensions.

The modelling approach employing the Schwarz-Christoffel transform to relate a complex potential in an auxiliary region where it may be easily determined to a harmonic function in a flow domain of arbitrary polygonal boundary is sufficiently general to accommodate more complicated tissue models which capture higher order vibrational modes of the vocal fold tissues, i.e., multi-mass cases where different parts of the medial surface of the vocal fold translate with respect to each other non-rigidly.

With specific reference to the outcomes of the simulations performed in conjunction with this thesis and presented in Chapter 4, in subsequent low-order or simplified VF-GF models, if desired, one may forego the effort to capture the effect of intraglottal vortices in the modeling process. The presence of the intraglottal vortices negligibly perturbs glottal volumetric flow rate, open and closed quotients, and the evolution of minimal glottal area waveform in time. The presence of intraglottal vortices has little to no effect on the mechanism which sustains the oscillation of the vocal folds in phonation; rather, their presence merely modifies, to a slight extent, measurable flow quantities. The interaction of intraglottal vortices with more detailed models has not been determined herein. No conclusion may be drawn regarding the inclusion of vortical modelling in conjunction with higher order fluid solvers and more substantial vocal fold tissue models. Additionally, it is quite possible that marginal effects of intraglottal vortices may be better modelled or captured in a more accurate visco-elastic model of vocal-fold tissue and glottal flow which incorporates viscosity as well as three-dimensionality of the vocal fold tissue and glottal flow. The viscosity of the fluid is involved in the mechanism which generates vortical roll-up in the separated shear layer of the glottal jet, and the pressure field which is modulated by the downstream vocal tract structures. It is not known whether these effects may or may not be discarded with higher fidelity models.

5.3 Future Work

Whereas the model was designed with one specific question in mind, the model framework is powerful and flexible and lends itself to several possible extensions which would render the model more useful in subsequent low-order modelling efforts. Some extensions are suggested herein. Also, a coupling to the acoustical field has been entirely skirted in this thesis. The model may be extended to accommodate this extension as well because the free stream may be allowed to evolve in time, and this may approximate disturbances in the velocity field due to reflected acoustical waves and similar phenomena. Also, the epilaryngeal pressure, which would be perturbed by a coupling to the acoustical field, feeds into the separation model, it is the pressure applied over the superior portion of the vocal fold downstream of the point of separation. This modification would reduce the pitching moments in this phase of the phonatory cycle.

The question of biomedical application of this work has also been given marginal mention. Nevertheless, it is the capacity of lower-order models to capture the fully coupled aerodynamic, structural, and acoustical multi-physics of voiced speech in a computationally tractable manner which lends such frameworks to scientific investigations of voiced speech. There is much to be learned about pathological speech especially towards clinical applications in the diagnosis and treatment of speech disorders. In particular, it is desirable to be able to predict normal and pathological speech performance with the goal of supporting clinical and surgical decisions to mitigate or fully resolve medical issues affecting a patient's speech. Significant work remains to be done to relate model parameters to clinical data corresponding to individual subjects in order that the outcomes of simulations accurately characterize the subject's speech pathology [30].

5.3.1 Asymmetric GF-VF Interaction

The simulation model presented herein enforced various symmetries about the midsagittal plane, a symmetric glottal configuration, a symmetric vortex configuration, and a symmetric glottal jet. Many speech pathologies introduce asymmetry. For instance, asymmetric glottal geometry due to polyps or similarly vocal fold defects induce an asymmetrical flow which leads to an asymmetrical glottal jet, both of which ultimately lead to an unequal aerodynamic loading on the medial surfaces of the vocal folds. Other pathologies lead to asymmetrical tissue properties, such as partial vocal fold paralysis. Asymmetrical mechanical properties lead to asymmetrical response of the vocal fold tissues which, in turn, yield an asymmetrical geometry, and the same situation as outlined above prevails yielding similar aerodynamic outcomes. The simulation model presented herein may be relatively easily extended by relaxing the constraints which preserve symmetry together with computation of the VF dynamics of each fold separately. The geometry generation algorithm will need to be modified accordingly. As well, two sets of mechanical parameters and initial conditions must be specified. These modifications may be easily implemented, perhaps

after some of the other extensions discussed amongst the recommendations of this section have been validated with the symmetric model.

5.3.2 Contact Models & Higher-Order VF Tissue Models

Vocal fold contact remains poorly understood [30]. In the present work, a contact model which consisted of a hydrostatic pressure of magnitude determined by the average transglottal pressure was employed. There have been numerous criticisms of such a model. The model is employed in the simulations merely due to its simplicity. Furthermore, the contact mechanics were not the focus of the investigation, rather the effect of the intraglottal vortices on the glottal dynamics were. What is essential for the model is that there is a contact force, otherwise the asymmetry of the subglottal pressure applied over the area of the vocal folds below the closure would impart an unmitigated pitching moment to the plate which would cause the glottis to open rapidly.

The extent to which the use of a constant pressure contact model leads to inaccuracy was not investigated. The use of more accurate, and therefore complicated, contact models was not investigated. In the search to identify more general and accurate contact models which would more accurately capture VF motion throughout contact., others have proposed VF contact models such as simple elastic hard-wall contact models and linear or non-linear spring based contact force models.

It may be speculated that the increasingly complicated contact models employed in conjunction with low-order VF tissue models may not yield additional benefit commensurate to the increased computational burden imposed. Nevertheless, in the absence of computational studies, these questions are merely speculative. The computational framework provided allows the simple extension of the model to incorporate a variable contact stress and a simple determination of the area over which it is applied. It is recommended that simulations be performed with several increasingly complicated but simple non-constant non-uniform contact models in order to characterize the impact upon model accuracy and simulation runtime. The purpose of pursuing such a study is the possibility that a justifiable balance may be stricken between the complexity of the contact model, in terms of implementation and runtime, and the quality of simulation outcomes.

The marginal gains in fidelity of models of the vocal source with increasing DOFs of the VF tissue has been demonstrated for models which capture self-oscillatory effects. However, the increasing tissue model fidelity has not been quantified in the presence of intraglottal vortices. The interaction of glottal shape with advecting vortices was examined merely in the case of a flat medial VF surface. For a VF tissue model which captures greater freedom of motion along the length of the vocal fold, perhaps, however unlikely, the simulation outcomes would demonstrate more significant variation due to the presence of intraglottal vortices than the present model suggests.

5.3.3 Boundary Integral Methods

The flow problem was approximated at each timestep with the assumption that the relative velocity vector of the fluid at the boundary remains normal to the moving wall. The wall-normal relative velocity condition may be restored to solve the Laplace equation with a wall-oblique velocity condition at each timestep. However, this strengthening requires boundary integral techniques in which the solution at any point within the flow domain is expressed as a contour integral in the complex plane around the boundary of the domain. This approach would similarly yield analytic expressions for the solution of the flow problem, and would additionally enable methods to incorporate a facility to include sophisticated wake models which would be implemented by integrating around the wake. These integrals may be numerically evaluated, especially by employing SC techniques in which the integrals are evaluated in an auxiliary domain and related back to the physical domain as was done in the present approach.

The difficulty of employing wake models is that they are phenomenological, but their description is based on ad hoc assumptions about pressure distributions which are not known a priori. A parametric study would need to be performed to obtain a wake structure which exhibits the same structure as the glottal jet which is observed at the glottal exit in real flows.

5.3.4 The Vortex Advection Scheme

The limitations discussed in Section 4.3 of the previous chapter suggested that the fundamental limitation of the vortex advection model with trailing edge separation is neither physically nor physiologically representative. The approach to introduce vortices into the model is more ad hoc than it is physical; the vortices are merely advected through the intraglottal space from an upstream starting position to ensure that they arrive at the diverging glottis at the appropriate moment. This is in contrast to a model in which the vortex roll-up would be a consequence of physical mechanisms which a model captures. Despite much work, practical characterization of vortices in terms of shedding frequency of vortices, whether periodic or not, or their strengths have not been determined in realistic conditions [65]. The simulation model presented herein may be extended to obtain physically reasonable vortex strengths which correlate to physically reasonable, i.e. observed, rates of vortex advection. This would allow the shortcomings of the model to be somewhat overcome by allowing the vortex to begin at some point near the medial VF surface downstream of a predicted separation point. The strength may be determined by a conservation principle. This is a non-trivial extension and it is not entirely clear how this would be implemented or how the ultimate vortex strength would be determined. If the vortex strength itself is not subject to ad hoc assumptions, the conclusions drawn from such a model would be perceived to be stronger. However, it remains unclear whether such an extension would yield significant evidence against the conclusions drawn in this thesis, that the intraglottal vortices do not systematically influence the rate of glottal closure in the closing phase of the phonatory cycle.

REFERENCES

[1] F. Alipour and R. C. Scherer. Pulsatile airflow during phonation: An excised larynx model. *J. Acoust. Soc. Am.*, 97(2):1241–1248, February 1995.

[2] F. Alipour and R. C. Scherer. Flow separation in a computational oscillating vocal fold model. *J. Acoust. Soc. Am.*, 116(3):1710–1719, 2004.

[3] P. Alku, T. Bäckström, and E. Vilkman. Normalized amplitude quotient for parametrization of the glottal flow. *J. Acoust. Soc. Am.*, 112(2):511–529, August 2002.

[4] J. J. Allen and A. J. Smits. Energy Harvesting Eel. *Journal of Fluids and Structures*, 15:629–640, 2001.

[5] T. Andreescu and D. Andrica. *Complex Numbers from A to...Z, 1 ed.* Birkhauser, New York, NY, 2005.

[6] R. J. Bakken and R. F. Orlikoff. *Clinical Measurement of Speech and Voice, 2nd ed.* Singular Publishing Group, San Diego, CA, 2000.

[7] A. Barney, C. H. Shadle, and P. O. A. L. Davies. Fluid flow in a dynamic mechanical model of the vocal folds and tract. i. measurements and theory. *J. Acoust. Soc. Am.*, 105(1):444–455, 1999.

[8] G. K. Batchelor. *An Introduction to Fluid Dynamics.* Cambridge University Press, Cambridge, UK, 2002.

[9] Y. Bazilevs, M.-C. Hsu, I. Akkerman, S. Wright, K. Takizawa, B. Henicke, T. Spielman, and T. E. Tezduyar. 3D simulation of wind turbine rotors at full scale. Part I: Geometry modeling and aerodynamics. *Int. J. Numer. Meth. Fluids*, 65:207–235, 2011.

[10] Y. Bazilevs, M.-C. Hsu, J. Kiendl, R. Wüchner, and K.-U. Bletzinger. 3D simulation of wind turbine rotors at full scale. Part II: Fluid-structure interaction modeling with composite blades. *Int. J. Numer. Meth. Fluids*, 65:236–253, 2011.

[11] Y. Bazilevs, K. Takizawa, and T. E. Tezduyar. *Computational Fluid-Structure Interaction : Methods and Applications*. Wiley Series in Computational Mechanics. John Wiley & Sons, Ltd., UK, 2013.

[12] G. S. Berke and B. R. Gerratt. Laryngeal biomechanics: An overview of mucosal wave mechanics. *Journal of Voice*, 7(2):123–128, 1993.

[13] P. Birkholz and B. J. Kröger. A survey of self-oscillating lumped-element models of the vocal folds. *Studientexte zur Sprachkommunikation: Elektronische Sprachsignalverarbeitung*, pages 184–194, 2011.

[14] J. W. Brown and R. V. Churchill. *Complex Variables and Applications*. Churchill-Brown Series. McGraw-Hill, New York, NY, 1995.

[15] D. D. Cook, E. Nauman, and L. Mongeau. Ranking vocal fold model parameters by their influence on modal frequencies. *J. Acoust. Soc. Am.*, 126(4):2002–2010, 2009.

[16] R. Courant and F. John. *Introduction to Calculus and Analysis 1*. Classics in Mathematics. Springer-Verlag, Berlin, 1999.

[17] K. E. Cummings and M. A. Clements. Glottal models for digital speech processing: A historical survey and new results. *Digital signal processing*, 5(1):21–42, 1995.

[18] M. P. de Vries, H. K. Schutte, A. E. P. Veldman, and G. J. Verkerke. Glottal flow through a two-mass model: Comparison of Navier-Stokes solutions with simplified models. *J. Acoust. Soc. Am.*, 111(4):1847–1853, 2002.

[19] M. P. de Vries, H. K. Schutte, and G. J. Verkerke. Determination of parameters for lumped parameter models of the vocal folds using a finite-element method approach. *J. Acoust. Soc. Am.*, 106(6):3620–3628, December 1999.

[20] D. R. Dickson and W. Maue-Dickson. *Anatomical and physiological bases of speech*. PRO-ED, Austin, Texas, 1982.

[21] E. H. Dowell. Panel flutter - A review of the aeroelastic stability of plates and shells. *AIAA Journal*, 8(3):385–399, 1970.

[22] E. H. Dowell and K. C. Hall. Modeling of Fluid-Structure Interaction. *Annu. Rev. Fluid Mech.*, 33:445–490, January 2001.

[23] T. A. Driscoll. *Schwarz-Christoffel Toolbox User's Guide*.

[24] T. A. Driscoll and L. N. Trefethen. *Schwarz-Christoffel Mapping*. Cambridge Monographs on Applied and Computational Mathematics. Cambridge University Press, Cambridge, UK, 2002.

[25] B. D. Erath and M. W. Plesniak. An investigation of jet trajectory in flow through scaled vocal fold models with asymmetric glottal passages. *Experiments in fluids*, 41(5):735–748, 2006.

[26] B. D. Erath and M. W. Plesniak. Three-dimensional laryngeal flow fields induced by a model vocal fold polyp. *Int. J. Heat Fluid Flow*, 35:93–101, June 2012.

[27] B. D. Erath and M.W. Plesniak. The occurrence of the coanda effect in pulsatile flow through static models of the human vocal folds. *J. Acoust. Soc. Am.*, 120(1):1000–1011, 2006.

[28] B. D. Erath and M.W. Plesniak. Viscous flow features in scaled-up physical models of normal and pathological phonation. *Int. J. Heat Fluid Flow*, 31:468–481, 2010.

[29] B. D. Erath and M.W. Plesniak. Impact of wall rotation on supraglottal jet instability in voiced speech. *J. Acoust. Soc. Am.*, 129(3):EL64–EL70, March 2011.

[30] B. D. Erath, M. Zañartu, K. C. Stewart, M. W. Plesniak, D. E. Sommer, and S. D. Peterson. A review of lumped-element numerical models of voiced speech. *Speech Communication*, 55(5):667–690, June 2013.

[31] F. H. Martini et al. *Human Anatomy, 3rd ed.* Prentice Hall, Inc., Upper Saddle River, New Jersey, 2000.

[32] S. Standring et al., editor. *Gray's Anatomy, 40th ed.* Elsevier Limited, United Kingdom, 2008.

[33] U. Eysholdt, F. Rosanowski, and U. Hoppe. Vocal fold vibration irregularities caused by different types of laryngeal asymmetry. *European Archives of Oto-rhino-laryngology*, 260(8):412–417, 2003.

[34] G. Fant. *Acoustic theory of speech production, with calculations based on X-ray studies of Russian articulations.* Mouton, The Hague, 1960.

[35] G. Fant. Introduction. *Phonetica*, 34(4):249–251, 1977.

[36] G. Fant. Some problems in voice source analysis. *Speech Communication*, 13:7–22, 1993.

[37] M. H. Farahani and Z. Zhang. A computational study of the effect of intraglottal vortex-induced negative pressure on vocal fold vibration. *J. Acoust. Soc. Am.*, 136(5):EL369–EL375, November 2014.

[38] H. Fletcher and R. H. Galt. The Perception of Speech and Its Relation to Telephony. *J. Acoust. Soc. Am.*, 22(2):89–151, 1950.

[39] Y. C. Fung. *Biomechanics: Mechanical Properties of Living Tissues.* Biomechanics. Springer, New York, NY, 1993.

[40] R. E. Greene and S. G. Krantz. *Function Theory of One Complex Variable, 3rd ed.* Graduate Studies in Mathematics. American Mathematical Society, Providence, RI, 2006.

[41] M. Hirano. Morphological structure of the vocal cord as a vibrator and its variations. *Folia Phoniatr.*, 26:89–94, 1974.

[42] M. Hirano. Phonosurgery - basic and clinical investigations. *Otologia*, 21:239–240, 1975.

[43] T. J. Hixon. *Respiratory function in speech and song.* College-Hill Press, 1987.

[44] G. C. J. Hofmans, G. Groot, M. Ranucci, G. Graziani, and A. Hirschberg. Unsteady flow through in-vitro models of the glottis. *J. Acoust. Soc. Am.*, 113(3):1658–1675, 2003.

[45] E. B. Holmberg, P. Doyle, J. S. Perkell, B. Hammarberg, and R. E. Hillman. Aerodynamic and acoustic voice measurements of patients with vocal nodules: variation in baseline and changes across voice therapy. *Journal of Voice*, 17(3):269–282, 2003.

[46] E. B. Holmberg, R. E. Hillman, and J. S. Perkell. Glottal airflow and transglottal air pressure measurements for male and female speakers in soft, normal, and loud voice. *J. Acoust. Soc. Am.*, 84(2):511–529, August 1988.

[47] J. Hron and M. Mádlík. Fluid-structure interaction with applications in biomechanics. *Nonlinear Analysis: Real World Applications*, 8:1431–1458, 2007.

[48] K. Ishizaka and J. L. Flanagan. Synthesis of Voiced Sounds From a Two-Mass Model of the Vocal Cords. *The Bell System Technical Journal*, 51(6):1233–1268, July-August 1972.

[49] J. H. Comroe Jr. *Physiology of Respiration: An Introductory Text, 2nd ed.* Year Book Medical Publishers, Inc., Chicago, IL, 1974.

[50] J. Katz and A. Plotkin. *Low-Speed Aerodynamics, 2nd ed.* Cambridge University Press, Cambridge, UK, 2001.

[51] S. M. Khosla, S. Murugappan, and E. J. Gutmark. What can vortices tell us about vocal fold vibration and voice production. *Current opinion in otoraryngologly and head and neck surgery*, 16(3):183–187, July 2008.

[52] S. M. Khosla, S. Murugappan, R. Paniello, J. Ying, and E. J. Gutmark. Role of vortices in voice production: Normal versus asymmetric tension. *The Laryngoscope*, 119(1):216–221, January 2009.

[53] S. M. Khosla, S. Muruguppan, E. J. Gutmark, and R. Scherer. Vortical flow field during phonation in an excised canine larynx model. *The Annals of otology, rhinology, and laryngology*, 116(3):217–228, April 2007.

[54] S. M. Khosla, S. Muruguppan, R. Lakhamraju, and E. J. Gutmark. Using particle imaging velocimetry to measure anterior-posterior velocity gradients in the excised canine larynx model. *The Annals of otology, rhinology, and laryngology*, 117(2):134–144, March 2008.

[55] P. Ladefoged and K. Johnson. *A Course in Phonetics, 6th ed.* Wadsworth, Cengage Learning, Boston, MA, 2011.

[56] H. Lamb. *Hydrodynamics, 6th ed.* Dover Publications, Inc., New York, NY, 1945.

[57] S. Lang. *Complex Analysis, 4 ed.* Graduate Texts in Mathematics (Book 103). Springer, New York, NY, 2003.

[58] J. Liljencrants. Numerical simulations of glottal flow. *STL-QPSR*, 30(1):069–074, 1989.

[59] J. Liljencrants. A translating and rotating mass model of the vocal folds. *STL-QPSR*, 32(1):001–018, 1991.

[60] MATLAB. *version 8.3.0.532 (R2014a).* The MathWorks Inc., Natick, Massachusetts, 2014.

[61] P. Mergell, H. Herzel, and I. R. Titze. Irregular vocal-fold vibration—high-speed observation and modeling. *J. Acoust. Soc. Am.*, 108(6):2996–3002, 2000.

[62] M. Mihaescu, S. M. Khosla, S. Murugappan, and E. J. Gutmark. Unsteady laryngeal airflow simulations of the intra-glottal vortical structures. *J. Acoust. Soc. Am.*, 127(1):435–444, January 2010.

[63] S. Miller. Voice therapy for vocal fold paralysis. *Otolaryngologic Clinics of North America*, 37(1):105–119, 2004.

[64] L. M. Milne-Thomson. *Theoretical Hydrodynamics.* Dover Publications, Inc., New York, NY, 1968.

[65] R. Mittal, B. D. Erath, and M. W. Plesniak. Fluid Dynamics of Human Phonation and Speech. *Annu. Rev. Fluid Mech.*, 45:437–467, 2013.

[66] J. Müller. *The physiology of the senses, voice and muscular motion, with mental facilities.* Taylor, Walton, and Maberly, London, UK, 1848.

[67] C. E. Mungan. The Bernoulli equation in a moving reference frame. *European Journal of Physics*, 32(2):517–520, 2011.

[68] S. Murugappan, S. M. Khosla, K. Casper, L. Oren, and E. J. Gutmark. Flow fields and acoustics in a unilateral scarred vocal fold model. *The Annals of Otology, Rhinology, and Laryngology*, 118(1):44–50, Feb. 2009.

[69] T. Needham. *Visual Complex Analysis.* Oxford University Press, Oxford, UK, 1997.

[70] J. Neubauer, Z. Zhang, R. Miraghaie, and D. A. Berry. Coherent structures of the near field flow in a self-oscillating physical model of the vocal folds. *J. Acoust. Soc. Am.*, 121(2):1102–1118, 2007.

[71] L. Oren, S. M. Khosla, and E. J. Gutmark. The formation of flow separation vortices inside the glottis during vocal fold closing. *J. Acoust. Soc. Am.*, 130:2441, 2011.

[72] L. Oren, S. M. Khosla, and E. J. Gutmark. Intraglottal geometry and velocity measurements in canine larynges. *J. Acoust. Soc. Am.*, 135(1):380–388, 2014.

[73] L. Oren, S. M. Khosla, and E. J. Gutmark. Intraglottal pressure distribution computed from empirical velocity data in canine larynx. *Journal of Biomechanics*, 47:1287–1293, 2014.

[74] D. O'Shaughnessy. *Speech Communication : Human and Machine*. Addison-Wesley series in electrical engineering. Addison-Wesley Publishing Company, Reading, MA, 1987.

[75] X. Pelorson, A. Hirschberg, R. R. van Hassel, A. P. J. Wijnands, and Y. Auregan. Theoretical and experimental study of quasisteady-flow separation within the glottis during phonation. Application to a modified two-mass model. *J. Acoust. Soc. Am.*, 96(6):3416–3431, December 1994.

[76] C. W. Peterson, J. H. Strickland, and H. Higuchi. The Fluid Dynamics of Parachute Inflation. *Annu. Rev. Fluid Mech.*, 28:361–387, January 1996.

[77] S. D. Peterson and M. Porfiri. Impact of a vortex dipole with a semi-infinite rigid plate. *Phys. Fluids*, 25(9), 2013.

[78] M. D. Plumpe, T. F. Quatieri, and D. A. Reynolds. Modeling of the Glottal Flow Derivative Waveform with Application to Speaker Identification. *Speech and Audio Processing, IEEE Transactions on*, 7(5):569–586, 1999.

[79] W. Rudin. *Pinciples of Mathematical Analysis 3 edition*. International Series in Pure and Applied Mathematics. McGraw-Hill, New York, NY, 1976.

[80] W. Rudin. *Real and Complex Analysis*. International Series in Pure and Applied Mathematics. McGraw-Hill, New York, NY, 1986.

[81] S. J. Rupitsch, J. Ilg, A. Sutor, R. Lerch, and M. J. Döllinger. Simulation based estimation of dynamic mechanical properties for viscoelastic materials used for vocal fold models. *Journal of Sound and Vibration*, 330(18):4447–4459, 2011.

[82] N. Ruty, X. Pelorson, A. van Hirtum, I. Lopez-Arteaga, and A. Hirschberg. An in vitro setup to test the relevance and the accuracy of low-order vocal folds models. *J. Acoust. Soc. Am.*, 121(1):479–490, 2007.

[83] M. R. Schroeder. A brief history of synthetic speech. *Speech Communication*, 13(1-2):231–237, October 1993.

[84] J. A. Seikel, D. W. King, and D. G. Drumright. *Anatomy & Physiology for Speech, Language, and Hearing, 4th ed.* Delmar, Cengage Learning, Clifton Park, NY, 2010.

[85] M. J. Shelley and J. Zhang. Flapping and Bending Bodies Interacting with Fluid Flows. *Annu. Rev. Fluid Mech.*, 49:449–465, January 2011.

[86] S. G. Llewellyn Smith. How do singularities move in potential flow? *Physica D*, 240:1644–1651, 2011.

[87] I. J. Sobey. The occurrence of separation in oscillatory flow. *Journal of Fluid Mechanics*, 134:247–257, 1983.

[88] M. Södersten, S. Hertegård, and B. Hammarberg. Glottal closure, transglottal airflow, and voice quality in healthy middle-aged women. *Journal of Voice*, 9(2):182–197, 1995.

[89] J. C. Stemple, L. E. Glaze, and B. K. Gerdeman. *Clinical voice pathology: Theory and management*. Cengage Learning, 2000.

[90] K. N. Stevens. Airflow and Turbulence Noise for Fricative and Stop Consonants: Static Considerations. *J. Acoust. Soc. Am.*, 50(4):1180–1192, 1971.

[91] K. N. Stevens. Physics of Laryngeal Behavior and Larynx Modes. *Phonetica*, 34(4):264–279, 1977.

[92] K. N. Stevens. *Acoustic Phonetics, 2nd ed.* The MIT Press, Cambridge, MA, 1998.

[93] B. H. Story. An overview of the physiology, physics and modeling of the sound source for vowels. *Acoustical Science and Technology*, 23(4):195–206, 2002.

[94] J. Švec and J. Pešák. Vocal breaks from the modal to falsetto register. *Folia phoniatrica et logopaedica*, 46(2):97–103, 1994.

[95] R. Tirncke, H. von Leden, and P. Moore. Laryngeal Vibrations: Measurements of the Glottic Wave. Part I. the normal vibratory cycle. *Arch Otolaryngol*, 68:1–9, 1958.

[96] I. R. Titze. Parameterization of the glottal area, glottal flow, and vocal fold contact area. *J. Acoust. Soc. Am.*, 75(2):570–580, February 1984.

[97] I. R. Titze. The physics of small-amplitude oscillation of the vocal folds. *J. Acoust. Soc. Am.*, 83(4):1536–1552, April 1988.

[98] I. R. Titze. *Principles of Voice Production.* Prentice Hall, Inc., Englewood Cliffs, New Jersey, 1994.

[99] I. R. Titze. Regulating glottal airflow in phonation: Application of the maximum power transfer theorem to a low dimensional phonation model. *J. Acoust. Soc. Am.*, 111(1):367–376, January 2002.

[100] I. R. Titze and B. H. Story. Rules for controlling low-dimensional vocal fold models with muscle activation. *J. Acoust. Soc. Am.*, 112(3):1064–1076, 2002.

[101] I. T. Tokuda, M. Zemke, M. Kob, and H. Herzel. Biomechanical modeling of register transitions and the role of vocal tract resonators. *J. Acoust. Soc. Am.*, 127(3):1528–1536, 2010.

[102] Jw. van den Berg. Myoelastic-aerodynamic theory of voice production. *Journal of Speech, Language, and Hearing Research*, 1(1-2):227–244, September 1958.

[103] Jw. van den Berg and T. S. Tan. Results of Experiments with Human Larynxes. *Pract. Otorhinolaryngol*, 21:425–450, 1959.

[104] Jw. van den Berg, J. T. Zantema, and P. Doornenbal Jr. On the Air Resistance and the Bernoulli Effect of the Human Larynx. *J. Acoust. Soc. Am.*, 29(5):626–631, May 1957.

[105] A. Yang, D. A. Berry, M. Kaltenbacher, and M. Döllinger. Three-dimensional biomechanical properties of human vocal folds: Parameter optimization of a numerical model to match in vitro dynamics. *J. Acoust. Soc. Am.*, 131(2):1378–1390, 2012.

[106] M. Zañartu, L. Mongeau, and G. R. Wodicka. Influence of acoustic loading on an effective single mass model of the vocal folds. *J. Acoust. Soc. Am.*, 121(2):1119–1129, 2007.

[107] C. Zhang, W. Zhao, S. H. Frankel, and L. Mongeau. Computational aeroacoustics of phonation, Part I: Computational methods and sound generation mechanisms. *J. Acoust. Soc. Am.*, 112(5):2134–2146, November 2002.

[108] C. Zhang, W. Zhao, S. H. Frankel, and L. Mongeau. Computational aeroacoustics of phonation, Part II: Effects of flow parameters and ventricular folds. *J. Acoust. Soc. Am.*, 112(5):2147–2154, November 2002.

[109] W. Zhao, S. H. Frankel, and L. Mongeau. Numerical Simulations of Sound from Confined Pulsating Axisymmetric Jets. *AIAA Journal*, 39(10):1868–1874, October 2001.

[110] X. Zheng, R. Mittal, and S. Bielamowicz. A computational study of asymmetric glottal jet deflection during phonation. *J. Acoust. Soc. Am.*, 129(4):2133–2143, April 2011.

APPENDIX

A | Complex Analysis, a Primer

The inclusion of this appendix is to gather important background in complex analysis which is essential for the developments in the body of the thesis. It is intended to bring the reader who is uninitiated in the geometry and analysis of complex numbers to a point that either he or she would fruitfully be able to explore the development of analytical potential flow models pursued in Chapter 3 and the derivations in Appendix B. The idea is that this thesis be somewhat self-contained, and, furthermore, it is the intention of the inclusion of this appendix that the reader be motivated and the essential ideas be presented inform the reader who is interested to continue the work begun in this thesis. It is this humble author's belief that the conspicuous absence of this material from many engineering curricula is unfortunate because complex analysis furnishes a language in which many two-dimensional problems of mechanical engineering may be succinctly expressed and, in many cases, rapidly solved. The analytical solutions of problems, when attainable, provide unique physical insight and unity which may otherwise be obfuscated by purely numerical solutions. The development is intended to be clear and aligned with the treatments of complex analysis textbooks in current circulation. The scope is almost identical to that presented as background in Milne-Thomson, [64], but, it is hoped, with greater emphasis on geometric insight, and consistent with the notation employed throughout this document.

This appendix proceeds from a brief development of the algebraic field of complex numbers, a discussion of modulus and argument, the relation to the polar form and the complex exponential, and the geometry of complex numbers in the plane together with a geometric interpretations. Several sections dealing with analysis follow. The sole requisite of the reader is an acquaintance with the analysis of functions $f : \mathbb{R}^n \to \mathbb{R}^m$, in particular, mappings of the plane (i.e., mappings f with $m = n = 2$). The development of derivatives, integrals, mappings, and series, with brief digression on point-set topology in the plane, is realized in this familiar framework. The concepts of differentiability in the real sense is related to complex differentiability of complex functions of a complex variable and the ideas of holomorphy and analyticity. A discussion of harmonic functions and conformal mapping is included as important background. A final section on integration of complex functions of a complex variable follows together with a relation between contour integrals in the real plane and the integral of complex functions of a complex variable.

The contents of this appendix are not original, save possibly the exposition itself. Moreover, the reader is encouraged to explore the following wonderful primary references from

which this author has learned much. Complex numbers and their geometry without discussion of analysis or topology is the focus of the book of problems *Complex Numbers from A to ... Z*, [5]. A geometrically motivated treatment, which inter-weaves topological and analytical topics including the geometry of analytic functions, is *Visual Complex Analysis*, [69]. *Complex Variables and Applications* by Churchill and Brown [14] builds intuition about mappings and extensively discusses physical applications despite that the authors don't preserve the distinction between holomorphy, differentiability, and analyticity. An advanced and complete treatment of point set topology is contained in Rudin's *Principles of Mathematical Analysis*, [79]. More advanced and encyclopædic treatments of complex analysis are provided by Lang in [57], which takes the primacy of series as a unifying perspective, the volume by Greene and Krantz, [40], which emphasizes the geometric aspect, and Rudin, [80], which provides exquisite detail in its development of real and complex analysis perhaps far beyond the scope necessary for engineering treatment, emphasises the analytic aspect in the framework of advanced analysis. These advanced treatments also include extensive discussion of infinite product expansions.

A.1 Complex Numbers and Their Geometry

A.1.1 The Algebraic Field $\mathbb{C}$ and Rectangular Form

The algebraic field of complex numbers is a set of objects $\mathbb{C}$ called complex numbers together with two binary operations, addition and multiplication, satisfying the field axioms; i.e. the operations are closed in $\mathbb{C}$, they are associative and commutative, multiplication distributes over addition, both operations have unique identity elements in $\mathbb{C}$, every complex number has a unique additive inverse, and every complex number different from the additive identity has a unique multiplicative inverse. More concretely, elements of $\mathbb{C}$ are ordered pairs of real numbers (x, y). In fact, that complex numbers are generated by combining simpler parts is the reason for the identifier *complex*. Addition is defined componentwise as in the familiar addition of vectors in the plane $\mathbb{R}^2$. So we have, for complex numbers $z = (z_1, z_2)$ and $w = (w_1, w_2)$,

$$z + w = (z_1, z_2) + (w_1, w_2) = (z_1 + w_1, z_2 + w_2)\,,$$

but multiplication is defined according to

$$zw = (z_1, z_2)\,(w_1, w_2) = (z_1 w_1 - z_2 w_2, z_1 w_2 + z_2 w_1)\,.$$

We make the following observations

$$(0,0) + (z_1, z_2) = (0 + z_1, 0 + z_2) = (z_1, z_2) = (z_1 + 0, z_2 + 0) = (z_1, z_2) + (0,0) \text{ and}$$
$$(1,0)(z_1, z_2) = (1z_1 - 0z_2, 1z_2 + 0z_1) = (z_1, z_2) = (z_1 1 - z_2 0, z_1 0 + z_2 1) = (z_1, z_2)(1,0)$$

and, also,

$$(z_1, z_2) + (-z_1, -z_2) = (z_1 + (-z_1), z_2 + (-z_2)) = (0, 0)$$
$$= ((-z_1) + z_1, (-z_2) + z_2) = (-z_1, -z_2) + (z_1, z_2)$$

so that it is immediately apparent that the additive and multiplicative identities are $(0, 0)$ and $(1, 0)$, respectively, and to each element (z_1, z_2) corresponds the additive inverse $(-z_1, -z_2)$. The multiplicative inverse is more interesting and will be found subsequently. Firstly, when we think about $\mathbb{R}^2$, the standard basis, written as row vectors, comprises $(1, 0)$ and $(0, 1)$. We have found that, in the field of complex numbers, the former is the multiplicative identity, but what role does the latter play? Consider the following decomposition

$$(z_1, 0)(1, 0) + (z_2, 0)(0, 1) = (z_1 \cdot 1 - 0 \cdot 0, z_1 \cdot 0 + 0 \cdot 1) + (z_2 \cdot 0 - 0 \cdot 1, z_2 \cdot 1 + 0 \cdot 0)$$
$$= (z_1, 0) + (0, z_2) = (z_1, z_2).$$

Furthermore, that for any product of the form $(\alpha, 0)(z_1, z_2)$ for $\alpha \in \mathbb{R}$, we have $(\alpha z_1, \alpha z_2)$ allows the above decomposition to be written more compactly in the form of a linear combination of vectors in $\mathbb{R}^2$ with real scalars z_1 and z_2,

$$z_1(1, 0) + z_2(0, 1) = (z_1, 0) + (0, z_2) = (z_1, z_2).$$

To introduce some additional notation, because $(1, 0)$ is the multiplicative identity, it is naturally denoted by 1, and we have $1z = z1 = z$ for any $z \in \mathbb{C}$. Also, if $(0, 1)$ is denoted i, from the above decomposition, we may write any complex number (z_1, z_2) as $z_1 + iz_2$. This is called the rectangular form of the complex number (z_1, z_2), the complex number i is called the imaginary number, z_1 is called the real part of (z_1, z_2), and z_2 is called the imaginary part of (z_1, z_2). Additionally, because $(0, 0)$ is the additive identity, it is naturally denoted by 0, and we have $0 + z = z + 0 = z$. Furthermore, with the rectangular form, addition and multiplication follow the approach taken in polynomial addition and multiplication with i playing the role of x with the additional possibility of reinterpreting x^2 as -1, e.g., $(a + bx) + (c + dx) = (a + c) + x(b + d)$ and $(a + bx)(c + dx) = ac + bdx^2 + x(ad + bc)$ and, with x taken as i, these become

$$(a + ib) + (c + id) = (a + c) + i(b + d) \text{ and}$$
$$(a + ib)(c + id) = ac - bd + i(ad + bc).$$

These are precisely the forms expected when the definitions of addition and multiplication are cast in rectangular form.

It is also worth stating that (z_1, z_2) is often called the geometric image of the complex number $z_1 + iz_2$ because it is a point in the plane corresponding to the complex number; this is the source of the interpretation of constructs of planar geometry in terms of complex numbers and vice versa. Because the rectangular form is easier to manipulate, it, rather than the vectorial form, is used persistently. This is unless one wishes to emphasize or to

draw attention to the geometry, as is often desirable. We develop this idea further in the subsection on geometry to which this is building.

Complex numbers admit an interesting operation which effectively reverses the sign of the imaginary part. The conjugate, $\bar{z}$, of a complex number, $z = a + ib$, is defined to be $a - ib$, so

$$\overline{a + ib} = a - ib.$$

We also have an operation which measures complex numbers in some sense (but nevertheless does not yield a total ordering of $\mathbb{C}$) and, as we will see, has an obvious geometric interpretation. The modulus, $|z|$, of a complex number, $z = a+ib$, is defined to be $\sqrt{a^2 + b^2}$, so

$$|a + ib| = \sqrt{a^2 + b^2}.$$

We make the following observation for a complex number $z = a + ib$,

$$z\bar{z} = (a + ib)\,\overline{(a + ib)} = (a + ib)\,(a - ib) = a^2 + b^2$$

so

$$z\bar{z} = |z|^2.$$

With these additional operations, we are now in a position to discuss the multiplicative inverses, z^{-1}, of non-zero elements $z \in \mathbb{C}$, i.e. elements $z = z_1 + iz_2$ with z_1 and z_2 not both vanishing. Observe

$$z\,\frac{\bar{z}}{|z|^2} = \frac{z\bar{z}}{|z|^2} = \frac{|z|^2}{|z|^2} = 1$$

so

$$z^{-1} = \frac{\bar{z}}{|z|^2}$$

is a suitable definition of the multiplicative inverse. Notice that it is perfectly well defined when the denominator is not vanishing, that is, when z is non-zero. In case the reader finds this to be difficult to remember, the process of dividing by a non-zero complex number in rectangular form may be achieved by choosing to multiply the numerator and denominator of the given quotient by the conjugate of the denominator as in

$$\frac{a + ib}{c + id} = \frac{a + ib}{c + id}\cdot\frac{\overline{c + id}}{\overline{c + id}} = \frac{(a + ib)\,(c - id)}{(c + id)\,\overline{(c + id)}} = \frac{ac + bd + i\,(bc - ad)}{|c + id|^2} = \frac{ac + bd}{|c + id|^2} + i\frac{(bc - ad)}{|c + id|^2}.$$

In particular, to obtain the multiplicative inverse of $z = z_1 + iz_2$, multiply numerator and denominator by the conjugate to obtain

$$\frac{1}{z} = \frac{1}{z_1 + iz_2} = \frac{1}{z_1 + iz_2}\cdot\frac{z_1 - iz_2}{z_1 - iz_2} = \frac{z_1 - iz_2}{|z_1 + iz_2|^2} = \frac{\bar{z}}{|z|^2}$$

as expected. Now, prior to exploring yet a third form of complex numbers and the corresponding geometric interpretations, we introduce yet another important definition, functions which retrieve real and imaginary parts of complex numbers in terms of the number

and its conjugate. Observe the following for the complex number $z = a + ib$,

$$\frac{z + \bar{z}}{2} = \frac{(a + ib) + \overline{(a + ib)}}{2} = \frac{(a + ib) + (a - ib)}{2} = \frac{2a}{2} = a,$$

the real part of z, and

$$\frac{z - \bar{z}}{2i} = \frac{(a + ib) - \overline{(a + ib)}}{2i} = \frac{(a + ib) - (a - ib)}{2i} = \frac{2ib}{2i} = b,$$

the imaginary part of z. These calculations lead to natural definitions for the functions $\mathfrak{Re}, \mathfrak{Im} : \mathbb{C} \to \mathbb{R}$ defined by

$$\mathfrak{Re}(z) = \frac{z + \bar{z}}{2}$$

and

$$\mathfrak{Im}(z) = \frac{z - \bar{z}}{2i}$$

which recover the real and imaginary parts of z, so that, to reiterate, for complex number $z = z_1 + iz_2$, $\mathfrak{Re}(z) = z_1$ and $\mathfrak{Im}(z) = z_2$. It should also be apparent that a complex number $z \in \mathbb{C}$ is purely real if and only if $z = \mathfrak{Re}\, z$ and that $z \in \mathbb{C}$ is purely imaginary, i.e. a non-zero real multiple of i, if and only if $\mathfrak{Re}\, z = 0$ but $\mathfrak{Im}\, z \neq z$.

We are now prepared to provide several more definitions, which are motivated by the geometric properties of complex numbers. We begin with the polar form, and interpret the algebraic properties and operations presented in this section in the geometric framework inherent in the definition of the complex number as ordered pair.

A.1.2 Polar Form and the Geometry of $\mathbb{C}$

Recall that a complex number $z \in \mathbb{C}$ with real part z_1 and imaginary part z_2 is defined to be the ordered pair (z_1, z_2). This is clearly a point, the geometric image of z, in the plane $\mathbb{R}^2$, as shown schematically in figure A.1 below. Upon inspection of Figure A.1, a geometric interpretation of modulus is immediate, it is simply the magnitude of the corresponding vector, the corresponding geometric image. We define the angle θ, measured counter-clockwise from the positive real axis to the ray which extends from the origin to the geometric image of the complex number, and call it the argument, denoted $\arg z$. With *modulus* and *argument* in hand, we may immediately define a polar representation of the complex number z; the quantities r and θ, with $r > 0$, completely and uniquely characterize the polar form of the complex number. In particular, for the complex number $z = z_1 + iz_2$, the relations between rectangular and polar co-ordinates are, of course,

$$\begin{aligned} r &= |z|\,, \\ \tan\theta &= \frac{z_2}{z_1}, \\ z_1 &= r\cos\theta, \text{ and} \\ z_2 &= r\sin\theta \end{aligned}$$

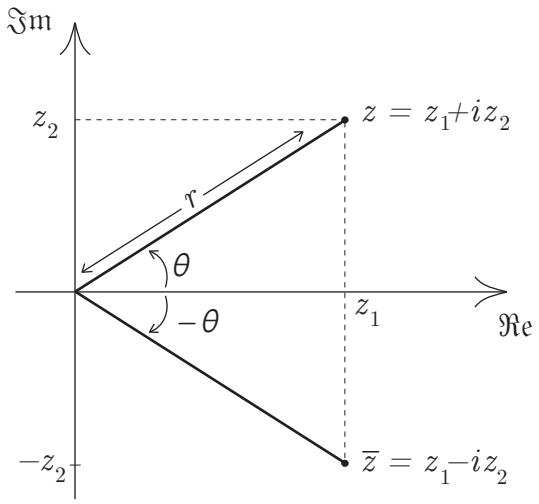

FIGURE A.1: This is a schematic of the geometric image (z_1, z_2) of the complex number $z = z_1 + iz_2$ in the complex plane. The horizontal axis is the real axis and is typically labelled by $\mathfrak{Re}$. Likewise, the vertical axis is known as the imaginary axis and is labelled $\mathfrak{Im}$. The modulus, $|z|$ is labelled as r, and the argument of z is the angle θ taken positive counter-clockwise from the real axis to the ray which extends from the origin to the geometric image. The conjugate, $\bar{z}$, is the reflection of z in the real axis.

The relation $\tan\theta = z_2/z_1$ defines θ implicitly. There is a subtlety which arises because tan is 2π-periodic, i.e., $\tan\theta = \tan(\theta + 2\pi)$. Consequently, $\arg z$ is a *multi-function*, a function which takes a complex number z in its domain but returns a set of possible outcomes. That is to say that, for a given complex number z, $\arg z = \{\theta + 2\pi k \,|\, k \in \mathbb{Z}\}$ where θ is simply an angle measured from the positive real axis to a ray which corresponds to the ray which extends from the origin to the geometric image of z. The angle θ depicted in Figure A.1 is one amongst many possible such angles. Sometimes, to avoid this difficulty, a principal argument is defined. We have, for complex number z with argument θ where θ is any element of the set $\arg z$, i.e., any angle which satisfies $\tan\theta = z_2/z_1$, the following. An angle α measured from the positive real axis is selected and fixed. For this angle, define $\mathrm{Arg}_\alpha z$ to be the element of $\arg z$ which falls into the interval $[\alpha, \alpha + 2\pi)$. $\mathrm{Arg}\, z$ is known as the principal argument of complex number z corresponding to the value of $\arg z$ which satisfies $\alpha \leq \arg z < \alpha + 2\pi$. We will drop the subscript α but understand implicitly that each time the principal argument is invoked, there is a particular range of values, known as the branch of arg, to which it corresponds, and that, because $\mathrm{Arg}_\alpha \neq \mathrm{Arg}_\beta$ when $\alpha \neq \beta$, the principal arguments with respect to different branches may not be manipulated carelessly.

Before proceeding with geometric interpretations of the algebraic operations on $\mathbb{C}$, we introduce the complex exponential, which allows the most expeditious expression of the polar form. Euler's formula, motivated by Maclaurin series for sin and cos but ultimately

taken as a definition, is

$$e^{i\theta} = \cos\theta + i\sin\theta. \tag{A.1}$$

Again, it should be apparent due to the 2π periodicity of sin and cos that

$$e^{i\theta} = e^{i(\theta+2\pi k)}$$

for any $\theta \in \mathbb{R}$ and any $k \in \mathbb{Z}$. So, with the relations between polar and rectangular components and with Euler's formula, we must have

$$z = z_1 + iz_2 = r\cos\theta + ir\sin\theta = r\left(\cos\theta + i\sin\theta\right) = re^{i\theta} \tag{A.2}$$

where $\theta = \arg z$. Equation (A.2) will be taken as the *polar form* of the complex number z. The complex exponential, a function $\exp : \mathbb{C} \to \mathbb{C}$, is defined

$$\exp z = e^z = e^{\mathfrak{Re}(z)+i\,\mathfrak{Im}(z)} = e^{\mathfrak{Re}(z)}e^{i\,\mathfrak{Im}(z)} = e^{\mathfrak{Re}(z)}\left(\cos\left(\mathfrak{Im}\left(z\right)\right) + i\sin\left(\mathfrak{Im}\left(z\right)\right)\right). \tag{A.3}$$

Further discussion of complex functions of a complex variable and their geometry, including the geometry of the exponential function, follows in section A.3 subsequently. We are now prepared to discuss the geometry of the algebraic operations in $\mathbb{C}$.

We have seen that the set of complex numbers $\mathbb{C}$ coincides with $\mathbb{R}^2$ where the real part of z is the x coordinate, the imaginary part of z is the y coordinate in the plane. It should be clear that the addition of complex numbers, by the very definition, corresponds to vectorial addition in the plane, multiplication of complex numbers by a real number corresponds to a pure scaling as in scalar multiplication of vectors. We have seen that the modulus of a complex number is simply the distance from the origin of the complex plane to the geometric image of the complex number, and that the argument is simply one of the many angles winding around the origin $k \in \mathbb{C}$ times, and measured from the real axis to a ray which coincides with the ray generated by the geometric image. Again, θ is taken positive counter-clockwise. The conjugate of a complex number is the geometric image of a reflection through the real axis of the number conjugated. What of multiplication and division? Consider the following for $z = z_1 + iz_2 = r_1e^{i\theta_1}$ and $w = w_1 + iw_2 = r_2e^{i\theta_2}$ in $\mathbb{C}$,

$$\begin{aligned}
zw &= r_1e^{i\theta_1}r_2e^{i\theta_2} = r_1r_2e^{i\theta_1}e^{i\theta_2} \\
&= r_1r_2\left(\cos\theta_1 + i\sin\theta_1\right)\left(\cos\theta_2 + i\sin\theta_2\right) \\
&= r_1r_2\big(\cos\theta_1\cos\theta_2 - \sin\theta_1\sin\theta_2 + i\left(\cos\theta_1\sin\theta_2 + \sin\theta_1\cos\theta_2\right)\big) \\
&= r_1r_2\big(\cos\left(\theta_1+\theta_2\right) + i\sin\left(\theta_1+\theta_2\right)\big) \\
&= r_1r_2e^{i(\theta_1+\theta_2)} \\
&= |z|\,|w|\,e^{i(\arg z + \arg w)}
\end{aligned}$$

So obtaining the relations

$$|zw| = |z|\,|w| \;\text{ and }\; \arg\left(zw\right) = \arg z + \arg w.$$

A similar argument entails for division that

$$\left|\frac{w}{z}\right| = \frac{|w|}{|z|} \text{ and } \arg\left(\frac{w}{z}\right) = \arg w - \arg z.$$

It is worthwhile to note that these relations do not hold for principal arguments because the sum of two principal arguments relative to the same branch of arg might actually fall outside of the branch and similarly for differences of principal arguments. With these observations, it is abundantly clear that multiplication of w by a complex number z corresponds to rotation of the geometric image of w about an angle $\arg z$ and a scaling of w by an amount $|z|$, whereas division of w by z corresponds to rotation of the geometric image of w about an angle $|\arg z|$ but oriented oppositely to $\arg z$ and a scaling of w by an amount $1/|z|$. In particular, z^{-1} is an inversion in the unit circle, $z/|z|$ together with a reflection through the real axis.

Now, prior to moving onwards to the discussion of complex functions of a complex variable, their geometry and analysis, in subsequent sections, a number of results are gathered and proven here. An important exercise is to keep the geometric interpretation in mind at all times. The proofs are algebraic, but the results themselves have significant geometric content, i.e., that the relation is true should be apparent from the geometry alone.

Theorem A.1.

1. $\bar{\bar{z}} = z$
2. $\mathfrak{Re}\,(\bar{z}) = \mathfrak{Re}\,(z)$
3. $\mathfrak{Im}\,(\bar{z}) = -\,\mathfrak{Im}\,(z)$
4. $\overline{z \pm w} = \bar{z} \pm \bar{w}$
5. $\overline{zw} = \bar{z}\,\bar{w}$
6. $\overline{\left(\frac{z}{w}\right)} = \bar{z}/\bar{w}$
7. $\overline{z^{-1}} = 1/\bar{z} = \bar{z}^{-1}$
8. $z\bar{z} = |z|^2$
9. $|\bar{z}| = |z|$
10. $|zw| = |z|\,|w|$
11. $\left|\frac{z}{w}\right| = \frac{|z|}{|w|}$
12. $|z^{-1}| = \frac{1}{|z|} = |z|^{-1}$
13. $\mathfrak{Re}\, z \leq |\mathfrak{Re}\, z| \leq |z|$
14. $\mathfrak{Im}\, z \leq |\mathfrak{Im}\, z| \leq |z|$
15. $|z \pm w| \leq |z| + |w|$
16. $||z| - |w|| \leq |z \pm w|$

Several of these have been proven, nevertheless, all of these results are proven again.

Proof. In the following, we take $z = z_1 + iz_2 = r_1 e^{i\theta_1}$ and $w = w_1 + iw_2 = r_2 e^{i\theta_2}$

1. $\bar{\bar{z}} = \overline{\overline{z_1 + iz_2}} = \overline{z_1 - iz_2} = z_1 + iz_2 = z$
2. $\mathfrak{Re}\,(\bar{z}) = \mathfrak{Re}\,\left(\overline{z_1 + iz_2}\right) = \mathfrak{Re}\,(z_1 - iz_2) = z_1 = \mathfrak{Re}\,(z)$

3. $\mathfrak{Im}(\bar{z}) = \mathfrak{Im}\left(\overline{z_1 + iz_2}\right) = \mathfrak{Im}(z_1 - iz_2) = -z_2 = -\mathfrak{Im}(z)$

4.
$$\begin{aligned}\overline{z \pm w} &= \overline{(z_1 + iz_2) \pm (w_1 + iw_2)} = \overline{(z_1 \pm w_1) + i(z_2 \pm w_2)} \\ &= (z_1 \pm w_1) - i(z_2 \pm w_2) = (z_1 - iz_2) \pm (w_1 - iw_2) \\ &= \bar{z} \pm \overline{w}\end{aligned}$$

5.
$$\begin{aligned}\overline{zw} &= \overline{(z_1 + iz_2)(w_1 + iw_2)} = \overline{z_1w_1 - z_2w_2 + i(z_1w_2 + z_2w_1)} \\ &= z_1w_1 - z_2w_2 - i(z_1w_2 + z_2w_1) = (z_1 - iz_2)(w_1 - iw_2) \\ &= \bar{z}\overline{w}\end{aligned}$$

6.
$$\begin{aligned}\overline{\left(\frac{z}{w}\right)} &= \overline{\left(\frac{z_1 + iz_2}{w_1 + iw_2}\right)} = \overline{\frac{z_1w_1 + z_2w_2}{|w_1 + iw_2|} + i\frac{z_2w_1 - z_1w_2}{|w_1 + iw_2|}} \\ &= \frac{z_1w_1 + z_2w_2}{|w_1 + iw_2|^2} - i\frac{z_2w_1 - z_1w_2}{|w_1 + iw_2|^2} = \frac{z_1w_1 + z_2w_2 - i(z_2w_1 - z_1w_2)}{|w_1 + iw_2|^2} \\ &= \frac{z_1w_1 + z_2w_2 + i(z_1w_2 - z_2w_1)}{|w_1 + iw_2|^2} = \frac{(z_1 - iz_2)(w_1 + iw_2)}{|w_1 + iw_2|^2} \\ &= \frac{(z_1 - iz_2)\overline{(w_1 - iw_2)}}{|w_1 + iw_2|^2} = \frac{\bar{z}\overline{\overline{w}}}{\overline{w}\overline{\overline{w}}} = \frac{\bar{z}}{\overline{w}}\end{aligned}$$

7. This result follows immediately from the previous by setting z to 1 and w to z.

8. $z\bar{z} = (z_1 + iz_2)\overline{(z_1 + iz_2)} = (z_1 + iz_2)(z_1 - iz_2) = z_1^2 + z_2^2 = |z|^2$

9. $|\bar{z}|^2 = \bar{z}\overline{\bar{z}} = \bar{z}z = z\bar{z} = |z|^2$ and, because the expression to be squared is positive, simply take square roots of both sides to obtain $|\bar{z}| = |z|$, as required.

10. $|zw|^2 = (zw)\overline{(zw)} = zw\bar{z}\overline{w} = z\bar{z}w\overline{w} = |z|^2|w|^2$ and, because the expression to be squared is positive, simply take square roots of both sides to obtain $|zw| = |z||w|$, as required.

11. $\left|\frac{z}{w}\right|^2 = \left(\frac{z}{w}\right)\overline{\left(\frac{z}{w}\right)} = \frac{z}{w} \cdot \frac{\bar{z}}{\overline{w}} = \frac{z\bar{z}}{w\overline{w}} = \frac{|z|^2}{|w|^2} = \left(\frac{|z|}{|w|}\right)^2$ and, because the expression to be squared is positive, simply take square roots of both sides to obtain $\left|\frac{z}{w}\right| = \frac{|z|}{|w|}$, as required.

12. This result follows immediately from the previous by setting z to 1 and w to z.

13. $\mathfrak{Re}\, z \leq |\mathfrak{Re}\, z| = \sqrt{(\mathfrak{Re}\, z)^2} \leq \sqrt{(\mathfrak{Re}\, z)^2 + (\mathfrak{Im}\, z)^2} = |\mathfrak{Re}\, z + i\,\mathfrak{Im}\, z| = |z|$

14. $\mathfrak{Im}\, z \leq |\mathfrak{Im}\, z| = \sqrt{(\mathfrak{Im}\, z)^2} \leq \sqrt{(\mathfrak{Re}\, z)^2 + (\mathfrak{Im}\, z)^2} = |\mathfrak{Re}\, z + i\, \mathfrak{Im}\, z| = |z|$

15. This is the *triangle inequality*. Consider $|z+w|^2$

$$\begin{aligned} |z+w|^2 &= (z+w)\,\overline{(z+w)} = (z+w)\,(\bar{z}+\overline{w}) = z\bar{z} + z\overline{w} + w\bar{z} + w\overline{w} \\ &= |z|^2 + \left(z\overline{w} + \overline{z\overline{w}}\right) + |w|^2 = |z|^2 + 2\,\mathfrak{Re}\,(z\overline{w}) + |w|^2 \\ &\leq |z|^2 + 2\,|\mathfrak{Re}\,(z\overline{w})| + |w|^2 \\ &\leq |z|^2 + 2\,|z\overline{w}| + |w|^2 = |z|^2 + 2\,|z|\,|w| + |w|^2 = \big(\,|z| + |w|\,\big)^2 \end{aligned}$$

so obtain $|z+w|^2 \leq (|z|+|w|)^2$ and, because the expressions to be squared are positive, obtain $|z+w| \leq |z| + |w|$. Replace w with its negative to obtain $|z-w| \leq |z| + |w|$.

16. This is a variation on the triangle inequality. Begin by considering $|z|$ then simultaneously add and subtract w inside of the absolute values. $|z| = |z-w+w| \leq |z-w| + |w|$, by triangle inequality, so $|z| - |w| \leq |z-w|$. Now swap z and w to obtain $|w| - |z| \leq |w-z| = |z-w|$ so $-|z-w| \leq |z| - |w|$. Combining, obtain $-|z-w| \leq |z| - |w| \leq |z-w|$ so $||z| - |w|| \leq |z-w|$ as required. Replace w with its negative to obtain $||z| - |w|| \leq |z+w|$.

□

A.2 Some Topology

A.2.1 Open Disk Topology

Definition (open disk)**.** *An* open disk *with centre* $z_0 \in \mathbb{C}$ *of* radius $r > 0$ *is a subset* $D(z_0, r)$ *of* $\mathbb{C}$ *defined according to*

$$D(z_0, r) = \big\{ z \in \mathbb{C} \;\big|\; |z - z_0| < r \big\}.$$

Sometimes $D(z_0, r)$ is called the disk *about* z_0. It should be clear from the definition that the boundary of the open disk $D(z_0, r)$ is the locus of points a fixed distance r from the given point z_0 in the plane, i.e., the circle of radius r centred at z_0.

Definition (open set)**.** *A subset* $U \in \mathbb{C}$ *is* open *if and only if, for every point* $z_0 \in U$*, a radius* $r > 0$ *exists and ensures that*

$$D(z_0, r) \subseteq U.$$

This definition identifies the open sets to be those subsets of the complex plane which have the property that, for any point z_0 of the set U, a stepsize $r > 0$ exists and ensures that, whenever a step of size r is taken from z_0 in *any* direction, the destination is also in U, i.e., stepsizes always exist so that boundaries are not overstepped. This may be written formally, U is open if and only if, for any $z_0 \in U$, a stepsize $r > 0$ exists and $z_0 + re^{i\theta} \in U$ for any θ. This characteristic of open sets allows the formulation of definitions (of things like differentiability and continuity) without regard to special boundary cases, and this turns out to be extremely convenient.

Now, revisiting the first definition in light of the second, $D(z_0, r)$ surely is a disk in the plane, but is it an open set? In other words, is it appropriate to call $D(z_0, r)$ the *open* disk about z_0? The answer is affirmative, and stated in the following.

Theorem A.2. *Open disks are open sets.*

Proof. Let U be an open disk of radius r about $a \in \mathbb{C}$. Let $z_0 \in U$. Clearly $|z_0 - a| < r$, so by the definition of inequality there is a $\delta > 0$ for which $|z_0 - a| + \delta = r$, i.e., $\delta = r - |z_0 - a|$. Claim that $D(z_0, \delta)$ is an open disk contained in U. This is proven by demonstrating that $D(z_0, \delta) \subseteq U$ simply by showing $|w - a| < r$ for an arbitrarily selected $w \in D(z_0, \delta)$. So, begin by supposing $w \in D(z_0, \delta)$. Then

$$|z_0 - w| < \delta = r - |z_0 - a|$$

so

$$|z_0 - w| + |z_0 - a| < r$$

but

$$|w - a| < |z_0 - w| + |z_0 - a|\,,$$

by the triangle inequality, so

$$|w - a| < r.$$

Consequently, w must be in U so $D(z_0, \delta) \subseteq U$ as required. □

So, *open disk* is indeed an appropriate appellation, it is compatible with the above theorem which confirms that open disks are in fact open. Another way to discuss open sets is in terms of interior points.

Definition (interior point and interior)**.** *A point $z \in U$ is an* interior point *of U whenever it is the centre of an open disk entirely contained in U. The* interior *of U, often denoted* $\text{int}(U)$*, is the set of all interior points of U. More formally,*

$$z \in \text{int}(U) \text{ if and only if } \exists r > 0 \text{ for which } D(z, r) \subseteq U.$$

It should be clear from this definition that open sets are those which comprise only their interior points, i.e., U is open if and only if $U = \text{int}(U)$. The locution *neighborhood of a point* is often used to identify an open region of arbitrary shape surrounding a given point.

The concept of neighborhood is a useful abstraction which plays a central role in the study of topological spaces, which are defined in terms of appropriate families of neighborhoods; herein, however, a neighborhood of a point will simply refer to an open disk centred on the given point. The utility of the notion of neighborhood, of open disks in particular, is that they enable a description of relative closeness of points in the plane. Concretely, given points z and w in the plane, consider $D(z,\delta)$. Either $w \in D(z,\delta)$ for all positive radii δ, entailing that the distance between w and z is zero, or there is a minimal distance δ for which $w \notin D(z,\delta)$, entailing that w is located a distance at least δ from z.

With the notion of neighborhood in hand, the notion of the open disk in particular, there are several other types of points referred to a given set which should be defined in order to establish a more complete vocabulary for discussion of points, curves, and regions in the plane. This is done to improve one's intuition of the spatial relation between points in the plane described in terms of open sets, and it is done prior to proceeding with preliminary classification of curves and regions which rely on these notions, important when discussing derivatives and integrals.

Definition (isolated point)**.** *A point $a \in A$ is an* isolated point of A *whenever a has a neighborhood which contains a but no other point of A; in particular, a radius $r > 0$ exists and ensures that*

$$D(a,r) \cap A = \{a\}\,.$$

The definition entails that isolated points of A are indeed elements of A. The definition captures the notion of isolation from the rest of A by asserting that no other point of A is within a certain distance r from a; to reiterate, if $D(a,r)$ contains no point of A besides a itself, the points of A must be at least r units from a, and, hence, a is isolated from the rest of A. Now, to contrast the notion of isolation with that of arbitrary closeness, limit points of a set are defined as those points which are arbitrarily close to points of the set; a *limit point* of a set A is a point not necessarily within A itself, but proximal to other points of A.

Definition (limit point)**.** *A point $z \in \mathbb{C}$ is a* limit point *of A (in $\mathbb{C}$) whenever every neighborhood of z contains points of A different from z, i.e.,*

$$\forall \epsilon > 0,\ \big(D(z,\epsilon)\backslash\{z\}\big) \cap A \neq \emptyset.$$

The set of all limit points of A is sometimes denoted A'. It follows that, if $z \in A$, and it is not an isolated point, it is a limit point. The definition is much more interesting when the limit point z is not an element of A. A limit point z of A with $z \notin A$ is arbitrarily close to points of A, that is, no matter what distance is established, there are always points of A which are within that distance to z. From the geometry of open disks $D(z_0,\delta)$, it should be evident that all of the points on the bounding circle, the locus of points satisfying $|z - z_0| = \delta$, are not on the disk but *are* limit points of the disk. This leads to the definitions of boundary point and boundary of a set, and of closedness and closure of a set.

Definition (boundary point and boundary)**.** *A point $z \in \mathbb{C}$ is a boundary point of a set A whenever all open disks centred on z simultaneously contain points of A and points not in A. The boundary of A, denoted ∂A, is the set of all boundary points of A.*

Several things should be clear from this definition, that isolated points are always boundary points and that, amongst limit points, those which are not interior points are boundary points. This is completely compatible with our intuition about boundaries. Draw any non-intersecting closed curve in the plane, there are points interior to the region contained within the contour, there are points which lie within the interior of the region outside of the contour, these may be termed *exterior points*, and the points on the contour lie arbitrarily close to both the interior and the exterior of the region within the contour. When a set contains its boundary, we say that it is closed. When a set, possibly not closed, is augmented with its boundary points, we obtain its closure.

Definition (closedness and the closure of a set)**.** *A set $A \subseteq \mathbb{C}$ is* closed *if and only if $A^{\complement}$ is open. The closure of a set A, denoted* $\mathrm{cl}(A)$*, is the set A together with its limit points, i.e.,*

$$\mathrm{cl}(A) = A \cup A'.$$

It should be evident from the definition of closedness that a set A is closed if and only if $A = \mathrm{cl}(A)$. An alternative definition for closure follows from the observation that, for any given set $A \subseteq \mathbb{C}$, $A \cup A' = A \cup \partial A$, so either take a set together with its limit points or together with its boundary points to obtain its closure. This is the case because the boundary comprises isolated points and limit points which are not simultaneously interior points. It is critical to note that any given set may be either open, closed, or neither open nor closed. A set is neither open nor closed when it contains some but not all of its boundary points; if a set contains any boundary point, it cannot be open, because boundary points cannot be interior points; if a set does not contain all of its boundary points, it cannot be closed.

A.2.2 Paths, Loops, and Continuous Regions of the Plane

Definition (path and loop)**.** *A* path *in some open set $U \subseteq \mathbb{C}$ is a continuous mapping $\gamma : [\alpha, \beta] \to U$. A* loop *is a path with $\gamma(\alpha) = \gamma(\beta)$.*

In other words, a loop is merely a closed path. Loops may have self intersections. When a loop does not intersect itself, except at the initial point, it is called a *simple closed curve.*

Definition (simple closed curve)**.** *A* simple closed curve *in $U \subseteq \mathbb{C}$ is a loop $\gamma : [\alpha, \beta] \to U$ with $\gamma(t_1) \neq \gamma(t_2)$ for any distinct $t_1, t_2 \in (\alpha, \beta)$.*

Simple closed curves are also called *Jordan curves.* The obvious claim, which was tacitly assumed in the discussion above, that a Jordan curve decomposes the complex plane into two disconnected regions, the interior and the exterior of the curve, is known as the Jordan Curve Theorem.

Definition (path homotopy)**.** *Let $\gamma_1, \gamma_2 : [\alpha, \beta] \to U \subseteq \mathbb{C}$ be paths in U with coinciding endpoints, i.e., $\gamma_1(\alpha) = \gamma_2(\alpha)$ and $\gamma_1(\beta) = \gamma_2(\beta)$. A* homotopy *between them is a continuous function $F : [\alpha, \beta] \times [0, 1] \to U$ with $F(t, 0) = \gamma_1(t)$, $F(t, 1) = \gamma_2(t)$, and, for all $s \in [0, 1]$, $F(\alpha, s) = \gamma_1(\alpha) = \gamma_2(\alpha)$, and $F(\beta, s) = \gamma_1(\beta) = \gamma_2(\beta)$.*

A homotopy is a continuous mapping between curves which share endpoints and are indexed by the second parameter. One may think of a homotopy as being a continuous deformation which continuously takes one path to another. It should be clear that any Jordan curve may be obtained via a homotopy of the unit circled centred at the origin.

We now define *connected* and *simply connected* regions of the plane.

Definition (disconnected set)**.** *A set $U \subseteq \mathbb{C}$ is disconnected whenever a family of disjoint open subsets of the plane, $\{U_i\}$ with $U_i \cap U_j = \emptyset$ whenever $i \neq j$, exists and*

$$U = \bigcup_i U_i.$$

Each U_i is called a component of U.

Definition (connected set)**.** *A set $U \subseteq \mathbb{C}$ is connected whenever it is not disconnected.*

A connected set is one which cannot be written as the union of disjoint open sets.

Definition (path-connected set)**.** *A set $U \subseteq \mathbb{C}$ is* path-connected *whenever any pair of points in U may be joined by a path in U.*

That a region is path-connected entails that it is connected but counterexamples confirm that the converse is not true. Finally, define the notion of a simply connected set.

Definition (simply connected set)**.** *A connected set U is* simply connected *if and only if any two simple closed curves in U are homotopic.*

A.3 Complex Functions of a Complex Variable

Complex functions of a complex variable, $f : \mathbb{C} \to \mathbb{C}$, are often defined by expressions of the form $f(\zeta) = u(\zeta) + iv(\zeta)$ where u and v are real valued functions of a complex variable, $u, v : \mathbb{C} \to \mathbb{R}$. Slightly abusing notation, one often writes $f(\zeta) = u(\xi, \eta) + iv(\xi, \eta)$ in which $\xi = \mathfrak{Re}(\zeta)$ and $\eta = \mathfrak{Im}(\zeta)$ and u and v in this instance are scalar valued functions of points in the plane, that is $u, v : \mathbb{R}^2 \to \mathbb{R}$. This abuse of notation is tolerated due to the definition of complex numbers as their geometric images. In this manner, if $z = x + iy$ and $z = f(\zeta) = u(\zeta) + iv(\zeta)$, with $\zeta = \xi + i\eta$, then $x = u(\xi, \eta)$ and $y = v(\xi, \eta)$ immediately provides a geometric interpretation of $f : \mathbb{C} \to \mathbb{C}$ as a geometric mapping from $\mathbb{R}^2$ to itself. Figure A.2 shows a schematic of a mapping from the ζ plane to the z-plane where the

points in the z-plane are given by functions of the points in the ζ-plane as $x = x(\xi, \eta)$ and $y = y(\xi, \eta)$.

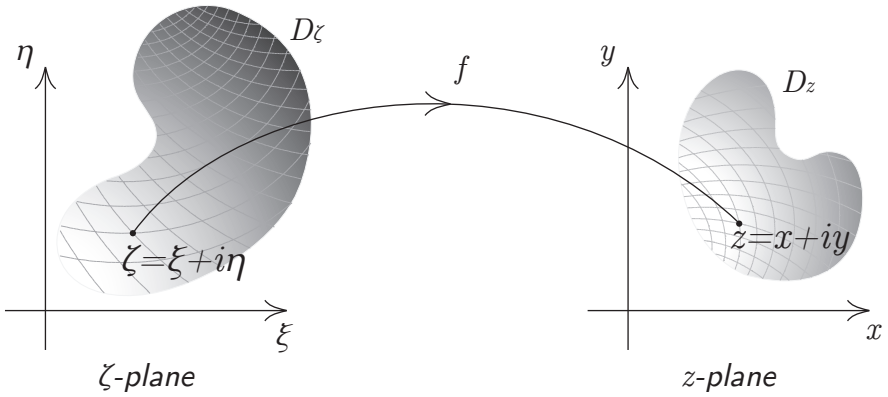

FIGURE A.2: This schematic of the mapping $f : D_\zeta \subseteq \mathbb{C} \to \mathbb{C}$ shows that it associates points in region D_z in the z-plane with points in domain D_ζ in the ζ-plane, i.e., that points $\zeta \in D_\zeta$ are mapped to points $z \in D_z$. So that real and imaginary parts, x and y, of the image are both functions of real and imaginary parts of ζ, i.e., $x = x(\xi, \eta)$ and $y = y(\xi, \eta)$.

An underlying thread which runs through all of complex analysis is that the definitions of the elementary complex functions of a complex variable are purely real when they are restricted to the real line, and they are defined in such a way that, when they are restricted to the real line, they behave identically to the corresponding elementary function defined on $\mathbb{R}$. So, for example, $\sin : \mathbb{C} \to \mathbb{C}$ is defined in such a way that, for $z = x$ purely real, one obtains $\sin z = \sin x$ in which the right hand side is the familiar real valued function sin of real variable x. The extensions of the familiar elementary functions to $\mathbb{C}$ are now provided and their geometry, interpreted as mappings of the plane, is discussed subsequently.

A.3.1 Elementary Functions Extended to $\mathbb{C}$

The complex exponential has already been defined in equation (A.3), the definition is repeated here for $z = x + iy$,

$$e^z = e^x\big(\cos y + i \sin y\big). \tag{A.4}$$

So, if $z = x + iy$, $z = f(\zeta) = e^\zeta$ entails that points in the ζ-plane under the mapping f are mapped to points in the z-plane given by $x = x(\xi, \eta) = e^\xi \cos \eta$ and $y = y(\xi, \eta) = e^\xi \sin \eta$. The geometry of the exponential map is exhibited in Figure A.3, in which three lines are mapped to the z-plane, a horizontal line, a vertical line, and a line inclined at slope α.

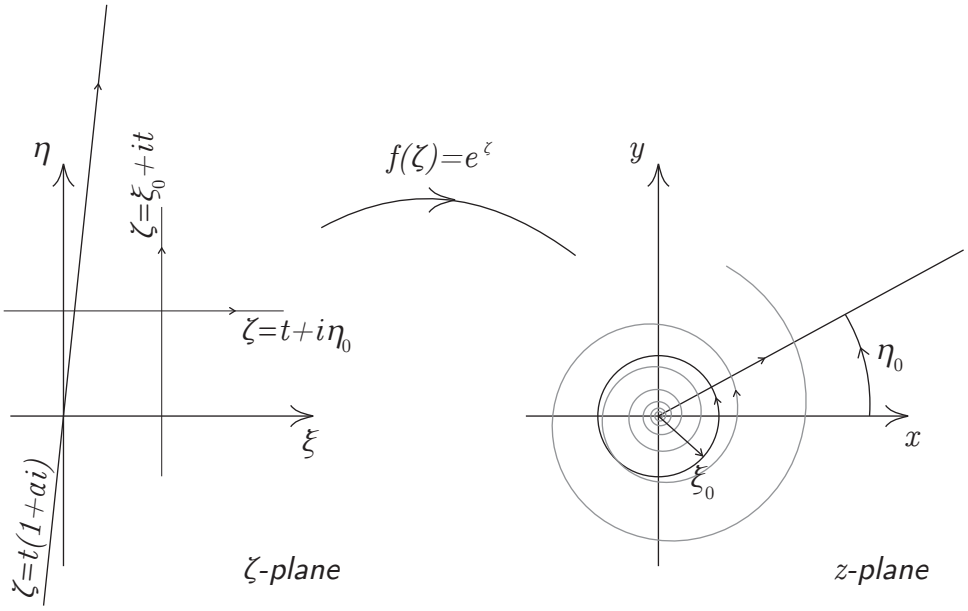

FIGURE A.3: This schematic of the mapping $f(\zeta) = e^{\zeta}$ applied to three different curves in the ζ-plane, one horizontal, one vertical, and one inclined at slope α. Their images are displayed in the z-plane. It should be evident that the exponential sends horizontal lines to concentric circles centred at the origin, vertical lines to open rays extending form the origin, and other lines to spirals.

To obtain definitions for trigonometric sine and cosine, we look to Euler's formula. If Euler's formula for z and for $-z$ are added and subtracted, the following are obtained

$$\cos z = \frac{e^{iz} + e^{-iz}}{2} \tag{A.5}$$

$$\sin z = \frac{e^{iz} - e^{-iz}}{2i} \tag{A.6}$$

The tangent function is defined as the ratio of sine and cosine,

$$\tan z = \frac{e^{iz} - e^{-iz}}{i\left(e^{iz} + e^{-iz}\right)}. \tag{A.7}$$

The remaining trigonometric functions are obtained from the reciprocal identities. For the hyperbolic sine and hyperbolic cosine, the definitions follow the standard definition, so it is apparent that when z is purely real, the definitions collapse to the familiar hyperbolic sin and hyperbolic cosine on $\mathbb{R}$. The following hold

$$\cosh z = \frac{e^{z} + e^{-z}}{2} \tag{A.8}$$

$$\sinh z = \frac{e^{z} - e^{-z}}{2} \tag{A.9}$$

The hyperbolic tangent is defined as the ratio of sinh to cosh as expected. The remaining hyperbolic functions are obtained from the reciprocal identities, as expected. It is via these expressions that we find relationships between the hyperbolic and trigonometric forms. In particular, we have the following four identities.

$$\sin iz = i \sinh z \tag{A.10}$$
$$\sinh iz = i \sin z \tag{A.11}$$
$$\cos iz = \cosh z \tag{A.12}$$
$$\cosh iz = \cos z \tag{A.13}$$

To see, for example, that $\sin iz = i \sinh z$, with $\sinh z = \frac{e^z - e^{-z}}{2}$ and $\sin z = \frac{e^{iz} - e^{-iz}}{2i}$ defined, set the argument to iz to obtain

$$\sin iz = \frac{e^{i^2 z} - e^{-i^2 z}}{2i} = -i\frac{e^{-z} - e^{z}}{2} = i\frac{e^{z} - e^{-z}}{2}$$

and obtain

$$\sin iz = i \sinh z$$

as required. The remaining equations are developed in a similar manner. Equation (A.10) is employed in the development of equation (B.3). The above four identities easily enable the discovery of hyperbolic identies similar to the identities for trigonometric functions. According to Osborn's Rule, one simply replaces cosines and sines in the trigonometric identities with their hyperbolic counterparts, and, for each pair of sines which are multiplied, toggle the sign of the corresponding term. This is a consequence of the imaginary number which appears in the four transformation formulae above. The hyperbolic identities are listed and some of them are immediately developed in order to see this.

$$\sinh(-z) = -\sinh(z) \tag{A.14}$$
$$\cosh(-z) = \cosh(z) \tag{A.15}$$
$$\cosh^2(z) - \sinh^2(z) = 1 \tag{A.16}$$
$$\sinh(z_1 + z_2) = \sinh(z_1)\cosh(z_2) + \cosh(z_1)\sinh(z_2) \tag{A.17}$$
$$\cosh(z_1 + z_2) = \cosh(z_1)\cosh(z_2) + \sinh(z_1)\sinh(z_2) \tag{A.18}$$
$$\sinh(2z) = 2\sinh(z)\cosh(z) \tag{A.19}$$
$$\cosh(2z) = \cosh^2(z) + \sinh^2(z) = 2\cosh^2(z) - 1 = 1 + 2\sinh^2(z) \tag{A.20}$$

So, for example, to demonstrate (A.16), take $\cos^2 z + \sin^2 z = 1$ and replace z with iz to obtain

$$\cos^2 iz + \sin^2 iz = 1$$
$$(\cosh z)^2 + (i \sinh z)^2 = 1$$

from equations (A.10) and (A.12) above, so

$$\cosh^2 z - \sinh^2 z = 1$$

as required. It is apparent that the toggling of the sign on the product terms in Osborn's Rule is a consequence of the fact that the product of an even number of imaginary numbers. For angle sum identities, the process is similar. Take the known expression for $\sin(z_1 + z_2)$, replace z_1 and z_2 with iz_1 and iz_2, and employ (A.10) and (A.12) as before.

$$\begin{aligned}
\sin(iz_1 + iz_2) &= \sin iz_1 \cos iz_2 + \cos iz_1 \sin iz_2 \\
\sin(i(z_1 + z_2)) &= i \sinh z_1 \cosh z_2 + i \cosh z_1 \sinh z_2 \\
i \sinh(z_1 + z_2) &= i \sinh z_1 \cosh z_2 + i \cosh z_1 \sinh z_2
\end{aligned}$$

and, upon cancelling the imaginary number from both sides of the equation, obtain the expression $\sinh(z_1 + z_2) = \sinh z_1 \cosh z_2 + \cosh z_1 \sinh z_2$ as required. For $\cos(z_1 + z_2)$, the process is similar,

$$\begin{aligned}
\cos(iz_1 + iz_2) &= \cos iz_1 \cos iz_2 - \sin iz_1 \sin iz_2 \\
\cos(i(z_1 + z_2)) &= \cosh z_1 \cosh z_2 - (i \sinh z_1)(i \sinh z_2) \\
\cosh(z_1 + z_2) &= \cosh z_1 \cosh z_2 + \sinh z_1 \sinh z_2
\end{aligned}$$

as expected. The remaining identities are obtained in identical manner.

A.3.2 The Complex Logarithm and Other Inverses

Consider the equation $\zeta = e^z$. We call z the logarithm of ζ. To determine an expression for z, simply replace the variables with their rectangular or polar forms, equate real and imaginary parts, and solve. We have

$$\begin{aligned}
\zeta &= e^z \\
\xi + i\eta &= e^x(\cos y + i \sin y) \\
\xi + i\eta &= e^x \cos y + ie^x \sin y
\end{aligned}$$

and, equating real and imaginary parts, obtain

$$\xi = e^x \cos y \text{ and } \eta = e^x \sin y$$

and, by taking ratios of these expressions and the sum of the squares of these expressions, obtain

$$\frac{\eta}{\xi} = \frac{\sin y}{\cos y} = \tan y \text{ and } \xi^2 + \eta^2 = (e^x)^2$$

thus, $e^x = |\zeta|$ and $y = \arg \zeta$, so $z = \ln|\zeta| + i \arg \zeta$ and the definition of the complex logarithm is immediate,

$$\log \zeta = \ln|\zeta| + i \arg \zeta. \tag{A.21}$$

Because arg is a multifunction, the complex logarithm is also a multifunction. In particular,

$$\log e^{\zeta} = \zeta + i2k\pi$$

for any integer k. This leads to the definition of the principal logarithm,

$$\operatorname{Log}\zeta = \ln|\zeta| + i\operatorname{Arg}\zeta, \tag{A.22}$$

defined for some specified or understood branch of the principal argument function, Arg.

Exponentials may be defined in the following manner

$$\zeta^{\beta} = e^{\beta\log(\zeta)} \tag{A.23}$$

where $\beta \in \mathbb{C}$.

Inverses of trigonometric and hyperbolic functions may be written in terms of logarithms. Consider the equation $\zeta = \sin z$, in which z is the inverse sine function, $z = \sin^{-1}\zeta$.

$$\begin{aligned}\zeta &= \sin z \\ \zeta &= \frac{e^{iz} - e^{-iz}}{2i} \\ 2i\zeta &= e^{iz} - e^{-iz}\end{aligned}$$

then, multiplying through by e^{iz}, obtain

$$2i\zeta e^{iz} = e^{iz}e^{iz} - e^{-iz}e^{iz}$$

or

$$\left(e^{iz}\right)^2 + 2i\zeta e^{iz} - 1 = 0$$

so

$$e^{iz} = i\zeta + \left(1-\zeta^2\right)^{1/2}$$

where the root is multiple valued. Now, taking logarithms, obtain

$$iz = \log\left(i\zeta + \left(1-\zeta^2\right)^{1/2}\right)$$

so, upon multiplication of both sides of the equation by $-i$, obtain the definition for the inverse sine function,

$$\sin^{-1}\zeta = -i\log\left(i\zeta + \left(1-\zeta^2\right)^{1/2}\right). \tag{A.24}$$

One may similarly obtain the following expressions for some of the other inverse functions

$$\cos^{-1}\zeta = -i\log\left(\zeta + i\left(1-\zeta^2\right)^{1/2}\right) \tag{A.25}$$

$$\tan^{-1}\zeta = \frac{i}{2}\log\left(\frac{i+z}{i-z}\right) \tag{A.26}$$

$$\sinh^{-1}\zeta = \log\left(\zeta + \left(\zeta^2+1\right)^{1/2}\right) \tag{A.27}$$

$$\cosh^{-1}\zeta = \log\left(\zeta + \left(\zeta^2-1\right)^{1/2}\right) \tag{A.28}$$

$$\tanh^{-1}\zeta = \frac{1}{2}\log\left(\frac{1+\zeta}{1-\zeta}\right) \tag{A.29}$$

as well as similar expressions for the inverses of the reciprocal functions.

A.3.3 An Infinite Product for sinc

The demonstration that $\frac{\sin \pi x}{\pi x} = \prod_{n=1}^{\infty} \left(1 - \frac{x^2}{n^2}\right)$ for $x \in (0,1) \subseteq \mathbb{R}$ is provided in the exquisite analysis textbook by Courant and John, *Introduction to Calculus and Analysis*, [16], via the integral of a series representation for $\cot x$ which is obtained via a Fourier series of $\cos \mu x$. In the case of complex argument z, the demonstration involves theorems of Mittag-Leffler and Weierstrass discussed in Rudin *Real and Complex Analysis 3rd ed.*, [80], and Greene and Krantz *Function Theory of One Complex Variable 3rd ed.*, [40], and also obtained in Lang *Complex Analysis 4th ed.*, [57], in which the expression is derived from infinite series representations of the Gamma function together with the identity $\Gamma(z)\Gamma(1-z) = \frac{\pi}{\sin \pi z}$ demonstrated therein. The equation for $\operatorname{sinc} \pi z$ is provided in equation (A.30) below. We have

$$\frac{\sin(\pi z)}{\pi z} = \prod_{n=1}^{\infty} \left(1 - \frac{z^2}{n^2}\right) \tag{A.30}$$

for all $z \in \mathbb{C}$.

A.4 Holomorphy, Harmonicity, and Conformality

A.4.1 Complex Differentiability, Holomorphy, Analyticity

Because complex functions of a complex variable represent mappings from $\mathbb{R}^2$ to itself, it is best to frame the notion of the derivative in terms of multivariable derivatives. Some important definitions and theorems from calculus of several variables are now stated.

Definition (differentiable at a point in the plane)**.** *$f : \mathbb{R}^2 \to \mathbb{R}^2$ is differentiable at some point $a \in \mathbb{R}^2$ if and only if a matrix $Df(a)$ exists and*

$$\lim_{x \to a} \frac{\|R(x)\|}{\|x - a\|}$$

where $R(x) = f(x) - (f(a) + Df(a)(x-a))$. The matrix $Df(a)$ is called the real derivative matrix or the real total derivative of f at a.

Definition (differentiable on a region of the plane)**.** *For some open set $U \subseteq \mathbb{R}^2$, $f : U \to \mathbb{R}^2$ is differentiable on U if and only if f is differentiable at every point of U.*

It can be shown that differentiability entails that the structure of $Df(a)$ obtains a particular form. So that, if

$$f(x,y) = \begin{pmatrix} u(x,y) \\ v(x,y) \end{pmatrix}$$

is differentiable at a, then

$$Df(a) = \begin{pmatrix} \frac{\partial u}{\partial x} & \frac{\partial u}{\partial y} \\ \frac{\partial v}{\partial x} & \frac{\partial v}{\partial y} \end{pmatrix}$$

Definition (continuous of order n)**.** *For an open set $U \subseteq \mathbb{R}^2$, $f : U \to \mathbb{R}^2$ is continuous of order n on U, written*

$$f \in \mathcal{C}^n(U)$$

if and only if all partial derivatives of f of order up to and including n exist and are continuous. In particular, $f \in \mathcal{C}(U)$, i.e., f is continuous of order zero, if and only if f is continuous on U; $f \in \mathcal{C}^1(U)$ if and only if all partials $\partial f_i/\partial x_j$, for $i, j \in \{1, 2\}$, exist and are continuous on U.

It can be shown that $f \in \mathcal{C}^1$ entails that f is differentiable. It can also be shown that differentiability implies continuity, i.e. that $f \in \mathcal{C}$, but that the derivative exists but is not necessarily continuous. Finally, we simply write down the inverse function theorem without proof,

Theorem A.3. *For a function $f : U \subseteq \mathbb{R}^2 \to \mathbb{R}^2$ with $f \in \mathcal{C}^1$ and $Df(a)$ invertible at a, the domain of f may be restricted to some open set $V \subseteq U$ with $a \in V$ so that f is invertible, $f^{-1} \in \mathcal{C}^1$, and $Df^{-1}(f(a)) = Df(a)^{-1}$*

With these concepts in hand, it is fruitful to interpret complex function of a complex variable as derivatives of real functions from the plane to the plane. This is the source of different expressions used to discuss the differentiability of such functions. These notions turn out to be equivalent via several theorems, nevertheless, the distinctions should be preserved so that the appropriate language is employed when one aspect over another is to be emphasized in any given situation.

A function $f : U \subseteq \mathbb{C} \to \mathbb{C}$, is differentiable, or, more specifically, real differentiable, whenever, taken as a function from $\mathbb{R}^2$ to $\mathbb{R}^2$, it is real differentiable as defined above. In this case, the matrix $Df(a)$ exists and is defined as discussed above. Several partial derivatives are now proposed in a natural way and employed in the discussion of complex differentiability and holomorphy.

Definition. *For $f : U \subseteq \mathbb{C} \to \mathbb{C}$ given by $f(z) = u(z) + iv(z)$, define the following*

$$\frac{\partial f}{\partial x} = \frac{\partial u}{\partial x} + i\frac{\partial v}{\partial x} \tag{A.31}$$

$$\frac{\partial f}{\partial y} = \frac{\partial u}{\partial y} + i\frac{\partial v}{\partial y}. \tag{A.32}$$

Thus, these partials are simply corresponding columns of the derivative matrix $Df(a)$. Now, if $x = (z + \bar{z})/2$ and $y = (z - \bar{z})/2i$, take partial derivatives of f with respect to z and $\bar{z}$ via chain rule. Obtain the following

$$\begin{aligned}\frac{\partial f}{\partial z} &= \frac{\partial f}{\partial x}\frac{\partial x}{\partial z} + \frac{\partial f}{\partial y}\frac{\partial y}{\partial z} \\ &= \frac{1}{2}\frac{\partial f}{\partial x} + \frac{1}{2i}\frac{\partial f}{\partial y}\end{aligned}$$

so

$$\frac{\partial f}{\partial z} = \frac{1}{2}\left(\frac{\partial f}{\partial x} - i\frac{\partial f}{\partial y}\right)$$

and, for derivative with respect to the conjugate of z,

$$\begin{aligned}\frac{\partial f}{\partial \bar{z}} &= \frac{\partial f}{\partial x}\frac{\partial x}{\partial \bar{z}} + \frac{\partial f}{\partial y}\frac{\partial y}{\partial \bar{z}} \\ &= \frac{1}{2}\frac{\partial f}{\partial x} - \frac{1}{2i}\frac{\partial f}{\partial y}\end{aligned}$$

so

$$\frac{\partial f}{\partial \bar{z}} = \frac{1}{2}\left(\frac{\partial f}{\partial x} + i\frac{\partial f}{\partial y}\right)$$

which motivates the following definition for partial derivatives of f with respect to z and with respect to $\bar{z}$,

Definition. *For $f : U \subseteq \mathbb{C} \to \mathbb{C}$ given by $f(z) = u(z) + iv(z)$, define the following partial derivatives*

$$\frac{\partial f}{\partial z} = \frac{1}{2}\left(\frac{\partial f}{\partial x} - i\frac{\partial f}{\partial y}\right) \tag{A.33}$$

$$\frac{\partial f}{\partial \bar{z}} = \frac{1}{2}\left(\frac{\partial f}{\partial x} + i\frac{\partial f}{\partial y}\right). \tag{A.34}$$

Multiples of equations (A.31), (A.32), (A.33), and (A.34) may be added and subtracted to obtain

$$\frac{\partial f}{\partial x} = \frac{\partial f}{\partial z} + \frac{\partial f}{\partial \bar{z}}, \tag{A.35}$$

$$\frac{\partial f}{\partial y} = i\left(\frac{\partial f}{\partial z} - \frac{\partial f}{\partial \bar{z}}\right), \tag{A.36}$$

$$\frac{\partial f}{\partial z} = \frac{1}{2}\left(\frac{\partial u}{\partial x} + \frac{\partial v}{\partial y} + i\left(\frac{\partial v}{\partial x} - \frac{\partial u}{\partial y}\right)\right), \text{ and} \tag{A.37}$$

$$\frac{\partial f}{\partial \bar{z}} = \frac{1}{2}\left(\frac{\partial u}{\partial x} - \frac{\partial v}{\partial y} + i\left(\frac{\partial v}{\partial x} + \frac{\partial u}{\partial y}\right)\right). \tag{A.38}$$

Also, from these definitions, the following natural formulae also hold, $\frac{\partial z}{\partial z} = 1$, $\frac{\partial \bar{z}}{\partial \bar{z}} = 1$, $\frac{\partial z}{\partial \bar{z}} = 0$, $\frac{\partial \bar{z}}{\partial z} = 0$, and, for any constant $a \in \mathbb{C}$, $\frac{\partial c}{\partial z} = \frac{\partial a}{\partial \bar{z}} = 0$.

Definition (complex differentiable)**.** *$f : U \subseteq \mathbb{C} \to \mathbb{C}$ is* complex differentiable *at $a \in \mathbb{C}$ if and only if the limit*

$$\left.\frac{df}{dz}\right|_a = \lim_{z \to a} \frac{f(z) - f(a)}{z - a} \tag{A.39}$$

exists and we say that the limit, $\left.\frac{df}{dz}\right|_a$, sometimes written $f'(a)$, is the derivative of f at a.

Definition (holomorphic)**.** *$f : U \subseteq \mathbb{C} \to \mathbb{C}$ is* holomorphic *on U if and only if f is complex differentiable at every point of U.*

Sometimes, instead of complex differentiable, some authors will say that the function is holomorphic at a point. Here, holomorphy refers to complex differentiability on an open set which is the domain of the function. Some authors use *analytic* instead of these, but, f is analytic at a point $z \in \mathbb{C}$ if and only if the Taylor series of f converges to f on a neighborhood of z. It turns out that wherever f is holomorphic, derivatives of every order of f exist, and consequently that f is analytic there. So, via a theorem, these notions are equivalent, however, they are employed when different aspects of differentiability are to be emphasized.

Definition (anti-holomorphic)**.** *For $f : U \subseteq \mathbb{C} \to \mathbb{C}$, when the limit*

$$\left.\frac{df}{dz}\right|_a = \lim_{z \to a} \frac{f(z) - f(a)}{\bar{z} - \bar{a}} \tag{A.40}$$

exists for every point $a \in U$, and we say that f is anti-holomorphic *on U.*

Theorem A.4. *For an open set $U \subseteq \mathbb{C}$ and function $f : U \to \mathbb{C}$, the following are equivalent:*

1. *f is holomorphic on U,*
2. *f is differentiable (in the real sense) but $\frac{\partial f}{\partial \bar{z}} = 0$, and*
3. *$\frac{\partial u}{\partial x} = \frac{\partial v}{\partial y}$ and $\frac{\partial u}{\partial y} = -\frac{\partial v}{\partial x}$*

consequently, if any one of the above hold, we may write

$$\frac{df}{dz} = \frac{\partial f}{\partial z}$$

by the definitions of partials above.

Theorem A.5. *For an open set $U \subseteq \mathbb{C}$ and function $f : U \to \mathbb{C}$, the following are equivalent:*

1. *f is anti-holomorphic on U,*
2. *f is differentiable (in the real sense) but $\frac{\partial f}{\partial z} = 0$, and*
3. *$\frac{\partial u}{\partial x} = -\frac{\partial v}{\partial y}$ and $\frac{\partial u}{\partial y} = \frac{\partial v}{\partial x}$*

consequently, if any ones of these hold, we may write

$$\frac{df}{d\bar{z}} = \frac{\partial f}{\partial \bar{z}}$$

by the definitions of partials above.

The equations in (3) in theorem A.4 are known as the *Cauchy-Riemann Equations* and turn out to be extremely important in the subsequent discussion of harmonic functions, they are repeated here in rectangular form for convenience

$$\frac{\partial u}{\partial x} = \frac{\partial v}{\partial y} \text{ and } \frac{\partial v}{\partial x} = -\frac{\partial u}{\partial y} \tag{A.41}$$

Finally, the complex form of the inverse function theorem is stated here without proof, the proof follows from the result for real functions on the plane.

Theorem A.6 (Inverse Function Theorem)**.** *$f : U \subseteq \mathbb{C} \to \mathbb{C}$ holomorphic in U and $f'(a) \neq 0$ for some $a \in U$ entails that f is invertible on a restriction of its domain, and the inverse f^{-1} will be holomorphic near $f(a)$ with*

$$\left.\frac{d}{dz} f^{-1}\right|_{f(z)} = \frac{1}{f'(z)}$$

on a neighborhood of $f(a)$.

A.4.2 Conformal Mapping and Harmonic Functions

A mapping $f : U \subseteq \mathbb{C} \to \mathbb{C}$ preserves orientation whenever $\det Df(a)$ is strictly positive, and reverses orientation whenever the determinant of the derivative matrix is strictly negative. It should be apparent, by the Cauchy-Riemann equations that holomorphic maps preserve orientation and antiholomorphic maps reverse it. In other words, antiholomorphic maps entail some sort of reflection whereas holomorphic maps disallow reflection. f is an isometry whenever it preserves distance, that is $|f(b) - f(a)| = |b - a|$ for all $a, b \in U$, when this doesn't hold, but when some fixed $k > 0$ exists and, for all $a, b \in U$, $|f(b) - f(a)| = k\,|b - a|$, f is a similarity transform or a scaling of factor k. Finally, a map is *conformal* when it preserves angles. This preservation of angles is illustrated in Figure A.4 in which the angles at intersections of gridlines remain identical at corresponding intersections in the pre-image and in the image. The notion of conformal is valid for real functions between spaces, and stated in general.

Definition (conformal)**.** *A mapping $f : U \subseteq \mathbb{R}^n \to \mathbb{R}^m$ is* conformal *at $a \in \mathbb{R}^n$ if and only if f preserves angles between curves at a, i.e. whenever*

$$\frac{Df\vec{u} \cdot Df\vec{v}}{\|Df\vec{u}\|\ \|Df\vec{v}\|} = \frac{\vec{u} \cdot \vec{v}}{\|\vec{u}\|\ \|\vec{v}\|}$$

for all vectors $u, v \in \mathbb{R}^n$. f is said to be conformal on U or simply conformal whenever f is conformal on its domain, i.e, at every $a \in U$.

For complex functions of a complex variable, we have the special case where $m = n = 2$. So, complex functions of a complex variable are conformal at a point whenever paths through the point have tangent vectors which are orthogonal.

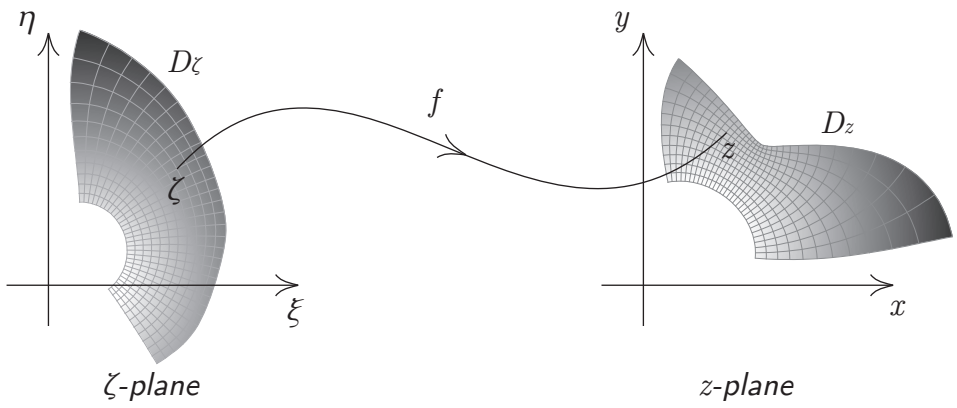

FIGURE A.4: This schematic of the conformal mapping $f : D_\zeta \subseteq \mathbb{C} \to \mathbb{C}$ shows that it associates points in region D_z in the z-plane with points in domain D_ζ in the ζ-plane, i.e., that points $\zeta \in D_\zeta$ are mapped to points $z \in D_z$. Paying close attention to the ruling of the regions with paths, where they intersect at ζ and at z, the angle between the curves remains fixed under the mapping.

Theorem A.7. *f is conformal at a if and only if either f is holomorphic or antiholomorphic at a with non-vanishing derivative at a. If U is connected, f is conformal in U if and only if either f is either holomorphic or antiholomorphic on U with non-vanishing derivative there.*

Proof. f is conformal at a point if and only if $Df(a)$ is a positive scalar multiple of an orthogonal matrix. Holomorphy and antiholomorphy ensure that the derivative matrix is a multiple of some orthogonal matrix. For the second part, because $f \in \mathcal{C}^2$ and U is connected and the derivative does not vanish on U, the determinant of Df is continuous and either always positive or always negative. That is, because it is continuous on a connected set where it doesn't obtain the value zero, it must be always positive or always negative. □

Definition (harmonic)**.** *$h : U \subseteq \mathbb{C} \to \mathbb{C}$. The two-dimensional Laplacian ∇^2 is the differential operator given by*

$$\nabla^2 h = \frac{\partial^2 h}{\partial x^2} + \frac{\partial^2 h}{\partial y^2}$$

in rectangular form. The mapping h is called harmonic *if and only if*

$$\nabla^2 h = 0$$

$\nabla^2 h = 0$ is a second-order partial differential equation know as Laplace's Equation.

Theorem A.8. *$f(z) = u(z) + iv(z)$ holomorphic on U, then u and v are both harmonic functions.*

v is known as the harmonic conjugate of u. The proof follows.

Proof. By CRE,

$$\frac{\partial^2 u}{\partial x^2} = \frac{\partial}{\partial x}\left(\frac{\partial u}{\partial x}\right) = \frac{\partial}{\partial x}\left(\frac{\partial v}{\partial y}\right) = \frac{\partial^2 v}{\partial x \partial y} = \frac{\partial^2 v}{\partial y \partial x} = \frac{\partial}{\partial y}\left(\frac{\partial v}{\partial x}\right) = \frac{\partial}{\partial y}\left(-\frac{\partial u}{\partial y}\right) = -\frac{\partial^2 u}{\partial y^2}$$

where the equivalence of the mixed partials is a consequence of the fact that $f \in \mathcal{C}^2$, so

$$\frac{\partial^2 u}{\partial x^2} = -\frac{\partial^2 u}{\partial y^2} \quad \text{or} \quad \frac{\partial^2 u}{\partial x^2} + \frac{\partial^2 u}{\partial y^2} = 0$$

as required. □

Theorem A.9. *If $h : U \subseteq \mathbb{C} \to \mathbb{C}$ is harmonic and if $f : V \subseteq \mathbb{C} \to U \subseteq \mathbb{C}$ is holomorphic, then $h \circ f$ is harmonic on V.*

Proof. Write $x + iy = f(s + it)$, $h = h(x + iy)$, and $v = h \circ f$. Chain rule entails that $v_s = h_x x_s + h_y y_s$ and $v_t = h_x x_t + h_y y_t$. Differentiating again via chain rule and product rule, obtain

$$v_{ss} = (h_{xx}x_s + h_{xy}y_s)x_s + h_x x_{ss} + (h_{yx}x_s + h_{yy}y_s)y_s + h_y y_{ss} \text{ and}$$
$$v_{tt} = (h_{xx}x_t + h_{xy}y_t)x_t + h_x x_{tt} + (h_{yx}x_t + h_{yy}y_t)y_t + h_y y_{tt}$$

and, adding, together with equality of mixed partials because $h \in \mathcal{C}^1$, obtain

$$\begin{aligned} v_{ss} + v_{tt} &= (h_{xx}x_s + h_{xy}y_s)x_s + h_x x_{ss} + (h_{yx}x_s + h_{yy}y_s)y_s + h_y y_{ss} + \\ &\qquad (h_{xx}x_t + h_{xy}y_t)x_t + h_x x_{tt} + (h_{yx}x_t + h_{yy}y_t)y_t + h_y y_{tt} \\ &= h_{xx}(x_s^2 + x_t^2) + h_{xy}(y_s x_s + y_t x_t) + h_x(x_{ss} + x_{tt}) + \\ &\qquad h_{yx}(x_s y_s + x_t y_t) + h_{yy}(y_s^2 + y_t^2) + h_y(y_{ss} + y_{tt}) \\ &= h_{xx}(x_s^2 + x_t^2) + 2h_{xy}(x_s y_s + x_t y_t) + h_{yy}(y_s^2 + y_t^2) + h_x(x_{ss} + x_{tt}) + h_y(y_{ss} + y_{tt}) \end{aligned}$$

the final two terms vanish because f is holomorphic, i.e. x and y are harmonic conjugates, so

$$v_{ss} + v_{tt} = h_{xx}(x_s^2 + x_t^2) + 2h_{xy}(x_s y_s + x_t y_t) + h_{yy}(y_s^2 + y_t^2)$$

and, again by holomorphy of f,

$$= h_{xx}(x_s^2 + y_s^2) + 2h_{xy}((y_t)y_s + (-y_s)y_t) + h_{yy}((-x_t)^2 + y_t^2)$$

so

$$v_{ss} + v_{tt} = (h_{xx} + h_{yy})(x_s^2 + y_s^2).$$

Finally, h is harmonic, so the right hand side vanishes, and we obtain

$$v_{ss} + v_{tt} = 0$$

and conclude that v satisfies Laplace's equation, i.e. v is harmonic, as required. □

A.5 The Complex Integral and Laurent Series

A.5.1 The Complex Integral

Complex integrals are path integrals defined in the complex plane. Complex integrals are defined in such a way that, when the path is restricted to the real axis, the path integral collapses to the familiar Riemann-Stieltjes integral in $\mathbb{R}$.

Definition (path integral)**.** *For an open set $U \in \mathbb{C}$, a path in U, $\gamma : [t_1, t_2] \to U$, and a function $f : U \to \mathbb{C}$ continuous on U, define the* path integral *of f along γ by*

$$\int_\gamma f(z)\,dz = \int_{t_1}^{t_2} f(\gamma(t))\,\gamma'(t)\,dt.$$

The complex integral defined above has several properties which follow from the real counterparts.

Theorem A.10 (linearity)**.** *Let γ be a path in an open set $U \subseteq \mathbb{C}$. Suppose $f, g : U \to \mathbb{C}$ are continuous functions on U and $c \in \mathbb{C}$, then the following hold*

$$\int_\gamma c\,f(z)\,dz = c\int_\gamma f(z)\,dz \quad \textit{and} \quad \int_\gamma f(z)+g(z)\,dz = \int_\gamma f(z)\,dz + \int_\gamma g(z)\,dz. \tag{A.42}$$

Theorem A.11 (additivity)**.** *for $f : U \to \mathbb{C}$ continuous,*

$$\int_\gamma f(z)\,dz = \sum_{k=1}^{n} \int_{\gamma_k} f(z)\,dz$$

where γ_k is the restriction of γ to the i^{th} interval.

The complex integral is independent of parameter. This is usually summarized as a change of parameter theorem. What this entails is that the same curve traversed in the same direction, yields an integral which is independent of the rate at which the curve is traversed. To see this, suppose $\sigma : [t_1, t_2] \subseteq \mathbb{R} \to [s_1, s_2] \subseteq \mathbb{R}$ invertible, increasing, and piecewise $\mathcal{C}^1$, $\gamma : [s_1, s_2] \to U \subseteq \mathbb{C}$ a path in U, $\beta : [s_1, s_2] \to U \subseteq \mathbb{C}$ a path in U defined by $\beta(t) = \gamma(\sigma(t))$ for $t_1 \le t \le t_2$, $f : U \to \mathbb{C}$ continuous, then

$$\int_\beta f = \int_\gamma f$$

to see this,

$$\begin{aligned}\int_{\beta} f(z)\,dz &= \int_{t_1}^{t_2} f(\beta(t))\beta'(t)\,dt \\ &= \int_{t_1}^{t_2} f(\gamma(\sigma(t)))\,(\gamma(\sigma(t)))'\,dt \\ &= \int_{t_1}^{t_2} f(\gamma(\sigma(t)))\gamma'(\sigma(t))\sigma'(t)\,dt\end{aligned}$$

with the substitution $s = \sigma(t)$, $ds = \sigma'(t)\,dt$, so

$$\begin{aligned}&= \int_{s_1}^{s_2} f(\gamma(s))\gamma'(s)\,ds \\ &= \int_{\gamma} f(z)\,dz\end{aligned}$$

as required.

Additivity and change of parameter theorems are employed when integration is performed along a path which is formed from existing contiguous paths and the integral along each part is defined.

Definition (arclength)**.** *The arclength $L(\gamma)$ of a path $\gamma : [t_1, t_2] \to U \subseteq \mathbb{C}$ is*

$$L(\gamma) = \int_{t_1}^{t_2} |\gamma'(t)|\,dt.$$

When a curve has an arclength computable by an integral of this form, it is called *rectifiable*. Path integrals are rectifiable because paths are piecewise continuous. In other words, the nature of paths γ, by their definition, ensure that integrals of the form L exist.

Theorem A.12 (estimation)**.** *Let $\gamma : [t_1, t_2] \to U$ be a path in an open set $U \subseteq \mathbb{C}$. Suppose $L = L(\gamma)$ and $M = \max_{z\in\gamma} ||$, then*

$$\left|\int_{\gamma} f(z)\,dz\right| \leq \int_{t_1}^{t_2} |f(\gamma(t))\gamma'(t)|\,dt \leq ML$$

Definition (antiderivative)**.** *$f, g : U \subseteq \mathbb{C} \to \mathbb{C}$, $g'(z) = f(z)$ for all $z \in U$, then $g = \int f$. In this case, we call g the antiderivative of f on U.*

Theorem A.13. *Let $U \subseteq \mathbb{C}$ be a non-empty connected open set, $f, g : U \subseteq \mathbb{C} \to \mathbb{C}$ be holomorphic with $f' = g'$ in U. Then there exists a $C \in \mathbb{C}$ so that $f = g + C$ in U.*

The theorem effectively states that antiderivatives are unique up to an additive constant.

Theorem A.14 (fundamental theorem of calculus)**.** *$\gamma : [t_1, t_2] \to U \subseteq \mathbb{C}$ a path in U, $f, g : U \subseteq \mathbb{C} \to \mathbb{C}$, f continuous, g holomorphic with $g' = f$ on U, then*

$$\int_\gamma f = g(z)\Big|_{\gamma(t_1)}^{\gamma(t_2)}$$

and, if γ is a loop,

$$\int_\gamma f = 0.$$

Definition (winding number)**.** *For a path $\gamma : [t_1, t_2] \to U \subseteq \mathbb{C}$ and a point $a \in \mathbb{C}$ not on γ, the* winding number*, sometimes called the* index *and denoted by $\mathrm{Ind}(\gamma, a)$, of γ about a is the net angular displacement as a point trajects along γ from $\gamma(t_1)$ to $\gamma(t_2)$. This is made precise by writing $\gamma(t) = a + r(t)e^{i\theta(t)}$ in which $r(t) = |\gamma(t) - a|$ and $\theta(t)$ is selected so that it is a continuum of angles, $0 \leq \theta(t_1) \leq 2\pi$, and defined by $\theta(t) = \arg(\gamma(t) - a)$. In this case,*

$$\mathrm{Ind}(\gamma, a) = \frac{\theta(t_2) - \theta(t_1)}{2\pi}.$$

It can be shown that, for a path $\gamma(t) = a + r(t)e^{i\theta(t)}$ as above,

$$\int_\gamma \frac{dz}{z - a} = \ln \frac{r(t_2)}{r(t_1)} + 2\pi i \,\mathrm{Ind}(\gamma, a)$$

and, for a loop γ, this collapses to

$$\mathrm{Ind}(\gamma, a) = \frac{1}{2\pi i} \int_\gamma \frac{dz}{z - a}.$$

A.5.2 Cauchy's Integral Theorem

Theorem A.15. *For an open subset of the plane $U \subseteq \mathbb{C}$ and function $f : U \to \mathbb{C}$ holomorphic on U, if $\mathcal{C}_1$ and $\mathcal{C}_2$ are homotopic paths in U,*

$$\int_{\mathcal{C}_1} f(z)\, dz = \int_{\mathcal{C}_2} f(z)\, dz.$$

The proof of this is found in the standard texts mentioned at the beginning of this appendix, in particular, [40, 57, 80] furnish particularly rigorous and complete proofs. This result immediately entails the remarkable result for closed curves. We have the following in

simply open connected sets U and functions $f : U \to \mathbb{C}$ holomorphic on U, and simply connected curves $\mathcal{C}$ which lie in U,

$$\oint_{\mathcal{C}} f(z)\, dz = 0.$$

A.5.3 Laurent Series and the Residue Theorem

Theorem A.16 (Taylor Series)**.** *Whenever $f(z)$ is holomorphic on a disk of radius $R < \infty$ about a point $c \in \mathbb{C}$, obtain*

$$f(z) = \sum_{n=0}^{\infty} a_n (z-c)^n$$

where

$$a_n = \frac{f^{(n)}(c)}{n!} = \frac{1}{2\pi i} \oint_{\mathcal{C}} \frac{f(z)}{(z-c)^{n+1}}\, dz$$

where $\mathcal{C}$ is taken to be the circular positively oriented path within the disk, i.e. with $r < R$, given by parameterization $z(t) = c + re^{it}$ for $t \in [0, 2\pi]$.

Proof. Before proceeding with the bulk of the proof, observe the following about finite geometric series

$$\begin{aligned} 1 + r + r^2 + \cdots + r^{N-1} + \frac{r^N}{1-r} &= \left(1 + r + r^2 + \cdots + r^{N-1}\right) + \frac{r^N}{1-r} \\ &= \frac{r^N - 1}{r-1} + \frac{r^N}{1-r} = \frac{1-r^N}{1-r} + \frac{r^N}{1-r} = \frac{1-r^N+r^N}{1-r} \\ &= \frac{1}{1-r}. \end{aligned}$$

We begin the proof of the main result. The proof follows for the case in which $c = 0$; however, the result for non-zero c follows simply by a geometric translation of the origin by c. Firstly, fix z within the disk of radius R centred at the origin. Select r with $|z| < r < R$ so that $\mathcal{C}$ is on the disk but contains z. By Cauchy's integral formula, obtain

$$\begin{aligned} f(z) &= \frac{1}{2\pi i} \oint_{\mathcal{C}} \frac{f(s)}{s-z}\, ds = \frac{1}{2\pi i} \oint_{\mathcal{C}} \frac{f(s)}{s} \frac{1}{1-\frac{z}{s}}\, ds \\ &= \frac{1}{2\pi i} \oint_{\mathcal{C}} \frac{f(s)}{s} \left(1 + \frac{z}{s} + \left(\frac{z}{s}\right)^2 + \cdots + \left(\frac{z}{s}\right)^{N-1} + \frac{\left(\frac{z}{s}\right)^N}{1-\left(\frac{z}{s}\right)}\right) ds \end{aligned}$$

and, with r replaced with z/s in the result about finite geometric series demonstrated earlier, this becomes

$$= \sum_{n=0}^{N-1} \frac{1}{2\pi i} \oint_{\mathcal{C}} \frac{f(s)}{s} \left(\frac{z}{s}\right)^n ds + \frac{1}{2\pi i} \oint_{\mathcal{C}} \frac{f(s)}{s} \frac{\left(\frac{z}{s}\right)^N}{1 - \left(\frac{z}{s}\right)} ds$$

so

$$f(z) = \sum_{n=0}^{N-1} \frac{1}{2\pi i} \oint_{\mathcal{C}} \frac{f(s)}{s^{n+1}} ds\, z^n + \frac{1}{2\pi i} \oint_{\mathcal{C}} \frac{f(s)}{s} \frac{\left(\frac{z}{s}\right)^N}{1 - \left(\frac{z}{s}\right)} ds.$$

Now, we try to bound the second term so that it vanishes as $N \longrightarrow \infty$. Set $M = \max_{s \in \mathcal{C}} f(s)$, consequently,

$$\left| \frac{1}{2\pi i} \oint_{\mathcal{C}} \frac{f(s)}{s} \frac{\left(\frac{z}{s}\right)^N}{1 - \left(\frac{z}{s}\right)} ds \right| \leq \frac{1}{2\pi} \frac{M}{r} \frac{\left(\frac{|z|}{r}\right)^N}{1 - \left(\frac{|z|}{r}\right)} \cdot 2\pi r$$

but $\mathcal{C}$ contains z so $|z| < r$, so the expression vanishes in the limit. So we take limits as $N \longrightarrow \infty$ and obtain

$$f(z) = \sum_{n=0}^{\infty} \frac{1}{2\pi i} \oint_{\mathcal{C}} \frac{f(s)}{s^{n+1}} ds\, z^n = \sum_{n=0}^{\infty} \frac{f^{(n)}(0)}{n!} z^n$$

where the second equality follows from the generalized Cauchy integral, and the desired result is obtained. □

Theorem A.17 (Laurent[1] Series)**.** *Whenever $f(z)$ is holomorphic on an annulus $0 < r < |z - c| < R < \infty$ about a point $c \in \mathbb{C}$, obtain*

$$f(z) = \sum_{n=-\infty}^{\infty} a_n (z - c)^n$$

where

$$a_n = \frac{1}{2\pi i} \oint_{\mathcal{C}} \frac{f(z)}{(z - c)^{n+1}} dz$$

where $\mathcal{C}$ is a closed rectifiable curve with no self-intersection and encloses c, but lies in the annulus as shown in Figure A.5.

[1] Pierre Alphonse Laurent (1813–1854), a French mathematician, discovered this result in 1843.

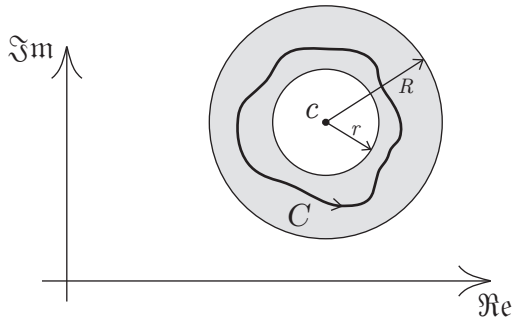

FIGURE A.5: Annular region in $\mathbb{C}$ about c with inner radius r and outer radius R with curve $\mathcal{C}$ lying in the annulus and surrounding the centre.

Definition (residue)**.** *A residue of f at $c \in \mathbb{C}$, denoted by* $\operatorname{Res}(f, c)$*, is the coefficient of a_{-1} in the Laurent series for f about c.*

Theorem A.18 (Residue Theorem)**.** *Let $U \subseteq \mathbb{C}$ be an open set. Suppose f is holomorphic on $U \backslash \{a_1, a_2, \ldots, a_N\}$ where f is singular at each a_k. For a closed rectifiable curve $\mathcal{C}$ in U which does not pass through any a_k,*

$$\oint_{\mathcal{C}} f(z)\, dz = 2\pi i \sum_{k=1}^{N} \operatorname{Ind}(\mathcal{C}, a_k) \cdot \operatorname{Res}(f, a_k)$$

where $\operatorname{Ind}(\mathcal{C}, a_k)$ *is the winding number of $\mathcal{C}$ about a_k.*

A.6 Schwarz-Christoffel Mapping

Consult *Schwarz-Christoffel Mapping*, [24], for detailed discussion of the MATLAB package, implementation and numerics, history, and motivation. Here, we work through an argument which shows how the map takes the upper half plane, $H^+ = \{\zeta \in \mathbb{C} \mid \mathfrak{Im}\, \zeta > 0\}$, to the interior of a polygon P, then suggest how a strip $S = \{\zeta \in \mathbb{C} \mid 0 < \mathfrak{Im}\, \zeta < 1\}$ in the auxiliary plane is mapped to a channel with constriction in the physical plane. Consider the conformal mapping of upper half plane to the interior of some polygon, $f : H^+ \to P \subseteq \mathbb{C}$, defined by

$$f(\zeta) = A + C \int^{\zeta} \prod_{k=1}^{n-1} (s - \zeta_k)^{\alpha_k - 1}\ ds \tag{A.43}$$

and define pre-vertices ζ_k and corresponding vertices z_k of polygon P according to the relation $z_k = f(\zeta_k)$ for ζ_k restricted to the real axis for all $k = 1, 2, \ldots, n-1$ and taken in order so that $\zeta_l < \zeta_m$ whenever $l < m$. Define $z_n = f(\infty)$. We now study the behaviour of this map on the boundary of the domain. The derivative of (A.43) is

$$f'(\zeta) = C \prod_{k=1}^{n-1} (\zeta - \zeta_k)^{\alpha_k - 1}$$

so the argument of the derivative, which gives insight into the orientation of the image, is

$$\arg\left(f'(\zeta)\right) = \arg C + \sum_{k=1}^{n-1} \arg\left((\zeta-\zeta_k)^{\alpha_k-1}\right) = \arg C + \sum_{k=1}^{n-1} (\alpha_k - 1)\arg\left(\zeta-\zeta_k\right).$$

So, when $\zeta \in \mathbb{R}$, either $\zeta < \zeta_k$ or $\zeta > \zeta_k$. Note that $\arg(\zeta-\zeta_k) = \pi$ in the former case and vanishes in the latter. Hence, the sum of arguments is the sum of step functions with steps at ζ_k. The sum simply accumulates the jumps and remains constant on each interval between. In particular, for $\zeta \in \mathbb{R}$,

$$\arg\left(\zeta-\zeta_k\right) = \begin{cases} (\alpha_k - 1)\,\pi, & \text{if } \zeta < \zeta_k; \\ 0, & \text{if } \zeta_k < \zeta \end{cases} \tag{A.44}$$

Consider the k^{th} vertex and its image as displayed in Figure A.6. Define $\beta_k = 1 - \alpha_k$. Observe that the jump in the argument at the k^{th} is by an angle $\beta_k\pi$. This is evident because the argument of f' is

$$\arg C + \pi \sum_{l=1}^{k-1} \beta_l$$

but as the pre-vertex ζ_k is crossed, the argument of f' jumps by $\pi\beta_k$ to

$$\arg C + \pi \sum_{l=1}^{k-1} \beta_l + \pi\beta_k.$$

From this, it is evident that the αs give interior angles at the vertices of the polygon, whereas the βs give angles through which the edges are rotated at each vertex. It should also be evident that H^+ is mapped to the interior of the polygon and the real axis to its boundary.

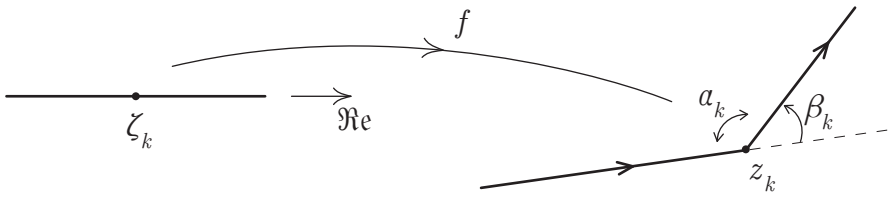

FIGURE A.6: The image on the left is a segment of the real axis in the ζ plane and contains pre-vertex ζ_k. The image on the right is around vertex z_k. The argument of f' remains constant along the edge leading up to z_k. The argument jumps by an amount β_k at the vertex, and the argument remains constant until the next vertex is reached, where there will be a similar finite jump in the argument of the derivative.

A.6.1 Mapping from the Horizontal Strip of Unit Width

From [24], the mapping from the horizontal strip $S = \{\zeta \in \mathbb{C} \mid 0 < \mathfrak{Im}\,\zeta < 1\}$ to the interior of a polygon P is given by

$$f(\zeta) = A + C \int^{\zeta} \exp\left(\frac{\pi}{2}(\alpha_- - \alpha_+)\, s\right) \prod_{k=1}^{n} \left(\sinh\left(\frac{\pi}{2}(s - \zeta_k)\right)\right)^{\beta_k} ds \tag{A.45}$$

The general scheme is that the hyperbolic sine maps S to a slit half plane. The ends of the strip map to ∞. $\exp\left(\frac{\pi}{2}(\alpha_- - \alpha_+)\, s\right)$ is inserted to account for the divergence angle at each end.

A.7 Connections to 2-D Potential Flow

For an incompressible flow, the continuity equation is

$$\nabla \cdot \vec{v} = 0 \tag{A.46}$$

in which $\vec{v}$ is the Eulerian velocity field of the flow. Furthermore, if the flow is inviscid, conservation of momentum is governed by Euler's equations for momentum,

$$\frac{D}{Dt}\vec{v} = -\frac{1}{\rho}\nabla P + \vec{f} \tag{A.47}$$

in which ρ is the density of the flow, P is the Eulerian pressure field, $\vec{f}$ is a field of conservative body forces per unit mass, and D/Dt is the material derivative, defined for a scalar quantity α as

$$\frac{D}{Dt}\alpha = \frac{\partial \alpha}{\partial t} + \vec{v} \cdot \nabla \alpha, \tag{A.48}$$

so the material derivative of a vector is taken componentwise. One would normally solve equations (A.46) and (A.47) together with appropriate boundary conditions on the velocity and pressure fields to obtain these fields, but, if the flow is irrotational, i.e., $\nabla \times \vec{v}$ vanishes, then $\vec{v}$ may be written as the gradient of a scalar field Φ, the velocity potential, as $\vec{v} = \nabla\Phi$. When this expression is substituted into equation (A.46),

$$0 = \nabla \cdot \vec{v} = \nabla \cdot \nabla\Phi = \nabla^2\Phi,$$

one obtains Laplace's equation for the velocity potential Φ,

$$\nabla^2\Phi = 0. \tag{A.49}$$

Equation (A.49) may be solved with corresponding boundary conditions, and the velocity field may be recovered simply by taking the gradient of Φ once it is known.

If, in addition to the above simplifying assumptions, if the flow is also two-dimensional, complex variables may be employed. The complex potential is defined by

$$F(z) = \Phi(z) + i\Psi(z) \tag{A.50}$$

in which $\Phi(z) = \Phi(x, y)$ is the velocity potential for a given flow and $\Psi(z) = \Psi(x, y)$, the harmonic conjugate of Φ, is the corresponding streamfunction. It turns out that a quantity called the complex velocity,

$$w(z) = \frac{dF}{dz}, \tag{A.51}$$

has the property that its conjugate corresponds to the velocity field of the flow, i.e.,

$$\vec{v} = \big(\mathfrak{Re}\,(\overline{w})\,,\, \mathfrak{Im}\,(\overline{w}) \big). \tag{A.52}$$

To see that this is so, observe that, via the discussion of differentiation in section A.4 above,

$$w(z) = \frac{dF}{dz} = \frac{d}{dz}\big(\Phi(z) + i\Psi(z)\big) = \frac{\partial \Phi}{\partial x} + i\frac{\partial \Psi}{\partial x},$$

but, by the Cauchy-Riemann eqations, (3),

$$\frac{\partial \Psi}{\partial x} = -\frac{\partial \Phi}{\partial y},$$

the complex velocity becomes

$$w(z) = \frac{\partial \Phi}{\partial x} - i\frac{\partial \Phi}{\partial y}.$$

Consequently,

$$\overline{w} = \frac{\partial \Phi}{\partial x} + i\frac{\partial \Phi}{\partial y}$$

and

$$\vec{v} = \big(\frac{\partial \Phi}{\partial x},\, \frac{\partial \Phi}{\partial y}\big)$$

so

$$\vec{v} = \big(\mathfrak{Re}\,(\overline{w})\,,\, \mathfrak{Im}\,(\overline{w}) \big)$$

as expected.

Because Laplace's equation is a linear PDE, a superposition of harmonic functions is also harmonic, so superpositions of complex potentials are complex potentials of flows which are due to a superposition of potentials. Consequently, one may build up solutions in a region of simple geometry if one knows the potentials due to which the flow arises.

This is process of building up potential functions due to known potentials is further enriched by conformal mappings and harmonicity already discussed. That is, if one has a complex potential defined in a region which corresponds to a flow, and additionally, one has a conformal mapping which maps that domain to another domain, the composition of the complex potential with the inverse of the conformal mapping is a complex potential on a region which is the range of the conformal mapping. This is the principal way in which complex potentials in new regions are obtained; they are related by conformal mappings between the regions.

B | Derivations

Complete derivations of results pertaining to the potentials and derivatives are supplied in this Appendix. The first half presents results pertaining to irrotational vortices in the unbounded plane and confined to the horizontal strip $S = \{\zeta \in \mathbb{C} \mid 0 < \mathfrak{Im}(\zeta) < 1\}$. The second half presents a derivation of the pressure equation evaluated via a frame affixed to the moving fluid-solid interface.

B.1 The Point Vortex and its Complex Potential

B.1.1 The Irrotational Vortex Model

It is possible to think of an irrotational vortex as inducing a velocity v which is identical at all points located at fixed distance r from the centre of the vortex. The velocity may be taken as having no radial component and the positive sense may be defined when the velocity is oriented counter-clockwise. Suppose $\vec{v}$ is the velocity induced at distance r by a positively oriented irrotational vortex located at the origin of the plane. The circulation Γ on a contour equidistant at r may be computed as

$$\Gamma = \oint_C \vec{v} \cdot d\vec{r} = 2\pi r v$$

so

$$v = \frac{\Gamma}{2\pi r}$$

That is, the magnitude of the velocity induced by the vortex at fixed distance r from its centre is directly proportional to the circulation but inversely proportional to the distance from its centre. A single vortex alone and distant from any solid surface in a quiescent fluid has no velocity. Near a wall, in disturbed fluid, or in proximity to other vortices, motion is induced at the centre of the vortex, and it advects at this rate. Exactly how this happens is the thrust of the first major section of this Appendix.

The Complex Potential of the Irrotational Vortex

External to the vortex core, for a vortex located at the origin of the complex plane and taken in the positive sense, at distance r from the origin, obtain velocity

$$\overline{w} = \frac{\Gamma}{2\pi r} e^{i(\theta+\pi/2)}$$

This is a velocity oriented counter-clockwise and tangential at all points on a circle of radius r centred at the origin. Rearranging, obtain

$$\begin{aligned} \overline{w} &= \frac{\Gamma}{2\pi r} i e^{i\theta} \\ w &= -i\frac{\Gamma}{2\pi r} e^{-i\theta} = -i\frac{\Gamma}{2\pi r e^{i\theta}} \\ w &= -i\frac{\Gamma}{2\pi z} \end{aligned}$$

and, taking the anti-derivative, obtain the complex potential for the vortex at the origin

$$\frac{\Gamma}{2\pi i} \log z.$$

Consequently, obtain the complex potential at $z \in \mathbb{C}$ of a vortex with centre at $z_0 \in \mathbb{C}$ inducing circulation Γ is

$$F(z) = \frac{\Gamma}{2\pi i} \log (z - z_0) \tag{B.1}$$

B.1.2 Complex Potential Due to Vortex Confined in Channel

To determine the complex potential due to a lone vortex of strength Γ (taken positive counter-clockwise) located at ζ_0 confined within the horizontal strip $0 \leq \mathfrak{Im}(\zeta_0) \leq 1$ in the pre-image plane, to ensure that the upper and lower walls of the channel remain streamlines, the method of images must be employed. The vortex at ζ_0 must be reflected and the reflections reflected ad infinitum. Consequently, the complex potential at ζ due to the vortex at ζ_0 is the accumulation of the contribution from the vortex and its infinitely many reflected images.

Figure B.1 shows a vortex of strength Γ at ζ_0. The location of the vortex reflected in the real axis is simply the conjugate of ζ_0. This pair may then be translated upwards or downwards by integer multiples of $2i$ in order to recover the locations of the remaining reflected vortices.

The contribution to the complex potential at ζ due to the vortex with strength Γ at ζ_0 is given by the expression for complex velocity, equation (B.1),

$$\frac{\Gamma}{2\pi i} \log (\zeta - \zeta_0),$$

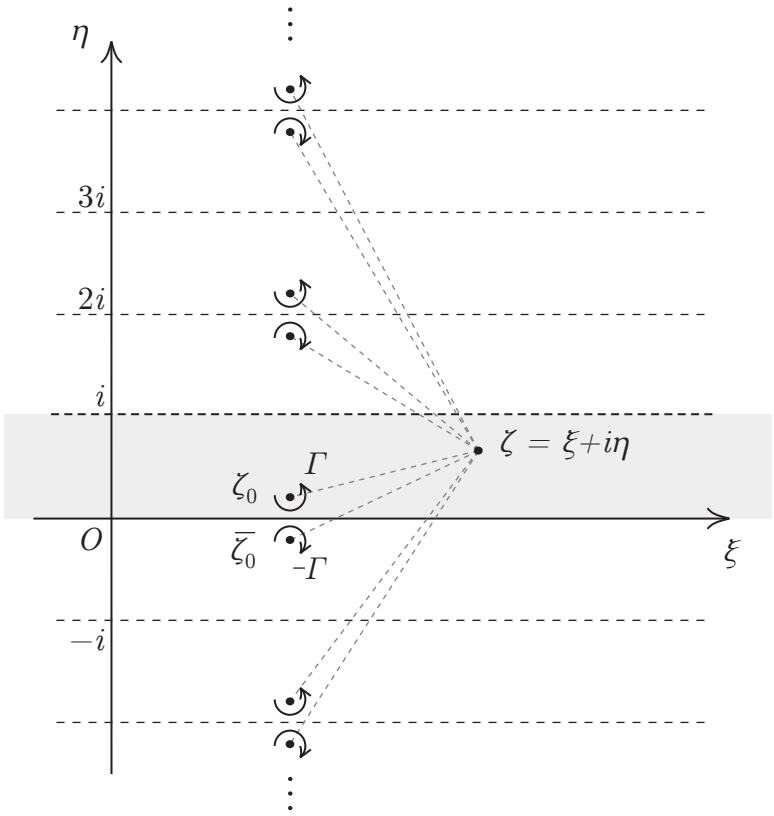

FIGURE B.1: For a vortex of strength Γ located at ζ_0 confined in the horizontal strip $0 \leq \eta \leq 1$, the method of images, whereby the vortex at ζ_0 is reflected above and below the strip infinitely many times, ensures that the boundaries are modelled by streamlines of the flow. The vortex and its reflections together contribute additively to the complex potential at ζ.

and, together with its reflection at $\overline{\zeta}_0$ with strength $-\Gamma$, by

$$\frac{\Gamma}{2\pi i}\left(\log\left(\zeta-\zeta_0\right)-\log\left(\zeta-\overline{\zeta}_0\right)\right).$$

Contributions from translates of this pair obtain the form

$$\frac{\Gamma}{2\pi i}\left(\log\left(\zeta-\left(\zeta_0+2ni\right)\right)-\log\left(\zeta-\left(\overline{\zeta}_0-2ni\right)\right)\right)$$

for $n \in \mathbb{Z}$ representing the n^{th} reflection upwards or downwards depending on whether n is positive or negative respectively. We may therefore write the complex potential at ζ due

to the infinity of vortices as

$$f(\zeta) = \frac{\Gamma}{2\pi i}\Bigg(\log\big(\zeta - \zeta_0\big) - \log\big(\zeta - \overline{\zeta}_0\big) + \\ \log\big(\zeta - (\zeta_0 + 2i)\big) - \log\big(\zeta - \big(\overline{\zeta}_0 - 2i\big)\big) + \\ \log\big(\zeta - (\zeta_0 + 4i)\big) - \log\big(\zeta - \big(\overline{\zeta}_0 - 4i\big)\big) + \cdots \\ + \log\big(\zeta - (\zeta_0 - 2i)\big) - \log\big(\zeta - \big(\overline{\zeta}_0 + 2i\big)\big) + \\ \log\big(\zeta - (\zeta_0 - 4i)\big) - \log\big(\zeta - \big(\overline{\zeta}_0 + 4i\big)\big) + \cdots \Bigg)$$

or, more compactly,

$$\begin{aligned} f(\zeta) &= \frac{\Gamma}{2\pi i} \sum_{n=-\infty}^{\infty} \log \frac{\zeta - (\zeta_0 - 2ni)}{\zeta - \big(\overline{\zeta}_0 - 2ni\big)} \\ &= \frac{\Gamma}{2\pi i} \log \prod_{n=-\infty}^{\infty} \frac{(\zeta - \zeta_0) - 2ni}{\big(\zeta - \overline{\zeta}_0\big) + 2ni} \end{aligned}$$

where the second line follows from the previous because the sum of logarithms is the logarithm of the product. Simplifying the product,

$$\begin{aligned} \prod_{n=-\infty}^{\infty} \frac{(\zeta - \zeta_0) - 2ni}{\big(\zeta - \overline{\zeta}_0\big) + 2ni} &= \frac{(\zeta - \zeta_0)}{\big(\zeta - \overline{\zeta}_0\big)} \prod_{n=1}^{\infty} \frac{(\zeta - \zeta_0) + 2ni}{\big(\zeta - \overline{\zeta}_0\big) + 2ni} \cdot \frac{(\zeta - \zeta_0) - 2ni}{\big(\zeta - \overline{\zeta}_0\big) - 2ni} \\ &= \frac{(\zeta - \zeta_0)}{\big(\zeta - \overline{\zeta}_0\big)} \prod_{n=1}^{\infty} \frac{(\zeta - \zeta_0)^2 - (2ni)^2}{\big(\zeta - \overline{\zeta}_0\big)^2 - (2ni)^2} \\ &= \frac{(\zeta - \zeta_0)}{\big(\zeta - \overline{\zeta}_0\big)} \prod_{n=1}^{\infty} \frac{-(2ni)^2 \left(1 - \frac{\left(\frac{\zeta - \zeta_0}{2i}\right)^2}{n^2}\right)}{-(2ni)^2 \left(1 - \frac{\left(\frac{\zeta - \overline{\zeta}_0}{2i}\right)^2}{n^2}\right)} \\ &= \frac{(\zeta - \zeta_0)}{\big(\zeta - \overline{\zeta}_0\big)} \cdot \frac{\prod_{n=1}^{\infty} \left(1 - \frac{\left(i\frac{\zeta - \zeta_0}{2}\right)^2}{n^2}\right)}{\prod_{n=1}^{\infty} \left(1 - \frac{\left(i\frac{\zeta - \overline{\zeta}_0}{2}\right)^2}{n^2}\right)}, \end{aligned}$$

so obtain

$$f(\zeta) = \frac{\Gamma}{2\pi i} \log \frac{(\zeta - \zeta_0)}{\big(\zeta - \overline{\zeta}_0\big)} \cdot \frac{\prod_{n=1}^{\infty} \left(1 - \frac{\left(i\frac{\zeta - \zeta_0}{2}\right)^2}{n^2}\right)}{\prod_{n=1}^{\infty} \left(1 - \frac{\left(i\frac{\zeta - \overline{\zeta}_0}{2}\right)^2}{n^2}\right)}.$$

This is a succinct expression for the complex potential, but it is not clear that it may be easily differentiable to obtain the complex velocity in the strip. The infinite products might

pose some difficulty; fortuitously, they have a familiar form. The Weierstrass product for $\operatorname{sinc} \pi z = \frac{\sin(\pi z)}{\pi z}$, equation (A.30) discussed in appendix A, which holds for all $z \in \mathbb{C}$, is

$$\frac{\sin(\pi z)}{\pi z} = \prod_{n=1}^{\infty} \left(1 - \frac{z^2}{n^2}\right) \tag{B.2}$$

so

$$\prod_{n=1}^{\infty} \left(1 - \frac{\left(i\frac{\zeta-\zeta_0}{2}\right)^2}{n^2}\right) = \frac{\sin\left(\pi i \frac{\zeta-\zeta_0}{2}\right)}{\pi i \frac{\zeta-\zeta_0}{2}}$$

and

$$\prod_{n=1}^{\infty} \left(1 - \frac{\left(i\frac{\zeta-\bar{\zeta}_0}{2}\right)^2}{n^2}\right) = \frac{\sin\left(\pi i \frac{\zeta-\bar{\zeta}_0}{2}\right)}{\pi i \frac{\zeta-\bar{\zeta}_0}{2}}$$

thus

$$\begin{aligned} f(\zeta) &= \frac{\Gamma}{2\pi i} \log \frac{(\zeta-\zeta_0)}{\left(\zeta-\bar{\zeta}_0\right)} \cdot \frac{\sin\left(\pi i \frac{\zeta-\zeta_0}{2}\right) / \pi i \frac{\zeta-\zeta_0}{2}}{\sin\left(\pi i \frac{\zeta-\bar{\zeta}_0}{2}\right) / \pi i \frac{\zeta-\bar{\zeta}_0}{2}} \\ &= \frac{\Gamma}{2\pi i} \log \frac{\sin\left(\pi i \frac{\zeta-\zeta_0}{2}\right)}{\sin\left(\pi i \frac{\zeta-\bar{\zeta}_0}{2}\right)}. \end{aligned}$$

Finally, via the relation (A.10), $\sin iz = i \sinh z$, obtain

$$f(\zeta) = \frac{\Gamma}{2\pi i} \log \frac{\sinh\left(\frac{\pi}{2}\left(\zeta-\zeta_0\right)\right)}{\sinh\left(\frac{\pi}{2}\left(\zeta-\bar{\zeta}_0\right)\right)}. \tag{B.3}$$

B.1.3 Complex Velocity Due to Vortex Confined in Channel

Complex Velocity at Non-Singular Points

Complex velocity $w(\zeta)$ is the complex derivative of the complex potential $f(\zeta)$, equation (A.51),

$$w(\zeta) = \frac{d}{d\zeta} f(\zeta).$$

The complex velocity has the fortuitous property that the real velocity field due to the complex potential is given by

$$\left(\mathfrak{Re}\left(\overline{w(\zeta)}\right), \mathfrak{Im}\left(\overline{w(\zeta)}\right)\right) \tag{B.4}$$

in which $\overline{w(\zeta)}$ is merely the conjugate of the complex velocity. In other words, the real vector field associated with the conjugate of the complex velocity is the velocity field we

are ultimately seeking. Consequently, because the real velocity field for the flow confined to the channel due to arbitrary vortices is of interest, the complex velocity for this flow at an arbitrary point ζ is obtained simply via the derivative of the complex potential (B.3) with respect to ζ. In the case of a lone vortex at ζ_0, firstly simplify (B.3), the complex potential due to a lone vortex, and subsequently obtain its derivative.

$$f(\zeta) = \frac{\Gamma}{2\pi i} \log \frac{\sinh\left(\frac{\pi}{2}\left(\zeta - \zeta_0\right)\right)}{\sinh\left(\frac{\pi}{2}\left(\zeta - \overline{\zeta}_0\right)\right)} = \frac{\Gamma}{2\pi i}\left(\log\sinh\left(\frac{\pi}{2}\left(\zeta - \zeta_0\right)\right) - \log\sinh\left(\frac{\pi}{2}\left(\zeta - \overline{\zeta}_0\right)\right)\right)$$

and, naturally,

$$\begin{aligned} w(\zeta) = \frac{df}{d\zeta} &= \frac{d}{d\zeta}\frac{\Gamma}{2\pi i}\left(\log\sinh\left(\frac{\pi}{2}\left(\zeta - \zeta_0\right)\right) - \log\sinh\left(\frac{\pi}{2}\left(\zeta - \overline{\zeta}_0\right)\right)\right) \\ &= \frac{\Gamma}{2\pi i}\left(\frac{1}{\sinh\left(\frac{\pi}{2}\left(\zeta - \zeta_0\right)\right)}\frac{\pi}{2}\cosh\left(\frac{\pi}{2}(\zeta - \zeta_0)\right) - \frac{1}{\sinh\left(\frac{\pi}{2}\left(\zeta - \overline{\zeta}_0\right)\right)}\frac{\pi}{2}\cosh\left(\frac{\pi}{2}(\zeta - \overline{\zeta}_0)\right)\right) \end{aligned}$$

so the complex velocity at ζ of the flow due to a vortex of strength Γ at ζ_0 confined to a channel is given by

$$w(\zeta) = \frac{\Gamma}{4i}\left(\coth\left(\frac{\pi}{2}\left(\zeta - \zeta_0\right)\right) - \coth\left(\frac{\pi}{2}\left(\zeta - \overline{\zeta}_0\right)\right)\right) \tag{B.5}$$

defined for all ζ within the strip $0 \leq \mathfrak{Im}\left(\zeta\right) \leq 1$ with $\zeta \neq \zeta_0$ because the complex potential and, consequently, the complex velocity are singular at ζ_0. To obtain the real velocity field, simply evaluate (B.4) with $w\left(\zeta\right)$ as given in (B.5).

In the case of N vortices in the channel, as shown in Figure B.2, the complex potential at ζ is the superposition of the complex potentials due to each of the N vortices, a superposition of expressions of the form of (B.3) with ζ_0 replaced with ζ_k for the contribution of the k^{th} vortex at ζ,

$$f\left(\zeta\right) = \sum_{k=1}^{N} \frac{\Gamma}{2\pi i} \log \frac{\sinh\left(\frac{\pi}{2}\left(\zeta - \zeta_k\right)\right)}{\sinh\left(\frac{\pi}{2}\left(\zeta - \overline{\zeta}_k\right)\right)}. \tag{B.6}$$

Where, again, $\zeta \neq \zeta_k$ for $k \in \{1, 2, \ldots, N\}$ because the k^{th} term in the summation is singular at the location of the k^{th} vortex. The complex velocity due to N vortices is the derivative of (B.6), a superposition of expressions of the form of (B.5) with ζ_0 replaced with ζ_k for the contribution of the k^{th} vortex,

$$w\left(\zeta\right) = \sum_{k=1}^{N} \frac{\Gamma}{4i}\left(\coth\left(\frac{\pi}{2}\left(\zeta - \zeta_k\right)\right) - \coth\left(\frac{\pi}{2}\left(\zeta - \overline{\zeta}_k\right)\right)\right). \tag{B.7}$$

Because expression (B.5) for the complex velocity due to a lone vortex is singular at ζ_0 and expression (B.7) for the complex velocity due to N vortices is singular at each ζ_k, one must ask, what of the velocities at the locations of the singularities? It should be apparent that the vortical velocities bear some relation to the velocities of the singular points. This is indeed the case, and expressions for these velocities, the vortical velocity for a lone vortex and the vortical velocities of the vortices of a system of N vortices confined in the channel, are derived below.

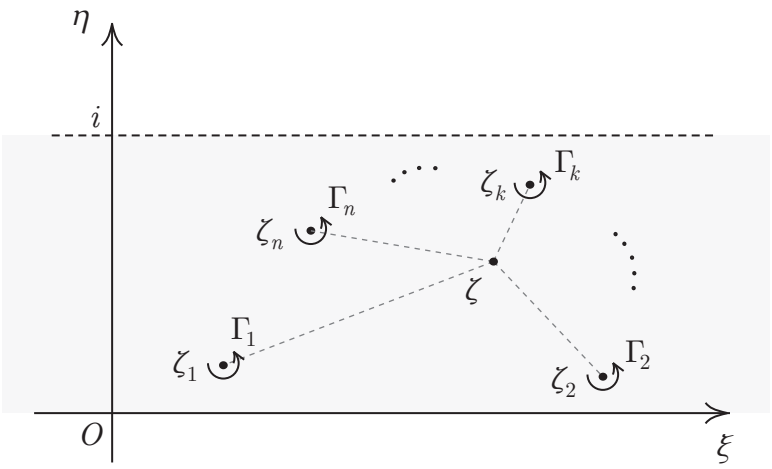

FIGURE B.2: N vortices arranged in the horizontal strip. The velocity at ζ is due to the contribution from each vortex. When ζ coincides with ζ_k, the desingularized complex velocity at the k^{th} vortex is employed to recover the complex velocity there.

Complex Velocity at Singular Points

The complex velocity of a vortex is slightly more involved than the expressions derived for the velocities of non-singular points of the flow field. Various equations of motion of singular points and generalizations are described in the survey *How do singularities move in potential flow?* [86]. The point vortex equation (PVE) described therein by Llewellyn Smith is the equation of motion of the point vortices within a potential flow. The PVE suggests that the velocity of a vortex is the desingularized velocity at the given point,

$$\widetilde{w}\left(\zeta_0\right) = \lim_{\zeta \to \zeta_0} \left(w\left(\zeta\right) - \frac{\Gamma}{2\pi i} \frac{1}{\zeta - \zeta_0} \right). \tag{B.8}$$

In (B.8), w is the complex potential due to vortices, including one at ζ_0, but possibly also the superposition of other sources which are non-singular at ζ_0. Consequently, there is a choice when computing the desingularized complex velocity. Suppose the total complex velocity is due, in addition to the vortex at ζ_0, to M sources, sinks, doublets, and vortices, with each contributing complex velocity w_m but all non-singular at ζ_0. We have

$$\widetilde{w}\left(\zeta_0\right) = \lim_{\zeta \to \zeta_0} w\left(\zeta\right) - \frac{\Gamma}{2\pi i} \frac{1}{\zeta - \zeta_0} = \sum_{m=1}^{M} w_m\left(\zeta\right) + \lim_{\zeta \to \zeta_0} \left(w_{sing}\left(\zeta\right) - \frac{\Gamma}{2\pi i} \frac{1}{\zeta - \zeta_0} \right)$$

in which $w\left(\zeta\right)$ is the total complex velocity which is then decomposed into the superposition of M complex potentials which are non-singular at ζ_0, together with w_{sing} which is singular there. This decomposition allows the determination of complex velocity by first determining the vortical velocity of a lone vortex, and any additional contributions due to non-singular complex potentials will be incorporated into the sum. So, for a single vortex

confined in the strip at ζ_0, given the complex potential in the strip $f(\zeta)$ provided in equation (B.3), the complex velocity is given by (B.5), so the complex velocity at ζ_0 is given by the desingularized velocity defined in (B.8),

$$\begin{aligned}
\widetilde{w}(\zeta_0) &= \lim_{\zeta\to\zeta_0}\left(w(\zeta) - \frac{\Gamma}{2\pi i}\frac{1}{\zeta-\zeta_0}\right)\\
&= \lim_{\zeta\to\zeta_0}\left(\frac{\Gamma}{4i}\left(\coth\left(\frac{\pi}{2}(\zeta-\zeta_0)\right) - \coth\left(\frac{\pi}{2}\left(\zeta-\overline{\zeta}_0\right)\right)\right) - \frac{\Gamma}{2\pi i}\frac{1}{\zeta-\zeta_0}\right)\\
&= \lim_{\zeta\to\zeta_0}\frac{-\Gamma}{4i}\coth\left(\frac{\pi}{2}\left(\zeta-\overline{\zeta}_0\right)\right) + \lim_{\zeta\to\zeta_0}\left(\frac{\Gamma}{4i}\coth\left(\frac{\pi}{2}(\zeta-\zeta_0)\right) - \frac{\Gamma}{2\pi i}\frac{1}{\zeta-\zeta_0}\right)\\
&= \frac{-\Gamma}{4i}\coth\left(\pi i\left(\frac{\zeta_0-\overline{\zeta}_0}{2i}\right)\right) + \frac{\Gamma}{2i}\lim_{\zeta\to\zeta_0}\left(\frac{1}{2}\coth\left(\frac{\pi}{2}(\zeta-\zeta_0)\right) - \frac{1}{\pi(\zeta-\zeta_0)}\right)
\end{aligned}$$

but $\coth(i\zeta) = \cosh(i\zeta)/\sinh(i\zeta) = \cos(\zeta)/i\sin(\zeta) = -i\cos(\zeta)/\sin(\zeta) = -i\cot(\zeta)$ so

$$\begin{aligned}
\widetilde{w}(\zeta_0) &= \frac{-\Gamma}{4i}(-i)\cot\left(\pi\ \mathfrak{Im}(\zeta_0)\right) + \frac{\Gamma}{4i}\lim_{\zeta\to\zeta_0}\left(\coth\left(\frac{\pi}{2}(\zeta-\zeta_0)\right) - \frac{1}{\frac{\pi}{2}(\zeta-\zeta_0)}\right)\\
&= \frac{\Gamma}{4}\cot\left(\pi\ \mathfrak{Im}(\zeta_0)\right) + \frac{\Gamma}{4i}\lim_{\zeta\to\zeta_0}\left(\coth\left(\frac{\pi}{2}(\zeta-\zeta_0)\right) - \frac{1}{\frac{\pi}{2}(\zeta-\zeta_0)}\right)
\end{aligned}$$

where the limit has the form $\lim_{z\to 0}\left(\coth z - \frac{1}{z}\right)$. Because coth is the ratio of hyperbolic cosine to hyperbolic sine, the zero of hyperbolic sine at the origin contributes a simple pole to the hyperbolic cotangent there. Thus, the Laurent series expansion for hyperbolic cotangent,

$$\coth z = \frac{1}{z} + \frac{1}{3}z - \frac{1}{45}z^3 + \cdots,$$

may simply be obtained by doing a long division of the power series representations of $\cosh z$ by $\sinh z$. Because the zero of hyperbolic sine at the origin is a first order zero, we expect that the hyperbolic cotangent has a simple pole at the origin, and this is manifested by the appearance of the $1/z$ term in the above series. So

$$\lim_{z\to 0}\left(\coth z - \frac{1}{z}\right) = \lim_{z\to 0}\left(\left(\frac{1}{z} + \frac{1}{3}z - \frac{1}{45}z^3 + \cdots\right) - \frac{1}{z}\right) = \lim_{z\to 0}\left(\frac{1}{3}z - \frac{1}{45}z^3 + \cdots\right) = 0.$$

Consequently,

$$\widetilde{w}(\zeta_0) = \frac{\Gamma}{4}\cot\left(\pi\ \mathfrak{Im}(\zeta_0)\right) \tag{B.9}$$

is the desingularized complex velocity of a vortex at ζ_0. Figure B.3 displays a plot of the desingularized complex velocity of a single vortex confined to a horizontal strip exhibited in equation (B.9). The complex velocity is purely real, and this entails that the velocity of a sole vortex is purely horizontal. Furthermore, vortices of positive strength equidistant to the channel walls remain stationary, they obtain negative velocity when closer to the upper wall and positive velocity when they are closer to the lower wall. The situation is reversed when the vortex strength is negative.

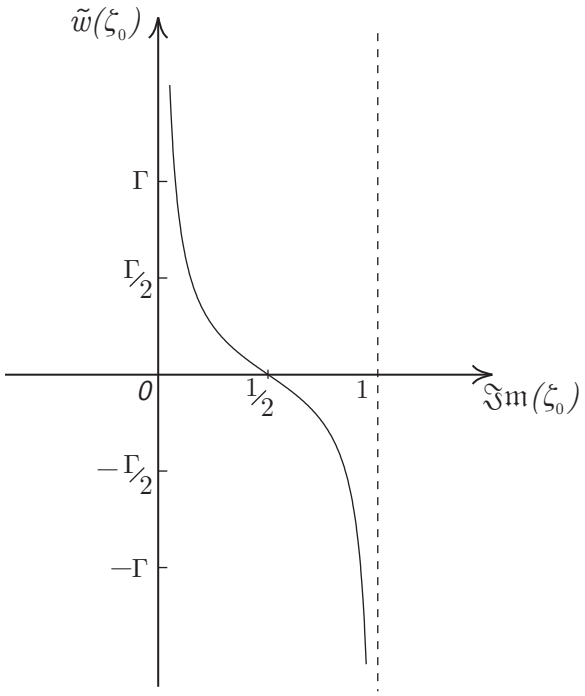

FIGURE B.3: The branch of $\Gamma/4 \cot\left(\pi\ \Im\mathfrak{m}\left(\zeta_0\right)\right)$ which lies on the interval $(0,1)$. The function is periodic with period 1 with zeros at $1/2+k$ and asymptotes at $1+k$ for all $k \in \mathbb{Z}$, but it is the restriction to $(0,1)$ which is of interest here because these values correspond to the possible vertical locations of a solitary vortex in the horizontal strip of width 1. This plot of the desingularized velocity confirms that vortices with positive circulation Γ will move to the right when they are near to the lower wall, will remain stationary when their vertical position is equidistant to the upper and lower walls, and will obtain a negative velocity and move leftwards when closer to the upper wall.

Streamlines corresponding to a single vortex located at the origin and offset towards the upper wall are shown in Figure B.4. When the vortex is disposed symmetrically between the upper and lower channel walls, the streamlines are symmetrical; however, proximity to one wall causes the streamlines to deform because the walls must remain streamlines of the flow.

Now, for a system of N vortices arranged arbitrarily at positions $\{\zeta_n\}_{n=1}^N$ with strengths $\{\Gamma_n\}_{n=1}^N$ (oriented positive counter-clockwise), as shown schematically in Figure B.2, the complex velocity at ζ_k due to vortices at $\{\zeta_n\}_{n=1}^N \backslash \{\zeta_k\}$, i.e., at all locations but ζ_k, is the superposition

$$\sum_{\substack{n=1 \\ n\neq k}}^{N} \frac{\Gamma_n}{4i}\left(\coth\left(\frac{\pi}{2}\left(\zeta_k - \zeta_n\right)\right) - \coth\left(\frac{\pi}{2}\left(\zeta_k - \overline{\zeta}_n\right)\right) \right).$$

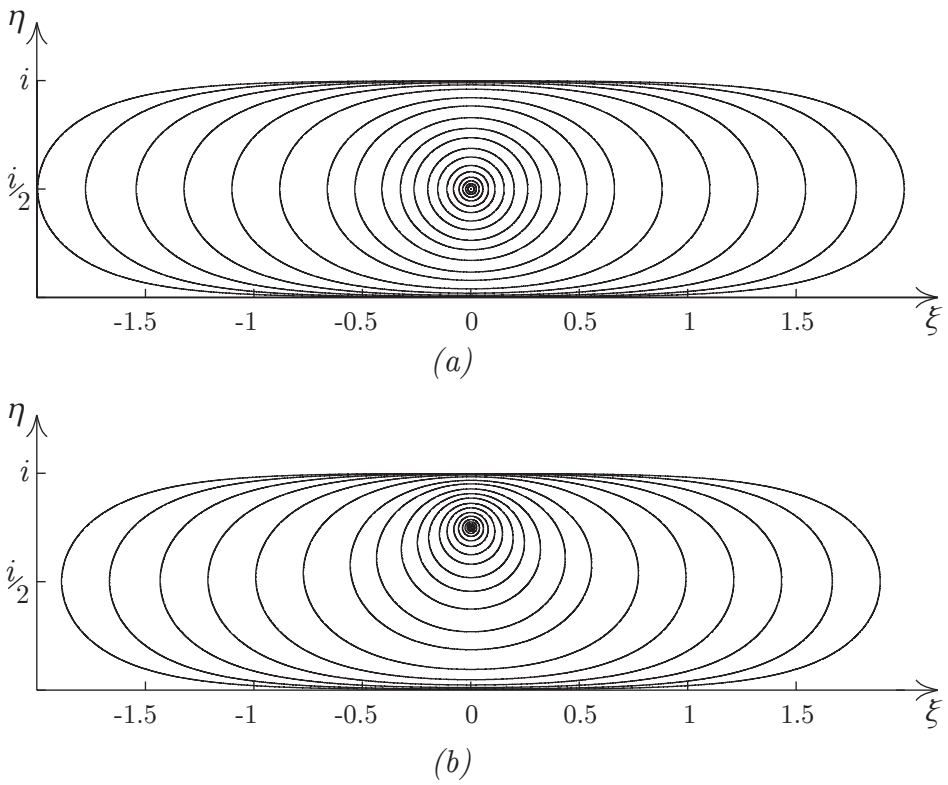

FIGURE B.4: Streamlines due to lone vortex confined in channel: (a) centred in channel, and (b) centred in upper half of channel.

The desingularized velocity at ζ_k is

$$\frac{\Gamma_k}{4}\cot\left(\pi\ \mathfrak{Im}\left(\zeta_k\right)\right).$$

Hence, the complex velocity at ζ_k due to the system of N vortices is the superposition of the preceding two expressions, i.e.,

$$\widetilde{w}\left(\zeta_k\right) = \frac{\Gamma_k}{4}\cot\left(\pi\ \mathfrak{Im}\left(\zeta_k\right)\right) + \sum_{\substack{n=1\\n\neq k}}^{N}\frac{\Gamma_n}{4i}\left(\coth\left(\frac{\pi}{2}\left(\zeta_k-\zeta_n\right)\right)-\coth\left(\frac{\pi}{2}\left(\zeta_k-\overline{\zeta}_n\right)\right)\right). \quad \text{(B.10)}$$

Equation (B.10) enables the computation of vortical velocity of the k^{th} vortex in a system of N vortices. If additional potentials influence its motion, such as a free stream or some source, the complex potentials due to these may be superimposed on this expression as well.

From the form of (B.8), it is evident that a vortex in an unconfined flow has no self-induced velocity; i.e., a lone vortex in an unconfined flow with no other contribution to the potential remains stationary. That is because the complex velocity of a vortex located at ζ_0 is the derivative of its complex potential, provided in equation (B.1). This is precisely

the expression subtracted from w in (B.8), so that the expression for $\widetilde{w}$ vanishes when w is due to one vortex alone. In contrast, when a single vortex is confined to a channel, the vortex will move because the potential of a vortex confined in a channel is due to the vortex and its infinitely many reflections. That is, unless the vortex lies along the centreline disposed symmetrically between two parallel walls. In this case, the walls have equal and opposite effects on the vortex, regardless of the sense of its strength, whether clockwise or counter-clockwise. Figure B.5 displays a plot of streamlines due to four vortices confined in a channel with no free stream.

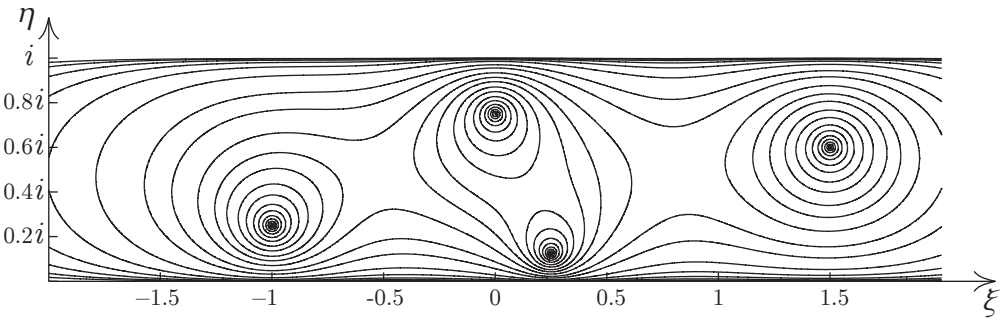

FIGURE B.5: Streamlines due to four arbitrary vortices confined to a channel.

B.2 An Unsteady Frame-Invariant Bernoulli Equation

The typical expression of the inviscid incompressible irrotational unsteady Bernoulli equation for pressure in the presence of conservative body force per unit mass $f = \nabla F$ (see, for example, [8, 56, 64], or, more recently, [50]) is

$$\frac{\partial \Phi}{\partial t} + \frac{P}{\rho} + \frac{1}{2}v^2 + F = K(t), \tag{B.11}$$

where P is pressure, ρ is fluid density, Φ is velocity potential so $\vec{v} = \nabla\Phi$, $v = \|\vec{v}\|^2$, and $K(t)$ is an arbitrary but fixed function of time, is not invariant under Galilean transformation, i.e., in a frame of reference translating with uniform velocity with respect to immersed solids, their surfaces perform work on the fluid [67]. Consequently, additional terms are required to be included to extend the validity of the Bernoulli equation for pressure in translating, and even to non-inertial frames of reference. This is essential in computing the force due to pressure on the immersed surfaces of moving boundaries of the flow domain. A frame-independent form of the incompressible and inviscid unsteady Bernoulli equation is obtained herein. The result is immediately specialized to the case of irrotational fluid, especially in the case in which the velocity potential is obtained via conformal mapping from an auxiliary plane where the temporal variation of the potential φ is easily tracked.

B.2.1 The Inviscid Incompressible Unsteady Bernoulli Equation

In the case that the Mach number,

$$Ma = \frac{V}{c},$$

in which V is a characteristic velocity scale and c is the speed of sound in the fluid medium, satisfies $Ma < 0.3$, the flow may be considered to be incompressible. The governing equations of such a flow, together with the assumption that the fluid medium is a homogeneous constant viscosity Newtonian fluid, are stated as

$$\frac{D\vec{v}}{Dt} = -\frac{1}{\rho}\nabla P + \nu\nabla^2\vec{v} + \vec{f} \tag{B.12}$$

$$\nabla \cdot \vec{v} = 0 \tag{B.13}$$

which are defined on flow domain $\Omega(t)$ and in which $\vec{v}$ is the Eulerian velocity field with respect to an inertial frame, P is the pressure field, ν is the kinematic viscosity of the fluid, ρ is the density of the fluid, and $\vec{f}$ represents the aggregate, on a per unit mass basis, of all conservative body forces acting in the flow domain. $\vec{f}$ is often simply due to gravitational force in flat earth, namely $\vec{f} = \vec{g} = -g\hat{K}$. Equations (B.12) and (B.13) are conservation of momentum, the Navier-Stokes equation, cast per unit mass, and the incompressible continuity equation respectively. Given appropriate boundary conditions for P and $\vec{v}$ on $\partial\Omega(t)$, they provide constraints for the unknown velocity field and pressure field, both defined in an inertial frame of reference. These equations may be specialized immediately. If the Reynolds number,

$$Re = \frac{VL}{\nu},$$

in which V is a characteristic velocity scale, $V = \|\vec{v}\|$ at some point in the flow, often in the far field, and L is a characteristic length scale, satisfies $Re \gg 1$, the viscous term in (B.12) is dominated by the inertia of the flow and may be discarded. In this case, we obtain Euler's equation of motion,

$$\frac{D\vec{v}}{Dt} = -\frac{1}{\rho}\nabla P + \vec{f}, \tag{B.14}$$

which governs conservation of momentum of incompressible and inviscid Newtonian fluids. This may be transformed by employing the vector identity

$$\nabla\left(\vec{A}\cdot\vec{B}\right) = \left(\vec{A}\cdot\nabla\right)\vec{B} + \left(\vec{B}\cdot\nabla\right)\vec{A} + \vec{A}\times\left(\nabla\times\vec{B}\right) + \vec{B}\times\left(\nabla\times\vec{A}\right),$$

with $\vec{A} = \vec{B} = \vec{v}$, to obtain

$$\nabla\left(\vec{v}\cdot\vec{v}\right) = \left(\vec{v}\cdot\nabla\right)\vec{v} + \left(\vec{v}\cdot\nabla\right)\vec{v} + \vec{v}\times\left(\nabla\times\vec{v}\right) + \vec{v}\times\left(\nabla\times\vec{v}\right)$$

or

$$\left(\vec{v}\cdot\nabla\right)\vec{v} = \nabla\left(\frac{1}{2}v^2\right) - \vec{v}\times\left(\nabla\times\vec{v}\right) = \nabla\left(\frac{1}{2}v^2\right) - \vec{v}\times\vec{\omega},$$

where the second equality follows from the definition of vorticity, $\nabla \times \vec{v} = \vec{\omega}$. This enables the material derivative to be recast in the following form

$$\frac{D\vec{v}}{Dt} = \frac{\partial \vec{v}}{\partial t} + (\vec{v} \cdot \nabla)\, \vec{v} = \frac{\partial \vec{v}}{\partial t} + \nabla \left(\frac{1}{2} v^2 \right) - \vec{v} \times \vec{\omega},$$

so (B.14) becomes

$$\frac{\partial \vec{v}}{\partial t} + \nabla \left(\frac{1}{2} v^2 \right) - \vec{v} \times \vec{\omega} = -\frac{1}{\rho} \nabla P + \vec{f} \tag{B.15}$$

or, if density is constant in the flow,

$$\frac{\partial \vec{v}}{\partial t} + \nabla \left(\frac{1}{2} v^2 \right) - \vec{v} \times \vec{\omega} = -\nabla \left(\frac{P}{\rho} \right) + \vec{f}. \tag{B.16}$$

Various forms of the Bernoulli equation are obtained via integration of equation (B.16) along streamlines of the flow and may be further specialized for irrotational fluids, etc.. Equation (B.16) holds at any interior point of the flow domain $\Omega(t)$ when the quantities are measured with respect to an inertial frame of reference. Equation (B.16) even holds on the boundary $\partial\Omega(t)$ at points at which the boundary is stationary with respect to the same inertial frame. In order to obtain pressures at points on a moving boundary, two approaches are possible. In one approach, equation (B.16) may be extended to non-inertial frames prior to integrating along a streamline of the flow which happens to be fixed when observed relative to the moving frame of reference. Alternatively, (B.16) may be integrated along a streamline of the flow to obtain B.11, and this, via relations which hold between derivatives of scalar quantities observed in frames of reference which are in motion relative to each other, obtain a form independent of frame. In the present development, equation (B.16) is integrated and specialized to obtain (B.11).

Both sides of (B.16) are integrated along a curve $C(t)$ which is observed within the global inertial frame,

$$\int_C \left(\frac{\partial \vec{v}}{\partial t} + \nabla \left(\frac{1}{2} v^2 \right) - \vec{v} \times \vec{\omega} \right) \cdot \, d\vec{r} = \int_C \left(-\frac{1}{\rho} \nabla P + \vec{f} \right) \cdot \, d\vec{r}$$

or

$$\int_C \left(\frac{\partial \vec{v}}{\partial t} + \nabla \left(\frac{1}{2} v^2 \right) - \vec{v} \times \vec{\omega} + \frac{1}{\rho} \nabla P - \vec{f} \right) \cdot \, d\vec{r} = 0.$$

Now, if density is constant, $1/\rho \nabla P = \nabla P/\rho$, and, because $\vec{f}$ is conservative, it may be written $\vec{f} = -\nabla F$ where F is an appropriate scalar potential, obtain

$$\int_C \left(\frac{\partial \vec{v}}{\partial t} + \nabla \left(\frac{1}{2} v^2 \right) - \vec{v} \times \vec{\omega} + \nabla \frac{P}{\rho} + \nabla F \right) \cdot \, d\vec{r} = 0$$

or

$$\int_C \left(\frac{\partial \vec{v}}{\partial t} - \vec{v} \times \vec{\omega} + \nabla \left(\frac{1}{2} v^2 + \frac{P}{\rho} + F \right) \right) \cdot \, d\vec{r} = 0.$$

which, if $\vec{X}$ and $\vec{X}_0$ are endpoints of C in the global frame, collapses to

$$\int_C \left(\frac{\partial \vec{v}}{\partial t} - \vec{v} \times \vec{\omega} \right) \cdot d\vec{r} + \left(\frac{1}{2} v^2 + \frac{P}{\rho} + F \right)_{\vec{X}_0}^{\vec{X}} = 0$$

because the gradient of a scalar field is conservative so the integral is independent of path. Finally, if C is taken to be a streamline of the flow observed in the global frame, $\vec{v} \times \vec{\omega}$ being orthogonal to $\vec{v}$ entails that the cross product term is everywhere orthogonal to the streamline, the cross product term vanishes, and we obtain

$$\int_C \frac{\partial \vec{v}}{\partial t} \cdot d\vec{r} + \left(\frac{1}{2} v^2 + \frac{P}{\rho} + F \right)_{\vec{X}_0}^{\vec{X}} = 0 \tag{B.17}$$

Equation (B.17) is the incompressible inviscid unsteady Bernoulli equation. However, if the flow is irrotational, additional simplification is possible.

When, in addition, $\vec{v}$ is irrotational in the region which contains C, $\vec{v} = \nabla\Phi$ for an appropriate scalar potential Φ, and, thus, $\vec{\omega} = \nabla \times \vec{v} = \nabla \times \nabla\Phi = 0$ because the curl of the gradient of a scalar field vanishes, $\int_C \vec{v} \times \vec{\omega} \cdot d\vec{r}$ vanishes along a streamline because $\vec{v}$ is parallel to the streamline while $\vec{v} \times \vec{\omega} \perp \vec{v}$ and, hence, perpendicular to $d\vec{r}$), and $\partial\vec{v}/\partial t$ becomes $\nabla\partial\Phi/\partial t$ under continuity assumptions, so obtain from the original integral

$$\int_C \nabla \left(\frac{\partial \Phi}{\partial t} + \frac{1}{2} v^2 + \frac{P}{\rho} + F \right) \cdot d\vec{r} = 0.$$

Because the argument of this integral is the gradient of some scalar field, it is irrotational. Because the integral is identically zero, the integrand must be the gradient of some function of time, $K(t)$, hence equation (B.11) follows as desired. However, more may be said, the integral is independent of path, i.e., we may integrate along any path between $\vec{X}_0$ and $\vec{X}$. Furthermore, because the contour of integration C is not necessarily a streamline, we obtain

$$\left. \frac{\partial \Phi}{\partial t} + \frac{1}{2} v^2 + \frac{P}{\rho} + F \right|_{\vec{X}} = \left. \frac{\partial \Phi}{\partial t} + \frac{1}{2} v^2 + \frac{P}{\rho} + F \right|_{\vec{X}_0}$$

for any pair of points $\vec{X}_0$ and $\vec{X}$, not required to be on the same streamline, within the flow field $\Omega(t)$. If $\vec{X}_0$ is taken as a point far upstream, where Φ remains constant and P obtains constant value P_0, $\frac{\partial \Phi}{\partial t}$ vanishes and $v = v_0$ there. So, in the further absence of conservative body force, obtain

$$P\big(\vec{X}, t\big) = P_0 + \frac{1}{2} \rho \left(v_0^2 - \|\nabla\Phi\|^2 \right) - \rho \frac{\partial}{\partial t} \Phi\big(\vec{X}, t\big). \tag{B.18}$$

The final term in (B.18) is evaluated at an inertial spatial location within the flow domain not at an accelerating non-inertial point. Consequently, equation (B.18) merely applies in

an inertial frame of reference. We seek to find an expression for the pressure when the quantity is evaluated within an accelerating frame of reference. The temporal derivative of Φ is evaluated at a fixed point in the flow domain, but, it is desirable to compute this within some moving frame.

B.2.2 Temporal Derivatives of Scalars Observed in Moving Frames

Consider the spatial relations between an inertial frame and translating and rotating frame exhibited schematically in Figure B.6 below. The XYZ frame with origin O is an inertial frame of reference. The flow domain $\Omega(t)$ deforms in time relative to the global frame. The boundary of the flow domain, $\partial\Omega(t)$, is the interface between the deformable solid domain and the flow domain. Translating and rotating xyz frame of reference has origin affixed to the boundary at A. A theorem due to Chasles[1] states that any rigid-body motion may be completely decomposed into a rotation of that body about some axis and a translation of the axis relative to the global frame. In fact, this section demonstrates the manner in which this decomposition may be carried out and determines the attendant velocities and accelerations with respect to frames of reference which exhibit relative motion. Note that, if P is affixed in the xyz frame, it has zero velocity measured with respect to A despite that it might exhibit absolute motion measured in the global frame.

The position of A and its translational velocity, measured in the global XYZ are $\vec{R}_{A/O}$ and $\vec{v}_{A/O}$ respectively. $\vec{v}_{A/O}$ will typically be written $\vec{v}_A$, and it will be understood that the velocity of A is then measured with respect to the global frame. The position of P is either $\vec{R}_{P/O}$ or $\vec{R}_{P/A}$ as measured in the global and local frames respectively. Consequently, the position of P may be decomposed according to the following

$$\vec{R}_{P/O} = \vec{R}_{A/O} + \vec{R}_{P/A}$$

or simply

$$\vec{R}_P = \vec{R}_A + \vec{R}_{P/A} \tag{B.19}$$

where we may write the resolutions of these vectors with respect to Cartesian $\{\hat{I}, \hat{J}, \hat{K}\}$ and $\{\hat{\imath}, \hat{\jmath}, \hat{k}\}$ coordinate vectors affixed to XYZ and xyz frames respectively

$$\vec{R}_P^{\,XYZ} = X\hat{I} + Y\hat{J} + Z\hat{K} \text{ and } \vec{R}_{P/A}^{\,xyz} = x\hat{\imath} + y\hat{\jmath} + z\hat{k}$$

when $\vec{R}_P$ and $\vec{R}_{A/P}$ are resolved relative to the global coordinate system and relative to the local coordinate system respectively. The resolved quantities will simply be denoted $\vec{X}$ and $\vec{x}$.

Differentiation of equation (B.19) yields

$$\vec{v}_P = \vec{v}_A + \vec{v}_{P/A} + \vec{\Omega} \times \vec{R}_{P/A} \tag{B.20}$$

[1] attributed to Michel Chasles (1793–1880)

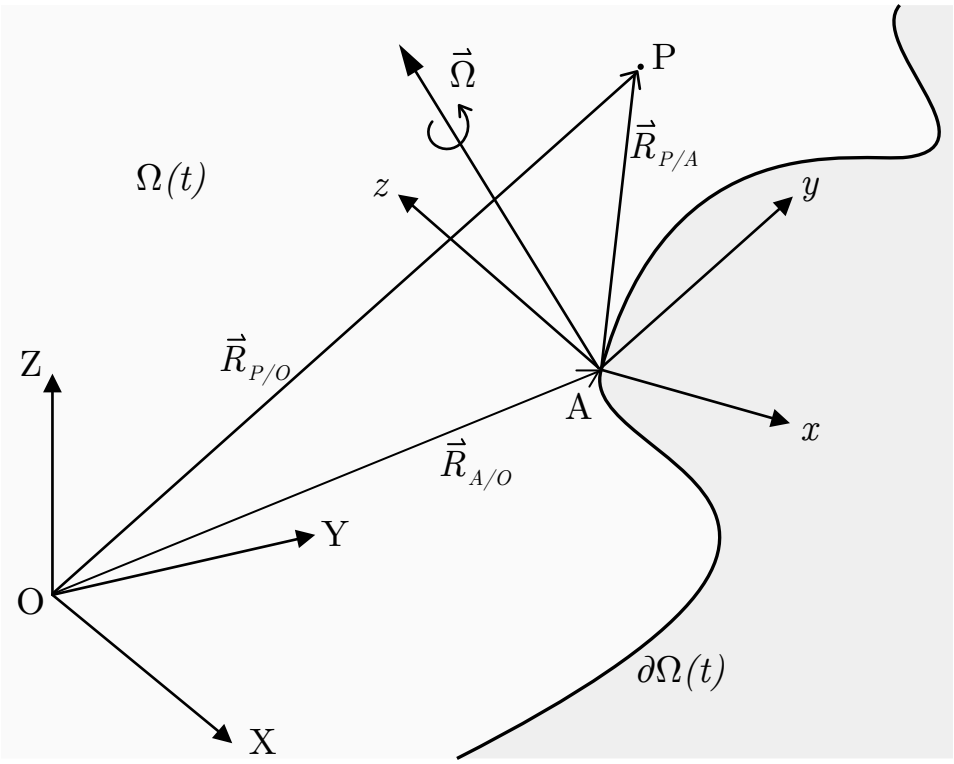

FIGURE B.6: The shaded part represents the solid with moving boundary $\partial\Omega(t)$. The schematic shows the kinematic relation between the inertial XYZ frame, which is fixed, and the boundary-fixed xyz frame which rotates with angular velocity $\vec{\Omega}$ and with origin A located by $\vec{R}_{A/O}$. The relative position of point P within flow domain $\Omega(t)$ is $\vec{R}_{P/A}$ referred to the boundary-fixed xyz frame or at $\vec{R}_{P/O}$ referred to the global inertial XYZ frame.

due to the angular velocity $\vec{\Omega}$ of the xyz frame about A. The cross product is well defined as long as both vectors of the product are resolved within the same coordinate system. Not germane to the current section, but for the sake of completeness, the temporal derivative of (B.20) for the acceleration is

$$\vec{a}_P = \vec{a}_A + \vec{a}_{P/A} + \vec{\Omega} \times \vec{v}_{P/A} + \dot{\vec{\Omega}} \times \vec{R}_{P/A} + \vec{\Omega} \times \left(\vec{v}_{P/A} + \vec{\Omega} \times \vec{R}_{P/A} \right)$$

or

$$\vec{a}_P = \vec{a}_A + \vec{a}_{P/A} + 2\ \vec{\Omega} \times \vec{v}_{P/A} + \dot{\vec{\Omega}} \times \vec{R}_{P/A} + \vec{\Omega} \times \left(\vec{\Omega} \times \vec{R}_{P/A} \right). \tag{B.21}$$

Now, within this framework, given some Galilean-invariant scalar quantity f observed in the inertial frame as $f(\vec{X}, t)$ and observed in the non-inertial frame as $\tilde{f}(\vec{x}, t)$, we must have $f(\vec{X}, t) = \tilde{f}(\vec{x}, t)$ when $\vec{X}$ is the position of some point P measured in the global frame and $\vec{x}$ is the position of P in the local frame, but, because the observers are in relative motion, the equation which relates the temporal derivatives of these quantities must have terms to account for this relative motion. The temporal derivatives of f either as measured with

respect to the inertial frame or as measured with respect to the moving frame are related according to the following theorem.

Theorem B.1. *Suppose f is some scalar quantity $f = f\left(\vec{R}_P, t\right) = \tilde{f}\left(\vec{R}_{P/A}, t\right)$ where $f\left(\vec{R}_P, t\right)$ and $\tilde{f}\left(\vec{R}_{P/A}, t\right)$ are observations of f at some point P within the inertial and the moving frames respectively. The temporal derivatives of f in the inertial frame and $\tilde{f}$ in the moving frame are related by*

$$\nabla_x \tilde{f} \cdot \left(\vec{v}_P - \vec{v}_A - \vec{\Omega} \times \vec{R}_{P/A}\right) + \frac{\partial \tilde{f}}{\partial t} = \nabla_X f \cdot \vec{v}_P + \frac{\partial f}{\partial t} \tag{B.22}$$

where ∇_x is the del operator resolved in the xyz frame and ∇_X is the del operator resolved in the XYZ.

Proof. Obtain the temporal derivative of both sides of $\tilde{f}\left(\vec{R}_{B/A}, t\right) = f\left(\vec{R}_B, t\right)$ by applying the chain rule,

$$\frac{\partial \tilde{f}}{\partial x}\frac{\partial x}{\partial t} + \frac{\partial \tilde{f}}{\partial y}\frac{\partial y}{\partial t} + \frac{\partial \tilde{f}}{\partial z}\frac{\partial z}{\partial t} + \frac{\partial \tilde{f}}{\partial t} = \frac{\partial f}{\partial X}\frac{\partial X}{\partial t} + \frac{\partial f}{\partial Y}\frac{\partial Y}{\partial t} + \frac{\partial f}{\partial Z}\frac{\partial Z}{\partial t} + \frac{\partial f}{\partial t}$$

$$\nabla_x \tilde{f} \cdot \frac{d\vec{R}_{P/A}}{dt} + \frac{\partial \tilde{f}}{\partial t} = \nabla_X f \cdot \frac{d\vec{R}_P}{dt} + \frac{\partial f}{\partial t}$$

In which the temporal partial derivatives are computed while holding the spatial variables fixed within their respective frames. Now, the temporal derivatives of $\vec{R}_P$ and $\vec{R}_{P/A}$ are merely velocities $\vec{v}_P$ and $\vec{v}_{P/A}$, and the latter may be obtained by rearranging equation (B.20),

$$\vec{v}_{P/A} = \vec{v}_P - \vec{v}_A - \vec{\Omega} \times \vec{R}_{P/A}$$

Upon substitution, we obtain

$$\nabla_x \tilde{f} \cdot \left(\vec{v}_P - \vec{v}_A - \vec{\Omega} \times \vec{R}_{P/A}\right) + \frac{\partial \tilde{f}}{\partial t} = \nabla_X f \cdot \vec{v}_P + \frac{\partial f}{\partial t}$$

as required. □

Two interesting cases follow. If P is a fixed point within the global frame, $\vec{v}_P$ vanishes, and equation (B.22) becomes

$$\frac{\partial f}{\partial t} = \frac{\partial \tilde{f}}{\partial t} - \left(\vec{v}_A + \vec{\Omega} \times \vec{R}_{P/A}\right) \cdot \nabla_x \tilde{f}$$

in which the temporal derivative on the left-hand side is the derivative of f in the inertial frame and the temporal derivative of $\tilde{f}$ on the right-hand side is the temporal derivative of

f written in the moving frame. Alternatively, if P is fixed within the moving frame, $\vec{v}_{P/A}$ vanishes, and, hence, $\vec{v}_P - \vec{v}_A - \vec{\Omega} \times \vec{R}_{P/A}$ vanishes, and we obtain

$$\frac{\partial \tilde{f}}{\partial t} = \frac{\partial f}{\partial t} + \vec{v}_P \cdot \nabla_X f$$

This is useful because pressure is Galilean-invariant because forces and areas are measured to be identical when observed from frames which are moving with constant velocity relative to one another [67]. These relations furnish a method to recover the potential observed fixed in a non-inertial frame to the corresponding point which is observed to be moving relative to the global frame. Consequently, we may recast the Bernoulli equation to account for the motions of bounding walls of the flow domain.

B.2.3 Frame-Invariant Unsteady Bernoulli Equation

Employing the machinery of the previous sub-sections and with reference to Figure B.6, the frame-invariant unsteady Bernoulli equation may be stated. This is an extension of the unsteady Bernoulli equation, equation (B.18), which allows the determination of the pressure at a fixed point in the flow domain subject to the assumptions of its derivation but employing quantities in a moving frame of reference at the moment a point in the moving frame of reference coincides with the identical point in the flow domain. Of specific interest is the situation in which pressure is obtained at a point on the moving boundary of the flow domain in terms of quantities measured within a frame of reference affixed to the boundary. The temporal derivative of Φ must be obtained and cast in appropriate form, and the expression for pressure may thus be obtained.

The velocity potential Φ may be written in the inertial frame as $\Phi(X, Y, Z, t)$ or in the moving frame as $\widetilde{\Phi}(x, y, z, t)$. At an instant at which $\vec{X}$ and $\vec{x}$ correspond to the same point, Φ and $\widetilde{\Phi}$ are equal to each other. Nevertheless, temporal derivatives of $\widetilde{\Phi}$ and Φ are not identical. By the discussion in preceding sub-sections, we have the temporal derivative of Φ at a point P in the flow domain,

$$\frac{\partial}{\partial t}\,\Phi\Big(\vec{R}_P, t\Big)\;\Big)_{\vec{R}_P} = \nabla_x \widetilde{\Phi} \cdot \vec{v}_{P/A} + \frac{\partial}{\partial t}\,\widetilde{\Phi}\Big(\vec{R}_{P/A}, t\Big)\;\Big)_{\vec{R}_{P/A}} - \nabla_X \Phi \cdot \vec{v}_P,$$

or, with $\vec{v}_P$ in terms of quantities measured in the moving frame, obtain

$$\frac{\partial}{\partial t}\,\Phi\Big(\vec{R}_P, t\Big)\;\Big)_{\vec{R}_P} = \nabla_x \widetilde{\Phi} \cdot \vec{v}_{P/A} + \frac{\partial}{\partial t}\,\widetilde{\Phi}\Big(\vec{R}_{P/A}, t\Big)\;\Big)_{\vec{R}_{P/A}} - \nabla_X \Phi \cdot \Big(\vec{v}_A + \vec{v}_{P/A} + \vec{\Omega} \times \vec{R}_{P/A}\Big).$$

Recognizing that the first two terms on the right hand side collapse to the total temporal derivative of $\widetilde{\Phi}$ observed in the moving frame, i.e.,

$$\nabla_x \widetilde{\Phi} \cdot \vec{v}_{P/A} + \frac{\partial}{\partial t}\,\widetilde{\Phi}\Big(\vec{R}_{P/A}, t\Big)\;\Big)_{\vec{R}_{P/A}} = \frac{d}{dt}\widetilde{\Phi}\left(\vec{R}_{P/A}, t\right),$$

we may write

$$\frac{\partial}{\partial t}\,\Phi\Big(\vec{R}_P,t\Big)\;\Big)_{\vec{R}_P} = \frac{d}{dt}\widetilde{\Phi}\left(\vec{R}_{P/A},t\right) - \nabla_X\Phi\cdot\left(\vec{v}_A+\vec{v}_{P/A}+\vec{\Omega}\times\vec{R}_{P/A}\right).$$

Finally, if the point P is fixed within the moving frame, $\vec{v}_{P/A}$ vanishes and we have

$$\frac{\partial}{\partial t}\,\Phi\Big(\vec{R}_P,t\Big)\;\Big)_{\vec{R}_P} = \frac{d}{dt}\widetilde{\Phi}\left(\vec{R}_{P/A},t\right) - \nabla_X\Phi\cdot\left(\vec{v}_A+\vec{\Omega}\times\vec{R}_{P/A}\right) \tag{B.23}$$

where, in the case of stationary $\vec{R}_{P/A}$,

$$\frac{d}{dt}\widetilde{\Phi}\left(\vec{R}_{P/A},t\right) = \frac{\partial}{\partial t}\,\widetilde{\Phi}\Big(\vec{R}_{P/A},t\Big)\;\Big)_{\vec{R}_{P/A}}.$$

Equation (B.23) gives an expression for the temporal derivative of Φ at point P within the flow domain entirely in terms of quantities which are observed at a point fixed within a non-inertial frame affixed to the boundary of the flow domain at the instant that fixed point coincides with spatial point P. The right hand side of (B.23) may be substituted into equation (B.18) to obtain the desired unsteady frame-independent form of the Bernoulli equation as follows.

$$P\big(\vec{X},t\big) = P_0 + \frac{1}{2}\,\rho\left(v_0^2 - \|\nabla_X\Phi\|^2\right) - \rho\left(\frac{d}{dt}\widetilde{\Phi}\left(\vec{x},t\right) - \nabla_X\Phi\cdot\left(\vec{v}_A+\vec{\Omega}\times\vec{x}\right)\right). \tag{B.24}$$

Equation (B.24) is the appropriate form of the frame-invariant unsteady Bernoulli equation. It has the appropriate simplicity and will enable the computation of the pressure along the moving boundary of a flow domain as is required in the computation of the pressure along the medial surface of the vocal folds. Within equation (B.24), all of the terms are known from the solution of the flow problem at time t except the temporal derivative of $\widetilde{\Phi}$ The following sub-section shows, given the temporal evolution of the potential in the auxiliary plane and the temporal evolution of conformal mappings between auxiliary plane and physical plane corresponding to the time history of states of the evolving glottal configuration, the approach to the evaluation of the temporal derivative of $\widetilde{\Phi}$.

B.2.4 Temporal Derivative of $\widetilde{\Phi}$

A second-order backward difference scheme for the numerical evaluation of the temporal derivative of $\widetilde{\Phi}$ at a fixed point z in a frame affixed to the moving boundary of the flow domain, specifically affixed to the medial surface of the vocal fold, is developed in this sub-section. Figure B.7 exhibits an overlay of three successive configurations of the medial VF surface and the corresponding configurations of the auxiliary plane. z is fixed in xy, but at time t_k, coincides with points Z_k of the global frame. At time t_k, because the potential

$\widetilde{\Phi}$ observed within the moving frame at position z coincides with the potential Φ observed within the global frame at position Z_k at the same instant of time, the following hold,

$$\begin{aligned}\widetilde{\Phi}\left(z, t_k\right) &= \Phi\left(Z_k, t_k\right), \\ \widetilde{\Phi}\left(z, t_{k-1}\right) &= \Phi\left(Z_{k-1}, t_{k-1}\right), \text{ and} \\ \widetilde{\Phi}\left(z, t_{k-2}\right) &= \Phi\left(Z_{k-2}, t_{k-2}\right).\end{aligned}$$

When these expressions are substituted into the expression for the second-order backward difference, the desired expression is obtained.

To briefly digress, Lagrange's interpolation formula,

$$P(x) = \sum_{j=0}^{n} f(x_j)\, L_j(x) \tag{B.25}$$

where

$$L_j(x) = \frac{(x - x_0)\,(x - x_1)\cdots(x - x_{j-1})\,(x - x_{j+1})\cdots(x - x_n)}{(x_j - x_0)\,(x_j - x_1)\cdots(x_j - x_{j-1})\,(x_j - x_{j+1})\cdots(x_j - x_n)}$$

is an n^{th} degree polynomial which passes through $(x_j, f(x_j))$ and smoothly interpolates between them. On three points, we have

$$P(x) = \sum_{j=0}^{3} f(x_j)\, L_j(x) = f(x_0)L_0(x) + f(x_1)L_1(x) + f(x_2)L_2(x)$$

so

$$P(x) = f(x_0)\frac{(x - x_1)\,(x - x_2)}{(x_0 - x_1)\,(x_0 - x_2)} + f(x_1)\frac{(x - x_0)\,(x - x_2)}{(x_1 - x_0)\,(x_1 - x_2)} + f(x_2)\frac{(x - x_0)\,(x - x_1)}{(x_2 - x_0)\,(x_2 - x_1)}.$$

The idea is that this is a suitable approximation of f on the interval $[x_0, x_2]$ so that P' is a suitable approximation of the derivative of f on the same interval. So, obtain

$$P'(x) = f(x_0)\frac{(x - x_1) + (x - x_2)}{(x_0 - x_1)\,(x_0 - x_2)} + f(x_1)\frac{(x - x_0) + (x - x_2)}{(x_1 - x_0)\,(x_1 - x_2)} + f(x_2)\frac{(x - x_0) + (x - x_1)}{(x_2 - x_0)\,(x_2 - x_1)},$$

and, when $x = x_2$, this is a suitable approximation of $f'(x_2)$ given knowledge of f at x_2 and at two preceding points, x_1 and x_0. So

$$f'(x_2) \approx f(x_0)\frac{x_2 - x_1}{(x_0 - x_1)\,(x_0 - x_2)} + f(x_1)\frac{x_2 - x_0}{(x_1 - x_0)\,(x_1 - x_2)} + f(x_2)\frac{(x_2 - x_0) + (x_2 - x_1)}{(x_2 - x_0)\,(x_2 - x_1)}.$$

When we take consecutive points x_{n-2}, x_{n-1}, and x_n equally spaced, so that $x_n - x_{n-1} = x_{n-1} - x_{n-2} = h$, this collapses to the second order backward difference on equally spaced intervals,

$$\begin{aligned}f'(x_n) &\approx f(x_{n-2})\frac{h}{(-h)\,(-2h)} + f(x_{n-1})\frac{2h}{(h)\,(-h)} + f(x_n)\frac{2h + h}{(2h)\,(h)} \\ &= \frac{3f(x_n) - 4f(x_{n-1}) + f(x_{n-2})}{2h}.\end{aligned}$$

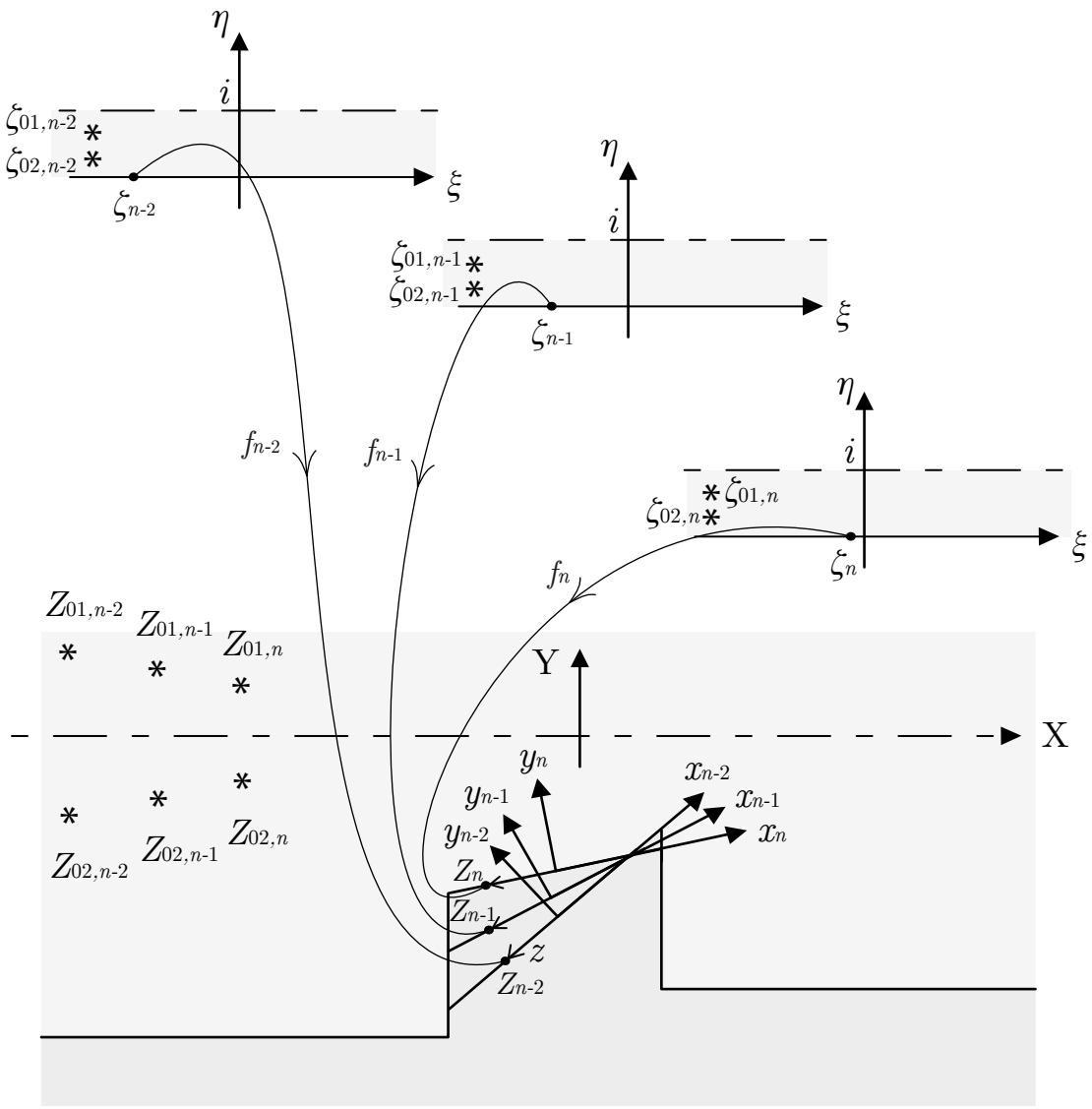

FIGURE B.7: Schematic of a single VF overlaid in the physical plane at three successive instants. XY is the global frame in the physical plane, and the xy frame is affixed to the medial VF surface and pitches and heaves with it. z is a fixed point in the translating xy frame, so that z remains constant in xy frame but obtains coordinates Z_k with respect to the global frame at each time t_k. The auxiliary $\xi\eta$ plane is shown separately at the corresponding successive instants of time. Conformal mappings f_k which generate these configurations are shown to map ζ_k from the boundary of the auxiliary plane to Z_k in the physical plane. Vortex pairs $Z_{01,k}$ and $Z_{02,k}$ are overlaid at the corresponding successive instants together with their pre-images $\zeta_{01,k}$ and $\zeta_{02,k}$ at time t_k in each corresponding instance of the $\xi\eta$ plane. By obtaining the complex potential at each instant in the auxiliary plane, depending on vortical positions and free stream, and consequently corresponding complex potential in the physical plane via the conformal mapping f_k which generates the k^{th} configuration, temporal derivatives may be computed at z fixed in the moving frame.

Keeping unequal spacing, but denoting the interval widths according to $x_n - x_{n-1} = h_1$, $x_{n-1} - x_{n-2} = h_2$, and $x_n - x_{n-2} = h$, obtain a backward difference estimate on three unequally spaced points,

$$f(x_n)\frac{h+h_1}{h\,h_1} - f(x_{n-1})\frac{h}{h_1\,h_2} + f(x_{n-2})\frac{h_1}{h\,h_2}. \tag{B.26}$$

Consequently, the backward difference estimate for $\tilde{\Phi}$ at time t on equally spaced intervals is

$$\frac{d}{dt}\widetilde{\Phi}(z,t) \approx \frac{3\,\Phi\left(Z_n,t\right) - 4\,\Phi\left(Z_{n-1},t-\delta t\right) + \Phi\left(Z_{n-2},t-2\,\delta t\right)}{2\,\delta t} \tag{B.27}$$

and on unequally spaced intervals,

$$\begin{aligned}\frac{d}{dt}\widetilde{\Phi}(z,t) \approx \Phi\left(Z_n,t\right)\frac{2\,\delta t^{(1)}+\delta t^{(2)}}{\delta t^{(\mathrm{tot})}\,\delta t^{(1)}} \\ - \Phi\left(Z_{n-1},t-\delta t^{(1)}\right)\frac{\delta t^{(\mathrm{tot})}}{\delta t^{(1)}\,\delta t^{(2)}} \\ + \Phi\left(Z_{n-2},t-\left(\delta t^{(2)}+\delta t^{(1)}\right)\right)\frac{\delta t^{(1)}}{\delta t^{(\mathrm{tot})}\,\delta t^{(2)}}\end{aligned} \tag{B.28}$$

where $\delta t^{(\mathrm{tot})} = \delta t^{(1)} + \delta t^{(2)}$, and z, fixed on the medial surface of the vocal fold, occupies position Z_n at time t, Z_{n-1} at time $t-\delta t^{(1)}$, and occupies position Z_{n-2} at time $t-\delta t^{(1)}-\delta t^{(2)}$.

Finally, if $f_k : S \to D_Z$ is the conformal mapping which takes the infinite horizontal strip in the auxiliary plane to the glottal configuration at time t_k and $F(\zeta,t)$ is the complex potential due to vortices at positions $\zeta_0 = f_k^{-1}(Z_0)$ together with free stream, then $F(f_k^{-1}(Z),t)$ is the complex potential in the physical plane at time t_k. Consequently, in equation (B.27) or (B.28), the Φs may be written as the real parts of the complex potentials. Because the solver tracks the vortices, the conformal maps f_k, and the positions Z_k for the control points along the medial VF surface at each time t_k, the temporal derivative of $\widetilde{\Phi}$ may be computed at each instant of time along the vocal fold as required by employing (B.27), even as the timesteps vary from iteration to iteration by employing (B.28).

B.3 Pressure Distribution in the Titze Model

To obtain the intraglottal pressure along the centreline of the glottis, Titze employs Bernoulli's equation to relate subglottal conditions to any point along the centreline at axial station x (equation (A7) in [99])

$$P_s + \frac{1}{2}\rho {V_s}^2 = P(x) + \frac{1}{2}\rho\frac{Q^2}{A^2(x)} \tag{B.29}$$

in which ρ is the fluid density, P_s is subglottal pressure and V_s is sublgottal velocity, Q is glottal mean volumetric flow rate, $A(x)$ is cross-sectional area of the glottis at axial

station x, and $P(x)$ is the pressure in the entire transverse section at x, therefore it is the projected pressure at the point on the medial vocal fold surface at axial station x as well. In other words, it is taken to be the vertical, i.e. y, component of the surface traction on the medial surface at axial station x. By a one dimensional conservation of mass, assuming incompressibility, we have

$$Q = V_s\, A_s = V(x)\, A(x) = V_d\, A_d = V_e\, A_e \tag{B.30}$$

in which V_s and A_s are subglottal velocity and area, $V(x)$ and $A(x)$ are velocity and area at axial position x, V_d and A_d are velocity and area at the point of detachment or separation, V_e and A_e are epilaryngeal velocity and area, and mean volumetric flow rate Q is equivalent to any one of the products. Each of the products in (B.30) assumes uniform axial velocity at each streamwise station, therefore, V_e must be taken far upstream after the glottal jet has reattached where V_e may be assumed to be uniform over epilaryngeal cross-sectional area A_e. Substituting the volumetric flow rate at separation from (B.30) for Q in (B.29),

$$P_s + \frac{1}{2}\rho {V_s}^2 = P(x) + \frac{1}{2}\rho \frac{{V_d}^2 {A_d}^2}{A^2(x)} = P(x) + \frac{1}{2}\rho {V_d}^2 \frac{{A_d}^2}{A^2(x)}, \tag{B.31}$$

and rearranging to obtain (equation (A10) in [99])

$$P(x) = P_s + P_{ks} - P_{kd} \frac{{A_d}^2}{A^2(x)} \tag{B.32}$$

where, P_{ks} and P_{kd} are subglottal dynamic pressure and dynamic pressure at separation. Titze argues in [99] that, for typical subglottal pressures, between 500 and 1000 [Pa], and typical subglottal velocities, approximately 0.7 [m/s], subglottal dynamic pressure is three orders of magnitude smaller than the subglottal static pressure, and therefore that subglottal dynamic pressure is to be neglected.

In order to obtain the dynamic pressure at separation, the kinetic energy recovery coefficient proposed by Ishizaka and Flanagan in [48] is employed. Consider the glottal configuration shown in Figure B.8 below with control volume as shown. Supposing that reattachment and pressure recovery are far downstream and that jet pressure is constant along the centreline, which enables the equating of centreline pressure at glottal exit with the jet pressure, and applying conservation of momentum in the x direction, obtain

$$\begin{aligned} P_d\, A_e - P_e\, A_e &= -\rho {V_d}^2\, A_d + \rho {V_e}^2\, A_e \\ P_d &= P_e - \frac{1}{2}\rho 2 {V_d}^2 \frac{A_d}{A_e} + \frac{1}{2}\rho 2 {V_e}^2 \end{aligned}$$

and, casting V_e in terms of V_d by equation (B.30),

$$\begin{aligned} P_d &= P_e - 2\left(\frac{1}{2}\rho {V_d}^2 \frac{A_d}{A_e} - \frac{1}{2}\rho {V_d}^2 \frac{{A_d}^2}{{A_e}^2}\right) \\ &= P_e - \frac{1}{2}\rho {V_d}^2 \left(2\frac{A_d}{A_e}\right)\left(1 - \frac{A_d}{A_e}\right). \end{aligned}$$

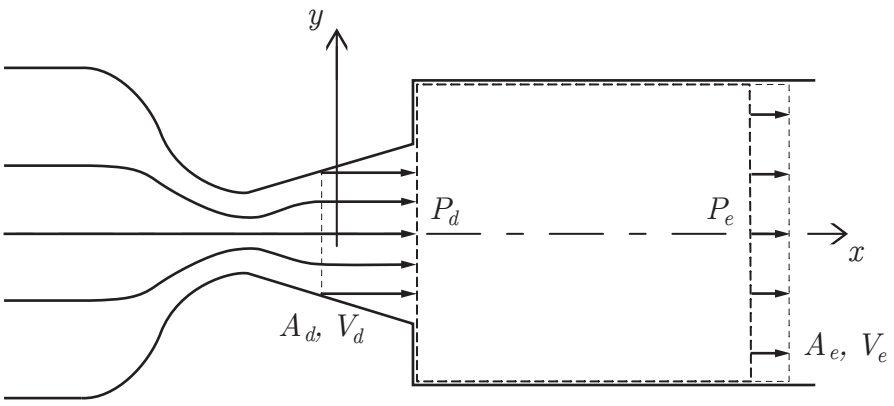

FIGURE B.8: The control volume employed to justify the kinetic energy recovery coefficient k_e on the basis of conservation of momentum.

Thus, we have (equivalent to equation (7) in [48]) which determines centreline pressures,

$$P_d = P_e - P_{kd}\left[2\,\frac{A_d}{A_e}\left(1 - \frac{A_d}{A_e}\right)\right]. \tag{B.33}$$

The coefficient of the dynamic pressure at separation is k_e, the kinetic energy recovery coefficient. That is (equation (A23) in [99])

$$k_e = 2\,\frac{A_d}{A_e}\left(1 - \frac{A_d}{A_e}\right). \tag{B.34}$$

Thus, equation (B.33) may be written (equation (A22) in [99])

$$P_d = P_e - k_e\,P_{kd} \tag{B.35}$$

Finally, applying Bernoulli between the subglottal region and the point of separation,

$$P_s + \frac{1}{2}\rho {V_s}^2 = P_d + \frac{1}{2}\rho {V_d}^2 = P_d + P_{kd}$$

and, neglecting subglottal dynamic pressure P_{ks} as before, obtain (equation (A24) in [99])

$$P_s = P_d + P_{kd} \tag{B.36}$$

which, upon substitution of (B.35) becomes

$$P_s = P_e - k_e\,P_{kd} + P_{kd} \tag{B.37}$$

or (equation (A25) in [99]),

$$P_{kd} = \frac{P_s - P_e}{1 - k_e}. \tag{B.38}$$

Therefore, the pressure distribution along the glottal centreline, due to the one-dimensional Bernoulli equation and accounting for pressure recovery, is

$$P(x) = \begin{cases} P_s - \frac{P_s - P_e}{1 - k_e} \frac{{A_d}^2}{A^2(x)}, & x < x_d \\ \frac{P_e - k_e P_s}{1 - k_e}, & x_d < x \end{cases} \tag{B.39}$$

where x_d is the axial location of the point of separation and k_e is as defined in (B.34). Equation (B.39), assuming constant jet pressure, takes the centreline pressure after the point of separation simply to be the static pressure at separation, P_d. Titze takes these pressures to determine the y components of forces along the medial surface of the vocal folds, therefore, $P(x)$ defined here is merely the y component of the wall normal surface traction along the medial surface of the vocal folds. The actual wall normal component of surface traction at the medial vocal fold surface is

$$\frac{P(x)}{\cos(\theta_{ng} + \theta)} \tag{B.40}$$

where $\theta_{ng} + \theta$ decomposes the absolute angular displacement of the right vocal fold into a mean angular displacement θ_{ng} determined by neutral glottal configuration, and a fluctuation or displacement from equilibrium position θ determined by the dynamical response of the vocal folds.

C | Simulation Code User's Manual

This appendix furnishes what is effectvely a user's manual for the simulation code developed in conjunction with this research project. The codes are written in MATLAB [60]. The simulation code for the 2-D potential channel flow extensively employs the freely available MATLAB package for manipulation of Schwarz-Christoffel mappings, the *SC Toolbox*, written by Trefethen and Driscoll. The package is documented extensively in the book by Trefethen and Driscoll, [24], and also in the online documentation for the toolbox [23]. The toolbox is available on Driscoll's website at http://www.math.udel.edu/~driscoll/SC/ (accessed at the time of writing).

The first section of this appendix furnishes a brief description of the SC toolbox, with a specific example of its use for generating an infinite polygonal region. The second section describes the scripts and functions of the implementation of the two-mass bar-plate dynamical model of the vocal folds together with the 1-D aerodynamic loadind model of glottal flow which provides the forcing of the dynamical model. The third section describes the scripts and functions of the fully 2-D unsteady ideal potential flow simulation code.

Descriptions of functions, including preconditions and postconditions, are provided. It must be strongly emphasized that, because MATLAB is a weakly typed language, in many cases it is essential that the parameters which are passed to functions be tested by the function to ensure that they conform to the expectations of the function. This is not always done, consequently, prior to runtime, the user is expected exercise extreme caution in ensuring that the variables passed are of the correct type. Especially when this verification is not performed by the function, the user must be aware of the types and ranges of values the function expects, the order of arguments the function expects, and the types and ranges of values the function produces as return values.

C.1 SC Toolbox

The SC tooblox for manipulation of Schwarz-Christoffel mappings in MATLAB is freely available at http://www.math.udel.edu/~driscoll/SC/ (accessed at the time of writing). The book [24] and package documentation [23] are tremendous resources and enable one to take full advantage of the package in a variety of polygonal configurations. Nevertheless,

a description of how to achieve various desirable outcomes with vertices at infinity are described below, including some pitfalls.

C.1.1 Functions

Overall, the SC package for MATLAB is employed in the following sequence

1. create a polygon with a call to `polygon`
2. create a map by calling the function which numerically solves for the required parameters (specific functions for different pre-images are enumerated in Table C.1 below)
3. parameters may be extracted by accessing the map object produced in 2. The map object may be used to visualize, compute forward transforms, inverse transforms, and derivatives of the transform.

`polygon` takes a pair of arguments, the first one is a vector of vertices, the second is a vector of interior angles. The various SC maps listed in table C.1 obtain the required parameters for differing pre-image regions and whether the range is the interior or exterior of some specified polygonal region.

TABLE C.1: Available SC mappings with different domains.

SC map	domain of pre-image	image
`diskmap`	$D(0,1)$, the unit disk about the origin	interior of polygon
`hplmap`	H^+, the upper half plane	interior of polygon
`stripmap`	infinite horizontal strip	interior of polygon
`extermap`	disk	exterior of polygon

Functions such as `plot` and `evalf` have been overridden to provide the functionality required in item 3.

C.1.2 An Example

In this example, a polygonal region in the physical plane will be specified and its pre-image will be determined. In order to specify an unbounded polygon, i.e., one with vertices at infinity, the interior angles must also be specified. Function `polygon` requires two parameters in this case, a list of vertices in the complex plane and a corresponding list of interior angles. For the polygon to fold back on itself at infinity, the interior angles there are zero. In particular, the polygon generated by the snippet of code

```
VERT = [ -1 - 1i, -1 - 0.5i, 1 - 0.3237i, 1 - 1i, Inf, ...
    1 + 1i, 1 + 0.3237i, -1 + 0.5i, -1 + 1i, Inf ];
alpha = Arg(VERT(2)-VERT(3));
ALPHA =[ 1/2, 3/2+alpha/pi, 3/2-alpha/pi, 1/2, 0, ...
    1/2, 3/2-alpha/pi, 3/2+alpha/pi, 1/2, 0];
p = polygon(VERT,ALPHA)
plot(p)
```

is shown in Figure C.1.

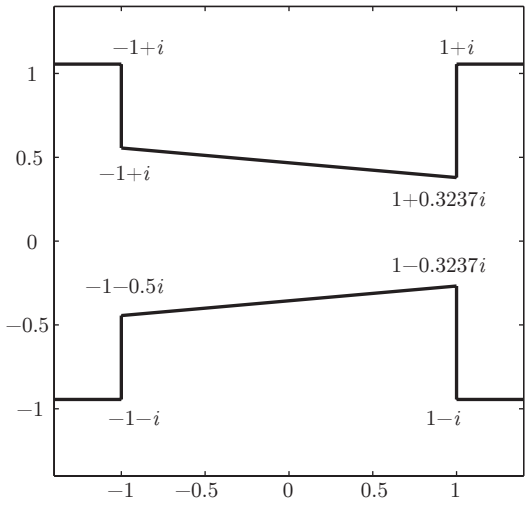

FIGURE C.1: Desired polygonal region.

Subsequently, the map object corresponding to the Schwarz-Christoffel map from the strip to this polygonal region may be obtained with a call to `stripmap`. Because the polygon has infinite vertices, the indices of the infinite vertices in the specification must be provided. The vertex at $-\infty$ as the vertex at index 10 in both vertex list `VERT` and corresponding list of interior angles `ALPHA`. The vertex at ∞ is the vertex at index 5. A call to `stripmap` determines the parameters corresponding to the SC mapping from the horizontal strip to the desired region. The following snippet of code,

```
ENDPOINTS = [10, 5];
f1 = stripmap(p,ENDPOINTS);
plot(f1)
```

generates the map object which may be plotted, and is shown in Figure C.2 (b). Figure C.2 (a), generaged by `plot(prevertex(f1),'.k')`, shows the pre-image of the SC mapping, (a) displays the horizontal strip together with the pre-images of the finite vertices.

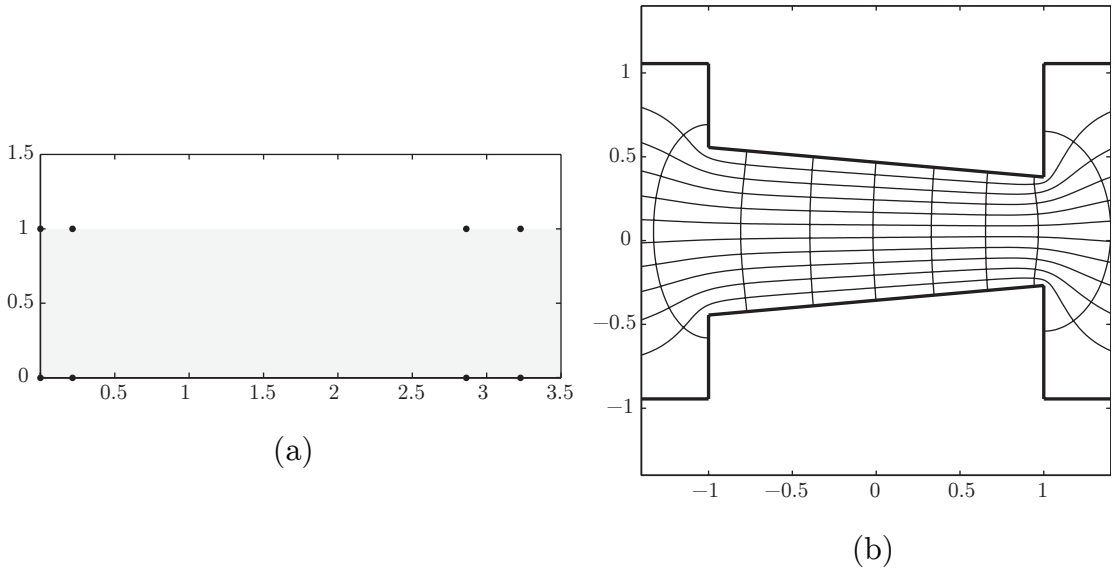

FIGURE C.2: Visualization of resulting SC map.

C.2 1-D Simulation Code

The 1-D simulation code replicates the 3 DOF body-cover model described in Titze [99] with loading due to 1-D incompressible potential flow with separation.

C.2.1 Scripts and Functions

Scripts and functions are enumerated in Table C.2. Script `Script_glottal_simulation` is the main script which specifies values of the parameters for each simulation and calls `glottal_simulation` for each set of parameters. The script also saves simulation results for each run. Various scripts for visualization have also been provided, and these may be modified as necessary. Functions employed by the 1-D simulation code which are not mentioned here are described in the section for the 2-D simulation code, Section C.3.

TABLE C.2: List of functions for 1-D simulation code.

functions and scripts
`glottal_simulation`
`Script_glottal_simulation`

C.2.1.1 `Script_glottal_simulation`

Within this script, a number of values which determine overall behaviour are set prior to calling `glottal_simulation`. `CORES` is the number of cores and is an integer between 1 and 4, but ultimately determined by the machines employed for simulation. The real duration of the simulation is established by setting `duration` to some positive floating point number, usually around 1 second. Variable `flow_model` is set to either `'attached'` or `'separation'` depending upon whether an attached flow or separated flow model is desired.

The simulation number set in `simulation_num` is an arbitrary integer between 0 and 9999 and determines the directory where the outputs of the run are stored. Similarly, the annotation set in `annotation` is a string which supplies an additional annotation to label the subdirectory where data files are stored. The script fails to execute if the number corresponds to a number which already exists. The output directory is

```
[ 'simulations\backslash' simulation_num_str '_' annotation ]
```

In each run, `glottal_simulation` is called with parameters determined by a structure of parameters, `simulation_parameters`. This is an array of structures, and, the structure at each index corresponds to a specific set of parameters for one run of the simulation. The fields of `simulation_parameters` is shown in Table C.3. Outputs are stored in a structure with fields `'index'`, `'simulation_parameters'`, `'time'`, and `'dynamics'`. The output is stored in the subdirectory created at the outset in a file named

```
[ 'glottal_simulation_at_index_' index_str '.mat' ]
```

in which `index_str` is a string which corresponds to the index of the simulation parameters for the run. The fields of structure `dynamics` are given in Table C.4.

C.2.1.2 `glottal_simulation`

Function `glottal_simulation` returns time and dynamics and takes simulation parameters as input. This function computes the time-domain simulation of the glottal flow and dynamics of the tissue model in the 1-D case. It is an implementation of the two-mass body-cover model presented in [99]. Structure `simulation_parameters` is unpacked immediately beginning with the dynamic parameters, then geometric parameters, equilibrium positions, initial conditions, flow parameters, and, finally timing. The simulation performs a temporal marching and returns a structure, `dynamics`, which contains the temporal evolution of the state of the dynamical system as well as the driving forces and pitching moments determined by the glottal flow model. Again, the fields of this return structure are listed in Table C.4. Return variable `time` is an array of times which align with the instants at which the entries in `dynamics` are obtained.

TABLE C.3: Fields of simulation parameter structure.

parameter	meaning
'max_iter'	maximal number of iterations is a hard limit
'duration'	overall duration of simulation [seconds]
't_nought'	nominal initial time
'delta_t'	time step, if empty, set by temporal scales
'M'	body mass
'm'	cover mass
'I_c'	moment of inertia of cover
'K'	translational stiffness of body
'k'	translational stiffness of cover
'kappa'	torsional stiffness of cover
'B'	translational damping of body mass
'b'	translational damping of cover
'B_c'	torsional damping of cover
'A_s'	subglottal cross sectional area
'A_e'	epilaryngeal cross sectional area
't'	vocal fold thickness
'fold_length'	vocal fold length (depth into page)
'z_n'	nodal point with respect to bottom of fold
'A_ng'	neutral glottal cross sectional area
'theta_ng'	neutral glottal angle of convergence
'rho'	fluid density
'P_L'	lung pressure
'P_s'	subglottal pressure
'P_e'	epilaryngeal pressure
'P_contact'	contact pressure – hydrostatic pressure
'Q'	volumetric flow rate within glottis
'V_s'	subglottal velocity
'theta_nought'	initial angular displacement from equilibrium & velocity
'xi_nought'	initial translational position & velocity of cover and body

TABLE C.4: Fields of dynamics output structure.

parameter	meaning
'theta'	absolute angular position of cover
'theta_dot'	angular velocity of cover
'eta'	absolute lateral displacement of cover from equilibrium
'eta_dot'	translational velocity of cover
'eta_b'	displacement of body mass from equilibrium
'eta_b_dot'	velocity of body mass from equilibrium
'Force'	resultant translational force
'Torque'	resultant pitching moment

C.3 2-D Simulation Code

The 2-D simulation code is an implementation of the simulation model developed in Chapter 3. The 3 DOF body-cover tissue model described in Titze [99] is coupled to a 2-D inviscid potential flow model of the glottal flow which is computed via conformal mapping techniques. The flow may be attached, it may separate from some point on the medial surface of the vocal folds, or it may separate at the trailing edge. The unsteady term in the pressure determination may or may not be included.

C.3.1 Scripts and Functions

Table C.5 lists the functions employed in the 2-D simulation code.

C.3.1.1 `num2zero_padded_str`

`num2zero_padded_str` takes a number and a number of digits and returns a string corresponding to the given number with an appropriate number of zeros prepended so that the length of the string is maximum of the desired number of digits and the length of the given number.

C.3.1.2 `Arg`

This function returns the principal argument, within numerical limits, of the input argument. Basically, this function packages `atan2`, i.e., it returns `atan2(imag(z),real(z))`.

TABLE C.5: List of functions for 2-D simulation code.

functions and scripts
Arg
complex_potential_at_zeta
geometry_gen
geometry_sep
geometry_sep_trailing_edge
glottal_simulation
log_output_to_disk
meet
minimal_glottal_area
num2zero_padded_str
pressure_force_and_pitching_moment
real_potential_at_z
symmetric_pair_update
velocity_at_z
vortical_velocity
Script_glottal_simulations
Script_visualization_plots_phase
Script_visualization_plots_series
Script_visualization_sync
Script_visualization_video

C.3.1.3 `Script_glottal_simulations`

This function is essentially identical to the one described for the 1-D simulation above. However, in the computation of the pressure field, the unsteady term may or may not be computed, this is established by setting boolean `d_PHI_dt_ON` to either `true` or `false`. The separation model is also one of separated flow which separates at some point on the medial vocal fold surfaces, always separates at the trailing edge, or reamins attached. This behaviour is established by setting `flow_model` to either `'separation'`, `'attached'`, or `'trailing_edge'`. Finally, initial vortex positions and strengths must also be provided to `glottal_simulation`, so `simulation_parameters` has two additional fields: `'z_0'` and `'Gamma'`. These are row vectors of initial positions and circulations arranged upper vortex – lower vortex.

C.3.1.4 `log_output_to_disk`

This function is a wrapper for save called inside of the `parfor` loop within the main script `Script_glottal_simulations`. `save` cannot be called within `parfor`, and, consequently

this function wraps save functionality so that data may be saved after each iteration of `parfor`. The function takes a string which identifies the filename of the output file, and, as a second parameter, the data which is to be saved.

C.3.1.5 `glottal_simulation`

The primary function called by `Script_glottal_simulations` for each set of simulation parameters. The function takes the structure of parameters, `simulation_parameters`, and two other variables which set the behaviour of the simulation: `d_PHI_dt_ON`, which is boolean and determines whether the unsteady term is computed in the determination of the pressure field; and `flow_model` which may be set, in `Script_glottal_simulations`, to either '`attached`' or '`separation`' or '`trailing_edge`' depending upon which separation model is desired. The function returns `time`, `geometry`, `dynamics`, `force_distribution`, and `vortices`. The first return variable is an array of times at which the state of the dynamical system was computed. The remaining structures contain geometric state, dynamical state, corresponding force and pitching moment distributions, and positions and strengths of vortices at each instant in `time`.

C.3.1.6 `pressure_force_and_pitching_moment`

Function `pressure_force_and_pitching_moment` computes pressures at control points along the medial surface of one vocal fold via the unsteady Bernoulli equation. The function obtains the resultant force and pitching moment and returns these along with the distributions from which they were obtained.

C.3.1.7 `geometry_sep` and others

The functions `geometry_gen`, `geometry_sep`, and `geometry_sep_trailing_edge` generate polygonal regions and corresponding map objects which correspond to a flow domain which is either attached, separating at some point on the medial vocal fold surfaces, or always separating at the trailing edge. The functions are specified as the following:

```
function [ P, CORNERS, CONTACT, VALID, MAP_OBJ ] = geometry_gen( ...
    h_1, h_2, t, node, delta, eta, theta, return_value, domain )

function [ P, VALID, MAP_OBJ ] = geometry_sep( ...
    h_1, h_2, delta, eta, theta, p, CORNERS, CONTACT, VALID )

function [ P, MAP_OBJ ] = geometry_sep_trailing_edge( ...
    h_1, h_2, p, CORNERS, CONTACT )
```

The functions require parameters `h_1` and `h_2`, which specify the upstream and downstream channel widths. In some cases other parameters, such as `t`, `delta`, `eta`, and `theta`, which completely specify the geometry are required. In `geometry_gen` `return_value` and `domain`, which specify whether a Schwarz-Christoffel map object will be returned and the structure of its domain are also required. These parameters define the geometry and the nature of the return values of the function call. The geometry dispalyed in Figures C.3 and C.4 show the definitions of and relations amongst the parameters. The first two function arguments specify inlet and outlet channel width for the horizontal channel symmetrically disposed about the horizontal axis. `t` specifies the glottal thickness, the horizontal dimension of the blockage as shown in Figure C.3. The blockage is disposed from $-l_{\text{node}}$ to $t_{VF} - l_{\text{node}}$ in the axial direction. `delta` is the minimal transverse glottal spacing for glottal flow; the flow is effectively shut off by the simulation in case the medial surfaces are in contact, and this condition is flagged by boolean return value `CONTACT`. `delta` is shown in Figure C.4 (b) and, in the same figure, `delta` is also the transverse spacing of the surfaces in (e) and (f) in the region of contact between vertices 3 and 4 in (f) and between vertices 2 and 3 in (f). Parameters `eta` and `theta` correspond to the y coordinate and angular displacement of the medial surface of the wall of the lower blockage as shown in Figure C.3. It is expected that `eta` is a value between $-(h_1 + h_2)/4$ and $-\delta/2$ and `theta` is expected to be $-\pi/2 < \theta < \pi/2$ when measured counter-clockwise from negative horizontal-axis. `return_value` is a string, either `'map'` or `'polygon'`, which determines whether or not a map object is returned. The final function argument is not necessary when a map is not requested. In the case `return_value` is set to `'map'`, `domain` is required. `domain` specifies the type of Schwarz-Christoffel transform which is returned as SC map object, `MAP_OBJ`. `domain` is a string, either `'strip'` or `'hp'` depending on whether the desired domain for the SC object is a horizontal strip or the upper half plane.

The return values are polygon `P`, array `CORNERS`, boolean `CONTACT`. Also, when input argument `return_value` is set to `'map'`, `MAP_OB`, which corresponds to the Schwarz-Christoffel map which maps from domain of type `domain` to the polygon `P`. `CONTACT` is boolean true if contact of surfaces occurs, i.e., when any part of the medial surfaces are within distance `delta` of each other, as shown in Figure C.4 (b), (e), and (f). `CONTACT` is false otherwise.

Function return value `CORNERS` is an array of indices of polygon `P` which correspond to the indices of the right medial vocal fold surface. In Figure C.4, the vertices along the lower surface are numbered. In (a), the fully open configuration, the indices of the right medial surface are 1 and 2. In (b), (c), (d), (g), and (h), the medial surface has indices 2 and 3. In (e) and (f), the medial surface comprises three vertices, 2, 3, and 4. `CORNERS` is important because it specifies the region of integration for the determination of the aerodynamic loading on the medial surface which is required for the force and torque inputs to the dynamical simulation of the vocal fold motion.

Due to the *crowding problem* for the numerical computation of the SC map object discussed in reference [24], the fully closed case is only computed once and persists in memory. This is achieved within the function by declaring several variables to be persisi-

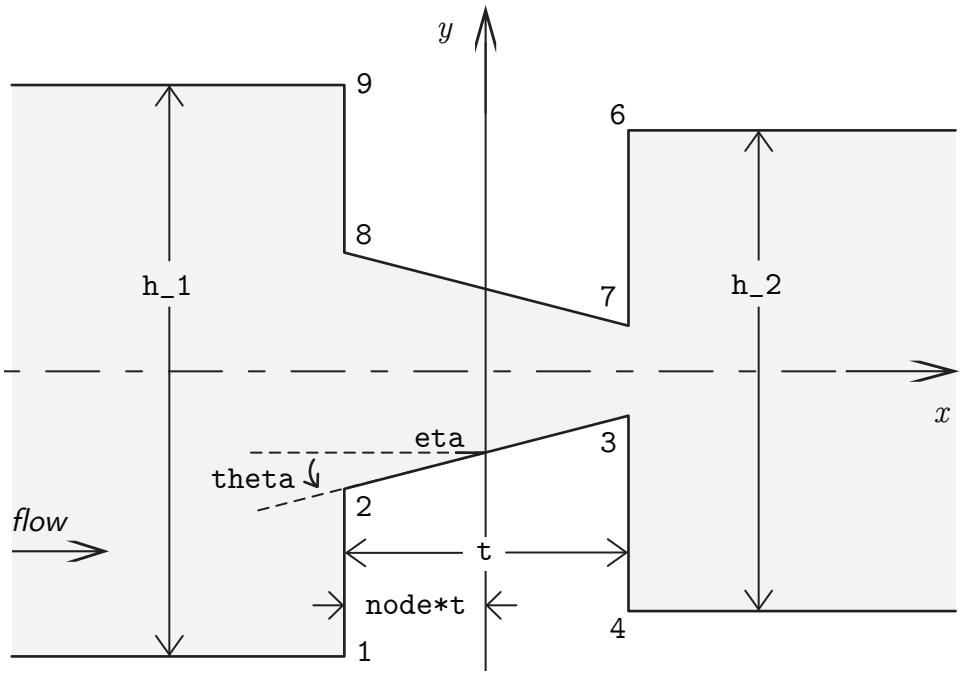

FIGURE C.3: Parameters of `geometry_gen` function explained. `h_1` and `h_2` determine inlet and outlet channel widths. `eta` determines y coordinate of the fulcrum of medial surface of the right vocal fold, and `theta`, the pitch angle measured counter clockwise from the negative horizontal axis. The width of the blockage is determined by `t`. The vertices of the polygonal region are numbered in the order shown with vertices 5 and 10 at ∞ and $-\infty$ respectively.

tent. Specifically, the inner corners of the right vocal fold (the lower surface) together with a map object which corresponds to a fully closed position, which is only computed the first time it arises. This prevents computation of the fully closed configuration, which is time consuming due to the crowding problem, but merely delays the simulations once.

Many distinct types of configurations have been identified as a consequence of particular choices of theta and eta; however, only a small number of these configurations will correspond to physically valid positions of the medial surface of the vocal fold. The remaining cases are required to mitigate the crowding problem if the simulation enters a situation in which it would occur, this is to prevent slowing of the simulation or its abrupt termination. The simulation code is capable of detecting and flagging the validity of the geometry.

Figure C.4 displays several possible glottal geometries. (a) shows a fully open case, which is the geometry which is returned whenever the medial surface determined by `eta` is below this region. (b) shows the fully closed case which typically occurs whenever `theta` is nearly zero while `eta` is greater than $-\delta/2$. (c) and (d) display diverging and converging glottal configurations respectively. (e) and (f) display cases of partial glottal closure. Finally, (g) and (h) exhibit the results of two calls to the `geometry_ gen` function,

one to determine the glottal geometry and one to determine the flow domain of a separated flow. In case (e), subglottal pressure is applied over the right medial vocal fold between vertices 1 and 2. In (f), epilaryngeal pressure is employed in the computation of force due to pressure between vertices 3 and 4. A fixed contact stress is applied over the medial surface where the vocal folds are in contact. In (g), separation exists at the trailing edge of the medial glottal surfaces, and, in (h), separation exists at some intermediate point along the medial glottal surfaces.

C.3.1.8 `meet`

`meet` returns either the real or the imaginary part of the point of intersection of two lines, one defined in terms of a point and slope, defined as the angle measured counter clockwise from positive real axis, and another line defined by a pair of points in the plane, given as complex numbers. The return values are `NaN` if no intersection exists, and the code warns of conditioning because it calls MATLAB's built in linear system solver. The final input argument specifies the part to be returned, by passing the string either `'real'` or `'imag'`.

C.3.1.9 `real_potential_at_z & complex_potential_at_zeta`

Function `real_potential_at_z` computes the potential at some point in the physical plane. The function obtains the pre-image of the desired point and the pre-images of the vortices and computes the complex potential at the pre-image of the desired point and returns the real part. Function `complex_potential_at_zeta` computes the complex potential some point within the horizontal strip

$$S = \{\zeta \in \mathbb{C} \mid 0 < \mathfrak{Im}\,\zeta < i\}$$

The potential at a given point on the strip is due to free stream and vortices. The coordinates of the vortices in the physical plane are passed to the function, so the function must obtain the pre-images of the vortices, which is why it also requires the geometry structure which contains the SC map object. The potential is computed according to the equations developed in Appendix B. A complex number representing the complex potential at the point is returned.

C.3.1.10 `minimal_glottal_area`

Glottal area, which is defined as the minimal projected transverse area of the glottis at any instant, is the most important correlate of voiced speech which is computed in these simulations. This function determines glottal area given the geometry of the vocal fold configurations. `minimal_glottal_area` takes the array of geometry structures and the vocal fold length and determines the minimal glottal area at each instant and returns an array of corresponding minimal areas. The function assumes the channel is symmetric, hence only the lower wall is traversed.

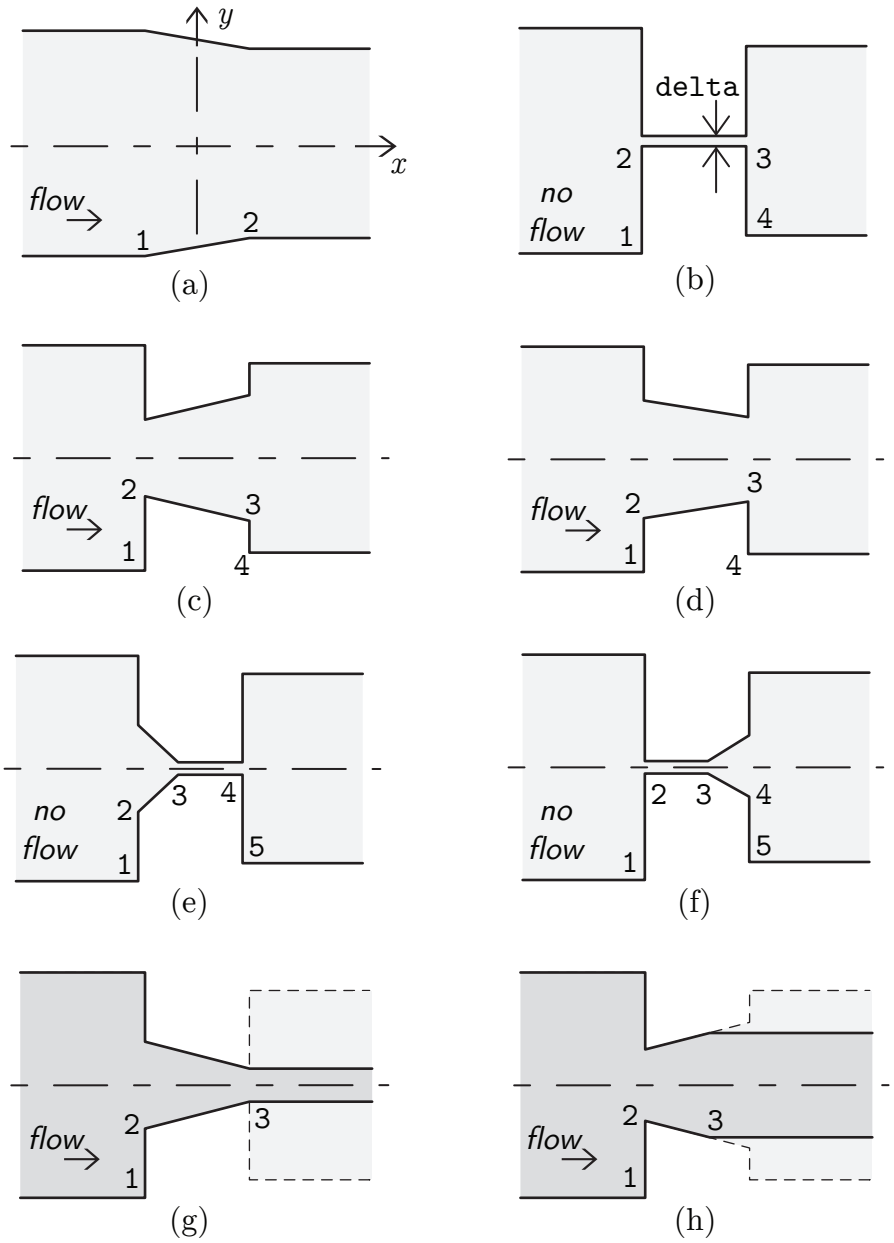

FIGURE C.4: (a) fully open, (b) fully closed, (c) diverging glottal, (d) converging glottal, and (e and f) partially closed configurations. P_s is applied between 2 and 3 in (e), P_e is applied between 3 and 4 in (f), and P_{contact} is applied at contact. (g) and (h) correspond to separated flow domains, where separation is either at the trailing edge, as in (g), or, in (h), at an intermediate point along the medial glottal surfaces.

C.3.1.11 `symmetric_pair_update`

Function `symmetric_pair_update` takes a lower vortex of a vortex pair and solves the vortex motion problem on the flow domain defined in map object and updates the position of the lower vortex. The position of the upper vortex is simply the complex conjugate of this point in the physical plane. In computing in this manner, a condition of symmetry about the midplane of the glottis is enforced.

C.3.1.12 `velocity_at_z`

`velocity_at_z` returns a single complex number which represents the velocity at a specified point in the physical plane due to upstream velocity and symmetric vortex pair. The function computes the pre-images of the given point and the given vortex centres, computes velocity at the pre-image, then scales the velocity by the conformal mapping to yield the velocity at the desired point in the physical domain.

C.3.1.13 `vortical_velocity`

Function `vortical_velocity` specified by

```
function [ velocity ] = vortical_velocity( ...
    z_0, Gamma, U_infinity, MAP_OBJ )
```

returns an array of complex numbers of the same size as `z_0`, and the values in the array represent the velocities of the vortices specified in `z_0` specified in the image plane due to the vortices and the free stream `U_infinity`. Vortices are located at points of `z_0` with strengths in corresponding positions in array `Gamma` The domain of the SC transformation is assumed to be an infinite horizontal strip between 0 and i. Circulation is taken positive counter-clockwise. `MAP_OBJ` contains the geometric information for the SC transformation. The function takes the pre-images of vortices specified in `z_0` to obtain `zeta_0`, then computes velocity of each vortex by using the point singularity equation (PSE) described in Stefan G. Llewellyn Smith *How do singularities move in potential flow?* [86], these velocities are scaled by the conformal mapping to yield the velocities at the original locations `z_0`. The exact formulation is derived in Appendix B.

C.3.1.14 Post Processing & Visualization

Several scripts are employed to post process the data to obtain phase portraits and plots of the temporal evolution. `Script_visualization_plots_phase` generates phase portraits and `Script_visualization_plots_series` generates plots of the temporal evolution of the dynamics. Other scripts generate video of the evolution of the geometry, such as `Script_visualization_sync` and `Script_visualization_video`. In all cases, within

the scripts, `data_directory` must be set to a string which identifies the directory where simulation results are stored, `sub_dir` must be set to a string which identifies the subdirectory in which the specific batch of simulations was saved, and `index` must be set to an array of indices corresponding to specific cases which are desired to be visualized.